Subject-Specific Efficacy Prediction of Mechanically Motivated Therapies for Heart Failure

Kevin L. Sack

Thesis presented for the degree of

DOCTOR OF PHILOSOPHY

In the Department of Human Biology

UNIVERSITY OF CAPE TOWN

December 2017

Supervisors

Associate Professor Thomas Franz

Department of Human Biology, University of Cape Town

Associate Professor Neil H Davies

Department of Surgery, University of Cape Town

Professor Julius M Guccione

Department of Surgery, University of California San Francisco

Assistant Professor Lik-Chuan Lee

Department of Mechanical Engineering, Michigan State University

Declaration

I, KEVIN LEIGH SACK, declare that this thesis titled, 'Subject-Specific Efficacy Prediction of Mechanically Motivated Therapies for Heart Failure' and the work presented in it are my own. I confirm that this work was done wholly or mainly while in candidature for a doctoral research degree at this University. I know the meaning of plagiarism and declare that all the work in the document, save for that which is properly acknowledged, is my own. I confirm that neither the whole work nor any part of it is being or is to be submitted for another degree in this or any other university. Where I have consulted the published work of others or included collaborative work, this is always clearly attributed.

I confirm that I have been granted permission by the University of Cape Town's Doctoral Degrees Board to include the following publications in my PhD thesis, and where co-authorships are involved, my co-authors have agreed that I may include the publications:

1. **K.L. Sack** , B. Baillargeon, G. Acevedo-Bolton, M. Genet, N. Rebelo, E. Kuhl, L. Klein, G.M. Weiselthaler, D. Burkhoff, T. Franz, and J.M. Guccione, *Partial LVAD restores ventricular outputs and normalizes LV but not RV stress distributions in the acutely failing heart in silico. International Journal of Artificial Organs*, 2016. 39(8): p. 421-430.
2. **K.L. Sack** , E. Aliotta, J.S. Choy, D. Ennis, T. Franz, G.S. Kassab, and J.M. Guccione, *Heart Failure but not Intra-Myocardial Algisyl-LVR™ Injectates Adversely Affects Tissue Structure in the Porcine Heart*. Journal of Applied Physiology, 2017. In review

Kevin Sack

Acknowledgements

Pursuing a PhD has a reputation for being a long, challenging and oftentimes infuriating task. Upon reflection, I can only consider the experience a fulfilling and positive one. The absence of frustration can only be attributed to the incredible people and intuitions that supported me during this process.

Firstly, my sincere gratitude goes to my primary supervisor associate Professor Thomas Franz for his guidance, encouragement and support. Tom, thank you for ensuring I got the most out of the research, for ensuring I was exposed to multiple opportunities and for promoting my interests as if they were your own.

I'm equally grateful to my co-supervisors, assistant Professor Lik-Chuan Lee, associate Professor Neil Davies and Professor Julius Guccione. A student is lucky if they have *one* good supervisor, and I was blessed with four! Thank you all for your support and guidance throughout the degree.

Additionally, I'd like to the thank Professor Guccione and Professor Mohammad Mofrad, for hosting me for visits to your labs at the University of California San Francisco and Berkeley, respectively. These trips provided invaluable experiences and opportunities, allowing me to connect and engage with outstanding collaborating researchers at multiple institutes.

The large portion of this research utilized data from animal studies at the California Medical Innovations Institute. My appreciation goes to Dr Jenny (Susy) Choy and Ghassan Kassab who performed and oversaw these experiments and provided the *in vivo* data associated with these experiments. Thank you for your continued collaboration, insight and meaningful scientific discussions. My thanks also goes to Eric Alliota and Professor Daniel Ennis from the University of California Los Angeles who provided the MRI and diffusion tensor data associated with these same experiments in the *ex vivo* state. Working with you all has been a stimulating privilege. I would also like to thank Professor Daniel Burkhoff for his continued collaboration and advice regarding ventricular assistance and the circulatory system.

I'd like to also thank Brian Baillargeon, Tom Battisti, Steven Levine and the rest of the team at the Living Heart project, Dassault Systèmes. The technical advice, the use of the model, and the opportunities to contribute to the project over the years, has been invaluable.

I'd also like to thank my colleagues and friends at both the Mechanobiology Lab and at the Centre for Research in Applied and Computational Mechanics. I am lucky to have shared a working environment with such intelligent, thoughtful and considerate colleagues.

My sincere appreciation goes to the funding and resources that were provided by the University of Cape Town, the National Research Foundation (NRF) and the Oppenheimer Memorial Trust. Thank you for seeing the value of this research and enabling me to pursue it.

I am fortunate to have the support of incredible family and friends. Especially my parents, Mike and Lin, who are unwaveringly encouraging and painstakingly determined to understand 'finite element modelling', 'continuum mechanics' and every other technical term in this thesis. They deserve a degree *ad honorem*.

My greatest appreciation is reserved for Zia Wasserman, who has and continues to be my greatest supporter, companion and partner. Thank you for putting up with all my shenanigans and sometimes encouraging them. This research wouldn't have been done without your encouragement.

Abstract

Predictive computational modelling in biomedical research offers the potential to integrate diverse data, uncover biological mechanisms that are not easily accessible through experimental methods and expose gaps in knowledge requiring further research. This is particularly relevant for investigating emergent therapies for heart failure, which remains a leading cause of death globally. In particular, two emerging mechanical therapies were considered here, namely, intra-myocardial biomaterial injection therapy and left ventricle mechanical assistance.

Recent preclinical trials have shown that alginate injections are a promising treatment for ischemic heart disease. Although improvements in heart function and global structure have been reported following alginate implants, the underlying mechanism is poorly understood. Using high-resolution *ex vivo* MRI and DT-MRI of hearts from normal control swine, swine with induced heart failure, and swine with heart failure and alginate injection treatment, we quantified the impact of intra-myocardial biomaterial injectates on the surrounding tissue structure in failing hearts.

This high-resolution data was then used to construct a precise fully subject-specific Finite-Element model of a healthy porcine heart. This model consists of coupled subsystems describing ventricular wall mechanics, lumped circulatory fluid flow and cellular mechanics. The model was calibrated using subject-specific clinical data, producing a realistic mechanical surrogate of the *in vivo* heart that predicts its dynamic strain and stress throughout the cardiac cycle.

These methods were extended to incorporate pathology and treatment, allowing for the creation of subject-specific Finite-Element models of control swine (n=3), swine with heart failure (n=3), and swine with heart failure and biomaterial treatment (n=3). This allowed for a regional quantification of stress and strain in both ventricles of the heart, allowing for the mechanical effect of the alginate injections to be properly characterized. Our findings show that alginate injections lower stresses in the myocardium globally (i.e. organ scale) and regionally according to proximity to the solidified gel injectates.

Additionally, a human heart was modelled to investigate the role of partial left ventricular assistance as a therapy for heart failure. By introducing modifications accounting for pathology and mechanically assisted flow, we were able to model the same heart under healthy normal conditions,

acute left heart failure and acute left heart failure with mechanical assistance between 2-4.5 l/min. Our findings show that acute left heart failure increases mean stresses throughout the heart. The introduction of partial assistance normalizes stresses in the left ventricle, but right ventricular stress was only partially improved.

Contents

List of Figures

List of Tables

Chapter 1 Introduction and background

This chapter contextualizes the subsequent research by summarizing the global burden of heart failure and identifying two novel mechanical therapies for further research. Thereafter a literature review is presented, focusing on advances in patient-specific computational modelling of cardiac mechanics, distinguishing specificity in cardiac geometry, myofibre architecture and mechanical tissue properties. Thereafter, the focus narrows to computational modelling of the mechanics of the infarcted heart and mechanically motivated concepts for treatments of heart failure. Particular attention is given to the modelling of intramyocardial biomaterial delivery and ventricular assistance devices as these treatments are investigated in this thesis. Subsequently the aim and objectives of the thesis are presented, followed by an outline of the thesis structure.

A publication resulting from this chapter entitled '*Personalised computational cardiology: Patient-specific modelling in cardiac mechanics and biomaterial injection therapies for myocardial infarction*' has been published in Heart Fail Reviews, 2016. **21**(6): p. 815-826. The sections that appear in this chapter are an extended version of that work, updated with recent literature findings and also include relevant findings of left ventricular assistance devices. Large sections of this chapter appear unchanged from the published manuscript

1.1 Problem identification

Cardiovascular disease (CVD) including myocardial infarction is the leading cause of death worldwide [1]. Low and middle income countries account for more than 80% of these deaths [1] - in South Africa, 33 people die per day due to heart attacks [2]. Considering that 30-40% of patients die from heart failure (HF) within one year of being diagnosed, alternative therapies are urgently needed. The plight of CVD places an extreme burden on healthcare systems, the global economic workforce and society in general. The economic costs for HF in the USA for 2012 totalled $30.7 billion and projections show that by 2020 this amount will increase almost 127% to $69.7 billion [3].

There has been significant recent interest in emerging mechanical therapies such as partial left ventricular assistance devices (LVADs) and biomaterial injection therapy as potential therapies to treat and limit the progression of HF.

LVADs treat HF by providing the left ventricle with sufficient mechanical circulatory support to allow for offloading, which in turn promotes myocardial remodelling and recovery [4-6]. Recent results show that miniaturized, less invasive, partial-support devices operating at low flow rates may have the potential to be used in more patients [7, 8]. What was once a therapy designed as a bridge to transplant has been increasing applied as destination therapy and even as a "bridge to recovery" whereby the device is explanted when mechanical assistance is no longer needed [9, 10].

In Biomaterial injection therapy, mechanically-tuned biomaterials are placed within the myocardial wall at or near infarcted regions of the heart. This therapy aims to support healing and to inhibit adverse remodelling that can lead to heart failure. Injectable biomaterials are showing promise in animal studies [11-13], although more research is needed to understand the specific mechanisms involved in improving cardiac function.

In an environment as complex as the failing heart there are a variety of factors that will influence the success of these therapeutic approaches. The biomechanical considerations relating to the mechanics, electrophysiology and biochemistry are intricate and complex. This is exacerbated by the number of independent parameters resulting from the biomaterial injection therapy (e.g. the timing, route of delivery and biomaterial properties) or LVAD therapy (e.g. flow rate, flow profile and duration).

Determining the impact of the various biomechanical parameters and how to optimize these therapies in their entirety would be an extremely challenging task for one to accomplish solely through *in vitro* and *in vivo* experimentation [14].

With the advancement of high performance computing and its accessibility, scientific models have the freedom to include more complex and realistic descriptions of the heart. Reliable computational models have the potential to provide a richer source of information for clinical decision-making, treatment, and the development of medical products. Already, patient-specific genetic, anatomical and physiological information is being incorporated in the clinical workflow.

The clinical desire to more accurately understand an individual's condition and treatment options, combined with advances in recent technologies, creates a compelling case to pursue subject-specific computational models. Subject-specific features allow for more accurate, realistic and representative models that increase the reliability of the findings and increase the suitability for utilizing computational models within the clinical workflow.

1.2 Introduction

Cardiovascular diseases are the single leading cause of death worldwide, accounting for 30% of all human mortality [15]. Despite recent advances in pharmaceutical, surgical, device and tissue-engineered therapy strategies, cardiovascular diseases remain one of the most costly, common and deadly medical conditions. Since predicted mortality of cardiovascular diseases is projected to increase, it is expected to remain the leading cause of death globally [15, 16].

Computational models can provide a unique framework for assessing efficacy of therapy approaches with relatively low resources: Therapeutic parameters can be easily modified and assessed in multiple concurrent *in silico* experiments, and computational sensitivity studies are easily conducted to optimize treatment efficacy. Advancing research and technologies have sparked a great deal of interest in integrating FE models into the clinical environment. This is becoming more achievable each year, making it likely that computational models will serve as the first line of the screening for future therapies in the years to come [17].

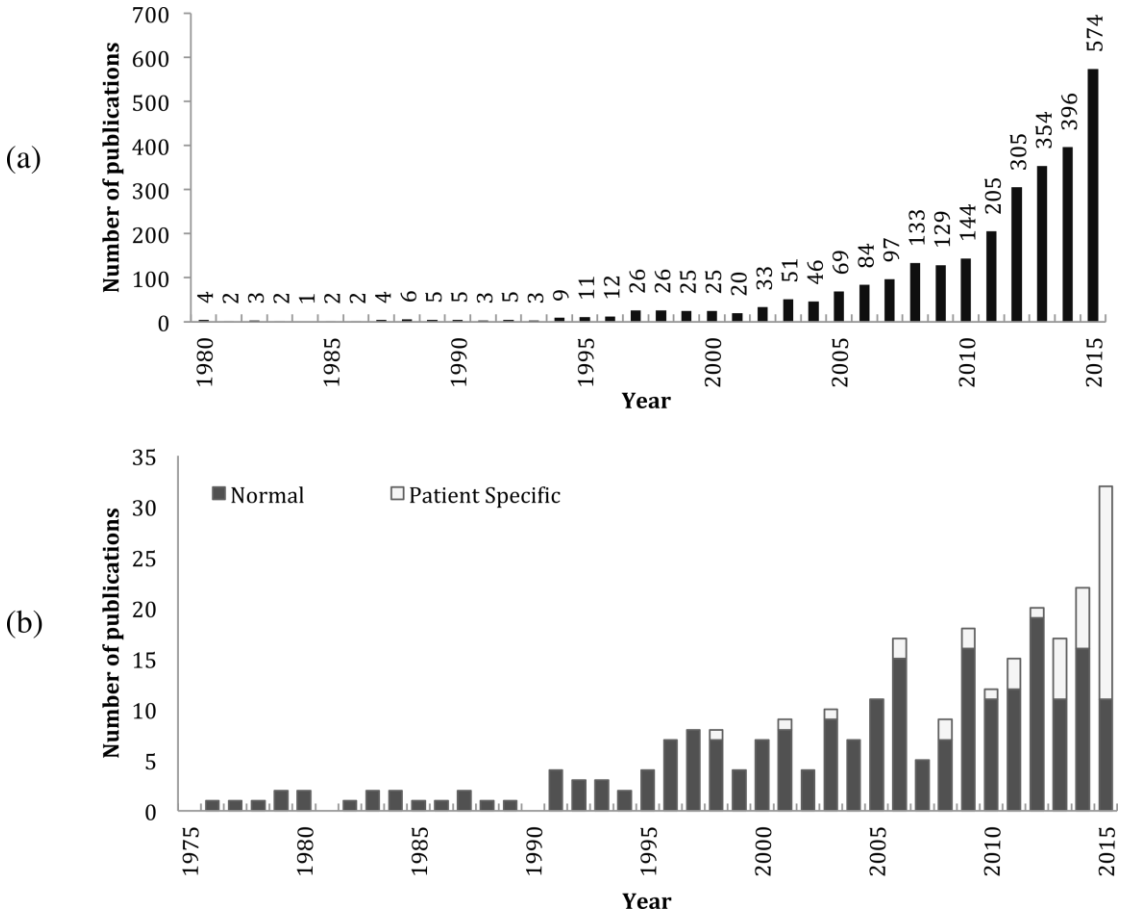

Figure 1.1: Number of yearly publications of peer-reviewed journal articles (a) with "patient-specific" or "subject-specific" contained in the title and (b) for finite-element-based studies focusing on cardiac ventricular mechanics. Source: Thomson Reuters ISI Web of Knowledge® and PubMed® databases, January 2016.

Reliable computational models can also provide a richer source of information for clinical decision support and treatment planning. Patient- and subject-specific research has been increasing at an exponential rate, as seen in *Figure 1.1*(a), and sources of patient-specific genetic, anatomical and physiological information are already being incorporated in the clinical workflow [18-20].

1.3 Patient-specific modelling of cardiac problems

1.3.1 Cardiac geometries

Anatomical simplification needs to balance model accuracy and computational demands. Until recently, this motivated the use of simplified left ventricular (LV) geometries introduced by various groups [21-23] as the primary computational tool for investigating cardiac mechanics. The use of patient-specific realistic geometries has, however, become prevalent in computational models *Figure 1.1*(b). This shift towards realistic geometries is indicative of the goal to create more representative computational models for use in clinical decision support.

The first three-dimensional patient-specific computational geometry of a heart was introduced by Okajima *et al.* [24] to study electrical activation. It took over two decades for deformable computational finite element (FE) approaches to incorporates realistic heart geometries [25]. Nielsen *et al.* [26] presented a realistic biventricular model that was novel for its accurate geometric description and definition of myofibre orientation. Stevens *et al.* [27] extended the model to account, in part, for the four valves. Since then, realistic geometrical models have become increasingly popular. The Living Heart Project recently developed the first full heart model that features a four-chamber human heart geometry with the four valves and the connecting large vessels [28].

To date, patient-specific cardiac geometries have been introduced as representative cases as proof of concept that a given computational approach can be applied in a patient-specific framework. Extending the concept to computational studies with a large number of patient-specific geometries could generate statistically meaningful results for a patient population. An alternative approach is to utilise a statistically averaged geometry that is representative of a patient population [29].

1.3.2 Myofibre orientation

The myofibre orientation has a critical influence on cardiac mechanics and electrophysiology. However the description of myofibre orientation is a highly intricate and sophisticated task, which has been the subject of substantial historical disagreement [30-32]. The intricacy stems from the complex multiscale branching and merging of cardiac myocytes at microscopic scale, creating anisotropy at

tissue level that changes dramatically throughout the structure. An accurate numerical portrayal of the myofibre architecture needs to incorporate the one-dimensional directional tangent of the myofibre and the description of the fibre sheets [32-34], which influences both passive and active material behaviour.

In recent work, two methods are predominant in describing the myofibre orientation in patient-specific cardiac models: Rule-based reconstructions and fibre orientation derived from diffusion tensor magnetic resonance imaging (DTMRI). Rule-based approaches typically describe the fibre orientation analytically, or through aggregated experimental data, whereby a dense fibre orientation field is constructed through interpolation functions [35, 36]. This has recently been cast in the form of a boundary value problem, whereby the fibre orientation is prescribed along the surfaces of the ventricular structure and solved for throughout the geometry [37]. Rule-based reconstructions can be advantageous in their application to highly irregular geometries and their efficient implementation. In DTMRI approaches, the myofibre orientation is calculated from the eigenvectors of diffusion tensors. Due to the challenges of *in vivo* cardiac DTMRI, this method is often limited to a single *post mortem* data set. In this case, the derived fibre orientations are projected (or mapped) onto other subject- or patient-specific geometries obtained from computed tomography (CT) or magnetic resonance imaging (MRI) [38-40]. Toussaint *et al.* [41] recently captured *in vivo* patient-specific myofibre orientation data and integrated these data in other LV models of other patients. This approach involved diffeomorphic data transformations between a realistic geometry and the prolate spheroidal coordinate system.

Considering the sensitivity of FE predictions to variations in fibre orientation [42-44], it is preferable to incorporate patient-specific DTMRI data whenever possible. DTMRI is, however, still limited as the diffusion tensor characterizes only the mean myofibre structure in a voxel volume. Improved accuracy may be achieved by increased spatial resolution of the DTMRI scan or by including a dispersion parameter accounting for the deviation of the fibre orientation within in a voxel. Whereas homogenous dispersion has been considered in modelling myocardial tissue [45], dispersion at voxel scale has not yet been considered. The ability to capture *in vivo* DTMRI as performed by Toussaint *et al.* [41] and others [46-48] is the most advanced approach at present. No computational models have investigated cardiac function using truly individual patient-specific fibre orientation.

1.3.3 Constitutive Properties

The first constitutive relationship for passive myocardial behaviour, in the form of an exponential strain energy formulation, has been credited to Yuan-Cheng Fung [49-51]. The first invariant-based constitutive model was described by Humphrey and Yin [52], introducing an additional “fibre specific” term to account for the material anisotropy, although limited to transverse isotropy [50].

Costa *et al.* [53] developed an extended orthotropic formulation featuring a fibre-specific coordinate system and principal material stiffness along the fibre, sheet and normal directions. With minor modifications, the formulations are commonly represented as a strain energy density function with the following form [54, 55]:

$$\Psi = \frac{1}{2}(Ce^{Q} - 1) + A_{incomp}. \tag{1.1}$$

Here, Q is a function of the material strains (usually Green-Lagrange), often given as

$$\begin{aligned} Q = b_{ff}E_{ff}^2 + b_{tt}E_{tt}^2 + b_{nn}E_{nn}^2 + \frac{b_{nf}}{2}\left(E_{nf}^2 + E_{fn}^2\right) + \frac{b_{nt}}{2}(E_{nt}^2 + E_{tn}^2) \\ + \frac{b_{tf}}{2}\left(E_{tf}^2 + E_{ft}^2\right), \end{aligned} \tag{1.2}$$

where E_{ij} are the components of the right Cauchy-Green deformation tensor in local fibre coordinates and b_{ij} are the corresponding material parameters. For further detail, the interested reader is directed to [53-55]. The strain energy function in the exponential form can also be constructed by considering the invariants I_i of the right Cauchy-Green strain tensor [56]:

$$\Psi = \frac{a}{2b}e^{b(I_1-3)} + \sum_{i=f,s}\frac{a_i}{2b_i}\left\{e^{b_i(I_{4i}-1)^2} - 1\right\} + \frac{a_{fs}}{2b_{fs}}\left\{e^{b_{fs}I_{8fs}^2} - 1\right\} + A_{incomp}, \tag{1.3}$$

The notation and material parameters detailed by Holzapfel and Ogden [56] have become the most widely used form of a passive material law for cardiac mechanics, often recalibrated with new material parameters [36, 57, 58]. More detail regarding this strain energy functions is provided in Section 3.2.4. The incompressibility of the material is handled through a penalty function A_{incomp}, of which multiple variations exist. Alternatively, incompressibility is often implemented through mixed formulation methods, or by splitting the deformation into purely isochoric and deviatoric components.

The incorporation of active tension into a mathematical description to capture the contractile behaviour of the heart is a significant task. The most common approach, introduced by Hunter and Smaill [59] and developed by Guccione *et al.* [60] relies on additive contribution of the active stress to the overall material stress, typically along the local fibre orientation. Active tension can be constructed using various physiologically meaningful parameters, which has been employed by many studies [28, 57, 61, 62]. Another emerging approach involves multiplicative decomposition of the tensor gradient of deformation [63-65], in a similar fashion to the theory of volumetric growth. Multiplicative decomposition is more mathematically robust whereas the additive approach can capture physiological phenomena more meaningfully [63]. The latter is due to a more flexible

formulation that allows for parameter calibration on a tensor component level [63, 64]. Contractile material behaviour can be coupled within an electromechanical framework, whereby a more realistic excitation-contraction pattern is incorporated into the model. Over the last decade, this multi-physics coupling has been introduced with great success in various computational models [66-72].

It is impossible to meaningfully determine the three-dimensional patient-specific material properties from ventricular pressure-volume relationships alone [73]. To remedy this, the identification of suitable values for the constitutive parameters (sometimes called calibration) often utilises additional data. *In vitro* bi-axial and shear stress-strain experiments [74, 75] on cardiac tissue have been used to calibrate numerous constitutive laws. The reliability of *in vitro* experiments may be questionable due to tissue damage or disruption in the process of extraction [76]. Inclusion of *in vivo* data in material calibration provides a more realistic mechanical environment for loading and deformation [77]. Obtaining these stress-strain data from magnetic resonance elastography (MRE) or tagged MRI provides additional advantages whereby patient-specific information can be captured into the constitutive law through optimization approaches [38, 73, 78-80]. This approach has recently been extended to additionally estimate infarct material parameters [81, 82]. Considering the anatomical variability amongst patients, it becomes increasingly attractive to incorporate as much *in vivo* data into the material calibration process as possible. Ideally, one would calibrate material laws using *in vivo* data that correspond to the same geometry and fibre distribution used in the computational model – an inherently patient- or subject-specific process that can easily be adopted to handle cardiac pathologies e.g. myocardial infarction.

1.4 Heart failure and infarct mechanics

Heart failure (HF) is a progressive and debilitating condition describing the inability of the heart to function properly. Depending on cause, HF can occur abruptly (acute HF), gradually, or may be congenital. Ischemic HF, which can manifest either abruptly or gradually, comprises the majority of all HF cases [83, 84].

Myocardial infarction (MI) is a result of ischemia in the heart muscle usually caused by an occlusion in a coronary artery, which interrupts blood supply to the affected region. This leads to substantial cell death and in immediate impairment of pump function in the affected ischemic region. In addition to the lack of regional contractility due to tissue damage, MI initiates a series of complicated physiological processes that alter the mechanical, structural and cellular properties of the heart.

Subsequent to ischemia the infarct region undergoes necrosis, fibrosis and remodelling. Over the course of several weeks, heart function declines, ventricular loading increases and the infarct region

typically becomes thinner, less contractile and stiffer than the surrounding healthy material [85, 86]. Depending on the size and location of the infarct, the compromised heart can experience acute failure or continued deterioration of function, which leads to heart failure.

1.4.1 Modelling infarction, heart failure and potential treatments

Non-invasive assessment of the failing heart is essential for optimal treatment. Local wall stress, in particular, can be a key factor in assessing cardiac function and predict post-MI effects, yet wall stress cannot be measured systematically and quantitatively with clinical modalities [87]. Imaging techniques provide high accuracy information regarding the strain distribution in the heart, yet cannot provide local stress information. Laplace's law, used to estimate cardiac wall stress, makes considerable assumptions with respect to the cardiac structure and provides considerably different results to anatomically accurate FE models [88].

FE models have been labelled as the most versatile approach for quantitatively predicting myocardial stress and strain distributions [89, 90]. The effects of MI on structure and function of the heart has received increasing attention for FE modelling. The understanding of the aforementioned is essential when developing a treatment to restore cardiac function and to attenuate adverse post-infarct remodelling. Simulating MI *in silico* allows the influence on heart to be directly quantified [65, 91-94], providing deeper insight into the underlying mechanisms involved. For example, by complementing a study on dosage efficacy of the ACE inhibitor Ramipril, FE models showed that apical wall stress is an independent predictor of ventricular remodelling [95].

Lee *et al.* [96] complemented a clinical study that investigated coronary artery bypass grafting (CABG) and biomaterial injections with accurate descriptions of cardiac performance through volumetric and stress measurements. Finite element models for three patients suffering with heart failure were created with geometries extracted from MRI images pre-treatment at three months and at six months post-treatment. The treatment restored left ventricular geometry, attenuating the remodelling process, and heart function improved. The FE models provided highly accurate predictions of cardiac function, including ejection fraction and wall thickness; ventricular shape, via a sphericity index, and compute stress states throughout the geometry using validated mathematical models. The changes due to treatment resulted in a more uniform distribution and 35% reduction in myofibre stress throughout the LV, measurements that would be unquantifiable without the FE models.

Surgical ventricular restoration (SVR) has been the focus of several computational studies [97-101]. The most recent SVR studies [99, 100] provide examples how FE models with increased complexity can contribute to elucidating physiological processes and guiding treatment development. For the

treatment of MI, Guccione *et al.* [102] investigated a 'myosplint' device aimed at restraining the epicardium to prevent remodelling. Wenk *et al.* [103] explored the Acorn CorCap Cardiac Support Device as treatment for dilated cardiomyopathy. Another ventricular restoration approach relies on the Parachute© device [104] which was the subject of a patient-specific FE study indicating that the reduction of end-diastolic wall stress underlies the therapeutic benefit [62].

A secondary adverse condition resulting from ventricular remodelling, and often associated with MI, is ischemic mitral valve regurgitation. This is a burgeoning research field for FE studies as computational models become increasingly sophisticated [105-108].

1.4.2 Modelling material injections in therapies for myocardial infarction and heart failure

There has been significant recent interest in intra-myocardial biomaterial injections as therapy for MI, whereby predominantly the infarcted region of the heart is injected with a biomaterial which aims to inhibit the adverse remodelling that leads to HF. Injectable biomaterials are showing promise in pre-clinical studies [11, 12, 109-114], resulting in a range of improvements to cardiac repair, with respect to wall thickness, ejection fraction and ventricular volume. Further research on the specific mechanisms by which these biomaterials improve cardiac function is needed to aid the development of more effective treatment.

Research into cardiac injection therapy has become diverse due to the choice of injectable material and the delivery method from a range of viable options [115, 116]. Due to this, the representation of intra-myocardial biomaterial injectates in computational models relies on either homogenisation approaches, whereby the injected material is averaged in the description of the myocardium wall, or through geometric approaches, whereby the injections are considered separate inclusions embedded within the wall.

Homogenisation techniques have shown consistently that bulking the myocardium with non-contractile material was sufficient to offset post-MI geometric changes and, consequently decrease stress in the myocardial wall [117]. Material injections that result in increased stiffness to the infarct region have also been shown to lower stresses in the infarcted and healthy regions of the heart in subject-specific ovine LV FE models [90] and for idealised ellipsoid LV models [118]. Improvements to cardiac function seen in the subject-specific ovine FE model such as wall thickening and increased ejection fraction [90] are consistent with *in vitro* and *in vivo* experiments [119]. In a combined experimental and computational study, Kichula *et al.* [120] used an ellipsoidal LV FE model to quantify the anisotropic increase in stiffness due to hydrogel injection and the reduction in local and global wall stresses. Dorsey *et al.* [114] developed subject-specific porcine LV FE models from

cardiac MRI data to estimate the *in vivo* diastolic material properties of infarcted tissue with therapeutic hyaluronic acid-based hydrogel injections.

For more viscous injectable materials or when the mechanical effects of the injectate at a microstructural level are being investigated [121-124], modelling the injected material as a discrete inclusion more meaningfully represents the mechanical considerations. Computational studies have consistently shown the beneficial impact to cardiac function from material injections of this nature. Wenk *et al.* [121] studied in an ellipsoidal LV FE model the optimal distribution of multiple spherical injectates. Kortsmit *et al.* [123] and Miller *et al.* [122] modelled the striated and bulk injectate distribution observed pre-clinically [11, 113, 119], as discrete sheet-like structures embedded within the myocardium in a canine biventricular model and a human LV model, respectively. These sheet-like hydrogel inclusions were shown to better improve cardiac performance in the ischemic infarct stage, but bulk-like injectates were shown to be better at improving LV function at the remodelling stage, complementing an experimental study in rats which investigated the effects of delayed gel-injection therapy [11]. Sirry *et al.* [125] presented a more realistic micro structurally detailed geometry of a striated polyethylene glycol hydrogel injectate in an infarcted rat heart.

Residual stress in the cardiac wall due to material injections has only recently been considered. Using a patient-specific LV FE model based on MRI data of a patient with HF, ischemic cardiomyopathy and hypertension, Lee *et al.* [126] revealed a complex regional stress field in vicinity of the a set of spherical hydrogel injectates located equidistant between the base and the apex of the LV. These first results warrant further investigation into the local changes the injections cause to tissue and fibre structure, as well as the mechanisms responsible for the clinically observed reduction of global stress [127].

Lee *et al.* [96] investigated a combination treatment of biomaterial injections and coronary artery bypass grafting with patient-specific models developed from MRI data of three patients suffering with HF. Simulating a longitudinal study with pre-treatment and three- and six-months post-treatment time points revealed a more uniform distribution and 35% reduction of myofibre stress throughout the LV.

These studies all consider simplified geometric representations for the representing the biomaterials under consideration and typically model their effects in low resolution (i.e. less than 10 000 elements).

1.4.3 Modelling ventricular assistance devices in heart-failure therapies

The use of LVADs as a successful intervention therapy for HF is increasing year on year [128], with the potential to dramatically increase with the introduction of partial (i.e. low-flow) LVADs as an early intervention therapy. While treatment using LVADs is expanding, the exact mechanisms

responsible for myocardial recovery and reversal of HF are still not fully understood, limiting the ability to predict long-term function, durable recovery or remission of HF. Myocardial recovery, to the point of device explantation occurs in a small percentage of patients, but could be further unlocked using patient-specific treatment and weaning strategies [10].

Over the last few decades, numerical and analytical models of circulatory flow and the introduction of ventricular assistance have been modelled extensively (e.g. [129-132]). These models represent heart function, without including geometric considerations (often referred to as 0D models). While some research has incorporated geometrically realistic ventricular assistance devices (VADs), these studies also ignore geometric representations of the heart [133-136].

The aforementioned research efforts were impeded by the substantial complexities involved in order to couple the circulatory system with geometrically realistic models of the heart. Only recently have computational models had the necessary sophistication to model this coupled behaviour (e.g. [28, 94]). Consequently, limited research exploring the effect of VAD function on ventricular wall mechanics has been investigated.

Jhun *et al.* [137] considered an idealized LV connected with a left ventricular assistance device (LVAD), investigating the mechanical role of the cannula tip and altered loading conditions on the idealized LV at the static time points of end-diastole and end-systole. McCormick *et al.* [138], [139] studied an FSI model of the LV under circulatory support, incorporating an accurate LVAD tip geometry inserted into the apex of the LV and modelled the fluid velocity and vorticity in the LV during VAD support. The primary focus of the former study was on fluid flow, with no emphasis was placed on wall stress nor strain, while the latter included additional analysis of the myocardial mechanics which they quantified in an energetic analysis. They found that LVAD support, particularly with a sinusoidal flow-rate lowered ventricular loading and reduced myocardial stresses in the LV

Lim *et al.* [140] coupled a biventricular mechanical model of the heart with a lumped circulatory system modelling both continuous and pulsatile LVAD support. Their study focused on the effect of LVAD support on LV peak pressure and energy consumption during systole. Their study reports some myofibre strains results, however stress values were excluded.

Evidently, the effect of VAD support on ventricular wall stress in the failing heart is under-investigated.

1.5 Discussion

The unique framework computational models provide for simulating and testing therapies with relatively low associated resources is unparalleled: Modifications to model parameters can be easily made; multiple studies can be performed simultaneously and resulting metrics are fully three-dimensional. Sensitivity and optimization studies are easily incorporated to aid in therapy design and increase treatment efficacy.

Advances in patient-specific modelling of cardiac mechanics over the last decade have been significant in almost every aspect. The quality of imaging and segmentation techniques coupled with computational resources becoming more abundant have allowed for unprecedented growth in the field. Cardiac structural and functional data is becoming increasingly available to researchers, allowing for new calibration methods and validation techniques. Geometrically realistic and reliable multi-physics models are becoming the new standard in computational cardiology.

The potential to create large-cohort patient-specific computational studies, whereby treatment or therapy for a cohort of patients could be simulated *in silico*, could unlock statistically meaningful findings for patient and population groups that would not be apparent from individual computational models. The unlimited ability to re-use models, perturb parameters and investigate sensitivity studies would provide an unprecedented wealth of information in the aid of treatment design. The use of patient-specific models shows equal promise in the tailoring of diagnosis, treatment planning and therapy design to an individual patient. Surgical ventricle restoration has in particular shown great promise in this regard, emphasising that medical treatment based on accurate patient-specific information has clear advantages over treatments that do not distinguish between one patient and another.

Despite these advantages, there has yet to be a single high resolution fully subject-specific computational model, constructed and calibrated using a single source of subject-specific data. Accounting for subject-specific myofibre structure, and calibrating material laws using comprehensive *in vivo* data is still largely excluded in computational models investigating cardiac mechanics. The local and global changes to myofibre structure in relation to MI and biomaterial injection therapy is also relatively unexplored in computational models.

Gel injection therapy has shown considerable promise as a viable treatment for acute MI with the potential not only to prevent heart failure but also to promote a reversal of the remodelling process, leading to healthier heart function. While recent modelling efforts have made significant progress, further research is needed to elucidate the exact mechanisms involved in improving heart function. Anatomically detailed gel injections, the structural changes in particular of the myofibre architecture

in the neighbourhood of injectate, fluid structure interactions, viscoelasticity and phase transformation are all underdeveloped aspects of these models.

Computational models have already been identified as a means to accelerate successful VAD design and treatment protocols due to the inherent ability of cheaply and efficiently perturbing treatment parameters. Currently, little is known about the regional effect of LVAD therapy on mechanical outcomes such as stress and strain in the heart. The further advancement of models to include subject-specific features can elucidate these mechanical changes and their relation to successful therapy. Additionally, subject-specific models incorporating LVAD therapy has the potential to create patient-specific treatments that maximize the possibility for myocardial recovery.

The long-term outlook of integrating computational models into the clinical workflow raises additional challenges. Constraints with respect to timing, availability of technology and financial resources must play a role in the model design. Advancing technology needs to be paced to incorporate the frontiers of medical science using resources available to the clinician.

Advances in technology and computational methods position patient-specific computer models as an inevitable and compelling tool with direct applications to diagnostics, therapy design and clinical decision support. The benefits of incorporating patient-specific computational models into the clinical sphere are overwhelmingly clear.

The creation of reliable, highly realistic predictive computational models requires comprehensive subject-specific *in vivo* data for calibration and validation. In the context of cardiac mechanics, current *in vivo* imaging technologies are not yet advanced enough to provide comprehensive clinical data required for truly patient-specific computational models. Until imaging modalities such as *in vivo* cardiac DTMRI become more available in the clinic, the shortage of patient-specific data requires the pursuit of pre-clinical subject-specific alternatives, where a richer resource of *in vivo* and *ex vivo* data can be utilized. Subject-specific computational modelling does offer significant potential to complement pre-clinical experimental research, to act as a necessary precursor to clinical research, and to perhaps play a crucial role in mechanical therapies for myocardial infarction and prevention of infarct induced heart failure.

1.6 Aim and objectives of the thesis

The aim of this research is the development of computational cardiac models that simulate ventricular function and myocardial mechanics in a subject-specific context that can be used to investigate mechanically motivated treatments for heart failure. Through computational modelling and

simulations, the biomechanical mechanisms associated with heart failure and mechanical stimulus associated with therapies can be determined and better understood.

The main objectives of this study are:

1. To develop computational models to simulate the mechanical environment in the failing heart.
    a. To establish subject-specific geometries for healthy, failing and treated hearts, suitable for finite element modelling.
    b. To establish physiologically meaningful three-dimensional (3D) descriptions of myofibre orientation to be utilized in healthy, failing and treated hearts. Investigating the spatial distribution and dispersion/reorientation of fibres in regions of the heart injected with biomaterials and utilize this geometric information in computational models.
    c. To establish constitutive models for the healthy and diseased myocardial tissue and the injectable biomaterials. Calibrate subject-specific models utilizing *in vivo* clinical data.
    d. To computationally simulate the ventricular biomechanics of healthy hearts, failing and mechanically treated hearts using biomaterial injection therapy and partial left ventricular assistance devices.
2. To demonstrate the feasibility of the developed methods and models for the computational investigation of subject-specific efficacy of intra-myocardial biomaterial injectate therapies towards clinical prognostic treatment guides.
    a. To determine the extent of fibre reorientation caused by biomaterial injection therapy and to investigate its impact on cardiac function and wall mechanics.
    b. To assess therapy efficacy using computational subject-specific model results. Analysing cardiac performance parameters and biomechanical metrics of stress and strain in the myocardial wall, in particular in the infarct region and functional border zone, is expected to provide further insight into therapeutic mechanisms.
3. To assess the therapeutic efficacy of partial left ventricular assistance devices in the treatment of acute left heart failure.
    a. To assess the biomechanical metrics of stress and strain in the left and right ventricle in the healthy, failing and treated heart in order to determine if partial (i.e. low flow rate) left ventricular assistance devices (LVADs) can normalize ventricular stress and function.

1.7 Data acquisition and animal studies

Development and validation of computational models will be facilitated with pre-existing pre-clinical cardiac imaging data. The experimental protocols and *in vivo* data acquisition was performed by collaborators at the California medical innovation institute. The *ex vivo* MRI and DT-MRI data acquisition was performed by collaborators at the University of California Los Angeles. This quantitative data set comprises three-dimensional ex vivo MRI and DT-MRI data acquired by myocardial strain for hearts. Pre-clinical data from porcine hearts is available from collaborator Prof J Guccione, University of California San Francisco

1.8 Computational software

The Abaqus software environment (version 6.14, Dasssult Systèmes, Providence, RI, USA) was chosen as the finite element solver for this research. For algorithmic detail regarding how this software implements key aspects of the solution method (i.e. enforcement of boundary conditions, time-stepping etc.) the interested reader is directed to the Abaqus theory guide [141]. As the required material laws for this research go beyond the available material choices within Abaqus, additional material laws for cardiac tissue were developed for this research defined in a FORTRAN subroutine that interfaces directly with the Abaqus solver. For the creation of geometries and finite element meshes, Simpleware ScanIP (Synopsys, Mountain View, USA) was used. Additional computational tools to interface with Abaqus, perform pre-processing tasks (e.g. the interpolation of fibre coordinates) and post-processing analysis were developed in Matlab (The MathWorks, Inc., Natick, Massachusetts, United States) and Python (Python Software Foundation. Python Language Reference, version 2.7).

1.9 Thesis structure

The following chapters comprise the following:

Chapter 2 describes the application of biomaterial injection therapy to porcine subjects and studies the impact the therapy has on the myocardial tissue structure. Additionally, key features of the biomaterial injectate geometry and orientation are reported, establishing critical information to be used in later chapters.

Chapter 3 describes the development of a fully subject-specific heart in the healthy state. The chapter details the methods, results and validation of the model, detailing its suitability to predict cardiac function *in silico*.

Chapter 4 describes the extension of methods to account for ischemic heart failure and inclusion of biomaterial injection therapy. The results of multiple subject-specific models are presented, these are analysed to reveal mechanical effects of ischemic tissue, biomaterial injection therapy and their interaction.

Chapter 5 describes the extension of methods to account for acute heart failure, the inclusion of a partial LVAD into the model description and studies the effect of pathology and mechanical treatment on ventricular function and stress.

Chapter 6 is a concluding chapter, which discusses the results of the study with relation to the original aims as a single body of work. Additionally this chapter highlights the key outcomes of this research and provides recommendations for future research in subject-specific computational cardiac modelling.

Consistent referencing is used throughout the thesis and a single combined bibliography is presented after Chapter 6.

1.10 Publications originating from this research

1) **K.L. Sack** , N.H. Davies, J.M. Guccione, and T. Franz, *Personalised computational cardiology: Patient-specific modelling in cardiac mechanics and biomaterial injection therapies for myocardial infarction*. Heart Fail Reviews, 2016. **21**(6): p. 815-826.
2) **K.L. Sack** , B. Baillargeon, G. Acevedo-Bolton, M. Genet, N. Rebelo, E. Kuhl, L. Klein, G.M. Weiselthaler, D. Burkhoff, T. Franz, and J.M. Guccione, *Partial LVAD restores ventricular outputs and normalizes LV but not RV stress distributions in the acutely failing heart in silico. International Journal of Artificial Organs*, 2016. 39(8): p. 421-430.

Chapter 2 Investigation into the effects of intramyocardial Algisyl-LVR™ injectates on myocardial tissue structure in the failing ischemic heart

Recent preclinical trials have shown that alginate injections are a promising treatment for ischemic heart failure. Although improvements in heart function and global structure have been reported following alginate injections, the underlying mechanism is poorly understood. This chapter describes the treatment protocol of porcine subjects treated with Algisyl-LVR™, an alginate-based biomaterial injection therapy, and studies the impact the therapy has on the myocardial tissue structure.

This is the first study to quantify the impact of intra-myocardial biomaterial injectates (solidified injections) on the structure of the surrounding tissue in hearts with heart failure. Using high resolution *ex vivo* MRI and DT-MRI techniques we characterized local myofibre orientations and wall thickness changes, revealing the direction of tissue displacement due to injectable biomaterial.

A manuscript of this study titled, *'Heart Failure but not Intra-Myocardial Algisyl-LVR™ Injectates Adversely Affects Tissue Structure in the Porcine Heart'* has been drafted and submitted to the Journal of Applied Physiology. The following sections are taken verbatim from this manuscript with permission of the UCT Doctoral Degree Board.

2.1 Introduction

There is considerable interest in intra-myocardial biomaterial (e.g., alginate) injections as a treatment of myocardial infarction (MI) and infarct-induced heart failure (HF). Injectable biomaterials have already shown promise in pre-clinical studies resulting in a range of improvements including increased ventricular wall thickness [11-13, 110-113], increased scar thickness [11, 13, 111], higher ejection fractions [11, 12, 110-112] and decreased ventricular dilation [11-13, 110-113]. Alginate

injections are known to have nonthrombogenic properties [142, 143] in addition to mitigating the effects of adverse ventricular remodelling following MI, which makes them a particularly viable potential therapy.

Human HF patients treated with Algisyl-LVR™, a commercialized injectable alginate polymer, and coronary-artery bypass-grafting showed dramatic improvements in ejection fraction, decreased ventricular wall stress, and increased wall thickness at 3 and 6 months post treatment [96]. Additionally, HF patients enrolled in clinical trials experienced significant improvement in NYHA class description, mean peak VO_2 and quality of life [144, 145]. These studies all recognize the potential of Algisyl-LVR™ as an emerging therapy for HF and recommend further development and investigation in order to aid the development of a more effective (and potentially patient-specific) treatment.

The degree of efficacy likely depends on a range of factors, especially the local interactions between the alginate material and the surrounding tissue. The impact on the surrounding myofibre structure and the nature of myocardial tissue displacement is poorly understood. For example, the increased wall thickness reported in several studies has been ascribed to several causes, including radial displacement of the tissue, tissue growth, or possibly an inflammatory response to the foreign material [146]. A better understanding of the mechanical effect of the alginate injectates can more clearly identify the mechanisms responsible for the observed efficacy and assist with design of better treatment protocols to maximize clinical outcome.

The objective of this study was to quantify the impact of Algisyl-LVR™ injections in healthy and HF myocardial tissue by investigating changes to regional myofibre orientations and global myocardial structure using *ex vivo* diffusion tensor magnetic resonance imaging (DT-MRI) techniques. DT-MRI is a well-established method for quantifying myofibre orientation [147, 148] and the laminar structure [149, 150] from *ex vivo* myocardium. We also sought to quantify the retention rate and morphology of the Alginate injectates.

2.2 Materials and Methods

Animals used in this study were treated under a protocol approved by the California Medical Innovations Institute's Institutional Animal Care and Use Committee and in compliance with the "Guide for the Care and Use of Laboratory Animals" prepared by the Institute of Laboratory Animal Resources, National Research Council, and published by the National Academy Press, revised 1996.

2.2.1 Experimental protocol

Eleven domestic swine with HF weighing 42.6 ± 1.9 kg and eight controls weighing 61.3 ± 13.4 kg were used in this study. The animals and subsequent data were divided into groups according to treatment as follows: Normal control (NC) subjects that served as a control (n=8); Heart-failure injected (HFI) subjects that received biomaterial injections (n=6), and heart-failure control (HFC) subjects that served as control (n=5).

To induce HF, the obtuse marginal branches of the left circumflex artery were occluded in each animal. This was achieved via the percutaneous placement of embolization coils using a microcatheter (Cantata 2.9, Cook Medical, Bloomington, IN) to access the artery. Delivery of one to three 2- or 3-mm diameter embolization coils (depending on the anatomical variation) at two different time points (week 0 and week 2) resulted in ischemia and subsequent HF. The animals designated for treatment recovered for eight weeks before biomaterial injection therapy. The control animals recovered for sixteen weeks without biomaterial treatment.

The calcium-alginate biomaterial Algisyl-LVR™ (LoneStar Heart Inc. Laguna Hills, CA) used in this study has previously been described in detail [144]. The separate material components are mixed immediately before use and then combined in one syringe for delivery as direct intramyocardial injections [151]. The polymer forms solid inclusions inside the myocardial wall and achieves its final material stiffness of 3–5 kPa.

Algisyl-LVR™ was directly injected in a circumferential pattern into the left ventricle (LV) free wall during an open chest procedure. A total of 12-14 injections (0.3 mL each) were administered in two rows: one above and one below the mid-ventricular plane between the base and the apex (from the anterior to the posterior wall). The injections were approximately 1.5 cm apart from each other. The animals were allowed to recover and were sacrificed eight weeks after the injection procedure. Excised hearts were fixed with buffered formalin (Carson-Millonig formulation).

2.2.2 *Ex vivo* imaging

After fixation, the left ventricular and atrial cavities were filled with a silicone rubber compound (Polyvinylsiloxane, Microsonic Inc., Ambridge, PA) in order to maintain a near end diastolic geometry during imaging. The hearts were then placed in a plastic cylindrical container filled with a susceptibility-matched fluid (Fomblin, Solvay Solexis, West Deptford, NJ) and held in place using open-cell foam. Magnetic resonance imaging (MRI) was then performed (Magnetom Prisma 3T, Siemens, Erlangen, Germany) with the following parameters: T1-weighted imaging using a 3D Fast Low Angle SHot (FLASH) sequence (0.3x0.3x0.8mm spatial resolution, echo time (TE)/repetition

time (TR)=3.15ms/12ms, scan time: 1.5hr); and T2-weighted imaging using a 2D multi-slice Turbo Spin Echo (TSE) sequence (0.3x0.3x0.8mm spatial resolution, TE/TR=94ms/15460ms, scan time: 2hr).

DT-MRI was performed using a readout-segmented diffusion-weighted spin-echo sequence [152] with b-value=1000s/mm^2 along 30 directions and one b-value=0s/mm^2 reference, TE/TR=62ms/18100ms and 1.0x1.0x1.0mm spatial resolution with 4-6 signal averages to improve signal-to-noise ratio (SNR) (scan time: 8-12hrs). Diffusion tensors were reconstructed from the diffusion weighted images using linear regression and custom Matlab (The MathWorks, Inc., Natick, Massachusetts, United States) routines.

2.2.3 Geometric segmentation and reconstruction

Ex vivo MRI data sets were imported and processed in Simpleware ScanIP (Synopsys, Mountain View, USA). Geometrically detailed segmentations of the LV were created along with segmentations of infarcted tissue and biomaterial injections when applicable. Segmentation relied on a combination of well-established techniques including region growing, level-set thresholding, and morphological smoothing [153, 154]. Manual intervention was used only if needed to eliminate spurious features. In order to preserve the detailed features of the infarct morphology and overall volume, smoothing was not applied in the segmentation of the infarcted tissue. Finally, the LV was truncated at the base (just below the mitral valve) and partitioned into the 17 AHA regions [155] to allow for a comparative analysis between animals. A complete diagram of the 17 AHA regions is provided in Figure 2.1(a-b) for reference.

LV wall volume measurements were recorded from the segmentations to quantify the amount of healthy tissue, fibrotic tissue and biomaterial in each heart. LV surfaces were mapped to the image coordinate space for the MRI and DT-MRI data to enable a clear segmentation of imaging data bound only between these surfaces.

We introduced prolate spheroidal coordinates [34, 41] into the image-coordinate space aligned with the long axis of the LV for each subject. The prolate spheroidal coordinates were used to describe relative myofibre orientations, determine mid-wall positions, measure wall thickness and accurately compare relative positions between subjects.

2.2.4 Myofibre orientation

DT-MRI provides diffusion tensors for each voxel that were decomposed into eigenvalues and corresponding eigenvectors. Primary eigenvectors associated with the largest eigenvalue were

identified as the orientation of the myofibre [147, 148, 150]. As illustrated in Figure 2.1(c-d), myofibre orientation is decomposed into two angles:

1. α_h, the inclination angle, quantifies the angle between the myofibre projected onto the longitudinal-circumferential tangent plane and the circumferential unit vector.
2. α_t, the transverse angle, describes the angle between the myofibre projected onto the circumferential-radial tangent plane and the circumferential unit vector.

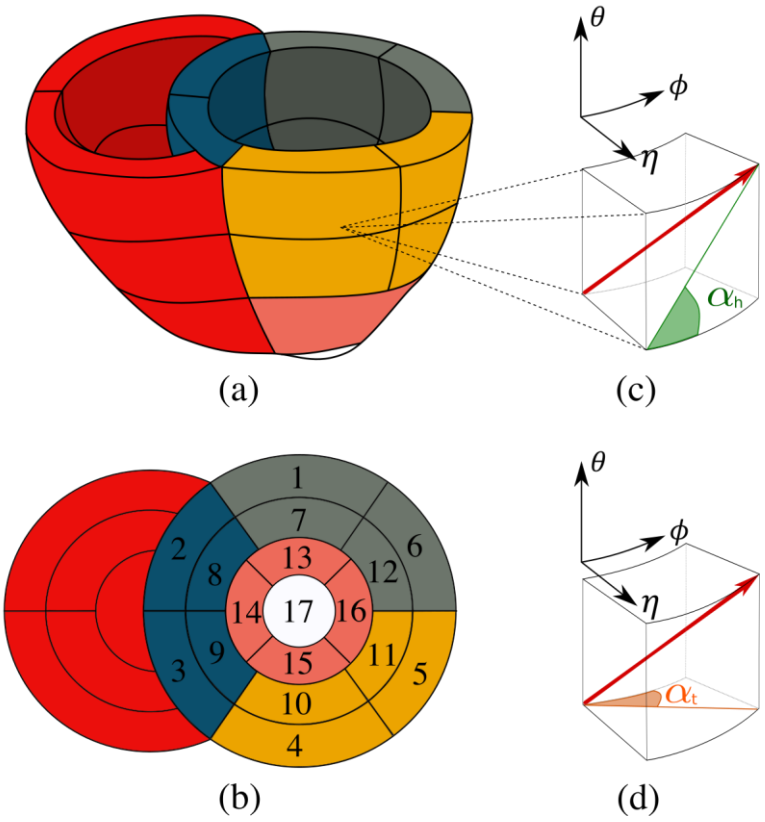

Figure 2.1:(a) Biventricular geometry with the LV partitioned into the 17 AHA regions. Regions are given distinct colours for ease of identification. (b) AHA labels that correspond to subfigure (a). AHA regions 1-6 partition the LV base, AHA regions 7-12 partition the LV mid-section and AHA regions 13-17 partition the LV apex. (c) The primary eigenvector (red arrow) is projected on the longitudinal-circumferential tangent plane (green line). The inclination angle α_h is quantified by measuring the angle between this projection and the circumferential unit vector. (d) The primary eigenvector (red arrow) is projected on the circumferential-radial tangent plane (orange line). The transverse angle α_t is quantified by measuring the angle between this projection and the circumferential unit vector. The triad of the local prolate spheroidal coordinate system is provided above subfigures (c-d).

Angles were collected for each AHA region, and a relative radial position was recorded with endocardial surface = -1 and epicardial surface = +1. This allowed for easy quantification of myofibre orientation in reference to the local coordinates of the LV. In order to ensure only voxels containing

cardiac tissue (and not gel, fat, air bubbles or voids) were included in the analysis of myofibre orientations, the requirements that eigenvalues of each voxel be strictly positive, and that the fractional anisotropy (FA), an invariant of diffusion tensors commonly used for tissue thresholding, is larger than 0.12, were imposed prior to analysis. This value for FA was found experimentally to be the lowest that would fully threshold out the gel and was reasonably different from values of FA for cardiac tissue [149, 150, 156].

Additionally, fibres that had large inclination angles (i.e., absolute value of α_h exceeding 85°) were removed from the analysis of α_t. These vectors have little or no component in the radial plane, making their projections (when normalized) and subsequently their calculated angles highly distorted. Tractography (using DT-MRI software package suite AFNI [157, 158]) was also performed on the LVs to depict the myofibre structure surrounding gel injections and visualize diffusion tensor (DT) metrics on the LV structure.

2.2.5 Gel morphology and retention

The segmentation of the Algisyl-LVR™ injectates was analysed for geometric features. Retention rates were calculated from volume measurements of *ex vivo* segmentation and injected volumes recorded for each heart at the time of treatment. Additionally, ellipsoidal descriptions associated with each injectate were constructed whereby a 3D ellipsoid surface described by:

$$\frac{x^2}{a^2}+\frac{y^2}{b^2}+\frac{z^2}{c^2}=1 \quad , \tag{2.1}$$

was fitted to each injectate surface using custom scripts (MATLAB and the Optimization Toolbox 2012b). Orientation, sphericity, and radial position of the fitted ellipsoids were assessed. Ellipsoid orientation followed the same approach as for myofibre orientation, i.e., inclination and transverse angle where the ellipsoid's long-axis served as reference. Values were quantified for each injectate and averaged over a single heart or entire group, as appropriate.

2.2.6 Statistical analysis

Data in this study are expressed as mean ± SD unless otherwise stated. The differences between the various groups were evaluated using analysis of variance (ANOVA) and Student's t-test. The differences were considered statistically significant at $p<0.05$.

2.3 Results

2.3.1 Wall volume and thickness

The mean LV wall volume was 119.6 ± 46.0 ml, 142.7 ± 29.5 ml, and 134.0 ± 29.3 ml, for the NC, HFC and HFI group, respectively. The mean volume fraction of biomaterial, infarcted tissue and healthy tissue was 1.9%, 7.8% and 90.3%, respectively, for the HFI group and 0%, 8.6% and 91.4%, respectively, for the HFC group. The results for each heart are presented in Table 2.1.

Table 2.1: Volume and volume fraction measurements for the individual hearts in the HFI and HFC groups.

Subject	Algisyl-LVR vol. (ml)	Infarcted tissue vol. (ml)	Total LV wall vol. (ml)	Algisyl-LVR vol. fr. (%)	Infarcted tissue vol. fr. (%)	Healthy tissue vol. fr. (%)
HFI 1	3.5	14.7	172.7	2.0	8.5	89.5
HFI 2	1.6	12.2	97.3	1.6	12.5	85.8
HFI 3	3.1	4.5	104.3	2.9	4.3	92.8
HFI 4	2.8	12.9	129.9	2.2	9.9	87.9
HFI 5	1.5	9.0	153.9	0.9	5.9	93.2
HFI 6	2.7	8.1	145.9	1.8	5.5	92.6
Mean ±SD	**2.5± 0.8**	**10.2 ± 3.7**	**134.0 ± 29.3**	**1.9 ± 0.7**	**7.8 ± 3.1**	**90.3 ± 3.0**
HFC 1	–	11.8	123.6	-	9.5	90.5
HFC 2	–	12.3	108.6	-	11.3	88.7
HFC 3	–	16.3	137.7	-	11.9	88.1
HFC 4	–	12.1	183.0	-	6.6	93.4
HFC 5	–	6.3	160.4	-	3.9	96.1
Mean ±SD	**0**	**11.8 ± 3.6**	**142.7 ± 29.5**		**8.6 ± 3.3**	**91.4 ± 3.3**

Abbreviations: vol., volume; fr., fraction.

Wall thickness was measured from a minimum of 1,800 data points for each LV and means were calculated for each AHA region to provide regional thickness values for each subject. Each subject's regional mean values were used to obtain group regional mean values shown in Figure 2.2. The group mean wall thickness for the unloaded ex vivo LV was found to be very similar between groups, i.e. 17.9 ± 3.4 mm for NC, 18.2 ± 3.6 mm for HFC, and 18.3 ± 2.1 mm for HFI (no statistical significance, n.s.). The only significant difference between groups was found in AHA region 6, where wall thickness of the NC (19.6 ± 2.1 mm) was substantially larger than that of the HFC (16.7 ± 2.8 mm) and the HFI (16.5 ± 2.3 mm) ($p<0.05$).

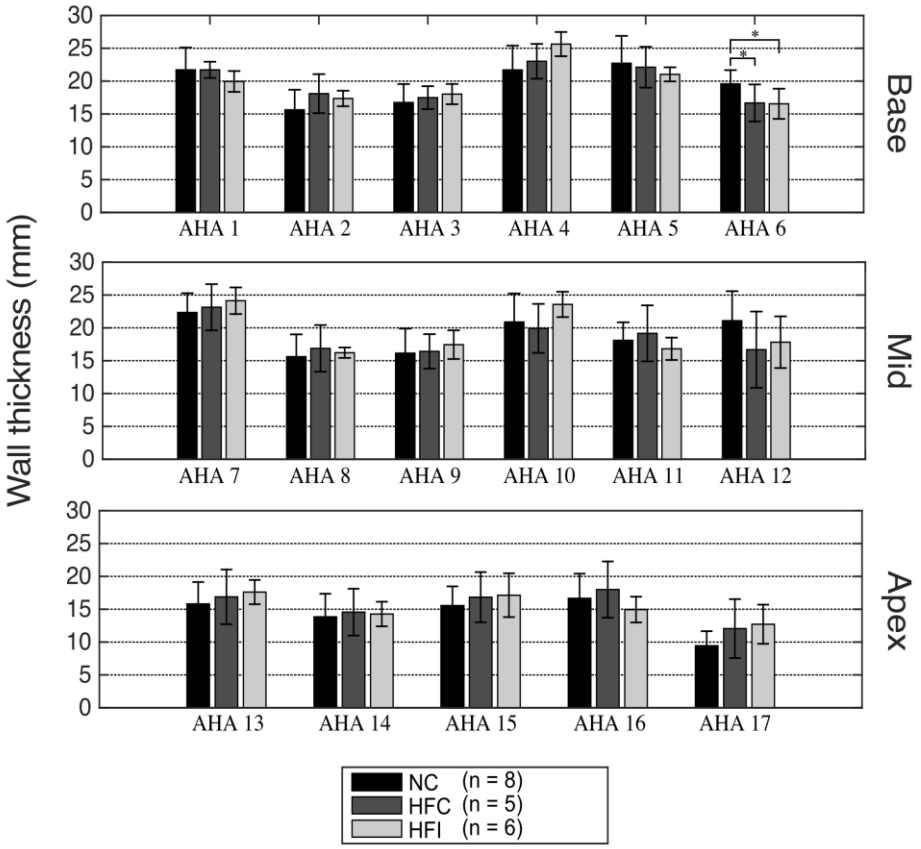

*Figure 2.2: Mean wall thickness and standard of deviation for each of the 17 AHA regions for each group. Regions are presented in separate rows for each longitudinal section. * $p<0.05$*

2.3.2 Myofibre orientation

The ratio eigenvalues can be used to determine if the directions identified through eigenvalue decomposition are indeed distinct. We found distinct values at all voxels with FA>0.12 with each eigenvalue arranges in descending order of magnitude. The mean ratio of the first and second eigenvalue was 1.58 ±0.23 and mean ratio of the second and third eigenvalue was 1.26 ±0.26.

The inclination fibre angles α_h in each group are presented in Figure 2.3 for LV free wall AHA regions 1, 4, 5, 6, 7, 10, 11 and 12, which are most likely to contain injectates. Inclination angles α_h are similar across groups, with a difference of 13.9° ±10.0° (NC versus HFC) and 12.5° ±10.4° (NC versus HFI) (n.s.).

The transverse fibre angles α_t for each group are presented in Figure 2.4 for the same LV free wall regions used for α_h. The regional mean values of α_t are close to 0° throughout the LV. The LV mean of α_t are -5.3° ±28° (NC), -2.8° ±31° (HFC), and -2.3° ±31° (HFI). Differences of α_t between groups were even smaller than those for α_h, namely 8.7° ±6.0° (NC versus HFC) and 6.9° ±5.8° (NC versus HFI) (n.s.).

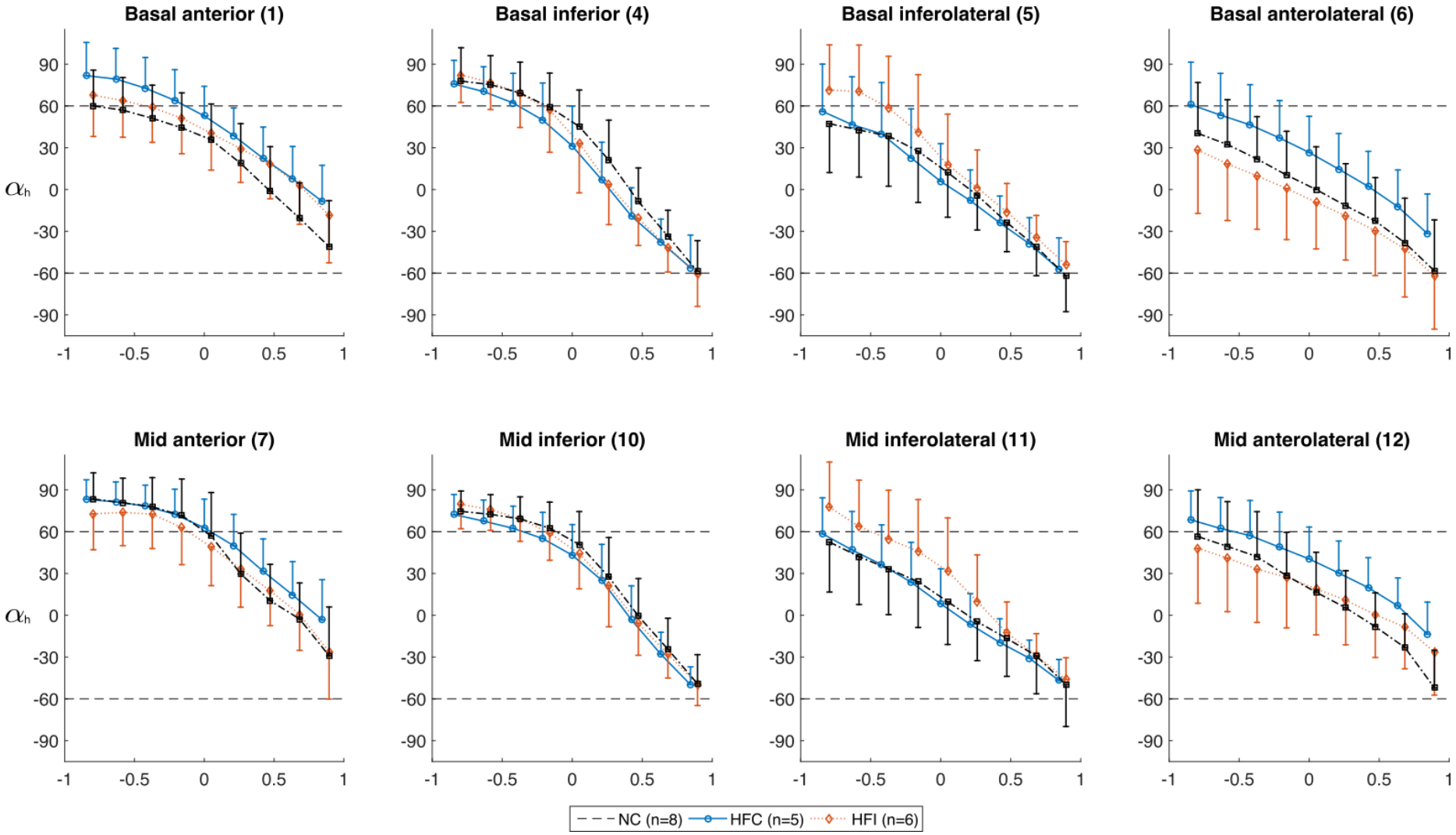

Figure 2.3: Inclination angles α_h in each group for the LV free wall regions showing the distribution along the radial depth. The AHA region number is given in parenthesis after each subtitle. Normalized radial coordinates were used to indicated the endocardium (-1), mid wall (0) and epicardium positions (+1). Standard deviations for each group are presented in one direction only for visual clarity. Dashed lines corresponding to +60° and -60° are plotted for ease of comparison and because a significant number of studies use these bounds when prescribing α_h in LV computational models.

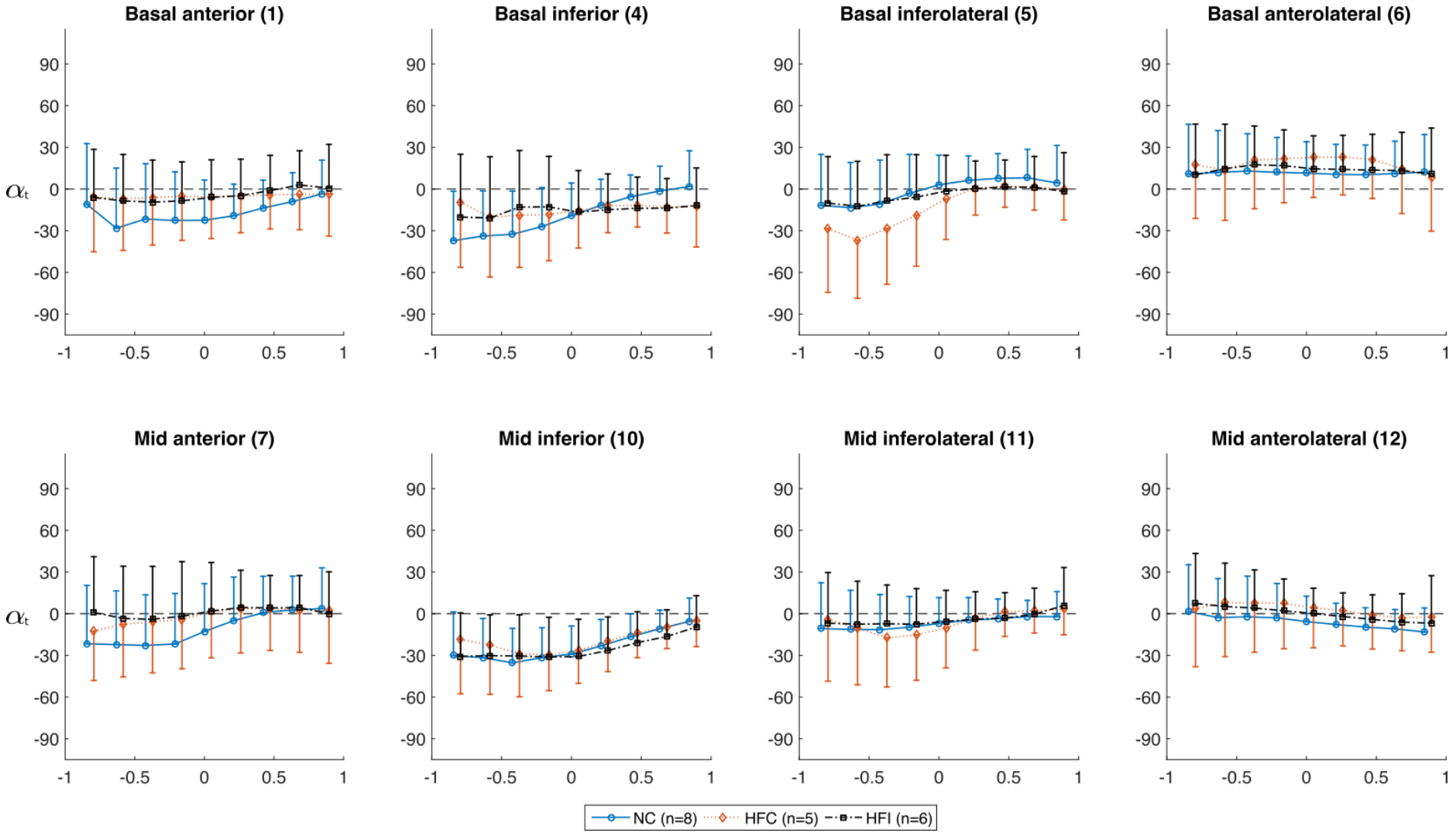

Figure 2.4: Transverse angles α_t in each group for the LV free wall regions showing the distribution along the radial depth. The AHA region number is given in parenthesis after each subtitle. Normalized radial coordinates were used to indicate the endocardium (-1), mid wall (0) and epicardium positions (+1). Standard deviations for each group are presented in one direction only for visual clarity. A dashed line at 0° is plotted for ease of comparison.

The myofibre orientation surrounding an injectate is shown in Figure 2.5, whereby tractography was used surrounding a short-axis image of an LV with a prominent injectate. Tracts displayed are only those that pass through a selected prism that isolates specific myofibre pathways. Tightly grouped myofibre tracts diverge near the injectate and pass the injectate longitudinally above and below Figure 2.5(b), whereas there is no visual evidence of radial deflection of the myofibres (Figure 2.5(c)). Online supplementary animations, which rotate the viewpoint around the Algisyl-LVR™ injectate, illustrate this point more clearly.

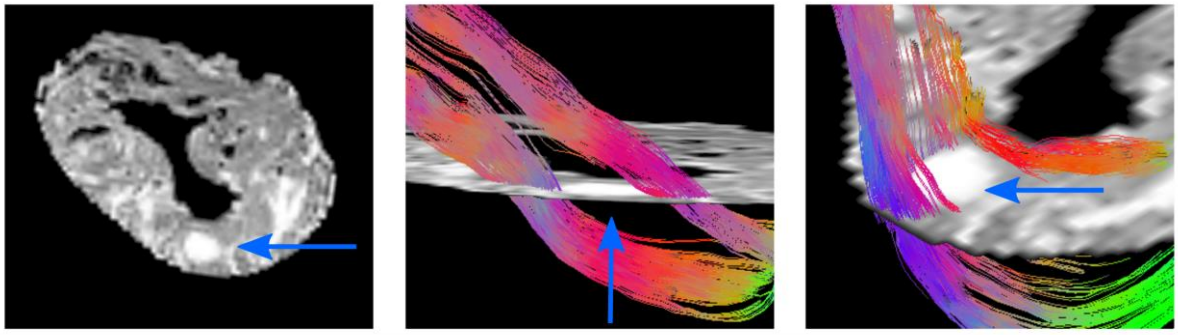

(a) (b) (c)

Figure 2.5: (a) A short axis slice for an LV region containing a prominent alginate injectate (blue arrow). (b) Selected tractography applied to the same short axis image in (a). Myofibre tracts displayed are only those that pass through a prism, with dimensions in mm for (x,y,z) as (1,1,6), which isolates myofibre tracts that pass longitudinally above and below a prominent alginate injectate (blue arrow). (c) Similar to (b), except the prism dimensions are (2,6,1) mm in order to isolate myofibre tracts that pass between the injectate and the epi- and endocardium walls.

2.3.3 Injectate morphology

Many of the injectates exhibited an ellipsoidal shape. The volumetric retention of injected material was 68.7% ± 21.3%. The mean injectate dimensions were 1.9 ± 0.6 mm, 2.9 ± 0.7 mm and 7.1 ± 2.7 mm along the three ellipsoidal axes. This resulted in a sphericity index (ratio of mean of short axes to long axis) of 0.37 ± 0.03. The injectates were located roughly mid-wall (between endocardial and epicardial surfaces) with the injectates' centre of mass found at normalized wall-depth coordinates of 0.28 ± 0.08. Individual subject results are presented in Table 2.2.

The ellipsoid (long axis) inclination angle was -4.9° ± 31.35°. The distribution of these results is shown in Figure 2.6(a). Injectates with sphericity index > 0.5 were assumed unable to form properly in situ and treated as outliers (also identified in Figure 2.6(b)). Excluding outliers, the ellipsoid inclination angle and myofibre inclination angle of the surrounding tissue correlate with R = 0.59

(p<0.01); see also Figure 2.6(b)). A typical arrangement of injectates in the myocardial wall is shown in Figure 2.7(a-b). Close up views in Figure 2.7(c-d) reveal the complex morphology of the injectates.

Table 2.2: Basic parameters quantifying the retention and morphology of the alginate injectates.

Animal #	Injections delivered	Injections identified	Volume (ml)	Retention rate (%)	Wall depth	Sphericity
HFI 1	13	13	3.5	91	0.37	0.33
HFI 2	12	10	1.6	44	0.38	0.35
HFI 3	12	10	3.1	85	0.20	0.40
HFI 4	12	11	2.8	78	0.30	0.40
HFI 5	12	8	1.5	40	0.24	0.39
HFI 6	12	11	2.7	74	0.18	0.38
Mean ±SD				**68.7 ± 21.3**	**0.28 ± 0.08**	**0.37 ± 0.03**

Wall depth is reported using normalized coordinates, whereby -1 is associated with the endocardium and +1 with the epicardium.

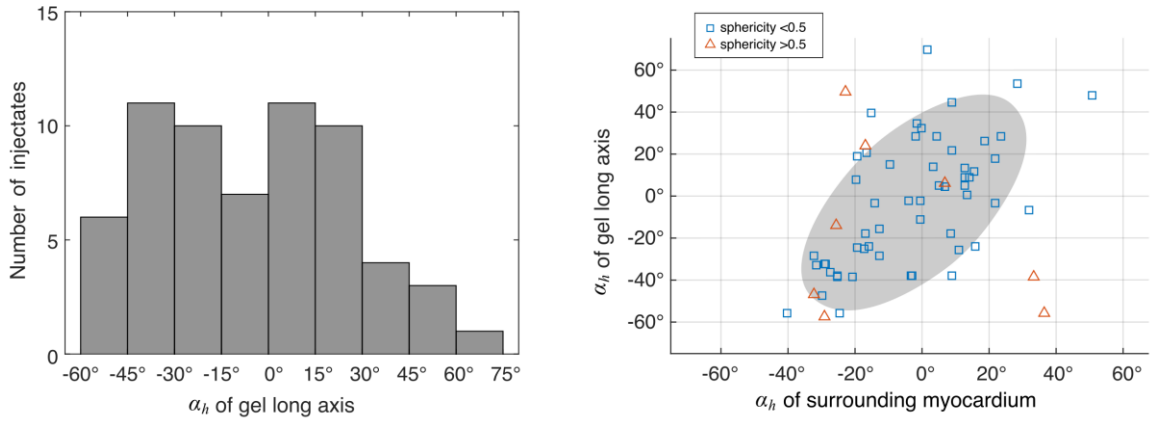

(a) (b)

Figure 2.6: (a) The distribution of α_h measured from the long-axis of the alginate injectate ellipsoids. Histogram bins have a width of 15°. (b) A scatter plot of the inclination angle of the injectate ellipsoids plotted against the inclination angle of the surrounding myocardium. Data were divided into two groups based on sphericity. We assumed that injectates unable to form properly would present as outliers and these could be isolated by a high sphericity (>0.5). An ellipsoid silhouette displayed under the data indicates the 99% confidence region found from the data, assuming a Gaussian distribution.

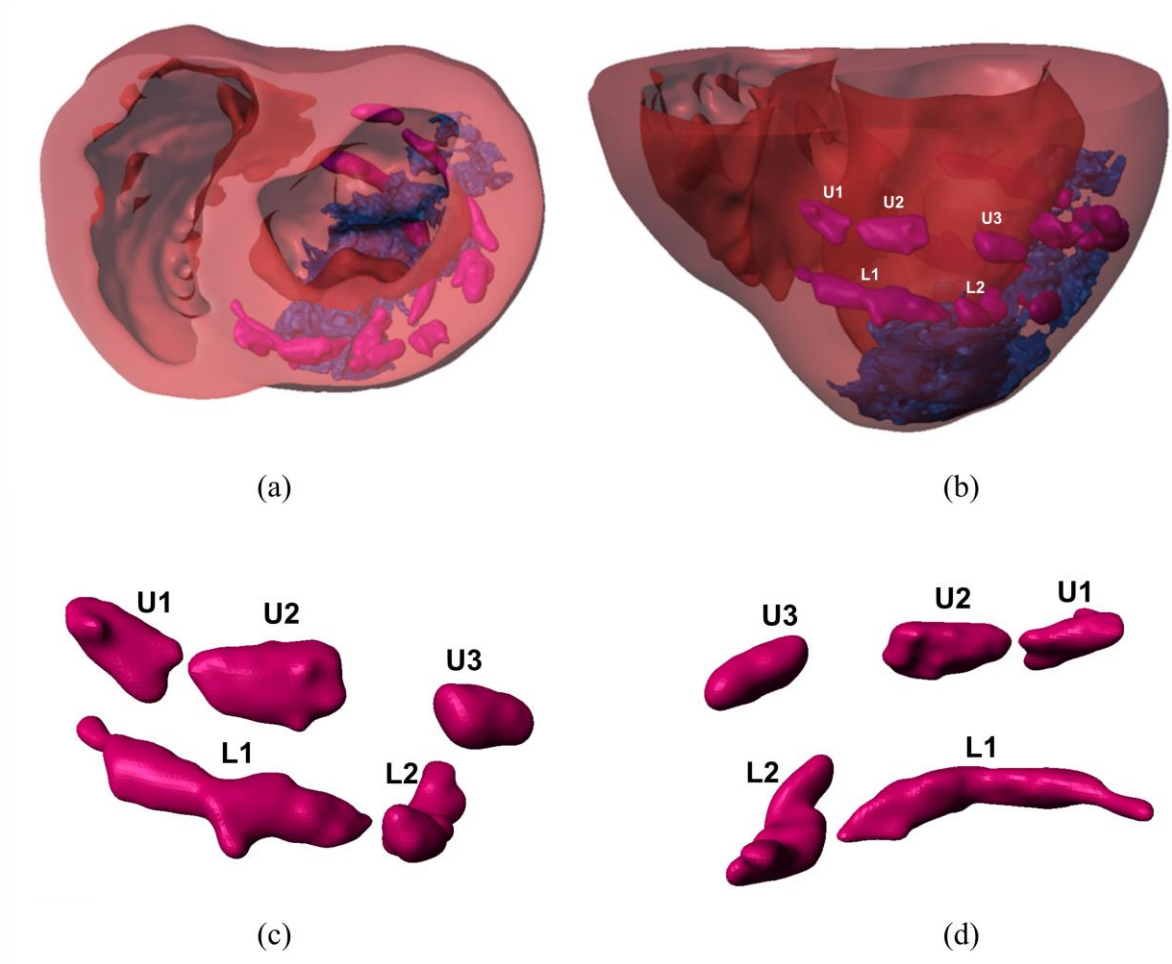

Figure 2.7: (a): Base-to-apex view of the truncated biventricular structure (red) of a porcine subject with MI (blue), revealing a typical injection pattern of Algisyl-LVR™ injectates (pink). (b): Anterior view of the same structure with injectates labelled according to their position in the upper (U) and lower (L) rows and circumferential position (1,2,3…). (c)-(d) Anterior and posterior close up views of the labelled Algisyl-LVR™ injectates revealing the complex (and sometimes merged) morphology.

2.4 Discussion

To the best of our knowledge, this study is the first to report the quantitative impact of intra-myocardial biomaterial injectates on the structure of the surrounding tissue in swine hearts with HF. Our major finding is that HF causes changes in myofibre orientation but Algisyl-LVR™ injections do not.

We compared the HFI group to the HFC and NC groups to examine the effects of the Algisyl-LVR™ injectates on myofibre orientation. Lower values of the myofibre inclination angle α_h in regions containing infarction (particularly the anterolateral region AHA 6) are consistent with values reported in other studies [156, 159]. No significant difference in α_h resulting from Algisyl-LVR™ injectates

was observed in HF: The similarity in the degree that α_h differs between the NC and the HF groups implies that HF, and not the injected material, is responsible for these changes.

The differences for the transverse myofibre angle α_t between both the HFC and the HFI groups and the NC group were even smaller than those for the myofibre inclination angle. The negligible effect of the Algisyl-LVR™ injectates on α_t indicates that radial displacement of tissue due to the biomaterial injection is minimal, and tissue volume is displaced predominantly longitudinally. This can be seen qualitatively in the visualization of myofibre tracts in Figure 2.5 (and supplementary videos), which show the fibre pathways diverted above and below the injectate in the longitudinal direction with no disturbance of fibre pathways in the radial direction.

In swine with HF, the smaller changes in fibre orientation in those that received Algisyl-LVR™ injections than in those who did not, namely α_h 12.5° vs. 13.9° and α_t 6.9° vs. 8.7°, indicates a beneficial overall effect of the injections on myofibre orientations in the failing heart. The exact mechanism of action is unclear, but we hypothesize that the long term presence of Algisyl-LVR™ injectates anchors the surrounding fibre structure, thereby mitigating adverse remodelling.

The mean myofibre orientation observed for normal control swine serves as a validation of our methods because the results agree well with those in other studies using large animal models [26, 149, 160-163] and previous regional DT-MRI myofibre analysis reported similar SDs [34, 148].

The Algisyl-LVR™ injectates conformed to the surrounding myocardial structure such that the long axis of the ellipsoidal injectates were typically aligned in a circumferential direction (Figure 2.6), which accords with the local myofibre direction at the mid-wall (approximate site of injection). We propose this particular alignment results from liquid Algisyl-LVR™ initially displacing interstitial fluid and subsequently separating myocardium along cleavage planes of least resistance during the injection process.

Achieving high retention for injected material into the heart is challenging given the significant motion and perfusion of the heart (i.e., some of the material may be removed through the coronary venous system). The observed retention rate in this study of 68.7% is considered high compared with rates reported in other studies [164-166]. It should be noted that sometimes the injections seem to have merged during the injection process, which results in fewer injectates than injections (see Table 2.1 and Figure 2.7).

An increase in wall thickness due to alginate injectates is not seen in the measurements of *ex vivo* unloaded hearts. This finding is at odds with our own *in vivo* measurements of the same subjects (*unpublished data, JS Choy 2017*) and multiple studies that found increases in wall thickness due to biomaterial injection therapy [11-13, 110-113]. These differences in *in vivo* and *ex vivo* findings may

reveal an important mechanism of the treatment. As these *in vivo* findings typically measure wall thickness at end-diastole, which had considerably lower cavity pressures in the treated cohorts, we can infer that these gains in wall thickness are likely due ventricular unloading. This would explain the lack of change in wall thickness in the unloaded state. Ventricular unloading is a well-established method to mitigate, or in some cases reverse, adverse remodelling effects of HF and is typically introduced via mechanical ventricular assistance devices [4-6].

The visualization of myofibre tracts in Figure 2.5 (and supplementary videos) provides further support for the preserved wall thickness after injections. As can be seen, a large injectate occupies more than half of the LV wall thickness without creating any bulging on the epicardial or endocardial surface.

2.5 Conclusions

Our study demonstrated that Algisyl-LVR™ treatment in HF swine preserved myofibre orientation compared to HF swine without treatment. This indicates a mitigation of the adverse remodelling due to heart failure. In addition, we found that heart failure, but not Algisyl-LVR™ injectates, led to a change in myofibre orientation. The minimal interference of Algisyl-LVR™ injectates with the myocardial structure indicates treatment safety. Furthermore, this study provides comprehensive data for the development of predictive computational models for the further advancement of biomaterial injection therapies in the heart.

Chapter 3 Subject-specific finite element modelling of a healthy biventricular heart

In this chapter a realistic, fully subject-specific computational model of the heart, able to capture heart function through multiple cardiac cycles is presented. As outlined in Chapter 2, and to the best of our knowledge, this is the first such model of its kind (i.e. fully subject specific), building on the latest developments produced in the literature [28, 167-169].

3.1 Introduction

For decades researchers have strived to create realistic computational models of the heart [170]. This challenging endeavour faces difficulties in accounting for the complex geometry, fibre structure and material description of the heart. Furthermore, the circulatory system and the cyclical function of the heart need to be considered as physiological heart function depends on changes in this system and its initial state.

During the cardiac cycle, significant changes in ventricular volume, pressure and chemical composition occur. These changes are divided into distinct stages, characterized by contractile behaviour of the ventricles: while the ventricles are contracting, it is classified as systole, when they are passive it is classified as diastole. A brief introduction on the cardiac cycle is presented here, for more detailed information the reader is directed to classical/seminal texts [171-173].

Diastole and systole can be further divided, defining four main phases of the normal cardiac cycle for the ventricles which can be identified as follows:

1. Passive filling: The mitral and tricuspid valves open, allowing blood to fill the ventricles. The cavity volumes increase as blood flows into the ventricles and the cavity pressures increase accordingly. The material behaves predominantly passively in this phase.
2. Isovolumetric contraction: The ventricles contract with all valves closed. The cavity volumes remain constant and the pressures in the cavities increase due to the rapidly increasing contraction of the heart muscle.

3. Ejection: Once the pressures within the left ventricle (LV) and right ventricle (RV) exceed the pressures in the aorta and pulmonary trunk respectively, the semilunar valves open. The cavity volumes decrease as blood is expelled from the contracting ventricles. The active tension of the heart muscle reaches a peak in this phase and starts to decrease.
4. Isovolumetric relaxation: Once the cavity pressures in the LV and RV drop below the pressures in the aorta and pulmonary trunk respectively, the semilunar valves close. The cavity volumes remain constant while the cavity pressures decrease. The active tension decreases dramatically and by the end of relaxation the cycle repeats itself.

These phases of the cardiac cycle are labelled in the Wiggers diagram presented in Figure 3.1.

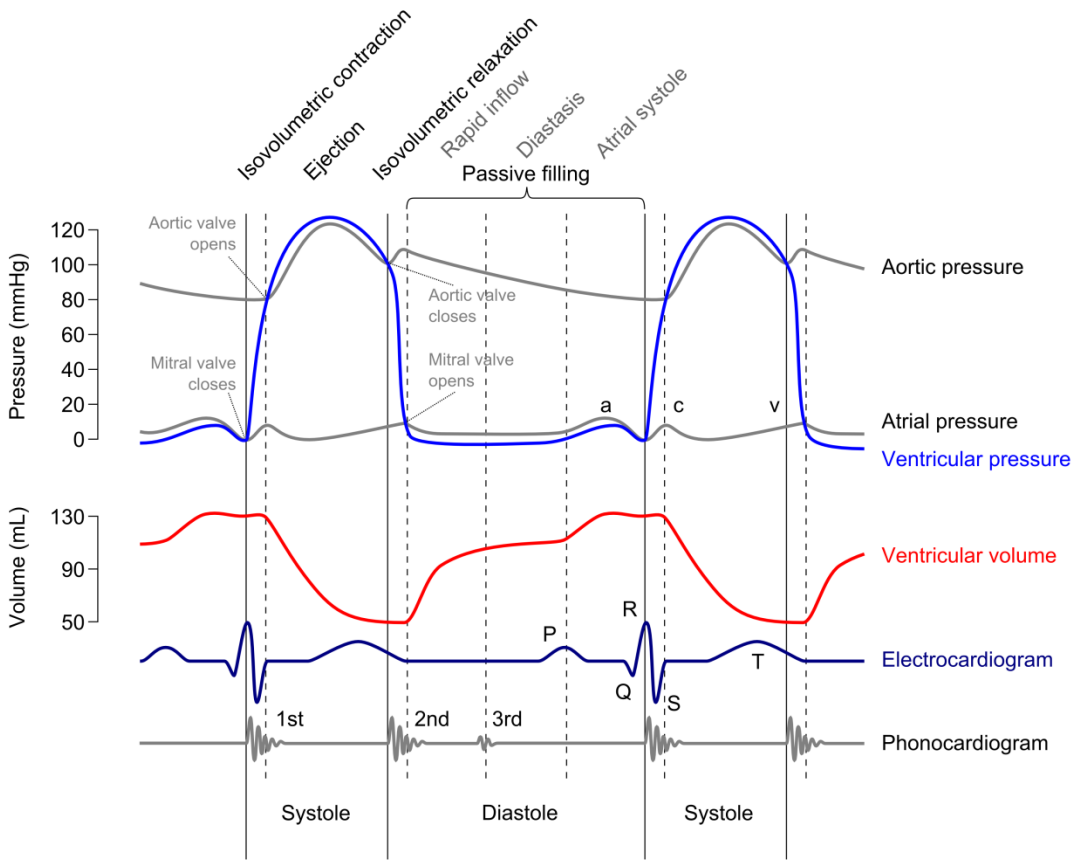

Figure 3.1: Wiggers diagram showing the cardiac cycle for the LV and connecting chambers. The electrocardiogram and phonocardiogram are included for completeness.

The cyclical function of these connected phases is often illustrated by plotting the pressure-volume relationship, revealing a loop. This is shown for the left ventricle in Figure 3.2.

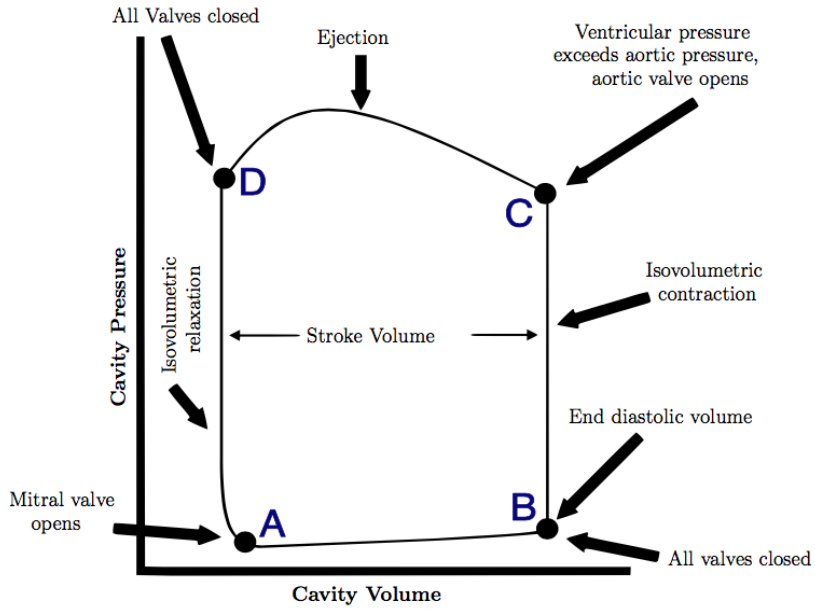

Figure 3.2: A representative pressure volume loop. Passive filling follows the path A-B, Isovolumetric contraction follows path B-C, ejection follows path C-D and isovolumetric relaxation follows path D-A.

3.2 Methods

3.2.1 Geometry construction

Geometrically detailed finite element (FE) meshes of the biventricular and atrial structure were constructed from T1 MRI data described in Chapter 2 using Simpleware ScanIP (Synopsys, Mountain View, USA). The segmentation process relied on a combination of well-established automatic techniques such as region growing, level-set thresholding and morphological smoothing operations [153, 154]. Manual intervention was used as a last resort to remove spurious features, likely caused by residual fluids sometimes present on the epicardial wall.

The full ventricular structure including all four valve openings of the heart was reconstructed. The segmented geometry and the cavity morphology are shown in Figure 3.3(a) and Figure 3.3(b), respectively. The segmented geometry was meshed with quadratic tetrahedral elements using Simpleware's built in FE meshing suite as shown in Figure 3.3(c) and the resultant mesh with the cavities enclosed is shown in Figure 3.3(d).

Since these geometries are constructed from *ex vivo* imaging, they provide the geometry in an unloaded state. This is advantageous for computational modelling of mechanics, as we do not need to modify the geometry to obtain the unloaded configuration.

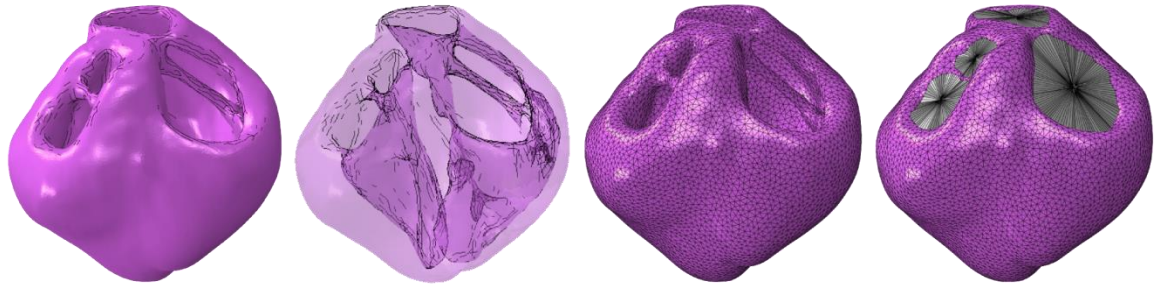

Figure 3.3: (a) Geometric segmentation. (b): Transparent geometries revealing the cavity morphology. (c) The mesh corresponding to the segmentation. (d) The mesh with the cavity structures enclosed using surface elements.

Ventricular chambers

Ventricular chamber volume is an important quantity for cardiac models to predict. A large number of health and efficacy metrics are defined from it. In order to accurately represent the volumes, these chambers were enclosed by constructing 2D triangular surface elements at each valve opening that were adjoined to a centre node Figure 3.3(d). Additional nodes were introduced at the centre of valve openings to enable a systematic description of 2D triangular surface elements.

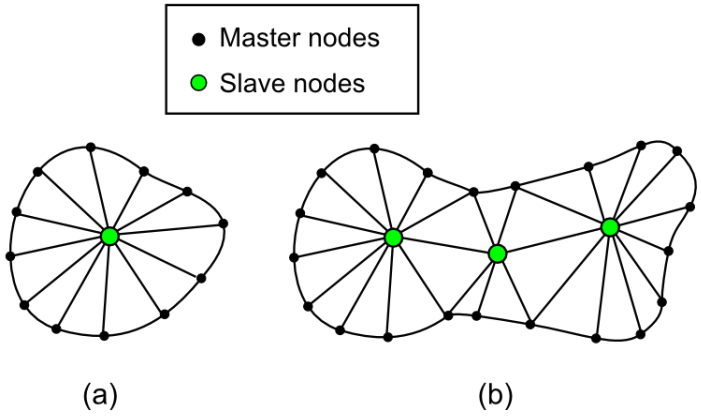

Figure 3.4: Central slave nodes are coupled to the surrounding master nodes on the surfaces enclosing the ventricular chambers. (a) Single node configuration. (b): Multiple node configurations.

The degrees of freedom of these centre nodes, designated as “slave nodes”, were coupled to the average motion of the surrounding nodes on the ventricular structure used to construct these surface elements, designated as “master nodes”. No material stiffness is associated with these elements. In this way, no additional degrees of freedom and no further stiffness are introduced in to the model. Depending on the morphology of the valve opening, either a single slave node or three slave nodes can be used. Orifice surfaces using a single slave node are shown in Figure 3.3(d). For clarity, the single and multiple slave node configurations are presented in Figure 3.4, highlighting the relationship between master and slave nodes. In this figure, lines correspond to the construction of 2D surface

elements. Each slave node (green) is coupled with the degrees of freedom of the entire set master nodes (black).

3.2.2 3D subject-specific myofibre orientations

The critical role of myofibre orientation on mechanical and electrical function is well recognized [35, 42, 43, 174, 175]. Fibre orientation, along with a second orthogonal vector within the laminar sheet provides sufficient information to establish a local orthonormal coordinate system whereby each basis vector corresponds to a principal anisotropic direction.

Diffusion tensor magnetic resonance imaging (DT-MRI) provides diffusion tensors $\boldsymbol{D}$, which can be deconstructed into eigenvectors $\boldsymbol{R}$ (i.e. representing the orientation of diffusion) and eigenvalues $\boldsymbol{\Lambda}$ (i.e. the shape of diffusion):

$$\boldsymbol{D} = \boldsymbol{R}\boldsymbol{\Lambda}\boldsymbol{R}^T \tag{3.1}$$

where each column of $\boldsymbol{R}$ is an eigenvector and $\boldsymbol{\Lambda}$ is a diagonal matrix with entries corresponding to eigenvalues of $\boldsymbol{R}$. These eigenvectors, at each voxel, correspond to the primary directions of diffusion, which in turn correspond to the principal directions of anisotropy. Primary eigenvectors associated with the largest eigenvalue were identified as the orientation of the myofibre [147, 148, 150].

However, DT-MRI data provides the average diffusivity properties for a voxel. These values have the highest validity at the centre of the voxel, but present a practical problem for quantifying the diffusivity of a point on the border of multiple voxels. For practical purposes of computational modelling, a fully continuous three-dimension field representation of the local material coordinates, derived from diffusion tensors is needed. Without further processing, DT-MRI data presents a discontinuous representation, motivating the incorporation of 3D interpolation techniques.

As diffusion permeates along a 1D line with no preferential direction, the deconstruction of a diffusion tensor can produce non-unique eigenvectors. This poses a problem if one considers interpolating features of neighbouring vector quantities. To overcome this, features associated with the tensor quantities are interpolated.

We follow the linear invariant approach introduced by Gahm *et al.* [176] whereby the diffusion tensor is decomposed into invariants and orientations, which are each in interpolated in turn and reconstructed into an interpolated tensor at the point of interest $\mathbf{x} \in \mathbb{R}^3$. We utilize first order tetrahedral shape functions for interpolation [198]. Consider that $\mathbf{x}_j$ are the nearest 4 point locations ($j = 1,2,3,4$) that coincide with the centre of voxel data and interpolants $N_i(\mathbf{x})$ ($i = 1,2,3,4$) are defined as smooth functions in $\mathbb{R}^3$ that connect these 4 points and satisfy the following:

$$N_i(\mathbf{x}_j) = \delta_{ij}, \tag{3.2}$$

$$\sum_{i=1}^{4} N_i = 1. \tag{3.3}$$

This enables a smooth interpolation field that is continuous across the 3D domain and preserves the data at voxel centres exactly (Eq. 3.2). These create piecewise smooth continuous descriptions of interpolated values. The orientations needed to complete the construction of an interpolated diffusion tensor are extracted from linearly combined diffusion tensors and is known as the Euclidian (EU) interpolated tensor. In our case, it is interpolated from the values of $\boldsymbol{D}_j$ at the four nearest surrounding data points that encapsulate $\mathbf{x}$ in a tetrahedron, this is expressed as

$$\boldsymbol{D}_{EU}(\mathbf{x}) = \sum_{j=1}^{4} N_j(\mathbf{x})\boldsymbol{D}_j. \tag{3.4}$$

The interpolated tensor $\boldsymbol{D}_{EU}$ is known to introduce micro-structural bias [176-178], motivating further efforts. To overcome this, we use only the orientation tensor $\boldsymbol{R}_{EU}$ that comes from eigenvector decomposition of $\boldsymbol{D}_{EU}$ via Eq. (3.1). To complete the construction of a new interpolated tensor $\widehat{\boldsymbol{D}}$, we compose the eigenvalue matrix $\widehat{\boldsymbol{\Lambda}}$ in the following way: First we define the set of invariants I_i from each diffusion tensor as

$$I_1 = \mathrm{tr}(\boldsymbol{D}), \tag{3.5}$$

$$I_2 = \sqrt{\frac{3}{2}\frac{\mathrm{tr}\left(\left(\boldsymbol{D} - \boldsymbol{I}\frac{I_1}{3}\right)^2\right)}{\mathrm{tr}(\boldsymbol{D}^2)}}, \tag{3.6}$$

$$I_3 = 3\sqrt{6}\,\det\left(\frac{\boldsymbol{D} - \boldsymbol{I}\frac{I_1}{3}}{\sqrt{tr\left(\left(\boldsymbol{D} - \boldsymbol{I}\frac{I_1}{3}\right)^2\right)}}\right). \tag{3.7}$$

These are interpolated as $\hat{I}_i(\mathbf{x})$ following Eq. (3.4). These interpolated values, $\hat{I}_1$, $\hat{I}_2$ and $\hat{I}_3$ can be reconstituted into eigenvalues and the eigenvalue matrix in the following manner:

$$\lambda_i = \frac{1}{3}\hat{I}_1 + \frac{2\hat{I}_1\hat{I}_2}{3\sqrt{3 - 2\hat{I}_2^2}}\cos\left(\frac{\arccos \hat{I}_3 + P_i}{3}\right) \tag{3.8}$$

$$\hat{\Lambda}_{ij} = \lambda_i \delta_{ij}. \tag{3.9}$$

Where, P_i = *0, -2π, 2π,* for i = 1, 2, 3. Using $\boldsymbol{R}_{EU}$ and $\hat{\boldsymbol{\Lambda}}$, the new interpolated diffusion tensor is constructed, again following Eq. (3.1).

Methods to report fibre orientations based on the inclination angle α_h and the transverse angle α_t follow those presented in Chapter 2. The sheet angle β is the measured angle between the third eigenvector projected onto the longitudinal-radial plane and the transverse plane [149, 179]. For $\beta = 90°$ the sheet-fibre plane is aligned in the transverse direction, for $\beta = 0°$ the sheet-fibre plane is aligned with the LV epicardium surface.

These angles were found using the established prolate spheroidal coordinate system. Angles were collected in each of the 17 AHA regions [155] and recorded with a relative transmural position such that -1 = endocardium and +1 = epicardium.

Additionally, for the purposes of visualization, tractography is applied to the cardiac DTMRI data utilizing the AFNI toolkit [180] and custom algorithms created within MATLAB 2012b (The MathWorks, Inc., MA, United States).

3.2.3 Incorporating *in vivo* measurements

Left ventricular pressure and volume data sets associated with the animal subject used in this research were provided from collaborators based at UCSF. Subject specific parameters were set as target values in the model calibration. For the subject presented in this Chapter, *in vivo* volume measurements were available (measured from pressure catheterization), while the pressure data was not. In the absence of subject specific data, a mean value constructed from the healthy baseline of a larger data set (containing multiple subjects) was used. The complete *in vivo* measurements used for this study are presented in Table 3.1.

Table 3.1: In vivo volume and pressure target values used in the model creation.

Measurement	Full structure	Source
LV EDV (ml)	73	Subject specific, segmented from echocardiogram
LV SV (ml)	40	Subject specific, segmented from echocardiogram
LV EDP (mmHg)	13.5 ±4.5	Mean + SD value from full data
LV ESP (mmHg)	87.6 ±23.7	Mean +SD value from full data
Min aortic pressure	60.6 ±17.8	Mean + SD value from full data

Abbreviations: EDV: End diastolic volume; SV: Stroke volume; EDP: End diastolic pressure; ESP: End systolic pressure.

3.2.4 Constitutive model

3.2.4.1 Passive Material parameter estimation

The passive material response of the cardiac tissue model was described by an anisotropic hyperelastic formulation based on that proposed by Holzapfel and Ogden [56]. The isochoric and volumetric responses are governed by the following strain energy potentials with parameters defined in Table 3.2:

$$\Psi_{iso} = \frac{a}{2b} e^{b(\bar{I}_1 - 3)} + \sum_{i=f,s} \frac{a_i}{2b_i} \left\{ e^{b_i (\bar{I}_{4i} - 1)^2} - 1 \right\} + \frac{a_{fs}}{2b_{fs}} \left\{ e^{b_{fs} (\bar{I}_{8fs})^2} - 1 \right\} \tag{3.10}$$

$$\Psi_{vol} = \frac{1}{D} \left(\frac{J^2 - 1}{2} - \ln(J) \right). \tag{3.11}$$

Table 3.2: Constitutive parameters for the passive material response

Passive Parameters	Description
a, b	Governs the isotropic response of the tissue
a_f, b_f	Governs additional stiffness in the fibre direction
a_s, b_s	Governs additional stiffness in the sheet direction
a_{fs}, b_{fs}	Governs coupling stiffness in the fibre and sheet directions
$\bar{I}_1$	The first isochoric strain invariant
$\bar{I}_{4i}$	A pseudo-invariant defined as $\boldsymbol{A}_i \cdot \overline{\boldsymbol{C}} \cdot \boldsymbol{A}_i$
$\bar{I}_{8fs}$	A pseudo-invariant defined as $\boldsymbol{A}_f \cdot \overline{\boldsymbol{C}} \cdot \boldsymbol{A}_s$
$\overline{\boldsymbol{C}}$	The isochoric Right Cauchy-Green tensor ($\overline{\boldsymbol{C}} = J^{-2/3}\boldsymbol{C}$)
$\boldsymbol{A}_i$	Vector in direction i
D	Multiple of Bulk modulus ($K = 2/D$)
J	The third deformation gradient invariant ($J = \det \boldsymbol{F}$)

The passive material parameters are first calibrated based on the fully orthotropic exponential material response measured in *ex vivo* shear experiments on small cubic heart specimens. Then the material parameters are scaled to match subject specific pressure volume measurements. This two-stage fitting process ensures reasonable material anisotropy and subject specific material responses. Details of this process are outlined below.

Shear calibration was carried out for a recent study of human tissue [181] and an older study of porcine tissue [75]. Calibration was performed using the Abaqus software environment (version 6.14, Dasssult Systèmes, Providence, RI, USA) as the forward solver, whereby the cubes with dimensions matching those of the study of interest was meshed into a uniform 27 linear hex element mesh. The material law described by Eq.(3.10) is not part of the Abaqus material library and therefore a custom

VUANISOHYPER_INV subroutine written in FORTRAN was developed to interface with Abaqus. Shearing was executed by specifying the translational displacement of a specified cube face, while enforcing zero displacement boundary conditions on the opposite cube face. The optimization was performed in MATLAB using a nonlinear least square optimization routine with the trust-region-reflective algorithm option to identify all eight material parameters in Eq.(3.10).

Here the minimization between FE model stress σ and experimental values $\bar{\sigma}$ can be explicitly defined through the minimization of an objective function φ_1 by

$$\min\varphi_1(\mathbf{v_1}) = \sum_i \sum_j \left(\sigma_j^i - \bar{\sigma}_j^i\right)^2, \tag{3.12}$$

where $i = \{fs, fn, sf, sn, nf, ns\}$ are the six combinations of shear modes, the vector of material parameters is given by $\mathbf{v_1} = \{a, b, a_f, b_f, a_s, b_s, a_{fs}, b_{fs}\}$ and the index j spans the data points in the shear vector for shear test i. To be thorough, the enforcement of incompressibility was investigated by perturbing the parameter D in Eq (3.11) and was found to have no effect on material parameters or deformation.

The resulting material parameters from shear calibration formed as the starting set of material parameters for the next stage of calibration, which scales these values to match subject specific left ventricular function.

Klotz *et al.* [182] introduced a mathematical description of the passive filling LV pressure volume curve that can reasonably fit the physiological pressure volume curve based on a single pressure, volume point (P_{LV}^*, V_{LV}^*). To adjust the material for each subject, passive material parameters resulting from shear calibration are scaled consistently to match the "Klotz curve" generated at EDP for a specified EDV [182]. Both exponential (b_i) and linear terms (a_i) were subject to uniform scaling by an exponential and scalar multiplier respectively. The error between the model and predicted *in vivo* pressure-volume relationship was similarly minimized using Abaqus as the forward solver and the same nonlinear least square optimization routine used in the shear calibration.

For the passive filling calibration, we defined our objective function φ_2 as the difference in pressure values along the pressure volume curve combined with a single measure of EDV, which we found to yield close fits to the PV curve and ensure EDV was met.

$$\min\varphi_2(\mathbf{v_2}) = \sum_i^N \left(P_j - \bar{P}_j\right)^2 + (EDV - \overline{EDV})^2, \tag{3.13}$$

where the vector of material parameters is given by $\mathbf{v_2} = \{A, B\}$, N refers to the total number of data points along the pressure volume curve and values from experimental data are given with the

"overbar" notation. To be thorough, the enforcement of incompressibility was investigated by perturbing the parameter D in Eq. (3.11). We found that at extreme values, i.e. $D < 0.02$ MPa and $D > 20$ MPa, non–physiological deformation was introduced. Within this range ($0.02 < D < 20$ MPa), the effect of incompressibility was minor on material parameter estimation. We chose to set $D = 0.2$, which we found sufficient to enforce incompressibility (99.8 % volume retained over passive filling) and avoid problematic deformations. This value produced a Bulk modulus roughly 1000 times larger than the largest linear terms (a_i) – a guideline also used by Goktepe *et al.* [57]

To ensure realistic loading of the LV cavity one needs to consider the trans-septal pressure originating from RV filling. To capture this, the RV cavity was also inflated to RV EDP during passive filling calibration.

3.2.4.2 Active material parameter estimation

In order to model the contractile function of the heart, additional constitutive models are introduced that handle active tension development [63].

The active tension in the cardiac muscle fibre direction can be defined by the following time varying elastance model [60, 183, 184]:

$$T_a\big(t, E_{ff}\big) = T_{max}\frac{Ca_0^2}{Ca_0^2 + ECa_{50}^2(l)}\,\frac{1-\cos\big(\omega(t,l)\big)}{2}, \tag{3.14}$$

where T_{max}, the maximum allowable active tension, is multiplied with a term governing the calcium concentration and a term governing the timing of contraction. Both of these terms depend on sarcomere length l. Furthermore,

$$ECa_{50}(l) = \frac{Ca_{0_{max}}}{\sqrt{e^{B(l(E_{ff})-l_0)}-1}}, \tag{3.15}$$

$$\omega(t,l) = \begin{cases} \pi\dfrac{t}{t_0}, & \text{when } 0 \le t \le t_0 \\ \pi\dfrac{t - t_0 + t_r\left(l\big(E_{ff}\big)\right)}{t_r}, & \text{when } t_0 \le t \le t_0 + t_r(l) \\ 0, & \text{when } t_0 + t_r(l) \le t \end{cases} \tag{3.16}$$

$$t_r(l) = ml + b, \tag{3.17}$$

$$l(E_{ff}) = l_r\sqrt{2E_{ff}+1}, \tag{3.18}$$

where E_{ff} is the Lagrangian strain tensor component aligned with the local muscle fibre direction. Following the material parameters values originating from Guccione and McCulloch [183]: Ca_0, the peak intracellular calcium concentration, is 4.35 μM; $Ca_{0_{max}}$, the maximum peak intracellular

calcium concentration, is 4.35 μM; B, a parameter that governs the shape of peak isometric tension-sarcomere length relation, is 4.75 μm^{-1}; l_0, the sarcomere length at which no active tension develops, is 1.58 μm; t_0, the time till peak activation, is 100 ms; m and b , Coefficients that govern the shape of the linear relaxation duration and sarcomere length relaxation, are set at 1.0489 s/ μm and -1.429s respectively. The value for l_r, the resting sarcomere length, was set to 1.85 μm [185, 186].

This mathematical description of active tension, given in Eqs. (3.15)-(3.18), ensures a smooth yet steep transition from zero to peak active tension, T_{max}, at time t_0 and then a smooth decline back to zero for the specified relaxation time t_r. The active tension T_a is driven by the difference between l_0 (the "resting length" of the sarcomeres) and the current sarcomere length $= l_r\sqrt{2E_{ff}+1}$. This accounts for "length-dependent" responses and enables a replication of Frank Starling's law (i.e. the strength of the heart's systolic contraction is directly proportional to its diastolic expansion).The VUANISOHYPER_INV user subroutine was extended to capture this active material description in the Abaqus software environment.

The total fibre stress, $\boldsymbol{\sigma_f}$, is equal to the passive stress, $\boldsymbol{\sigma_{pf}}$, combined with the active tension in the fibre direction:

$$\boldsymbol{\sigma_f} = \boldsymbol{\sigma_{pf}} + T_a\, \mathbf{e_f} \otimes \mathbf{e_f} \tag{3.19}$$

Biaxial investigations on actively contracting rabbit myocardium revealed significant stress development in the cross-fibre direction that could not be attributed to fibre dispersion or deformation effects [187]. This has motivated computational efforts to consider a proportion of the active stress developed in the fibre direction to be transferred onto the stress in the sheet and sheet-normal direction by a scalars $n_s, n_n \in (0,1)$, such that

$$\boldsymbol{\sigma_s} = \boldsymbol{\sigma_{ps}} + n_s\, T_a\, \mathbf{e_s} \otimes \mathbf{e_s} \quad \text{and} \quad \boldsymbol{\sigma_n} = \boldsymbol{\sigma_{pn}} + n_n\, T_a\, \mathbf{e_n} \otimes \mathbf{e_n} \tag{3.20}$$

Using the same nonlinear least square optimization routine in the passive regime (and Abaqus as the forward solver), T_{max}, n_s and n_n were subject to optimization to ensure the correct stroke volume (SV=EDV-ESV) for each subject was achieved. Additionally, to ensure physiological deformation modes during contraction, left ventricular long axis shortening (LVLS) was included in the minimization routine. Typical values for LVLS are between 15-20% [188, 189] for humans so this was set as a low weighted target in the minimization routine to ensure a LVLS>0% in our *in silico* model. This in turn ensures that the optimization routine doesn't converge on a parameter set that produces ventricular elongation and/or wall thinning. For active calibration we defined our objective function φ_3 as the difference in pressure values along the pressure volume curve combined with a single measure of EDV, which we found to yield close fits to the PV curve and ensure EDV was met.

$$\min\varphi_3(\mathbf{v_3}) = (SV - \overline{SV})^2 + 0.2\,(LVLS - \overline{LVLS})^2 \tag{3.21}$$

where the vector of active material parameters is given by $\mathbf{v_3} = \{\mathrm{T_{max}}, n_s, n_n\}$ and target values SV and LVLS are given with the "overbar" notation.To adjust the timing of a single cardiac cycle t_0 and b where subject to heuristic modification by an amount of 20% of their default value.

3.2.5 Circulation

In order to realistically model the beating heart, the circulatory system must be included. This is especially important as the physiological heart is connected to multiple fluid chambers that experience dynamic changes in pressures and volumes during each cardiac cycle.

We introduce a closed loop circulatory model adapted from simple lumped parameter representations [190, 191] of different compartments in the cardiovascular system. In order to achieve this, the ventricular chambers are defined as fluid filled cavities fully enclosed by the combined meshed faces of the tetrahedral elements on the cavity surface and the surface elements described in Section 3.2.1 that close off the chamber. The coupling of the lumped circulatory system and mechanical function was performed in Abaqus. Details on the numerical underpinnings for this are provided in the Abaqus theory guide [141], here we provide a brief overview concerning the relation of pressure, volume, compliance, resistance and fluid exchange within a lumped system. The volume V_i and pressure P_i inside a fluid cavity chamber i are related in the following manner

$$V_i(t) = V_i(0) + C_i P_i(t) \tag{3.22}$$

where C_i is the compliance of the vessel. For the LV and RV the compliance is highly nonlinear, depending on both the strain state of the material and time (outlined in Sections 3.2.4.1 and 3.2.4.2), as compliance is inversely proportional to stiffness. Following Eq. (3.22), we define additional compliance vessels representing key components of the circulatory system.

Unidirectional fluid exchanges governing the flow between chambers are driven by the pressure gradients between these chambers, as defined by

$$Q(t) = \frac{\Delta P(t)}{R}. \tag{3.23}$$

The finite element model of the heart is connected to this lumped representation as illustrated in Figure 3.5. In each simulated cardiac cycle, the ventricles contract, increasing the pressure in their chambers until it exceeds the pressure in the connected chamber, driving the flow of blood in the circuit and simulating the physiological circulatory system. As the total amount of volume in the circulatory system is constant, i.e.

$$\frac{d}{dt} V_{TOT} = \frac{d}{dt} \sum_i V_i\,(t) = 0, \tag{3.24}$$

the system will converge if run for multiple cardiac cycles.

Simplicity of the circulatory model was central as the finite element ventricular modelling (and not the circulatory circuit) is the central focus of this research. We therefore sought to model a working circulatory system with as few components and assumptions as possible. This resulted in a circulatory system with three compliance vessels representing the systemic arteries (*SA*), systemic veins (*SV*) and the pulmonary circuit (*P*).

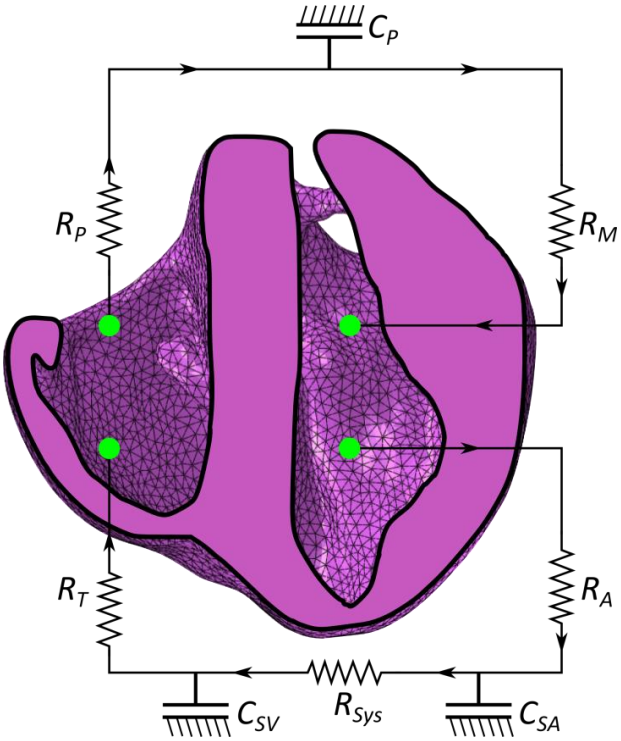

Figure 3.1: Schematic of the electromechanical model coupled with the circulatory system. R_M is mitral valve resistance, R_A is aortic valve resistance, C_{SA} is systemic arterial compliance, R_{SYS} is systemic arterial resistance, C_{SV} is venous compliance, R_T is tricuspid resistance, R_P is pulmonary valve resistance and C_P is pulmonary system compliance.

Resistance and compliance values were based on literature values [190-193] and adapted heuristically to ensure realistic flow. The control values for these parameters are presented in Table 3.3 alongside literature values for comparison.

Table 3.3 Control values for the lumped circulatory flow model and literature values for comparison.

Variable	Units	Current study	Literature
R_M	mmHg s ml^{-1}	0.03	0.0 - 0.20 [190-192]
R_A	mmHg s ml^{-1}	0.03	0.0 - 0.20 [190-192]
R_{SYS}	mmHg s ml^{-1}	1.70	1.05 - 4.00 [190-192]
R_P	mmHg s ml^{-1}	0.03	0.0 - 0.06 [190-192]
R_T	mmHg s ml^{-1}	0.03	0.0 - 0.02 [190-192]
C_P	ml mmHg^{-1}	4.43	1.0 - 7.0 [191-193]
C_{SA}	ml mmHg^{-1}	0.80	0.3 – 2.1 [191-193]
C_{SV}	ml mmHg^{-1}	16.6	6.0 - 17.0 [191, 192]

Valves

While the valves are not considered geometrically, their purpose and function is incorporated into the model. Flows from the pulmonary circuit into the LV and from the systemic circuit into the RV are set

to zero during the contractile stages of heart function (i.e. during isovolumetric contraction, ejection and isovolumetric relation). Outflow from the LV and RV only occur when the pressures in these cavities exceed the pressures in the chambers they are ejecting into. Combining these restraints with the imposed unidirectional flow of the circuit is sufficient to produce realistic fluid exchanges analogous to the physiological circulatory system (e.g. the isovolumetric portions of the cardiac cycle).

3.2.6 Boundary conditions

The physiological heart does not experience rigid constraints on its motion. However, boundary conditions are needed in computational models to prevent rigid body motion and ensure the problem is mathematically well posed. To accomplish this without placing overly restrictive constraints on the computational heart's motion we exploit the coupled degrees of freedom introduced in the ventricular caps (Section 3.2.1). The slave nodes on these caps are coupled to the ventricular valve motion, without being a part of the actual myocardium. By enforcing a fully rigid constraint on any one of these nodes adequately prevents the model from experiencing rigid body motion. The valve coupled to this nodes experiences minimal restriction in its motion: only the average deformation around this fixed point must summate to zero, enabling the valve to expand and contract during the heart cycle. For our model we applied this rigid constraint on the slave node associated with the truncated pulmonary trunk. This boundary condition was sufficiently far from the LV to not interfere with its motion, allowing us to calibrate the model free from the influence of boundary conditions.

Further analysis on multiple configurations of boundary conditions was performed after calibration to ensure prescribed boundary conditions were optimal.

3.2.7 Initial conditions

In order to initiate the cardiac cycle each compliance vessel was loaded with fluid until it experienced the physiological pressure at ED. Where possible, pressure catheterization readings from *in vivo* subject-specific measurements were used. The set of initial conditions used in this study is given in Table 3.4.

Table 3.4: Initial pressure state of the compliance vessels in the subject-specific model.

Cavity	Units	Current study	Motivation
C_P	mmHg	15	Needed to ensure LV fills past 12mmHg
C_{SA}	mmHg	65	Needed to ensure ejection begins at ~ 65mmHg
C_{SV}	mmHg	4	Needed to ensure RV fills past 2mmHg
LV	mmHg	13.5	Determined from *in vivo* data
RV	mmHg	4	Based on literature: 1-7mmHg [172] 3.9 ±1.6 [194]

3.2.8 The *in silico* cardiac cycle

The initial conditions outlined above are all that are needed to initiate the dynamic beating of the computational heart model. Two steps are introduced to model the full cardiac cycle:

1. Active contraction: From the initial conditions, i.e. ED, contraction is initiated which increases the pressure in the ventricular chambers. These rise until LV and RV pressures exceed the pressures in C_{SA} and C_p respectively. At this stage, fluid exchanges occur and the ventricles empty while the pressures and volumes in C_{SA} and C_p increase. Once LV and RV pressures drop below the pressures in C_{SA} and C_p respectively, the fluid exchanges stop, and the LV and RV pressures decrease with the decline in active tension. The step duration is 480ms which is sufficient to achieve isovolumetric contraction, ejection and isovolumetric relaxation. This compares well with literature values for the timing of isovolumetric contraction 66 – 90 ms [195] , ejection 270 – 347ms [195, 196] and isovolumetric relaxation 64 – 93ms [195, 197], respectively.
2. Passive filling: This step follows immediately from the active contraction step and in it, all components in the circulatory system behaves purely passively. Pressure differences between the compliance chambers in C_{SV} and C_p and the RV and LV, respectively, drive the passive filling of the ventricular chambers. The majority of the volume transferred in the passive filling stage occurs in the early portion of the step when the pressure difference is largest. As such, adjusting the timing of this step is the simplest way to adjust the timing of the total cardiac cycle, without effecting global function. The step duration is chosen as 300ms, which is sufficient time for the cavities to inflate to the ED state and results in a heart rate of 77 bpm.

Multiple steps of active contraction and passive filling can be simulated in a continuous sequence until convergent behaviour over the cardiac cycle is reached. Assessments of outputs from the FE model that are associated with the elements (e.g. myocardial stress) were volume normalized to account for different element size contributions. For example, volume normalized stress for element i is defined in the following manner:

$$\sigma_i^v = \frac{V_i}{\bar{V}}\sigma_i \tag{3.25}$$

with V_i denoting the volume of element i, $\bar{V}$ is the mean volume for all elements and σ_i is the original stress value.

3.2.9 Damping

Mass proportional Rayleigh damping [198] is introduced to dampen unrealistic oscillatory behaviour of the low frequency modes. Physiologically these would be eliminated by the surrounding soft connective tissue in the chest cavity.

Similarly, isotropic time dependent linear viscoelasticity is defined as part of the material constitutive behaviour to damp out the high frequency response during active contraction. While cardiac tissue is generally known to exhibit viscoelastic behaviour [50], suitable experimental data on porcine cardiac viscoelasticity were not available; hence, the model incorporates a small amount of viscoelasticity to eliminate unrealistic transient behaviour.

3.2.10 Model validation

In vivo strain echo data (TomTec 4D LV-Function, Version 4.6, Build 4.6.3.9, Unterschleißheim, Germany) of the endocardial surface was provided, which enables an independent data source to perform model validation. These *in vivo* strains are calculated by partitioning the endocardial surface into 16 segments, and measuring local deformation in longitudinal and circumferential directions [199]. An illustration of this 16 segment partition is shown in Figure 3.6 (a-b).

These *in vivo* strain measurements reference ED as the reference configuration, and as such, provide relative change in length through a single cardiac cycle compared to the ED state. For purposes of validation, we select ES as the primary point of comparison for measuring heart deformation.

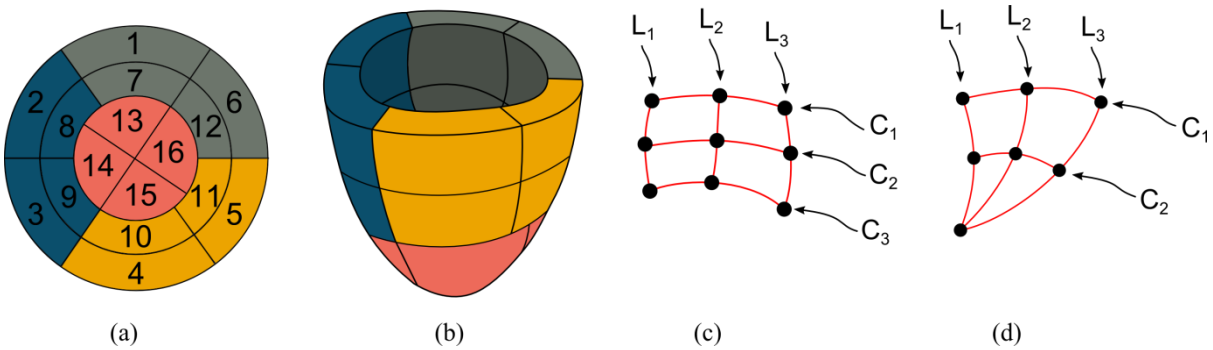

Figure 3.6: The 16 LV segment breakdown used in the in vivo strain calculation illustrated on (a): a radial map and (b): a simplified LV model. (c): A quadrilateral surface segment defined by 9 nodes. Nodes are joined by 3 circumferential cubic splines, C_i, and 3 longitudinal cubic splines, L_i. (d): A triangular surface segment defined by 7 nodes. Nodes are joined by 2 circumferential cubic splines, C_i, and 3 longitudinal cubic splines, L_i.

In order to provide comparable strain measures from our FE model, the endocardial nodes were partitioned into the same 16 segment division as the TomTec data. This resulted in 12 quadrilateral

segments for the LV trunk and 4 triangular segments for the apical region. Control nodes placed at the corners and midpoints of the regions were identified. Similar to the speckle-tracking imaging technology used to determine strain in the *in vivo* case, the nodal deformations of these control points were extracted at different time points in the cardiac cycle. By fitting cubic splines through these control points, longitudinal and circumferential measurements are created. The change in longitudinal and circumferential spline length provides a consistent strain measurement (i.e. engineering strain) analogous to the strain measurements provided by the *in vivo* TomTec strain measurements. The quadrilateral and triangular surfaces, the control nodes and the fitted cubic splines are illustrated in Figure 3.6 (c-d).

3.3 Results

3.3.1 Geometric segmentation

The visualization of the 3D heart structure directly from MRI data is given, along with our ventricular segmentation in Figure 3.7. Structural details extracted from MRI imaging conform to ventricular features reported experimentally for the porcine heart [200].

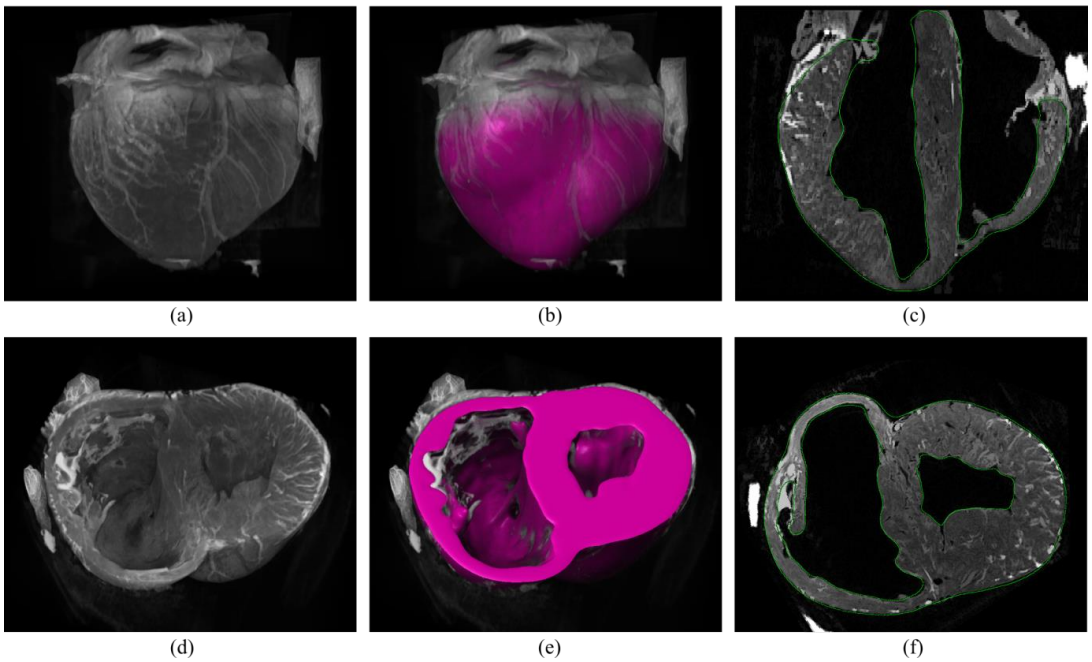

Figure 3.7: (a): 3D constructed visualizations of the full ventricular structure from MRI data. (b): Geometric segmentation of the full ventricular structure superimposed over the same background MRI data as (a). (c): Long axis cut plane of the MRI data superimposed with contours (green lines) for the full ventricular segmentation. (d): 3D constructed visualizations of the truncated ventricular structure from MRI data, revealing the endocardial ventricular structure. (e): Geometric segmentation of truncated ventricular structure superimposed over the same background MRI data in (d). (f): Short axis cut plane of the MRI data superimposed with contours (green lines) for the both ventricular segmentations.

A mesh convergence analysis was performed in Abaqus to identify suitable mesh refinement, using the truncated biventricular geometry and a single cardiac cycle. This is presented in the appendix section A1. Based on the mesh convergence analysis, the segmented model geometry was meshed using quadratic tetrahedral elements with roughly 85 000 elements.

3.3.2 Subject-specific myofibre orientations

3.3.2.1 Realistic DTMRI data interpolation results

For validation purposes, the segmented DTMRI data for the isolated LV was interpolated to double the resolution in each direction. This resulted in interpolated diffusion tensors, occupying voxel dimensions $1/8^{th}$ of the original data set. The interpolated invariant $\bar{I}_1$ is plotted alongside the original in Figure 3.8(a-b) for a short axis cut plane of the LV with the resolution corresponding to voxel size. Note, the interpolation scheme considers contributions from all directions, therefore the interpolated image in Figure 3.8(b) contains contributions from voxels above and below it. Tractography constructed from original and interpolated tensors are presented in Figure 3.8(c-d). Tracts are coloured by the RGB vector convention whereby vector components [x,y,z] correspond to colour [R,G,B] (i.e. a vector purely aligned in the z direction is coloured blue).

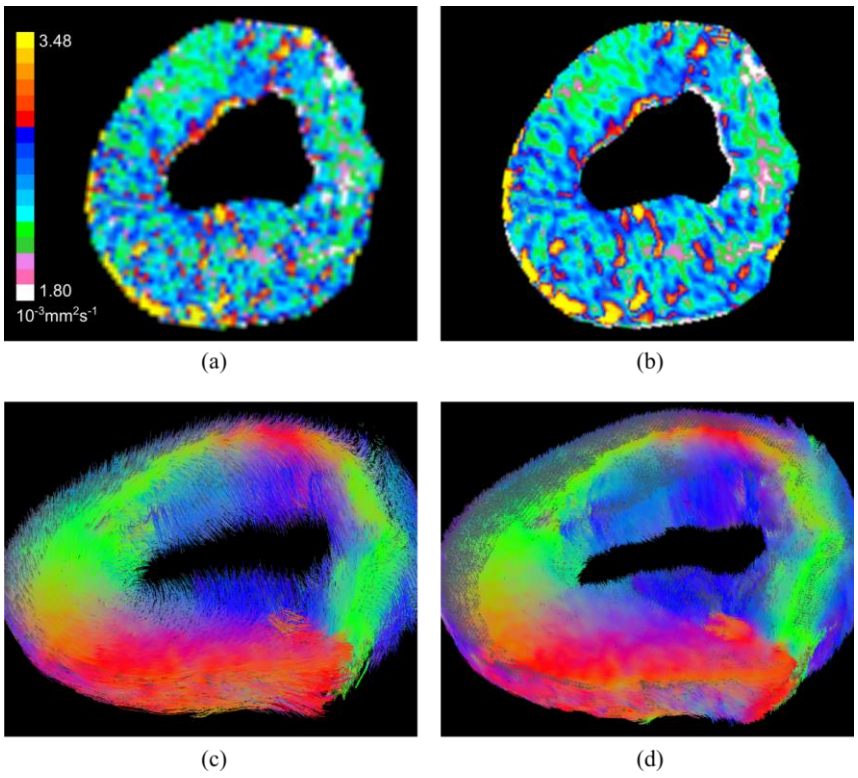

Figure 3.8: Diffusion invariant I1 for (a) the original and (b) the "higher resolution" interpolated state. Tractography of the base of the LV for (c) the original and (d) the "higher resolution" interpolated model. Tracts are coloured by the RGB vector convention whereby vector components [x,y,z] correspond to colour [R,G,B]

Resulting myofibre orientations presented as tracts in Figure 3.8(c-d) reveal consistent orientations between original and interpolated result. Regions in the original data set Figure 3.8(c) missing sufficient diffusion data to construct viable myofibre tracts have been "filled" due to interpolation in Figure 3.8(d). This is evident in the top right hand quadrant of each image and along the endocardial and epicardial surfaces. This results in more consistent and fully populated tracts throughout the domain. Furthermore, interpolation preserves unique features of the original data set and creates smooth transitions between them and the surrounding data. This is seen in both the invariant images Figure 3.8(a-b) and the tractography images Figure 3.8(c-d).

3.3.2.2 Subject specific myofibre orientation results

Results for the inclinations angles α_h in the porcine LV are presented graphically in Figure 3.9 for each AHA segment. Inclination angles, excluding the apex, vary from 67.0º ± 17.6º on the endocardium to -43.8º ± 21.1º on the epicardium in a predominantly linear fashion. This regional presentations of α_h, partitioned by AHA region and further subdivided by transverse wall depth, presents with tightly contained distributions of data. This is reflected in the distribution of standard of deviations, which present with a mean of 17.6º ± 6.3 º. The apical region did not have enough data points to accurately predict mean values throughout the myocardial, but is included for completeness.

Results for the transverse angles α_t in the porcine LV are presented graphically in Figure 3.10 for each AHA segment. Unlike α_h, there is no consistent global trend across all regions. The distributions reveal mean angles of α_t close to zero degrees in the lateral regions (-3.5º ±12.1º). In septal regions α_t varied linearly from -54.3º ±11.2º on the LV endocardium to 39.8º ±20.9º on the RV endocardium. The anterior and interior regions all displayed negative values of largely different degrees on the endocardial surface (-70.6º ±36.6º) which varied to values of α_t close to zero on the epicardial surface (6.9º ±16.9º), indicating relative alignment with the epicardium surface. The endocardial regions of the anterior sections displayed large standard of deviations much larger than those found in other regions.

The analysis of sheet angles β revealed no strong correlation between sheet angle and transmural depth. Histogram analysis was therefore chosen as the best representation of this data and is presented in Figure 3.11. While the regional results present with large standard of deviations, the distributions still present with a clear mean direction. The dominant sheet angle is found at 60.1° if all regions, excluding the apex, are considered. When septal regions (AHA 2, 3, 8, 9 and 14) are excluded this value increases to 67.1° (i.e. the sheet plane is further aligned to the transmural-circumferential plane).

These myofibre orientations are interpolated to the centroid of each element in the FE mesh. Images revealing the geometry with and without myofibre orientations are presented in Figure 3.12. In addition to the characteristics presented quantitatively above, other qualitative features are visible

from this. Firstly, myofibre orientations are predominantly tangential with geometric surfaces. This can be seen in Figure 3.12(b,d), by the abundance of featured myofibres protruding through cut surfaces relative to those seen protruding through geometric surfaces. Secondly, myofibres are closely aligned with papillary structure morphology, as can be seen in Figure 3.12(c-e). Finally, the variation in inclination angle in the LV, varying from positive on the endocardium through to negative on the epicardium, is easily identified from the global myofibre arrangement. This is shown in Figure 3.12(f).

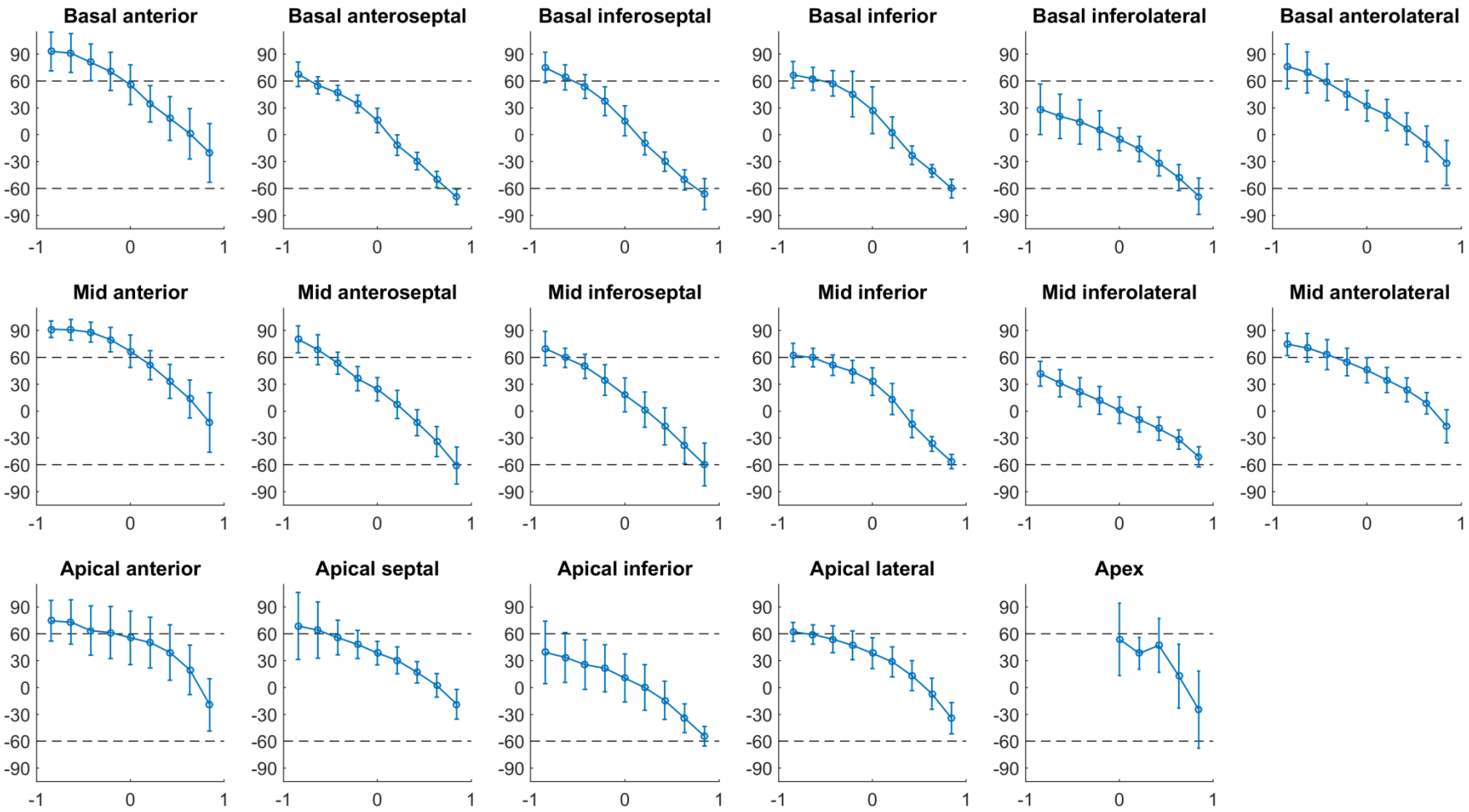

Figure 3.9: Inclination angles α_h in the 17 AHA LV regions showing the distribution along the radial depth. Normalized radial coordinates were used to indicated the endocardium (-1), mid wall (0) and epicardium positions (+1). Dashed lines corresponding to +60° and -60° are plotted for ease of comparison and because a significant number of studies use these bounds when prescribing α_h in LV computational models.

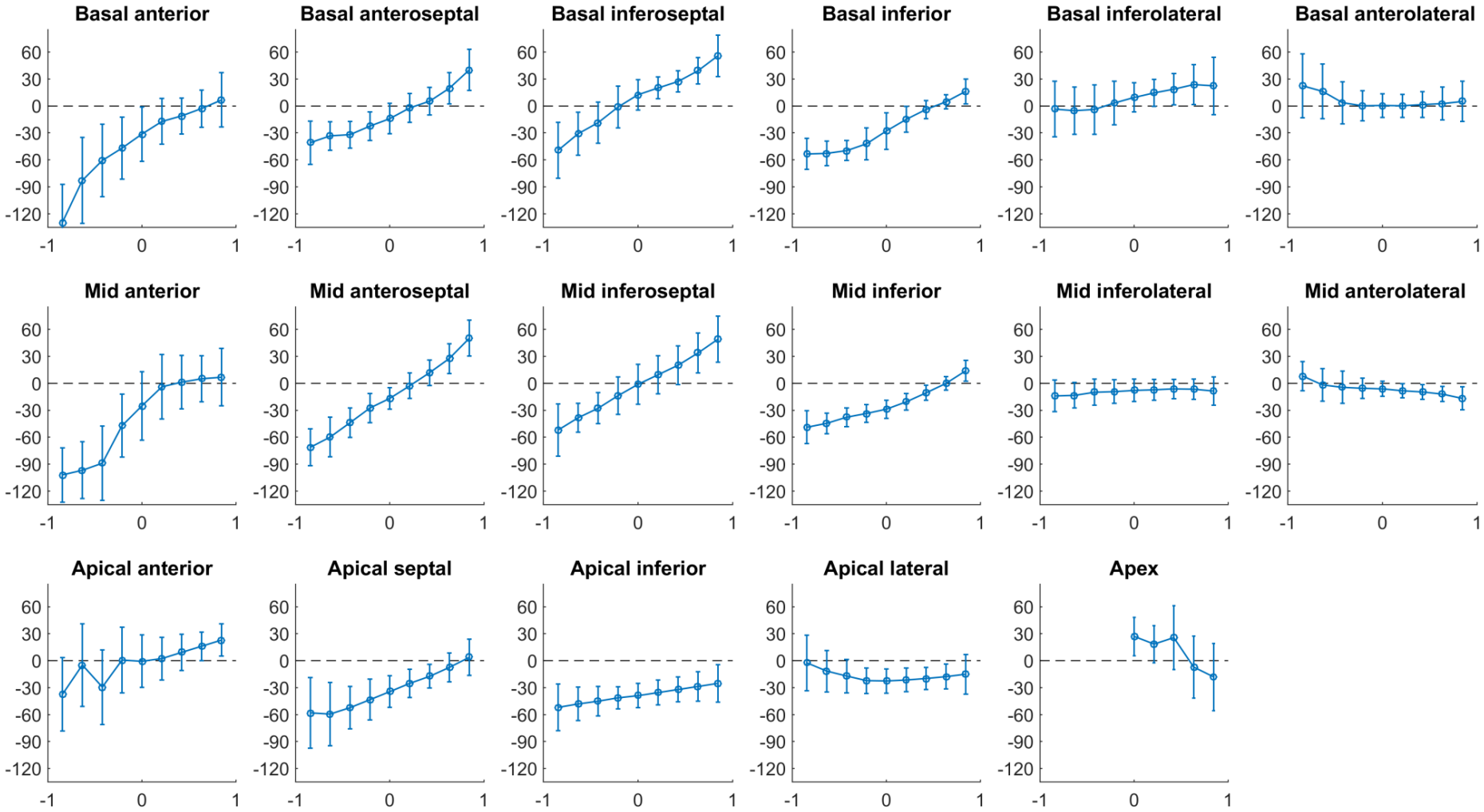

Figure 3.10: Transverse angles α_t in each cohort for the LV free wall regions showing the distribution along the radial depth. Normalized radial coordinates were used to indicated the endocardium (-1), mid wall (0) and epicardium positions (+1). A dashed line at 0° is plotted for ease of comparison.

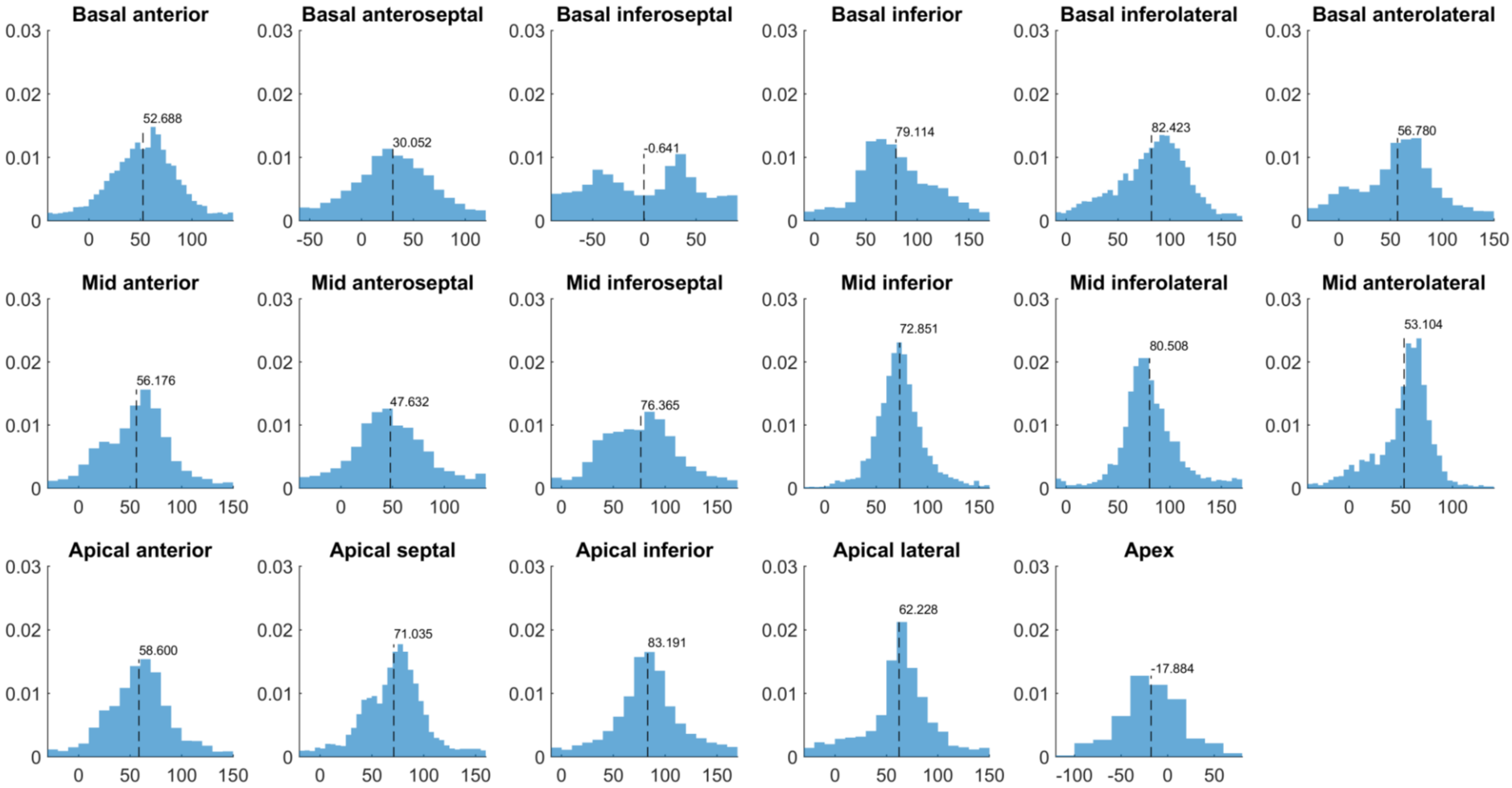

Figure 3.11: Histogram distributions of sheet angles β in the 17 AHA LV regions. Dashed lines and values correspond to the mean value. Histograms are normalized by probability density (PD), i.e. the area under each distribution sums to 1.

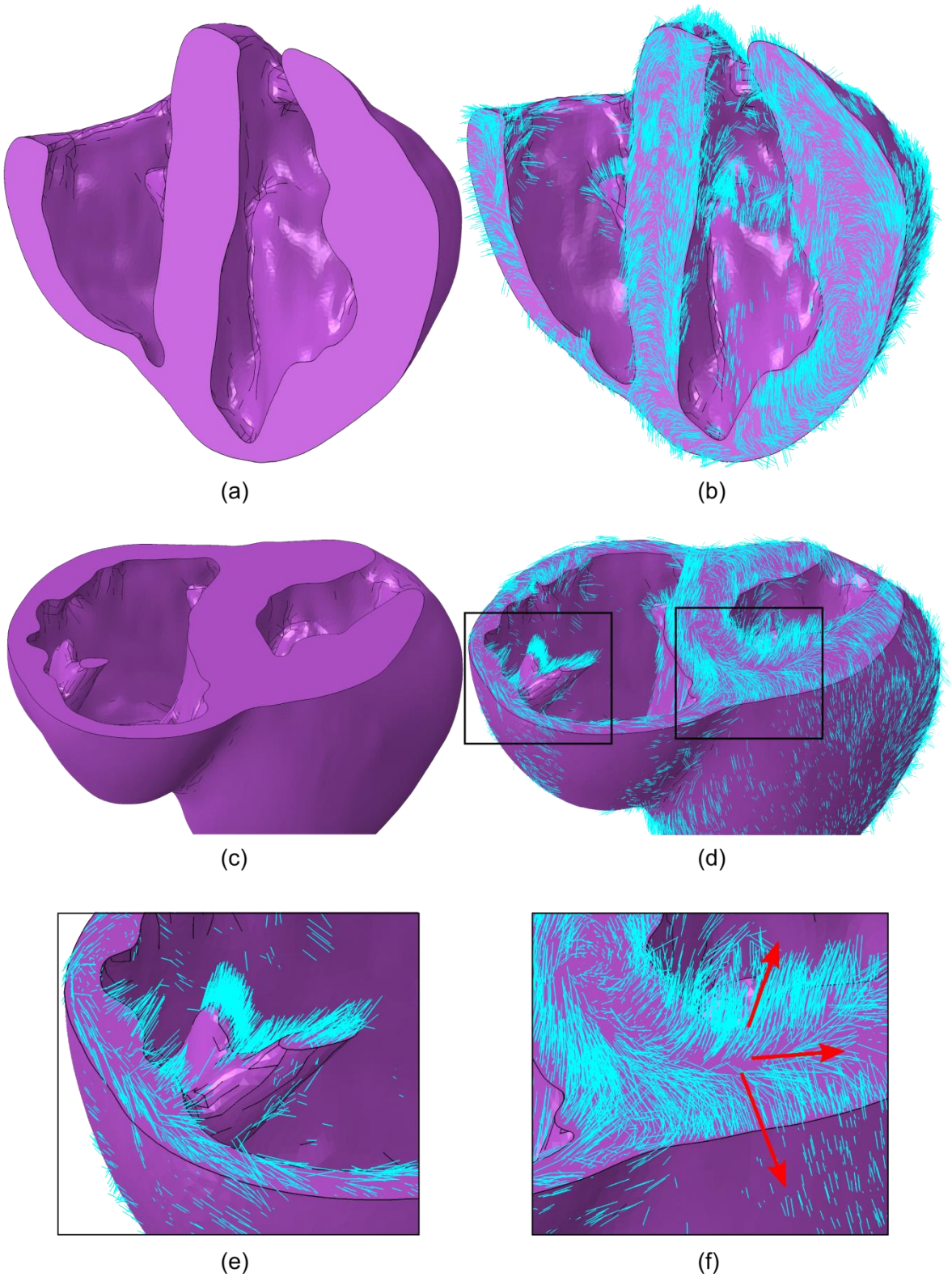

Figure 3.12: (a): Porcine geometry bisected longitudinally to reveal the endocardial surfaces. (b): Myofibre orientations plotted in cyan lines for the same geometry revealed in (a). (c): Porcine geometry cut along a short axis to reveal cut papillary structures in the RV and the short axis plane in the LV. (d) Myofibre orientations plotted in cyan lines for the same geometry revealed in (c). (e) Zoomed in image of the cut RV papillary structure with fibres from (d). (f) Zoomed in image of the LV short axis plane from (d). Red arrows aligned with the local myofibre orientation are added for regions in the epicardial, mid wall and endocardial regions.

3.3.3 Passive material estimation

The best fit the human shear data [181] is illustrated in Figure 3.13, whereby model response (solid lines) is plotted against experimental data (circles). The corresponding calibrated material parameters are reported in *Table 3.5*, alongside those obtained using porcine data. For the porcine study, literature values are also included for comparison. The human study is too recent to have calibrated results from other studies.

Table 3.5: Calibration results (bold text) and literature values for comparison.

Study	a (kPa)	b	a_f (kPa)	b_f	a_s (kPa)	b_s	a_{fs} (kPa)	b_{fs}	
Dokos 2002	**0.261**	**10.767**	**19.539**	**13.615**	**3.406**	**5.652**	**0.313**	**14.068**	Current study
	0.236	10.810	20.037	14.154	3.725	5.165	0.411	11.30	Wang *et al.* [201]
	0.496	7.209	15.193	20.417	3.283	11.176	0.662	9.466	Goktepe *et al.* [57]
	0.059	8.023	18.472	16.026	2.481	11.12	0.216	11.436	Holzapfel *et al.* [56]
Sommer 2015	**1.051**	**7.542**	**3.465**	**14.472**	**0.481**	**12.548**	**0.283**	**3.088**	Current study

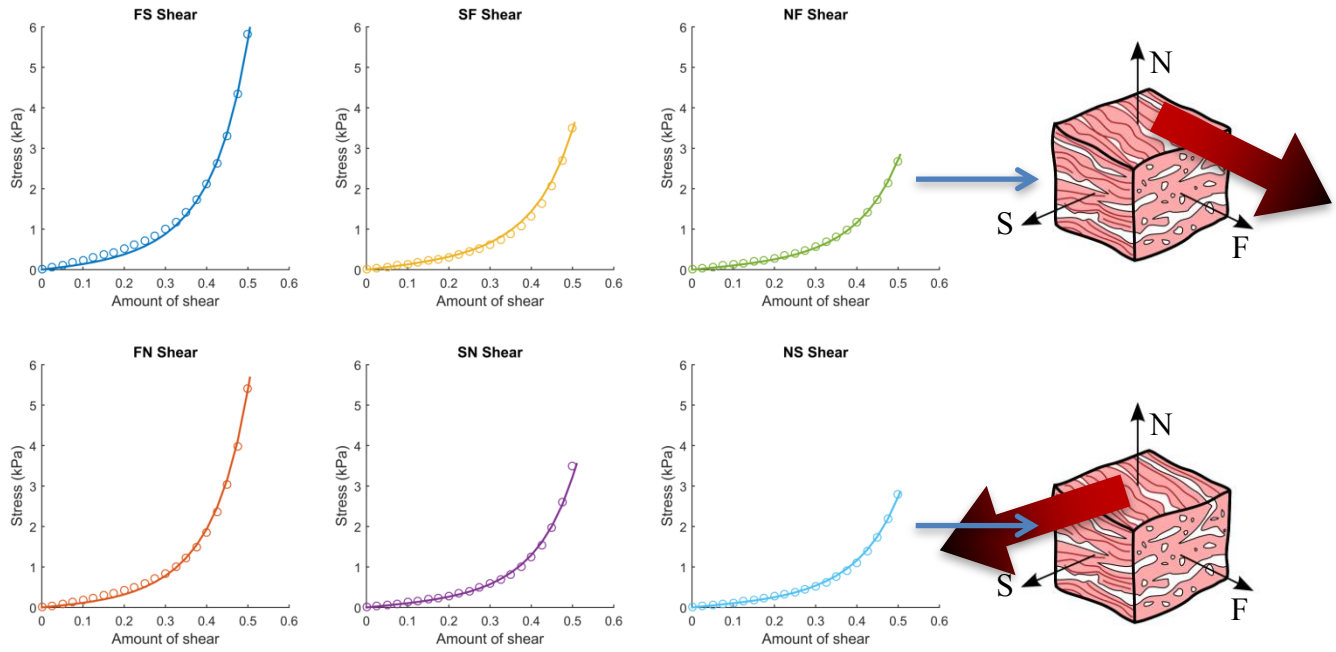

Figure 3.13: Passive material response of all 6 shear modes of an idealized tissue cube (Left) and illustrations of the two shear modes NF and NS (right).

The second stage calibration, whereby the material law was scaled to minimize the error between the Klotz curve and the model response in the passive filling stage, converged on a material parameter set that scaled the linear terms of the material law (a_i) by an amount of 0.31 and the exponential terms (b_i) by an amount 0.73. The passive filling curve resulting from this optimization is given in Figure

3.14(a). The final calibrated EDV matches closely with the target value at 13.5mmHg: 73.02 vs. 73.00 ml. Fitting metrics evaluated from 200 data points along the passive filling curve results in an R^2 value of 0.98 and RMSE value of 0.66 mmHg. Long axis and short axis profiles of the ventricular structure in the unloaded (i.e. initial) and the ED configuration are presented in Figure 3.14(b-c).

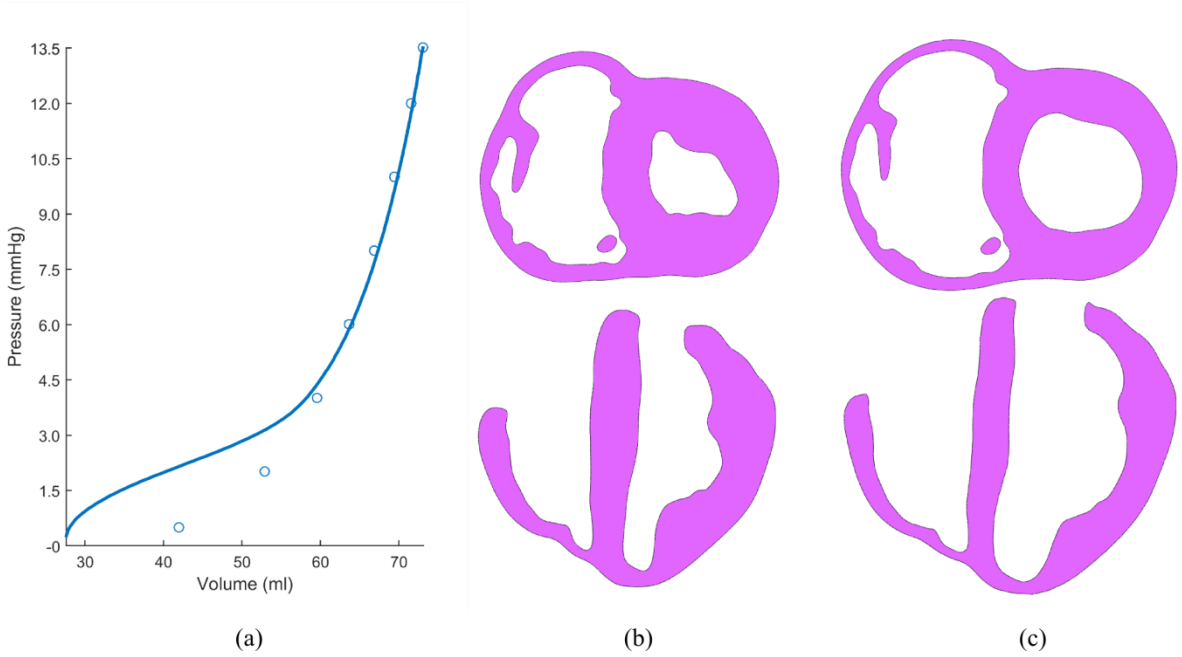

Figure 3.14: (a) Klotz curve (circles) and model response (straight lines) for the porcine subject after calibration. (b) Long axis and short axis views of the ventricular structure at the unloaded configuration. (c) Long Axis and short axis views of the ventricular structure at the ED configuration.

3.3.4 Active tension

For comparison we reproduce the analytical results shown in Guccione *et al.* [60], which demonstrate the active tension as a function of time for multiple sarcomere length choices in the deformed configuration. The full active tension development was reproduced for $t \in (0,1000)$ ms and is in Figure 3.15.

The active calibration optimization routine converged on a material parameter set that produced an SV of 40.12ml and LVLS of 5%. This was achieved with $T_{max} = 130$ kPa, $n_s = 0.07$ and $n_n = 0.0$. The resulting full PV loop, starting from the unloaded configuration, is presented in Figure 3.16(a). A comparison of target values and results for LV pressure and volume outcomes is presented alongside this PV loop in Figure 3.16(b).

A further mechanical analysis on the left and right ventricle at this stage would be premature. Rather, we perform this after simulating multiple cardiac cycles, whereby the mechanical aspects of the ventricles converge with the lumped parameter circulatory system. This results in a configuration that

incorporates a degree of pre-strain, has converged on a single steady state PV loop and is a more realistic representation of heart function.

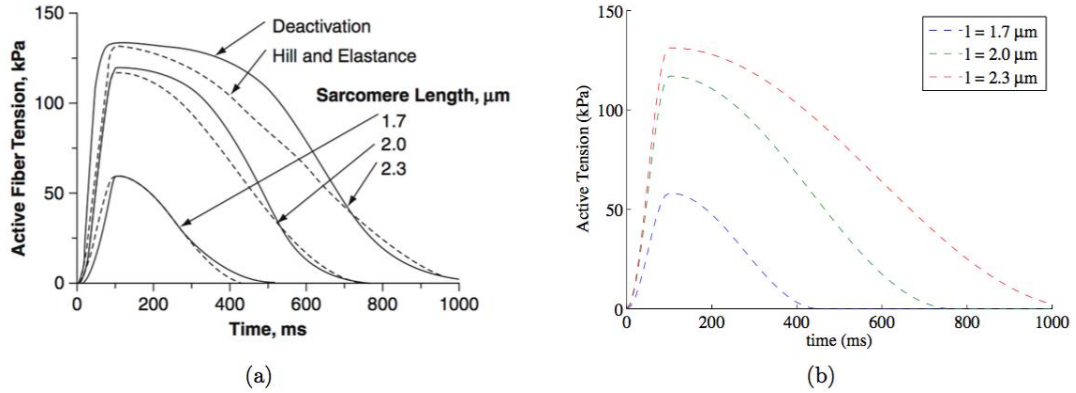

Figure 3.15: (a) Graph taken directly from Guccione et al. [60], illustrating isometric twitches predicted by the authors "deactivation" model and their "Hill and elastance" models at a range of sarcomere lengths. (b) Reproduction of "Hill and elastance" model results for multiple sarcomere lengths l, for verification purposes.

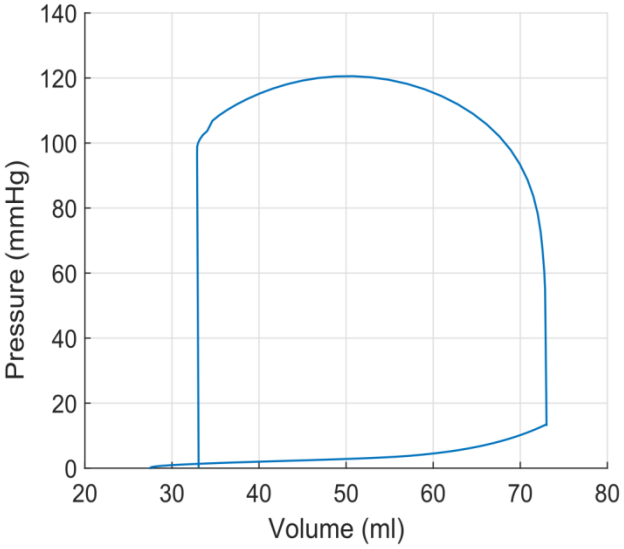

Measurement	Target	Result
LV EDV (ml)	73.00	73.02
LV SV (ml)	40.00	40.12
LV ESV (ml)	33.00	32.90
LV EDP (mmHg)	13.5 ±4.5	13.50
LV ESP (mmHg)	87.6 ±23.7	98.90

(b)

Figure 3.16: (a): PV loop of the LV after calibration procedure. (b): Comparison of LV volumetric and pressure targets and results from calibration.

3.3.5 Coupled mechanical and circulatory model

The model simulation converged on reproducible PV loop after 4 cardiac cycles. This is illustrated in Figure 3.17. There were minor changes between converged output results in the LV and those from a single cardiac cycle. LV EDV was 72.6 ml and LV SV was 37.9 ml in the converged cardiac cycle. The RV converges on a PV loop with almost exactly the same SV as the LV at 37.1 ml and with an EDV of 118.5 ml. This translates to ejection fractions of 52.2% and 31.3% in the LV and RV respectively. A summary of these results is given in Table 3.6.

Table 3.6: Metrics of performance over a cardiac cycle in the fully calibrated subject-specific heart

Metric	LV	RV
EDV (ml)	72.6	118.5
EDP (mmHg)	12.47	1.35
SV = EDV- ESV (ml)	37.9	37.1
EF	52%	31%
maxP (mmHg)	125.4	42.9

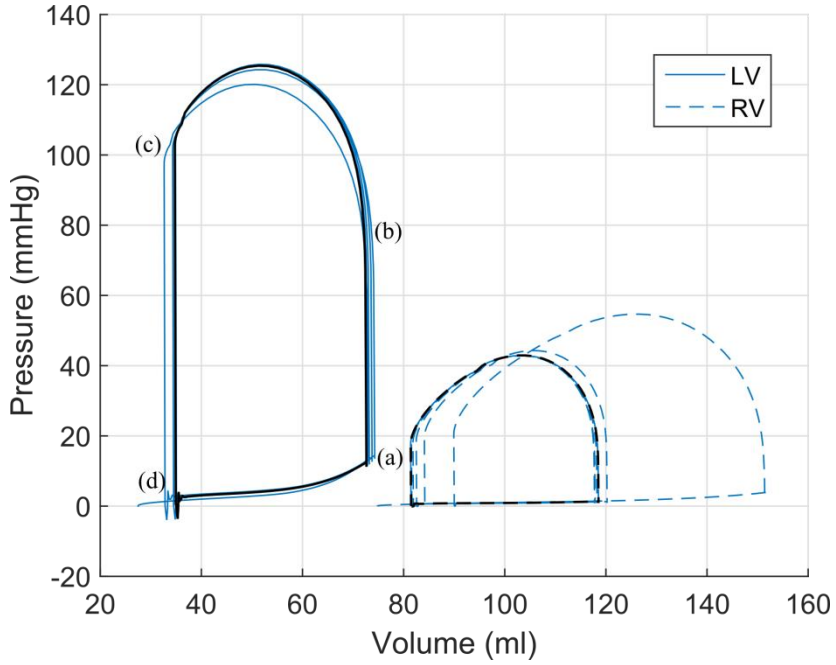

Figure 3.17: Pressure volume relation for the right and left ventricle over six simulated cardiac cycles. The final cardiac cycle, taken as the converged solution, is plotted in black. Key parts of the cardiac cycle are labelled on the LV PV loop, which correspond to (a) End diastole, (b) Start ejection, (c) End systole and (d) End relaxation.

Using the key parts of the cardiac cycle as presented in Figure 3.17, myofibre stress and strain values were assessed for each ventricle. These values were volumetrically averaged (i.e. normalized by element volume) to proportionally weight results by element volumes (see Eq. (3.25)). The mean volumetrically averaged myofibre stress is at its lowest at the end of relaxation (ER); it increases during passive filling, reaching a peak passive stress at end diastole (ED) and then rapidly increases during the systolic phase of the heart. By the start of ejection (SE) the myofibre stress is already high (order of magnitude greater than passive stress), which enables the continued contraction of the heart through ejection. While the myofibre stresses are high at end systole (ES), they continuously decline from this point, reaching the lowest values at ER, when the cycle repeats.

The mean volumetrically averaged myofibre stresses in the LV was found to be 1.51 ± 1.95 kPa, 24.42 ± 10.78 kPa, 19.13 ± 12.57 kPa and 0.03 ± 0.09 kPa at ED, SE, ES and ER respectively. For the RV the mean volumetrically averaged stress was found to be 1.01 ± 4.33 kPa, 22.68 ± 31.48 kPa, 20.24 ± 23.65 kPa and 0.01 ± 0.09 kPa for the same respective time points. These values are presented in Table 3.7 while the full histogram distributions of these stresses are presented in Figure 3.18. Additionally, myofibre stress contours are presented in Figure 3.19 over long and short axis cut planes of the ventricular structure. These contour plots reveal qualitative details about the myofibre stress distributions associated with geometric position.

Table 3.7: ED and ES volumetric-averaged mean stress and strain results for the converged heart presented separately for the LV and RV. Results are presented with standard deviations.

Time Point	LV myofibre stress (kPa)	RV myofibre stress (kPa)	LV myofibre strain (%)	RV myofibre strain (%)
ED	1.51 ± 1.95	1.01 ± 4.33	9.12 ± 4.62	6.28 ± 5.05
SE	24.42 ± 10.78	22.68 ± 31.48	-2.03 ± 9.16	-6.59 ± 9.35
ES	19.13 ± 12.57	20.24 ± 23.65	-10.67 ± 4.08	-11.44 ± 5.54
ER	0.03 ± 0.09	0.01 ± 0.09	0.65 ± 1.10	-0.39 ± 1.88

Abbreviations: ED, end-diastole; SE, start-ejection; ES, end-systole; ER, end-relaxation.

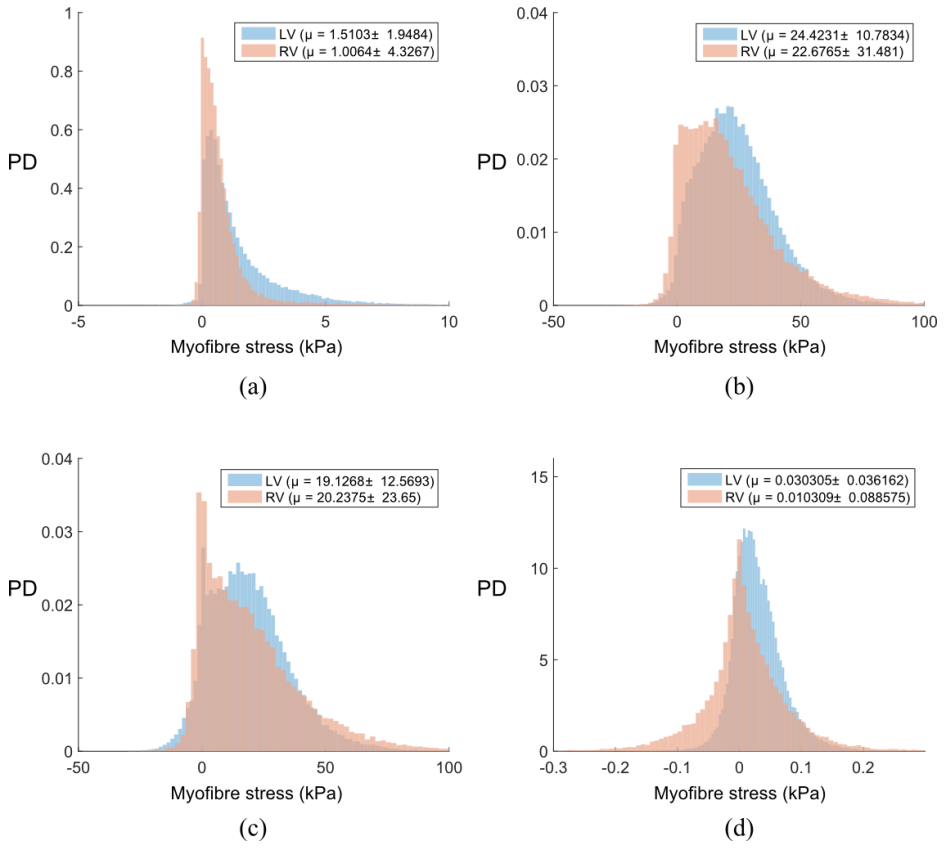

Figure 3.18: Myofibre stress distributions at (a): end-diastole, (b) start of ejection, (c) end-systole, and (d) end-relaxation. Histograms are normalized by probability density (PD), i.e. the area under a distribution sums to 1.

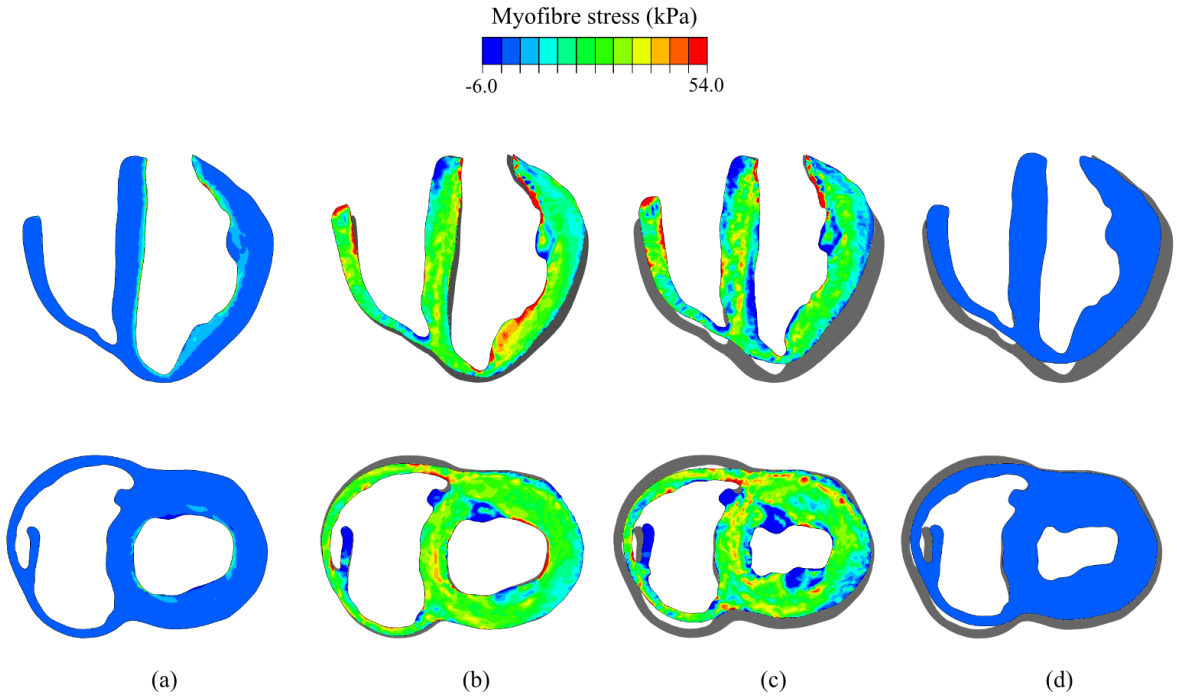

Figure 3.19: Myofibre stress at (a): end-diastole, (b) start of ejection, (c) end-systole, and (d) end-relaxation. Top and bottom rows are cut planes of the ventricles in the long axis and short axis respectively. Non symmetric contour limits were chosen to allow for a single set of limits to be used across the whole cardiac cycle.

Similar to the presentation of myofibre stress results, strain results were analysed at the same key points in the cardiac cycle. The mean volumetrically averaged myofibre strain is at its largest at ED. Once contraction begins, the active tension development causes myofibre shortening which is seen moderately at SE and prominently at ES. After ES and during relaxation the myofibres experience elongation returning to values similar to their resting configuration, albeit not entirely. The mean volumetrically averaged myofibre strain in the LV was found to be 9.12 ± 4.62 %, -2.03 ± 9.16 %, -10.67 ± 4.08 % and 0.65 ± 1.10 % at ED, SE, ES and ER respectively. For the RV the mean volumetrically averaged strain was found to be 6.28 ± 5.05 %, -6.59 ± 9.35 %, -11.44 ± 5.54 and -0.39 ± 1.88 % for the same respective time points. These values are presented in Table 3.7 while the full histogram distributions of these stresses are presented in Figure 3.20. Additionally, myofibre strain contours are presented in Figure 3.21 over long and short axis cut planes of the ventricular structure. These contour plots reveal qualitative details about the myofibre strain distributions associated with geometric position.

A detailed analysis of regional strain in the LV with respect to the local longitudinal and circumferential directions is presented in the following section on model validation.

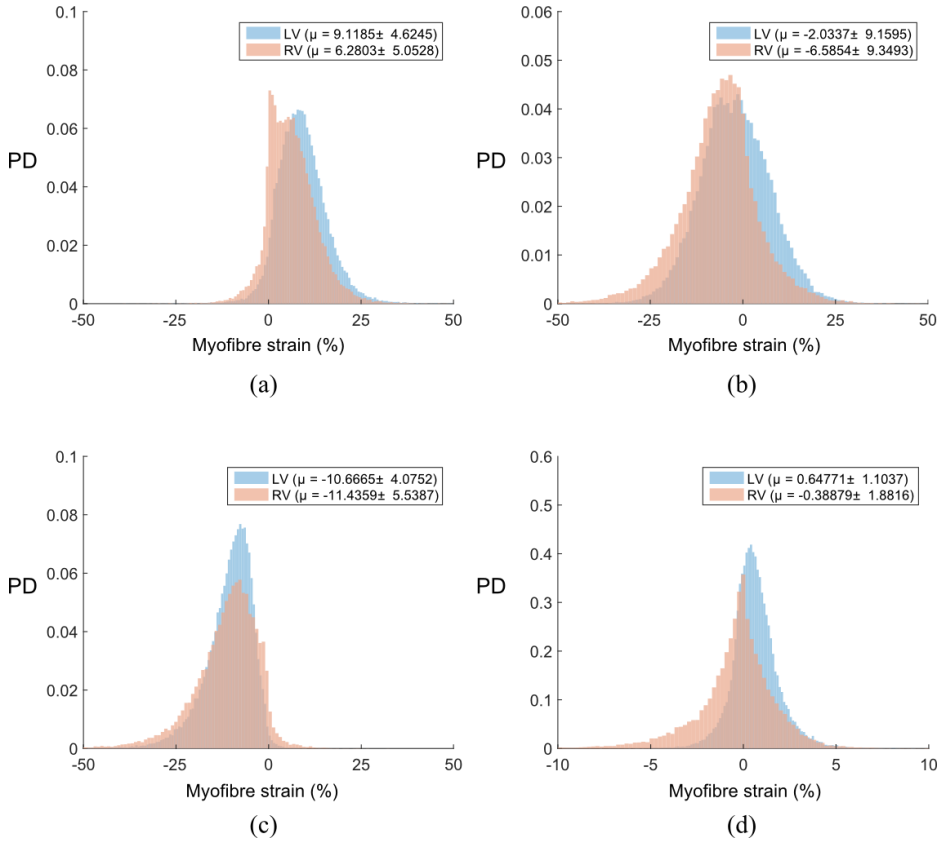

Figure 3.20: Myofibre strain distributions at (a): end-diastole, (b) start of ejection, (c) end-systole, and (d) end-relaxation. Histograms are normalized by probability density (PD), i.e. the area under a distribution sums to 1.

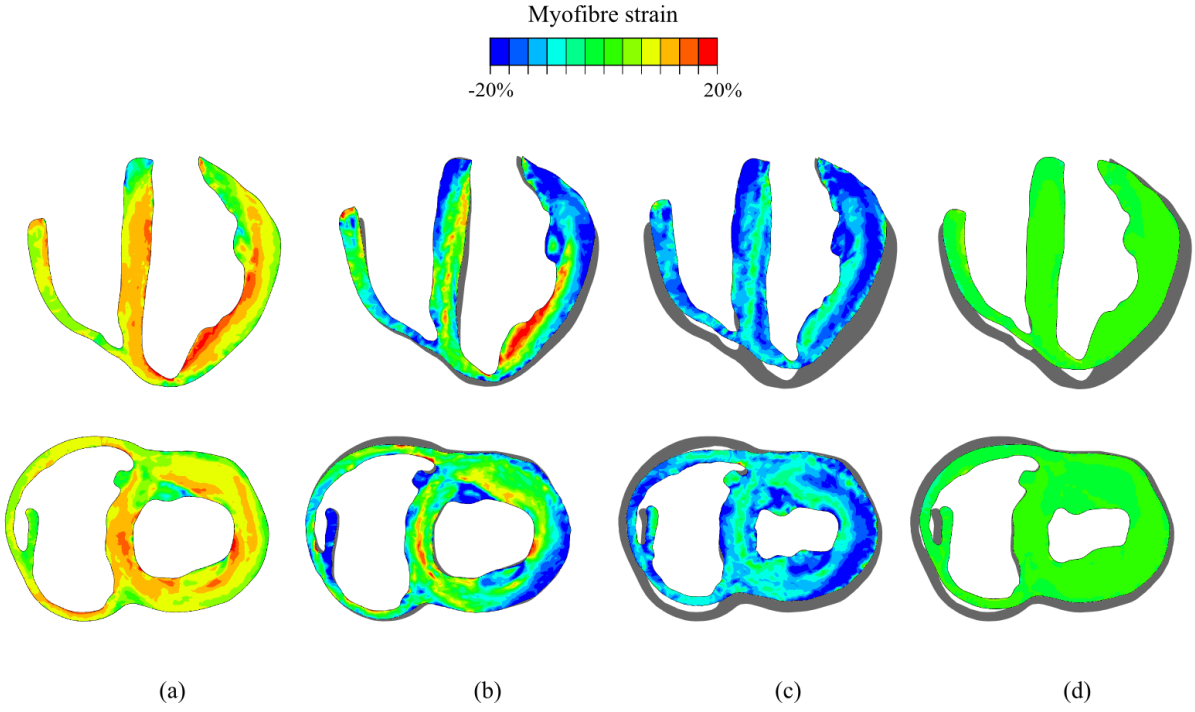

Figure 3.21: Myofibre strain at (a): end-diastole, (b) start of ejection, (c) end-systole, and (d) end-relaxation. Top and bottom rows are cut planes of the ventricles in the long axis and short axis respectively.

3.3.6 Model validation

Initial comparison of the endocardial strains revealed moderate agreement of global strains (i.e. averaged over the entire surface). Global longitudinal strain (GLS) was -13.6% for the FE model simulation, which compares well with the *in vivo* recorded value of -17.8% originating from the TomTec data. The global circumferential strain (GCS) for the FE simulations and the *in vivo* recording was -26.5% and -21.3% respectively. For the circumferential strains, the GCS is representative of regional strain comparisons: The FE simulations produced a greater reduction in circumferential directions in basal, mid and apical regions, as shown in Figure 3.22.

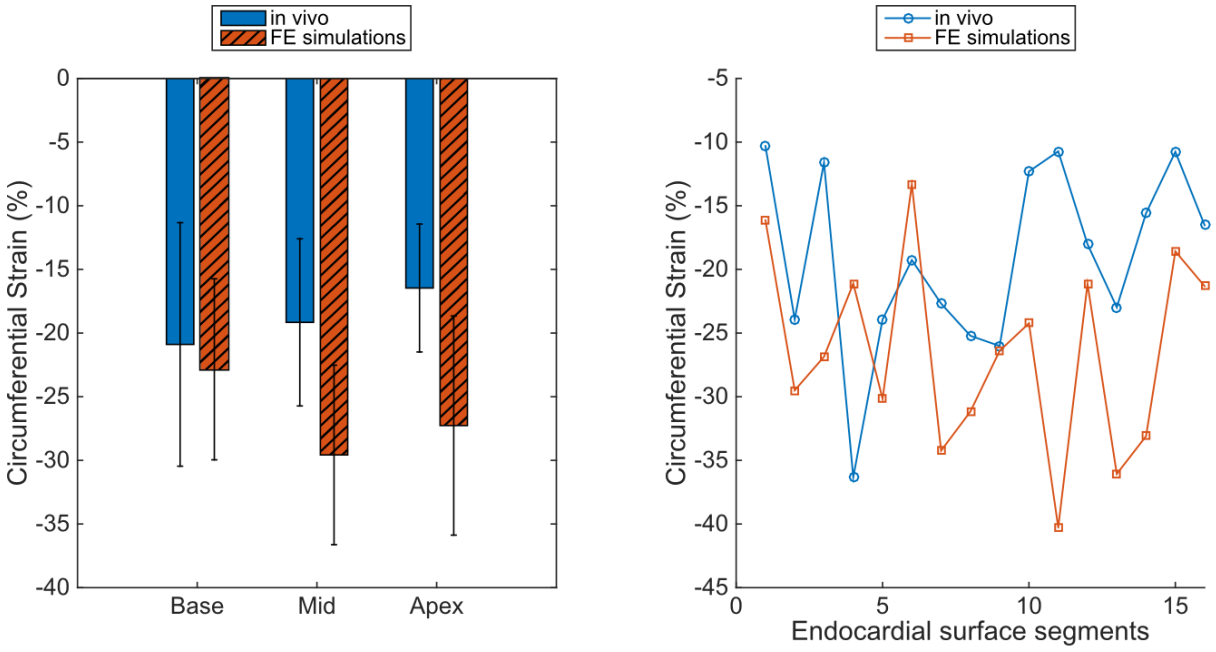

(a) (b)

Figure 3.22: Circumferential endocardial strain comparison between the FE simulation and the in vivo recordings of the same porcine subject. (a) Mean strain results for each longitudinal region. (b): Strain results for each of the 16 endocardial surface regions.

This was not the case with longitudinal strains, whereby a regional analysis of the longitudinal strains revealed poor agreement between simulated and measured *in vivo* strains. This is particularly poor at the base of the LV model. To identify if boundary conditions were the cause of this disagreement, the model simulations were rerun using multiple configurations of enforced boundary conditions. This did not change strain results. This brief analysis is presented in the appendix section A2.

The FE simulation resulted in apical regions experiencing longitudinal strains roughly three times the values seen in the *in vivo* model recordings. Conversely, the basal regions experience longitudinal strains roughly a third of the values seen in *in vivo*. This can be seen in Figure 3.23.

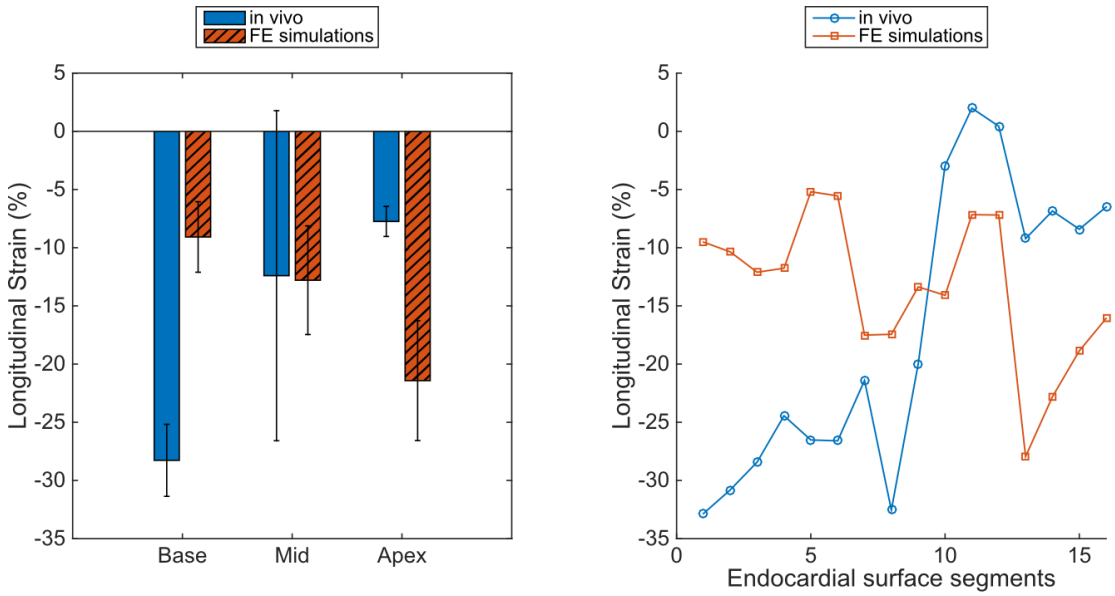

(a) (b)

Figure 3.23: Longitudinal endocardial strain comparison between the FE simulation and the in vivo recordings of the same porcine subject. (a) Mean strain results for each longitudinal region. (b) Strain results for each of the 16 endocardial surface regions.

3.4 Discussion

3.4.1 Geometric segmentation

The geometric model construction used in this study is one of the most sophisticated ventricular structures produced for mechanical FE modelling of the heart compared to those found in the literature.

While biventricular representations of the heart have become popular geometric choices for mechanical FE studies in recent years, for example [39, 103, 202-208], none of these models include papillary structures and/or all four valve openings[1]. Recent publications using the cardiac model from the Dassault Systèmes Living Heart Project [28, 167, 169, 209] include this level of detail (and atrial structures); however this heart geometry is an idealized "artistic" representation and not subject-specific. It should be noted that some electrophysiology studies have included high precision geometrical models (with incredibly fine structural details) for almost a decade [210, 211].

[1] The geometric models of Krishnamurthy *et al.* [200] and Fritz *et al.* [201] include all four valve openings (and atria), but lacks papillary structures and other high resolution morphology.

Constructing a model of this geometric detail has drawbacks. Specifically, segmentation of the valve openings and the precise boundary between the atrial structures is time consuming. Fine ventricular features, such as the branching papillary structure connecting the right ventricular free wall to the septal wall or the thin connective tissue separating the aortic and mitral valve (as seen in Figure 3.3) requires much smaller elements and increases the overall mesh size. Not only does this increase the problem size to be solved but it also impacts the explicit time stepping solution method in the FE analysis, which is limited by the smallest elements in the mesh.

However, these intricate geometric details can and should be included at the very least to elucidate their role in mechanical simulations. Future simplifications to model geometries can then be made under informed circumstances, which can contextualize computational results in absence of these features.

3.4.2 Subject Specific myofibre orientation

3.4.2.1 Interpolation

Interpolation of diffusion tensor data preserves features of the original data while also producing smooth continuous representations of diffusion invariants and orientations. The interpolated invariant $\bar{I}1$ shown in Figure 3.8(b) clearly illustrates this. Qualitatively, it looks like a more "in focus" version of the original data set shown in Figure 3.8(a). The interpolated fibre tracts, representing the interpolated myofibre orientations, present with consistent vector components compared to the original data. This is seen by a visual inspection of the colour of vectors, which is dependent on the underlying vector components, in each plot Figure 3.8(c-d). Interpolation results in denser representations, not only due to the higher resolutions, but also due to the interpolation of myofibres through regions in the domain that may have been excluded for lack of viable diffusion data in the original state.

3.4.2.2 Myofibre angles

The values from α_h conform well to other studies of large animals in terms of mean values [26, 149, 160-163] and typical standard of deviations expected from regional DTMRI myofibre analysis [34, 148]. In addition to standard qualitative features, features within the geometric segmentation align with physiological expectations. Consider the mid and basal regions for the "trunk" of the LV wall shown in Figure 3.9. The fibre arrangement of regions adjacent to each other longitudinally is extremely similar.

Our data reveal larger angles (i.e. close alignment with the longitudinal direction) in the anterior endocardial region when compared to other AHA regions circumferentially. Anterior regions (and to a lesser extent, inferior regions) typically contain large papillary muscles on the endocardium, which would explain this. These endocardial values of α_h in the anterior and inferior regions plateau before declining linearly as a position of wall depth. Considering that other AHA regions have a fairly linear change in α_h across the wall thickness, this could serve as a threshold to identify geometrically where the papillary muscle transition to standard myocardial wall tissue. The study of fibre orientation in papillary muscles is relatively unreported in the literature, due to their difficulty to segment from *in vivo* imaging. However, in the early experimental work of Streeter *et al.* [160], the authors also identified a plateau of myofibre angle α_h of roughly 90º in papillary muscles.

Values of α_t are not as commonly reported in the literature as α_h. Scollan *et al.* [148] reports a single value for α_t in the LV free wall of -7.9º (towards the endocardium) and Geerts *et al.* [163] reports a mean value of -3º. When calculated, the mean value for α_t in the LV free wall for our results (i.e. -7.1º) compares well with these findings. Lombaert *et al.* [34] reported transverse angles measured *in vivo* and found values of α_t that were low in the epicardium with high variability (7º±31º), low in the mid wall region with more consistency (9º±12º) and relatively high on the endocardium wall (34º±29º). Qualitatively, we see the same trends in our data albeit in the other direction: Specifically, the presence of large standard of deviations (SD) near the endocardial wall.

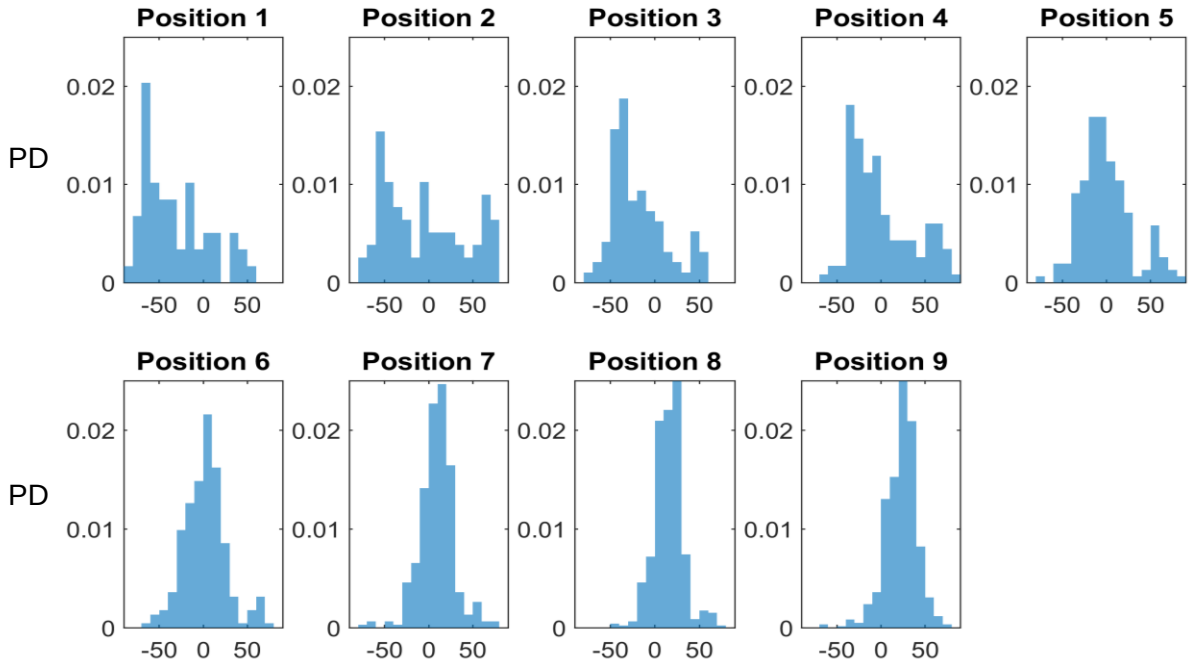

Figure 3.24: Distributions of transverse angles α_t for the apical anterior region (i.e. AHA 13) for positions along the wall depth. Each distribution at a position corresponds to the mean and SD values presented in Figure 3.10. Position 1 corresponds to the most endocardial position and position 9 to the most epicardial. Histograms are normalized by probability density (PD), i.e. the area under each distribution sums to 1.

Upon detailed investigation into the large SD values of α_t, it was found that these regions presented with non-normal distributions of fibre angles. A typical example is given in Figure 3.10 AHA 13. Here, the SD values are large at the endocardium and tighten as the transmural position approaches the epicardium. The associated distributions of fibre angles α_t at each transmural position are given in Figure 3.24. Positions 1-4 have a non-normal distribution which corresponds to the large SD bars in Figure 3.10. The non-normal distribution is the result of a lack in dominant transverse alignment or multiple overlapping families of alignment. This is highly likely in the papillary-myocardium transition.

3.4.2.3 Sheet angles

Regional sheet angle results presented a clear mean direction within each region, albeit surrounded by a large SD. Together, this is indicative of two highly reported features of laminar sheets:

1. The branching and merging laminar structure [32, 33, 212-214].
2. The presence of a dominant sheet angle consistent across regions [75, 149, 179, 215].

The dominant sheet angle finding of 60.1° is consistent with reported literature values: Costa *et al.* [215] reported mean sheet angle ranging from 50° to 60° from a collection 8 canine subjects; Dokos *et al.* [75] found a similar result for pigs reporting mid wall sheet angles of ~45°; A single Human subject study found dominant sheet angles at 50° [179].

A secondary population of laminar sheets from the same specimen sample has been reported in several studies [32, 150, 179], but not in others [148, 215, 216]. Helm et al. found that regions from a single subject had only one dominant population, however when their data was pooled across 7 canine subjects a bimodal distribution was obtained [149].

Hooks et al. found that in 6 porcine subjects a dominant laminar structure existed and that only some regions showed "pockets" of a secondary population which were roughly orthogonal [217]. This is strongly in line with our findings, whereby the majority of regions display a dominant sheet angle population, and only some regions display evidence of a secondary population. The basal inferoseptal region, and to a lesser degree the basal anterolateral region, display two distinct populations of sheet angles both roughly orthogonal to each other. Similarly, Dokos *et al.* [75] reported qualitative results on porcine laminar structure, in which half of their samples from porcine subjects showed "evidence" of a secondary population sheet structure orthogonal to the dominant direction.

3.4.3 Passive material estimation

The method of a two stage calibration considering small specimens and global LV filling has been used in other literature studies [39, 218].

When assessing the specimen response in the shear experiments, the porcine study displayed *much* stiffer material behaviour, especially in the fibre direction. As the human study was performed over a decade after the porcine study, more sophisticated methods were utilised in preventing contracture of heart muscles in the specimen extraction process. In particular they perfused a cardioplegic solution *in vivo* before organ extraction, and kept the removed hearts in a cardioplegic solution with an additional nucleophile agent 2;3-butanedione monoxime (BDM). In contrast, the porcine study had no *in vivo* considerations and placed the explanted hearts in saline. The coronary arteries were cannulated and perfused a cardioplegic solution (with BDM) up to 15min after excision.

As seen in Figure 3.13 the calibrated material response is close to those measured in the experiments. Also, as seen in Table 3.5, the resulting material parameters are in line with those found through analytical methods [56, 57]. Small differences are present and expected, as we are comparing numerical deformation obtained from FE simulations to those derived through analytical means.

Considering the differences in stiffness and material preparation, the human data is likely a closer representation of the material *in vivo* and was thus chosen as the first estimate for the material parameters to be used for the second stage of fitting.

This two stage method of cardiac tissue calibration, which utilizes small specimen data and pressure-volume data, is becoming a common method for obtaining realistic (and subject-specific) parameters [39, 218, 219]. It ensures that the resulting material parameters produce a material that conforms to the anisotropy uncovered from mechanical experimentation and realistic *in vivo* function.

3.4.4 Active material estimation

Contraction is initiated by sarcomere shortening in series, which in turn contracts myofibrils. While the mechanical analysis of this multi-scale phenomenon would seem to only occur in the myofibre direction, contraction has also been recorded in cross-fibre directions [187]. The active material calibration resulted in $T_{max} = 130$ kPa, $n_s = 0.07$ and $n_2 = 0.0$, which accounts for cross-fibre contraction. Furthermore, the fact that the optimization algorithm found $n_n = 0.0$, is encouraging, as there seems to be little mechanical justification for contraction to occur between laminar sheets (i.e. fibre dispersion is much greater within the fibre-sheet plane). The value found for T_{max} is in line with the values reported in Genet *et al.* [168]: 130 – 155kPa. Their study inflated human LVs to an EDP of

9mmHg (vs. our EDP of 13.5mmHg), which would explain why our values are on the lower end of the spectrum of reported values.

3.4.5 The *in silico* subject specific heart

The converged *in silico* beating heart contain the qualitative expectations of healthy heart function [172, 173, 220]. Explicitly, these are 1) the increase of pressure in the passive filling stage, 2) the preservation of volume in the isovolumetric stages, 3) a curved pressure volume course during ejection that ends at a higher pressure point than when ejection began and 4) the maximum ventricular pressure occurs during ejection but before ES. The fact that these are derived from the mechanical beating of the *in silico* heart coupled with the lumped circulatory system, and not from prescribing pressure and volume exchanges, is an enormous strength of the model.

The patient specific metrics used to calibrate the material model of the heart are preserved in the converged cardiac cycle simulation with an error of <5%. This is hardly a shortcoming as a physiological *in vivo* heart operates within a range of values, often experiencing variances in SV, pressure and timing from cardiac cycle to cardiac cycle. For instance, the *in vivo* pressure data set (from which our *in vivo* target of 13.5mmHg is drawn) shows that each subject experiences a variation of 1-2mmHg for the measured ED point within a few cardiac cycles.

The RV PV loop converges to a state quite different to its first cardiac cycle. Without any subject-specific pressure volume data for the RV, we assumed the same material properties as the LV and loaded the RV using a mean EDP from literature values. While it appears this initial loading state was far from the converged solution, it had comparatively little impact on the LV's function. Rather, the RV experienced the majority of the functional change to enable hemodynamic equilibrium to be met. It is reassuring to see that despite the lack of appropriate data for the RV, the combined ventricular function converges to a state closely in line with LV *in vivo* targets. This makes sense as the LV is also the major mechanical component of the heart and contributes the most energy into the circulatory system.

Qualitatively, the strain results conform to expectations. As can be seen in the distributions in Figure 3.20 and Figure 3.21, the myofibre elongation is at its greatest at ED, its minimum during systole (due to the contractile material behaviour) and returns to almost the original length before the start of the passive filling. Using myofibre strain applied to the prescribed resting sarcomere length provides a further metric of comparison. This results in sarcomere lengths ranging from 1.65–2.02 μm over the cardiac cycle, which compares well to literature findings [185, 221-223].

An accurate determination of stress within complex mechanical problems is an unrivalled advantage of computational modelling and the finite element method in particular. This is especially relevant for

cardiac mechanics as changes in ventricular wall stress are thought to initiate pathological remodelling [224-226]. A unique problem pertaining to biological materials is that *in vivo* stresses cannot be accurately replicated under *in vitro* experimental protocols and thus, cannot be measured directly [87]. Imaging techniques are ever improving, allowing for clinicians and researchers to extract reliable strain information from *in vivo* hearts. However, the conversion of strain data to stress data without a geometric computational model cannot occur without severe assumptions.

At the time of compiling these results, no directly equivalent model (i.e. porcine biventricular model with subject specific geometry and fibre description) has been published in the literature to enable a reasonable comparison of stress values. In light of this, computational studies of human heart models are selected as a useful "litmus test" accepting the limitations of direct comparisons.

Our stress results show that the LV and RV have similar myofibre stresses at ED and ES, despite their different interventricular pressures. The mean values of the LV myofibre stresses compare well with literature values [168, 169], while the RV values do not. For convenience this data is tabulated in Table 3.8. The standards of deviations lie in between the two of these studies, reflecting the degree of geometric detail included in the model. As addressed in Sack *et al.* [169], larger standards of deviations are linked to the degree of anatomical complexity included in the geometric model. Genet *et al.* [168] used smoothed truncated LV geometries, lacking any fine geometric detail. The model used in Sack *et al.* [169] contains an incredible amount of papillary and small feature detail, however this geometry is ultimately an artistic rendition meant to be representative. The model presented in our current study is extracted, with excellent precision, from high resolution *ex vivo* MRI data. Compared to the previously mentioned studies, the inclusion of anatomical detail in our model is more reliable. A comparison of the degree of anatomical complexity included in these three models is presented in Figure 3.25.

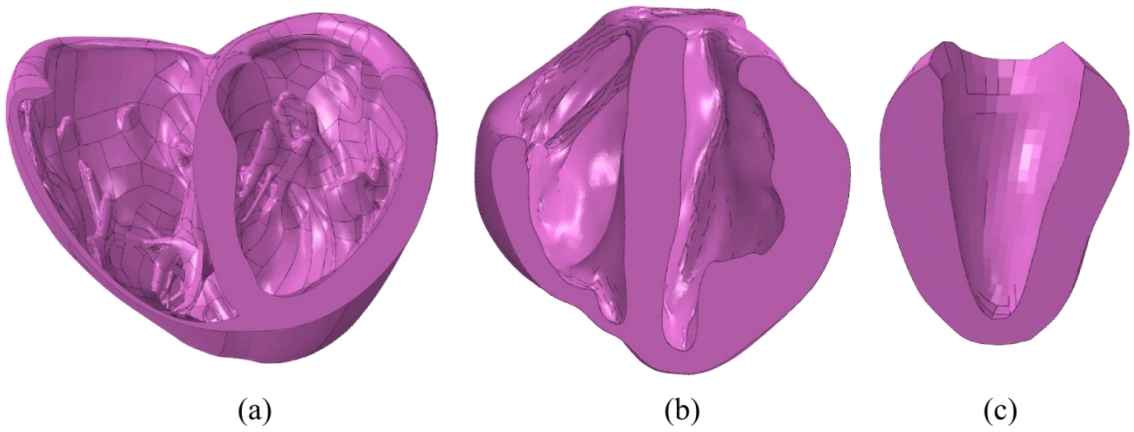

Figure 3.25: Geometric detail used in a) Sack et al. [169] b) this study and c) Genet et al. [168] Geometries are arranged from most to least complex.

These geometric differences, either due to artistic influence or species specificity, make the comparison of RV stresses in Sack *et al.* [169] unsuitable. For instance, it is likely that the prominent and detailed papillary structure in that model (see Figure 3.25(a)) is compressed at ES, contributing significantly to the mean RV stress values, while our model does not contain these features.

Table 3.8: Stress comparison between the myofibre stress results presented for this model and the recently published results of Sack et al. [169] and Genet et al. [168].

Simulation		**Sack *et al.* [169]**	**Current study**	**Genet *et al.* [168]**
Cavity	**Metric**	**Values (kPa)**		
LV	**ED**	1.47 ± 20.72	1.51 ± 1.95	2.21 ± 0.58
	ES	14.45 ± 106.72	19.13 ± 12.57	16.54 ± 4.73
RV	**ED**	1.7 ± 18.06	1.01 ± 4.33	-
	ES	1.51 ± 81.78	20.24 ± 23.65	-

3.4.6 Model validation

Contextualizing the disagreement between simulated and measured *in vivo* results is challenging. Firstly, *In vivo* strains derived from echocardiogram data are difficult to measure accurately, for example, consistent strain data reproducibility inter vendor (and inter observer) are the subject of multiple medical studies, some showing very poor outcomes [227, 228]. Currently, clinical expertise is confident about the reliability of global deformation metrics, (i.e. GCS and GLS) while questioning the reliability of 3D strain data to accurately quantify regional deformation. A recent joint guideline from the American Society of Echocardiography and the European Association of Cardiovascular Imaging expresses this clearly: "Despite promising data, quantitative assessment of the magnitude of regional LV deformation cannot be recommended at this stage because of lack of reference values, suboptimal reproducibility, and considerable inter vendor measurement variability." [229].

If we purely considered the global strain measurements there is reasonable agreement between the FE simulated results and the *in vivo* strains. Since the regional deformation of the echocardiogram measurements isn't as reliable, a 1:1 evaluation of the 16 regional endocardial surface segments isn't an appropriate comparison. However, the grouping of these regions into apical, mid and basal regions, as shown in Figure 3.22(a) and Figure 3.23(a) should be assessed, at least qualitatively. Using this comparison, our circumferential strain results are reasonably in line with those measured *in vivo*. The mild mismatch between them could be justified when considering the different degree of surface resolution between echocardiogram (low resolution, likely excluding finer morphological features) and the FE model (high resolution, detailed endocardial surface).

The differing endocardial surface resolution cannot justify the disagreements seen in apical, mid and basal longitudinal strains. While the GLS compares well, the basal and apical regions are mismatched. The strain behaviour displayed in these *in vivo* strains, reporting that longitudinal strains increase from the apex to the base is contrary to literature guidelines on normal endocardial strains, which show the opposite trend, i.e. the magnitude of strains are largest at the apex and decrease toward the base [195, 230-232].

The abnormal presentation of regional *in vivo* strains makes it difficult to validate this model. The model predictions of regional longitudinal strains are qualitatively consistent with reliable literature findings. This indicates that the mismatch between *in vivo* and FE model predictions of regional longitudinal strains may lie in the *in vivo* data acquisition and not the FE model results.

3.4.7 Model limitations

While geometrically detailed, our computational model is still lacking physiological features such as the atria, the pericardial sac and the diaphragm. Ventricular motion is likely coupled with the presence (and weight) of the atria and their function [208]. By excluding these, we expect there to be discrepancies between physiological *in vivo* strains and the resulting strains from our computational model. It is better to have these discrepancies, and be able to contextualize them, than introduce unquantifiable boundary conditions.

Another possible source of error that should be considered is related to the mean fibre orientation identified via DT-MRI. Assuming these as the correct local material directions (i.e. fibre, sheet and sheet-normal), the constitutive model treats mechanical anisotropy homogenously at each material point. However, we know from the invariants of these diffusivity tensors that there are degrees of anisotropy that vary regionally. A constitutive model that considers subject specific local directions through DT-MRI (i.e. the presumed fibre, sheet and sheet-normal directions) *and* the magnitude of diffusion in these directions (either via diffusion tensor invariants or eigenvalues) would be able to prescribe regional dispersion in the mechanical model and more accurately describe the regional material anisotropy.

3.5 Conclusions

This chapter details the production of a fully subject-specific cardiac model for a biventricular porcine heart model, which includes all four valve openings. Subject specificity is introduced through geometric features, local myofibre directions, loading conditions, and hemodynamics.

This geometrically detailed representation of the heart forms the centre of the computational model. Passive and active material properties are prescribed using hyperplastic strain energy functions that define a nearly incompressible, orthotropic material capable of contractile function. These materials were calibrated using a sophisticated multistep approach to match subject-specific hemodynamic targets for the LV to ensure realistic cardiac function. This mechanically beating heart is coupled with a lumped parameter representation of the circulatory system, allowing for a closed loop definition of fluid exchanges. The circulatory model incorporates unidirectional fluid exchanges driven by pressure gradients of the model, which in turn are driven by the mechanically beating heart. This creates a computationally meaningful representation of the dynamic beating of the heart coupled with the circulatory system.

While sophisticated, our model has limitations. Firstly, our computational model lacks the connecting physiological features such as the atria, the pericardial sac and the diaphragm, which likely influence the mechanical movement of the heart. Secondly, an average value of EDP had to be used when determining the *in vivo* targets. Thirdly, our material model of the heart does not include dispersion, micro-structural mechanics or regional heterogeneity of the tissue.

The comparison of global strains in our model and those measured through the *in vivo* process revealed consistent values relatively well aligned with each other. The regional comparison was poorer, especially with longitudinal strains, which we suspect is due to the unreliability of echocardiogram-derived measurements of regional strain.

Stress and strain values presented in this study for both ventricles and at multiple time points during the cardiac cycle is the first (at the time of writing) for any large mammalian computational model. Moreover, considering how little generalizations were included in this model these presented values are likely more reliable than representative computational models lacking subject-specificity.

Chapter 4 Subject-specific modelling of alginate injection therapy for the treatment of ischemic heart failure

4.1 Introduction

The global burden of ischemic HF resulting from MI is substantial, placing it as one of the leading cause of death worldwide [233]. In the US alone 550 000 new incidents of MI occur annually, approximately once every 42 seconds [234]. The occurrence of HF following MI is high, ranging from 14.2–36.0% at one and five years post-MI respectively [235, 236]. Even with optimal modern therapy, the annual mortality rate of these patients range from 31.0–45.5 % [235, 237], strongly motivating the need for new therapies.

Intra-myocardial biomaterial injections, an emerging treatment for HF, has already shown promise in the pre-clinical [11-13, 110-113] and early clinical studies [144, 145]. As identified in Chapter 2, the degree of efficacy likely depends on a range of factors; especially, the local interactions between the alginate material and the surrounding tissue. In that chapter we were able to quantify various aspects of the gel morphology, its retention and the tissue displacement resulting from its injection. Absent from that study, was a quantification of the mechanical effect these injectates have on the pathological hearts they are embedded in.

Computational modelling and particularly the Finite Element (FE) method are well suited to investigate these mechanical effects. Modelling infarct mechanics *in silico* allows the effect of infarction on heart function to be directly quantified [65, 91-94, 202, 238-240] while simultaneously collecting critical information such as regional ventricular wall stress, an otherwise unobtainable metric thought to initiate pathological remodelling [224-226].

Recently, the emergence of FE models have assisted in elucidating the mechanisms involved in biomaterial injection therapy and contributed to the development of the treatment. Homogenisation techniques have shown that bulking the myocardium with a stiffer, non-contractile material was

sufficient to offset post-MI geometric changes and, consequently decrease stress in the myocardial wall [90, 114, 117, 118, 120]. With the inclusion of patient specific features, Lee *et al.* [96] showed how Algisyl-LVR™ with coronary artery bypass grafting produced dramatic improvements to cardiac output while decreasing ventricular wall stress and increase wall thickness in humans at 3 and 6 months post treatment. The inclusion of biomaterial injectates as discrete structures embedded within the myocardium has been equally positive. Kortsmit *et al.* [123] and Miller *et al.* [122] modelled striated and bulk injectate distributions, as discrete sheet-like structures embedded within the myocardium. These sheet-like hydrogel inclusions were shown to better improve cardiac performance and reduce ventricular wall stress. Wenk *et al.* [121] studied the optimal distribution of multiple spherical injectates in an idealized geometry, showing that the injectates lowered mean myofibre wall stress at end-diastole (ED) and end-systole (ES).

This study extends the work carried out in these seminal studies by including highly realistic, subject-specific features and advanced cardiac modelling techniques. Specifically, the models presented in this chapter contain geometrically realistic and subject-specific representations of infarcted tissue, gel injectates and myofibre descriptions with the latter two representing completely novel work. Furthermore, our models include the full ventricular structure, the endocardial papillary structure and all four valve openings. Our advanced cardiac modelling techniques simulate heart function by coupling a lumped parameter circulatory model with each subject-specific FE model. This enables closed-loop volume exchanges, modelling of multiple cardiac cycles of the dynamic beating heart with realistic volume and pressure changes akin to the physiological beating heart.

Our study aims to quantify the mechanical impact of alginate injections in subjects with HF by investigating regional stress and strain values in realistic, subject-specific and multi-physics computational heart models of porcine subjects.

Normal and HF hearts with Alginate injections in comparison with HF hearts without injections were used to evaluate the role of alginate injections on myocardial function and mechanics. The findings of this study are fundamental to understand the underlying mechanisms of action of biomaterial injection therapy. A better understanding of the mechanical effect of the alginate injectates can assist with the design of better treatment protocols to maximize clinical outcomes.

4.2 Methods

The porcine subjects involved in this study correspond to those described previously in Chapter 2. As the creation of these subject-specific and multi-physics computational heart models is an involved and lengthy process, only a subset of these subjects were chosen to reduce the required workload. The

subjects with the most complete sets of data (i.e. pressure catheterization, MRI quality and echo strain data) were chosen to establish the following equally sized groups: Normal control (NC) subjects that served as a control (n=3); Heart-failure injected (HFI) subjects that received biomaterial injections (n=3), and heart-failure control (HFC) subjects that served as control (n=3). The descriptions of HF and biomaterial treatment are described in detail in Chapter 2.

The methods described in Chapter 3 are used for the construction of the FE models in this study. For the NC group, the subject presented in that chapter is combined with two further subjects to complete the group. The creation of these models follows the exact same procedure.

For the HFC and HFI groups, modifications and extensions of pre-existing methods had to be introduced to account for pathology and treatment. To avoid repetition, only these modifications and extensions are presented in this section.

4.2.1 Modifications accounting for pathology

The passive material response for diseased myocardium follows our previously used constitutive model for anisotropic hyperelastic myocardium [56] with a modification in the isochoric part of the strain energy density, Eq. (3.10), allowing for the description of homogenized, pathological tissue:

$$\Psi_{iso} = \frac{\bar{a}}{2b} e^{b(I_1-3)} + \sum_{i=f,s} \frac{\bar{a}_i}{2b_i} \left\{ e^{b_i (I_{4i}-1)^2} - 1 \right\} + \frac{\overline{a_{fs}}}{2b_{fs}} \left\{ e^{b_{fs} (I_{8fs})^2} - 1 \right\}, \tag{4.1}$$

where the new parameters $\bar{a}$, $\bar{a}_i$ and $\bar{a}_{fs}$ govern the homogenization of healthy and pathological tissue using a scalar parameter H_{INDEX} representing the volume fraction of tissue health. For example $\bar{a}_i$ is defined in the following manner:

$$\bar{a}_i = a_i \left[H_{INDEX} + (1 - H_{INDEX}) P_{scaling} \right]. \tag{4.2}$$

Here, $H_{INDEX,}$ bound by [0, 1], governs the health of the material point. $P_{scaling}$ linearly scales the passive response. The parameters $\bar{a}$ and $\bar{a}_{fs}$ are defined similarly using H_{INDEX}, $P_{scaling}$, a and a_{fs} and assuming that $P_{scaling}$ uniformly impacts the material parameters. Note that

$$H_{INDEX} = 1 \quad \xrightarrow{yields} \quad \bar{a}_i = a_i \tag{4.3}$$

$$H_{INDEX} = 0 \quad \xrightarrow{yields} \quad \bar{a}_i = a_i P_{scaling}. \tag{4.4}$$

And $\bar{a}_i$ transitions linearly between these values for different values of H_{INDEX} bound by [0, 1]. The description of active force development is also modified to include this description of tissue health:

$$T_a(t, E_{ff}) = \frac{T_{max}}{2} \frac{Ca_0^2}{Ca_0^2 + ECa_{50}^2(E_{ff})} \left(1 - \cos\left(\omega(t, E_{ff}) \right) \right) H_{INDEX.} \tag{4.5}$$

When H_{INDEX}=0, the contractile force is zero at the material point. H_{INDEX} is a regionally varying field, continuous over the domain. The field variable is defined at the nodal points of the model by linearly interpolating the binary (i.e. infarcted or healthy tissue only) segmentation of the high resolution *ex vivo* data onto the biventricular FE mesh. This allows for regionally detailed descriptions of infarcted tissue and border zone material incorporated into the model in a continuous and physiologically accurate manner. This is illustrated in Figure 4.1. Note that the exact cut plane in the MRI data is difficult to reproduce analytically in the FE model, resulting in slight mismatches in Figure 4.1(a-b). The zoomed in portion of these images, i.e. Figure 4.1(c-d), do correlate excellently (i.e. dark blue sections) and illustrate the geometrically realistic "border zone" (i.e. rainbow colours in between red and blue sections).

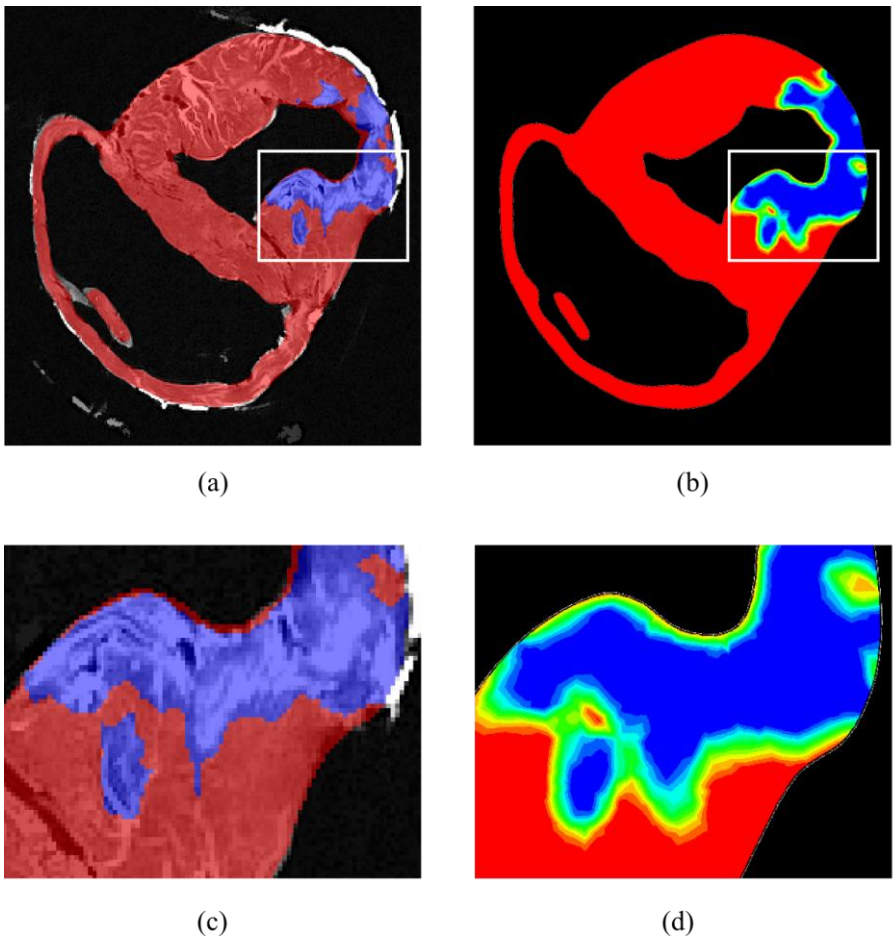

Figure 4.1: (a) Binary segmentation of infarcted tissue (blue) and healthy tissue (red) on a short axis MRI of a porcine subject from the HFC group. (b) A short axis slice of the FE model displaying the interpolated HINDEX field with 0 represented as blue and 1 represented as red. (c) Zoomed in section corresponding to the box in (a). (d) Zoomed in section corresponding to the box in (b).

Additionally, distance measures between pathological tissue and the centroid of each element are constructed to display results as functions of distance from fibrotic tissue.

4.2.2 Modifications accounting for gel injection therapy

To account for the injected alginate material, each injectate was individually segmented and meshed within the FE model. This results in geometrically accurate FE injectate descriptions that coincide with the orientation, placement and retained volume of each injection applied to each subject in the HFI group. This is illustrated in Figure 4.2, whereby a comparison between short axis segmentation is presented alongside a short axis cut plane of the FE mesh.

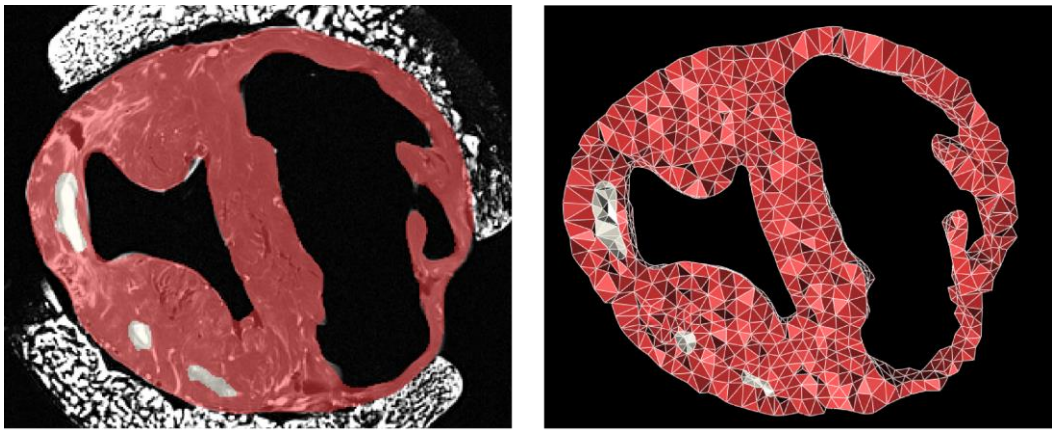

(a) (b)

Figure 4.2: (a) Image segmentation revealing healthy tissue (pinkish red) and gel injectates (white) overlaid on a MRI short axis slice. (b) Corresponding FE mesh for the same short axis region.

An illustration of a fully meshed porcine heart with alginate injectates is presented in Figure 4.3. The meshed alginate injectates share boundary nodes with the surrounding myocardium. In this sense, the entire ventricular structure is modelled as a single continuum with two separate materials. This assumption is consistent with the modelling approach of other studies [121-123], and simplifies the need to model contact mechanics.

A compressible Neo-Hookean constitutive law is used to describe the material behaviour of the alginate injectates:

$$\Psi_{gel} = C_1[\bar{I}_1 - 3] + D_1(J-1)^2, \tag{4.6}$$

whereby $\bar{I}_1$ is the first invariant of the isochoric Right Cauchy-Green tensor and J is the third invariant of the deformation gradient. The parameters C_1 and D_1 define the material stiffness and compressibility constraints respectively. In the case of a purely incompressible material, $J = 1$ and therefore $\bar{I}_1 = I_1$. This allows the above expression to be simplified as

$$\Psi_{gel} = C_1[I_1 - 3]. \tag{4.7}$$

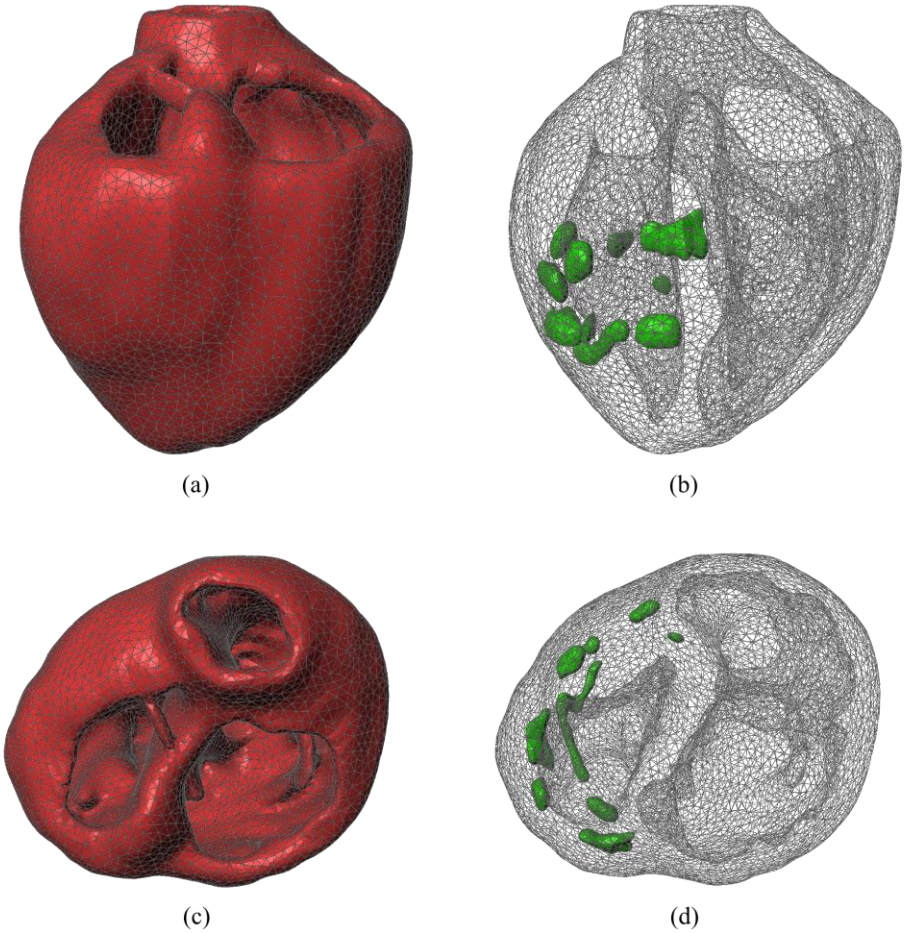

Figure 4.3: The meshed ventricular geometry of a subject from the HFI group. (a) Inferior view of the meshed ventricular structure. (b) Inferior view of the meshed ventricular structure with myocardium elements transparent, revealing the alginate injectates embedded around the LV cavity. (c-d) are the same as (a-b) from a superior view of the ventricular structure.

As the effect of gel injection therapy is of interest, distance measures between gel surfaces and the centroid of each element in the myocardial structure are constructed to display results as functions of distance from the gels.

4.2.3 Calibration of material parameters

4.2.3.1 Alginate injectates

Experimental uniaxial data for the alginate injectate has been reported in Wenk *et al.* [121] that is appropriate for calibrating the Neo-Hookean constitutive model. Assuming the material incompressible allowed the use of a closed form expression for relating stress and stretch for our constitutive law [241]. This is given by

$$\sigma_{11} = C_1\left(\lambda_1 - \frac{1}{\lambda_1^2}\right), \tag{4.8}$$

where λ_1 is stretch in the direction of extension. We were able to calibrate the material parameter C_1 using a least squares minimization routine scripted in MATLAB.

4.2.3.2 Diseased Myocardium

Following Eqs.(4.1)-(4.2), passive material stiffness is determined by the health of the material point, H_{INDEX}, the pathological scaling of infarcted material, $P_{scaling}$; and the material parameters a_i and b_i, which govern the linear and exponential response of the cardiac tissue in different modes of deformation.

H_{INDEX} is determined from the mapping of the segmented infarcted tissue from the *ex vivo* MRI data onto the FE mesh, as described in Section 4.2.1. Without detailed experimental data, we have to rely on literature values to determine the pathological scaling of the material, $P_{scaling}$. Even though multiple studies have investigated and pursued the quantification of infarct mechanics, there isn't a clear consensus on infarct stiffness readily available. Holmes *et al.* [85] presents an excellent account of changes in infarct stiffness while reviewing studies performed prior 2005. The infarct at the remodelling phase (i.e. scar tissue) is relevant to our study, and has been quantified as 2-10 times [81, 82, 242, 243] as stiff as remote non-infarcted tissue.

Particularly relevant is a recent study performed by McGarvey *et al.* [82] which allows us to narrow this range of infarct stiffness. In that study they quantify the *in vivo* stiffness of infarct and remote tissue of porcine subjects using FE methods and *in vivo* imaging techniques. As they have a similar model of MI and report values for late stage infarcts (i.e. 12 weeks) their results are most applicable to our study. Using the ratio of their results for infarcted and remote tissue, the value of $P_{scaling}$ is determined to be 4.56.

With the values of H_{INDEX} and $P_{scaling}$ already determined, the remaining material parameters a_i and b_i, were found in the same manner as presented in Chapter 3. In short, initial values for a_i and b_i are determined from the shear calibration of myocardium specimen samples [181]. To adjust the material for each subject, these initial values are scaled consistently to match the "Klotz curve" [182] generated for the diastolic pressure-volume (PV) relation of each subjects' left ventricle (LV) [182]. Both exponential (b_i) and linear terms (a_i) were subject to uniform scaling by parameters B and A, an exponential and scalar multiplier respectively. These values were found by minimizing the error between the *in silico* diastolic PV course of each subject to the analytical Klotz curve starting from the unloaded LV volume V_0 until the end-diastolic volume (EDV) was reached at the specified end-diastolic pressure (EDP) value given in Table 4.1.

4.2.3.3 Active tension

The calibration of active tension is determined in the same manner as described in Chapter 3, with a single modification. The results from Chapter 3 showed that active stress development in the cross-fibre direction n_n (i.e. contraction between sheets of myofibres) converged to zero. Further investigation into this found that it was detrimental to systolic function and as such it was always set to zero for these material parameter identifications. T_{MAX}, and n_s (the fraction of active tension applied in the sheet direction, see Section 3.2.4.2) were subject to optimization to ensure the correct stroke volume (SV) for each subject was achieved, using the same optimization techniques outlined previously.

4.2.4 Subject specific hemodynamic considerations

In vivo LV volume measurements were available for all subjects presented in this Chapter, while the LV pressure data was only available for the HF subjects. As was done in the previous chapter, mean values constructed from the healthy baseline of a larger data set (containing multiple subjects) were used in place of subject specific data. The complete *in vivo* measurements used for this study are presented in Table 4.1. No right ventricle (RV) pressure data was available for any of the subjects. As such, literature values were used as described in Chapter 3.

Table 4.1: Subject specific hemodynamic measurements of each subject in the NC, HFC and HFI groups.

Pig #	LV EDV (ml)	LV ESV (ml)	LV SV (ml)	LV EDP (mmHg)	LV ESP (mmHg)	AO min (mmHg)	AO max (mmHg)
NC 1	73.0	33.0	40.0	n.a.	n.a.	n.a.	n.a.
NC 2	57.8	26.9	30.9	n.a.	n.a.	n.a.	n.a.
NC 3	70.2	37.0	33.2	n.a.	n.a.	n.a.	n.a.
HFC 1	78.8	53.8	25.0	18.5	90.0	70.0	105.0
HFC 2	103.0	70.0	33.0	29.6	130.0	90.0	130.0
HFC 3	94.8	62.4	32.4	8.5	57.0	42.0	71.3
HFI 1	113.3	70.6	42.7	16.9	68.0	47.0	80.0
HFI 2	134.4	70.9	63.5	14.9	73.0	52.0	87.0
HFI 3	77.0	45.5	31.5	8.6	78.0	43.0	70.0

Abbreviations: n.a.: Not available; LV: left ventricle, EDV: End-diastolic volume; ESV: End-systolic volume; SV: Stroke volume; EDP: End-diastolic pressure; ESP: End-systolic pressure; AO min: Minimum aortic pressure; AO max: Maximum aortic pressure.

Determination of the initial pressures of the remaining cavities in the circulatory circuit considers the pressure measurements presented in Table 4.1. A summary of the initial pressures of all cavities in the circulatory model for each group is presented in Table 3.4.

Table 4.2: Initial pressure state of the compliance vessels in the subject-specific model.

Cavity	Units	NC	HFC	HFI	Comment
LV	mmHg	13.5	Subject specific	Subject specific	Determined by *in vivo* data from Table 1.
RV	mmHg	4	4	4	Based on literature: 1-7mmHg [172] 3.9 ±1.6 [194].
C_P	mmHg	15	Subject specific	Subject specific	Determined by *in vivo* data from Table 1.
C_{SA}	mmHg	65	Subject specific	Subject specific	Determined by *in vivo* data from Table 1.
C_{SV}	mmHg	4	4	4	Based on RV initial pressure listed above.

Abbreviations: LV: left ventricle; RV: right ventricle C_P: Pulmonary compliance vessel; C_{SA}: Systemic Arterial compliance vessel; C_{SV}: Systemic Venous compliance vessel.

4.2.5 Modelling the cardiac cycle in subjects with heart failure

The modifications to account for diseased myocardium and gel injection therapy do not interfere with the methods outlined in Chapter 3 on modelling the cardiac cycle. In this sense, the boundary conditions, timing and modelling of diastole and systole are the same across all simulations and correspond to the presented methods in Chapter 3.

For simplicity the same lumped parameter model presented in Section 3.2.5 is also used for all subjects in this study. Compliances and resistance parameters from Section 3.2.5 were used as the initial parameters for all models. Initial chamber pressures of the circulatory model are altered to match the hemodynamic measurements of each subject corresponding to Table 4.1.

We recognize that the circulatory system of a subject with HF would likely be compromised, but the lack of available experimental data limits our ability to introduce meaningful changes to the model and justify them sufficiently. If however, the converged PV loop was strikingly different from the initial PV loop (i.e. more than 3ml difference to stroke volume) then changes to the compliance and resistance vessels were introduced to compensate. This only affected subjects HFI 1 and HFI 2. Both experienced volume retention in the arterial chamber C_{SA}, which was corrected by decreasing the systemic resistance R_{SYS} by 40% and increasing the compliance C_{SA} by 25%. These values were found heuristically and enabled the converged PV loops to maintain the calibrated SV within 3ml.

Statistical Analysis

Data in this study are expressed as mean ± SD unless otherwise stated. The differences between the various groups were evaluated using analysis of variance (ANOVA). The differences were considered statistically significant at $p<0.05$.

4.3 Results

4.3.1 Subject-specific geometric models of infarction

Figure 4.4 provides full geometric representations for each of the HF FE models revealing the complex and subject-specific distributions of H_{INDEX} throughout the myocardium. A similar representation of NC subjects is given in the appendix, Figure B1.

As these geometries are constructed from *ex vivo* imaging, we assume they coincide with the unloaded state.

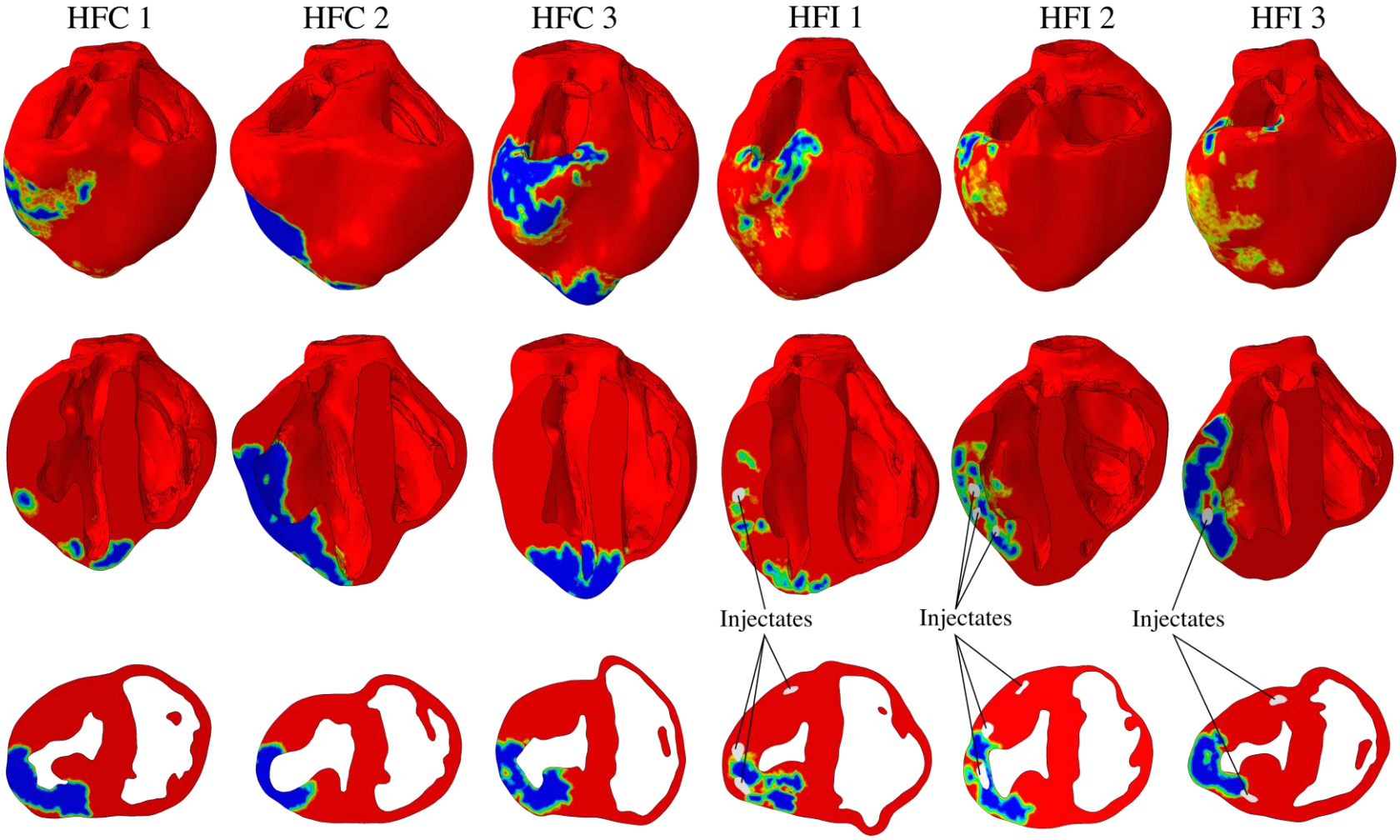

Figure 4.4: Unloaded FE model geometry of each of the HF subjects (columns) displaying the interpolated H_{INDEX} field with 0 represented as blue and 1 represented as red. Top row displays the full geometry, the middle row displays a long-axis bisected view and the bottom row displays a short-axis slice. Injectates are coloured grey and identified in the HFI subjects.

4.3.2 Material parameter identification

Alginate biomaterial

The parameter C_1 governing material stiffness of the alginate injectates was found to be 4.45 kPa using the optimization routine. This resulted in the best fit of the material response to experimental data as illustrated in Figure 4.5.

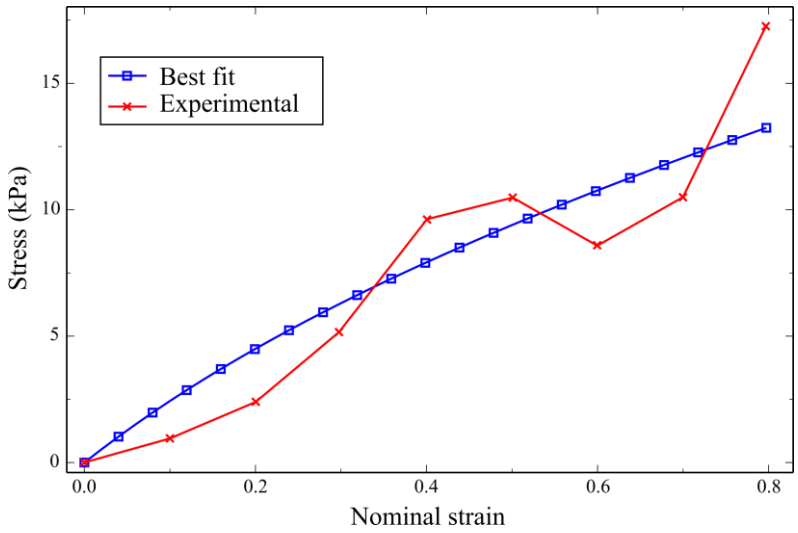

Figure 4.5: Numerical material response of the calibrated Neo-Hookean model and the experimental data of the alginate material to which it was calibrated.

Investigation of a compressible form of the Neo-Hookean material found that modelling the material as a nearly incompressible material (i.e. with Poisson's ratio $\nu > 0.495$ [2]) preserved the material stress response to an order of 1×10^{-4} kPa over the same strain loading presented in Figure 4.5. Note, that the derivation of stress as presented in Eq. (4.8) is not valid in the compressible case, but can be evaluated using iterative numerical methods (e.g. Newton Raphson) or through material response evaluations built into commercial software, such as Abaqus.

Myocardium tissue

The subject-specific calibration resulted in suitable values for the passive material scaling parameters *A* and *B* (fitting metrics between our FE models and Klotz curves sampled at 200 data points along the curve produce a R^2 value of 0.96 ±0.03 and RMSE of 0.86 ±0.33 mmHg).; and the active material parameters T_{MAX} and n_s. These are presented in Table 4.3 along with the initial unloaded LV cavity volumes V_0, as these are fundamental to the resulting material parameters.

[2] This produces a value for $D_1 > 440$ kPa.

Table 4.3: Initial Volumes and calibrated material parameters for subjects in the NC, HFC and HFI groups.

Pig #	V_0	*A*	*B*	T_{MAX}	n_s
NC 1	27.5	0.31	0.73	130.0	0.07
NC 2	17.5	0.16	0.73	118.0	0.07
NC 3	29.6	0.63	0.75	102.0	0.01
NC mean ± SD	**24.9 ± 5.3**	**0.37 ± 0.24**	**0.74 ± 0.01**	**116.7 ± 14.0**	**0.05 ± 0.03**
HFC 1	31.9	0.55	1.08	97.6	0.00
HFC 2	47.1	1.69	0.87	140.6	0.14
HFC 3	29.4	0.10	0.59	141.8	0.13
HFC mean ± SD	**36.1 ± 7.8**	**0.78 ±0.81**	**0.85 ± 0.25**	**126.7 ± 25.2**	**0.09 ± 0.08**
HFI 1	18.7	0.08	0.31	110.0	0.05
HFI 2	32.8	0.22	0.37	207.3	0.17
HFI 3	26.2	0.17	0.81	119.3	0.04
HFI mean ± SD	**25.9 ± 5.7**	**0.15 ± 0.07**	**0.50 ± 0.27**	**145.5 ± 53.6**	**0.09 ± 0.07**

Abbreviations: V_0: unloaded cavity volume; A: passive scalar scaling parameter; B: passive exponential scaling parameter; T_{MAX}: Peak active tension; n_s: Fraction of active tension in the sheet direction.

4.3.3 Functional output

Cardiac function was simulated for six consecutive cardiac cycles to ensure converged solutions were achieved. All values and results reported in the following sections correspond to the final and converged solution.

In vivo volumetric and pressure measurements used in the calibration of the each model are compared to the *in silico* converged results for each subject in Table 4.4. A comparison between the *in vivo* and *in silico* LV functional output metrics, i.e. SV and ejection fraction (EF), of each subject are presented in Table 4.5. While there are individual subjects that present with "above average" differences, i.e. HFC 3 simulates LV function with a SV 2.7 ml less than the *in vivo* measured amount, the mean group function is quite accurate. This is true for LV SV, which presents with errors of -0.6 ± 1.4, 0.4 ± 2.2 and -0.4 ± 1.2 ml; and LV EF which present with errors of -0.6 ± 1.5, 0.9 ± 3.5 and 0.7 ± 0.6 % for the NC, HFC and HFI group respectively.

Worth noting from these values are LV EDP, which was 13.3± 2.0, 16.7 ± 5.9 and 12.3 ± 2.7 mmHg, and LV EF, which was 51.9 ± 3.2, 32.6 ± 1.1 and 41.9 ± 4.0 % in the NC, HFC and HFI groups respectively. Additional diastolic PV curves for each subject are presented in the appendix, Figure B2.

Table 4.4: Comparison of converged volumetric and pressure values for each subject in the NC, HFC and HFI groups compared to the in vivo values.

Pig #	*In vivo* LV EDV (ml)	*In silico* LV EDV (ml)	*In vivo* LV ESV (ml)	*In silico* LV ESV (ml)	*In vivo* LV EDP (mmHg)	*In silico* LV EDP (mmHg)
NC 1	73.0	72.6	33.0	34.7	n.a.	12.5
NC 2	57.8	59.2	26.9	27.0	n.a.	16.1
NC 3	70.2	68.1	37.0	36.0	n.a.	11.3
Mean ± SD	**67 ± 6.6**	**66.6 ± 5.6**	**32.3 ± 4.1**	**32.6 ± 4.0**	n.a.	**13.3 ± 2.0**
HFC 1	78.8	77.1	53.8	49.7	18.5	16.0
HFC 2	103.0	98.7	70.0	64.2	29.6	24.3
HFC 3	94.8	98.5	62.4	68.8	8.5	9.9
Mean ± SD	**92.2 ± 10**	**91.4 ± 10.1**	**62.1 ± 6.6**	**60.9 ± 8.1**	**18.9 ± 8.6**	**16.7 ± 5.9**
HFI 1	113.3	106.9	70.6	65.6	16.9	14.0
HFI 2	134.4	132.5	70.9	70.0	14.9	14.4
HFI 3	77.0	77.7	45.5	44.9	8.6	8.6
Mean ± SD	**108.2 ± 23.7**	**105.7 ± 22.4**	**62.3 ± 11.9**	**60.2 ± 10.9**	**13.5 ± 3.5**	**12.3 ± 2.7**

Abbreviations: n.a.: Not available; LV: left ventricle; EDV: End-diastolic volume; ESV: End-systolic volume; EDP: End-diastolic pressure.

Table 4.5: Functional outputs for each subject in the NC, HFC and HFI groups compared to the in vivo values.

Pig #	*In silico* LV SV (ml)	*In vivo* LV SV (ml)	ΔSV (ml)	*In silico* LV EF (%)	*In vivo* LV EF (%)	ΔEF (%)
NC 1	37.9	40.0	-2.1	52.2	54.8	-2.6
NC 2	32.2	30.9	1.3	54.4	53.4	1.0
NC 3	32.1	33.2	-1.1	47.1	47.4	-0.2
Mean ± SD	**34.1 ± 2.7**	**34.7 ± 3.9**	**-0.6 ± 1.4**	**51.2 ± 3.0**	**51.9 ± 3.2**	**-0.6 ± 1.5**
HFC 1	27.4	25.0	2.4	35.5	31.7	3.8
HFC 2	34.5	33.0	1.5	35.0	32.0	2.9
HFC 3	29.7	32.4	-2.7	30.2	34.2	-4.0
Mean ± SD	**30.5 ± 3**	**30.1 ± 3.6**	**0.4 ± 2.2**	**33.5 ± 2.4**	**32.6 ± 1.1**	**0.9 ± 3.5**
HFI 1	41.3	42.7	-1.4	38.6	37.7	0.9
HFI 2	62.5	63.5	-1.0	47.2	47.2	-0.1
HFI 3	32.8	31.5	1.3	42.2	40.9	1.3
Mean ± SD	**45.5 ± 12.5**	**45.9 ± 13.3**	**-0.4 ± 1.2**	**42.7 ± 3.5**	**41.9 ± 4.0**	**0.7 ± 0.6**

Abbreviations: LV: left ventricle; SV: Stroke volume; EF: Ejection fraction.

The performance of these groups is best represented through a normalized pressure volume loop of the final converged cardiac cycle, presented in Figure 4.6. The mean PV relation for each group is presented, whereby the volume is normalized to the mean EDV of each group allowing for a comparative presentation of cardiac performance.

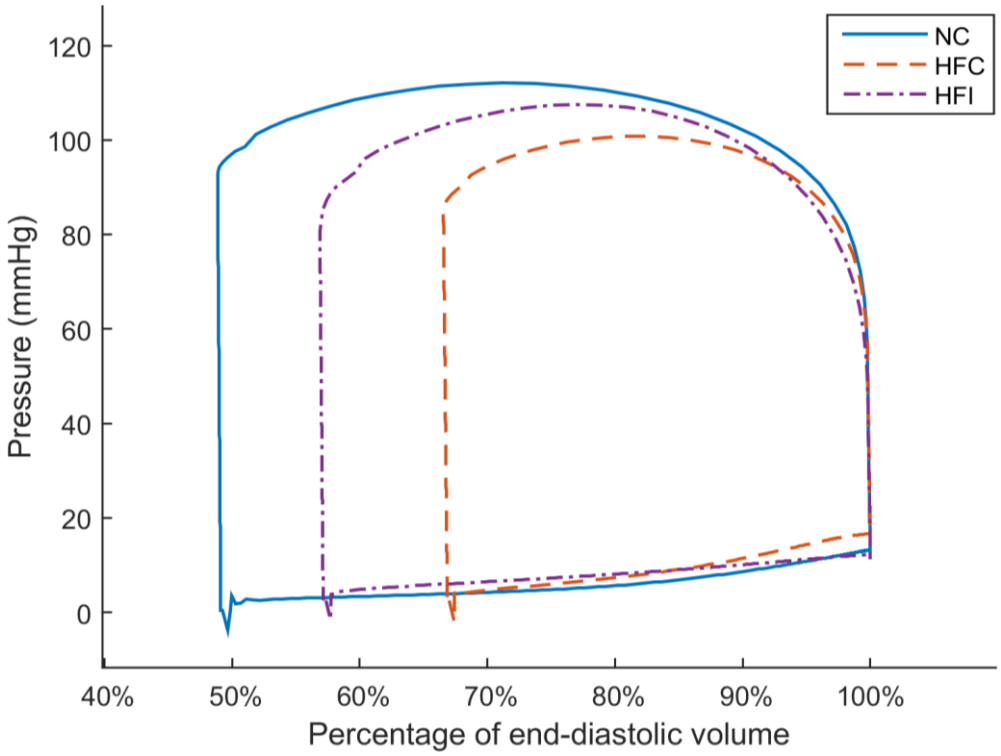

Figure 4.6: Mean pressure volume loops of the final converged cardiac cycle for the NC, HFC, and HFI groups. Volume was normalized to the EDV for each group.

4.3.4 Strains

Grouped myocardial strain

Volumetrically averaged (i.e. normalized by element volume) myofibre strain results are presented to remove potential mesh artifact responses. These strains are calculated using the unloaded state as a reference configuration, allowing for strain points at ED and ES to be reported. Each subject has roughly 85, 000 elements resulting over 250 000 data points of analysis for each group, allowing for precise determinations of mean values.

The mean volumetrically averaged myofibre strain in the LV at ED was found to be 8.3 ± 5.9, 6.6 ± 6.6 and 9.4 ± 9.3 % ($p<0.05$) for the NC, HFC and HFI group respectively. The corresponding values at ES were found to be -10.0 ± 5.0, -6.4 ± 7.9 and -8.8 ± 9.9 % ($p<0.05$). These values are represented

graphically in Figure 4.7(a). Qualitatively, the HFC group experiences diminished strains at ED and ES compared to the other groups while the HFI group experiences a similar range of strain to the NC cohort, albeit slightly elevated. The RV strains of all groups display similar values, as seen in Figure 4.7(b). For completeness, myofibre strains for each subject at ED and ES are presented in the appendix, Table B1.

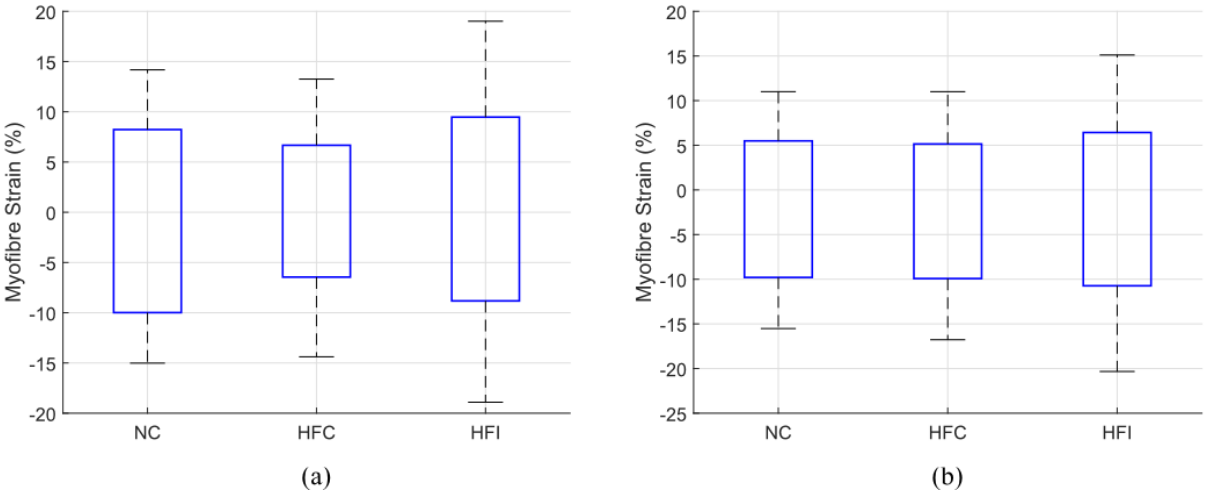

Figure 4.7: Mean myofibre strain presented as box plots for the (a) LV and (b) RV of the NC, HFC and HFI groups. The lower and upper edges of each box correspond to the mean ES and ED value respectively. The error bar at each end of the box plot corresponds to the SD of that associated mean value.

Grouped endocardial strain in local coordinates

Strain analysis of the endocardial surface segments (as per section 3.2.10) reference the ED state as the initial configuration and report strains at ES, giving an evaluation of systolic performance. These show that HFC subjects experience diminished longitudinal and circumferential strains. This can be seen in Figure 4.8, which presents these mean values grouped by apical, mid and basal regions.

The reduced strains experienced at base, mid and apex of HFC subjects translates to reduced global deformation. LV global longitudinal strain (GLS) was found to be -9.8 ± 5.9, -5.4 ± 6.2 and -12.6 ± 9.3 % ($p < 0.05$) and global circumferential strain (GCS) was -24.3 ± 5.2, -15.2 ± 7.3 and -21.1 ± 9.0 % ($p<0.05$[3]) for the NC, HFC and HFI group respectively.

[3] Only HFC is significantly different to other mean values.

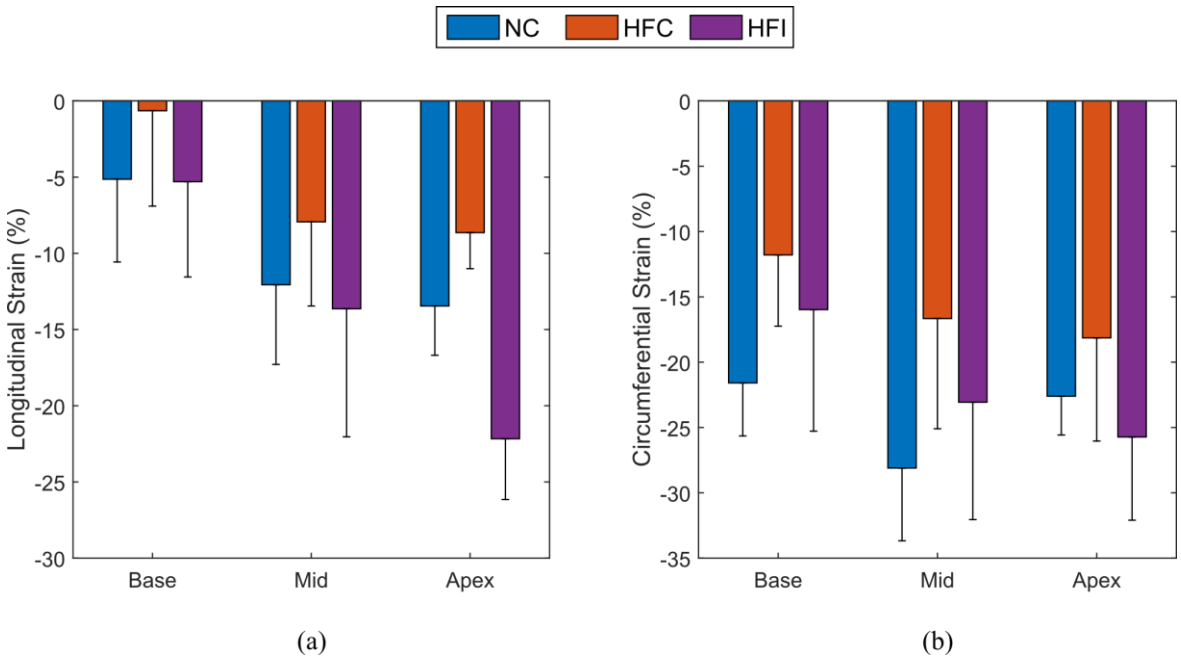

Figure 4.8: Mean values of the regional endocardial segments for the NC, HFC and HFI groups given for (a) longitudinal and (b) circumferential strain. Error bars correspond to the SD of each group.

Subject-specific endocardial strain results compared to in vivo values

The subject-specific longitudinal and circumferential strain results across each of the 16 endocardial segments are presented in Figure 4.9 and Figure 4.10 respectively. The left panes present the strains derived from FE model simulations while the right panes present the comparative *in vivo* derived strains.

Qualitatively, longitudinal strains reported from the FE simulations are strikingly consistent across subjects within each group, especially with the HFC and HFI subjects. There are also strain patterns that are consistent across all subjects and correlate with physiological regions in the heart. For example, longitudinal strain "peaks" at regions 6 and 12, which are regions in the LV free wall above and below each other respectively. Additionally, regions in the septal wall (i.e. 2, 3, 8 and 9) display longitudinal strain "valleys". Basal regions consistently experience smaller strain values than other regions in the LV. Circumferential strains reported from the FE simulations show less consistency in the NC group than in the HFC and HFI groups, which show consistent peaks and valleys in similar regions to the longitudinal strains.

The *in vivo* reported strain values show less consistency between subjects. No obvious patterns between regions and subjects are noticeable. Some instances show almost opposite strain behaviour, i.e. in Figure 4.9(b) show concave and convex strain patterns in regions 1-6 for different subjects.

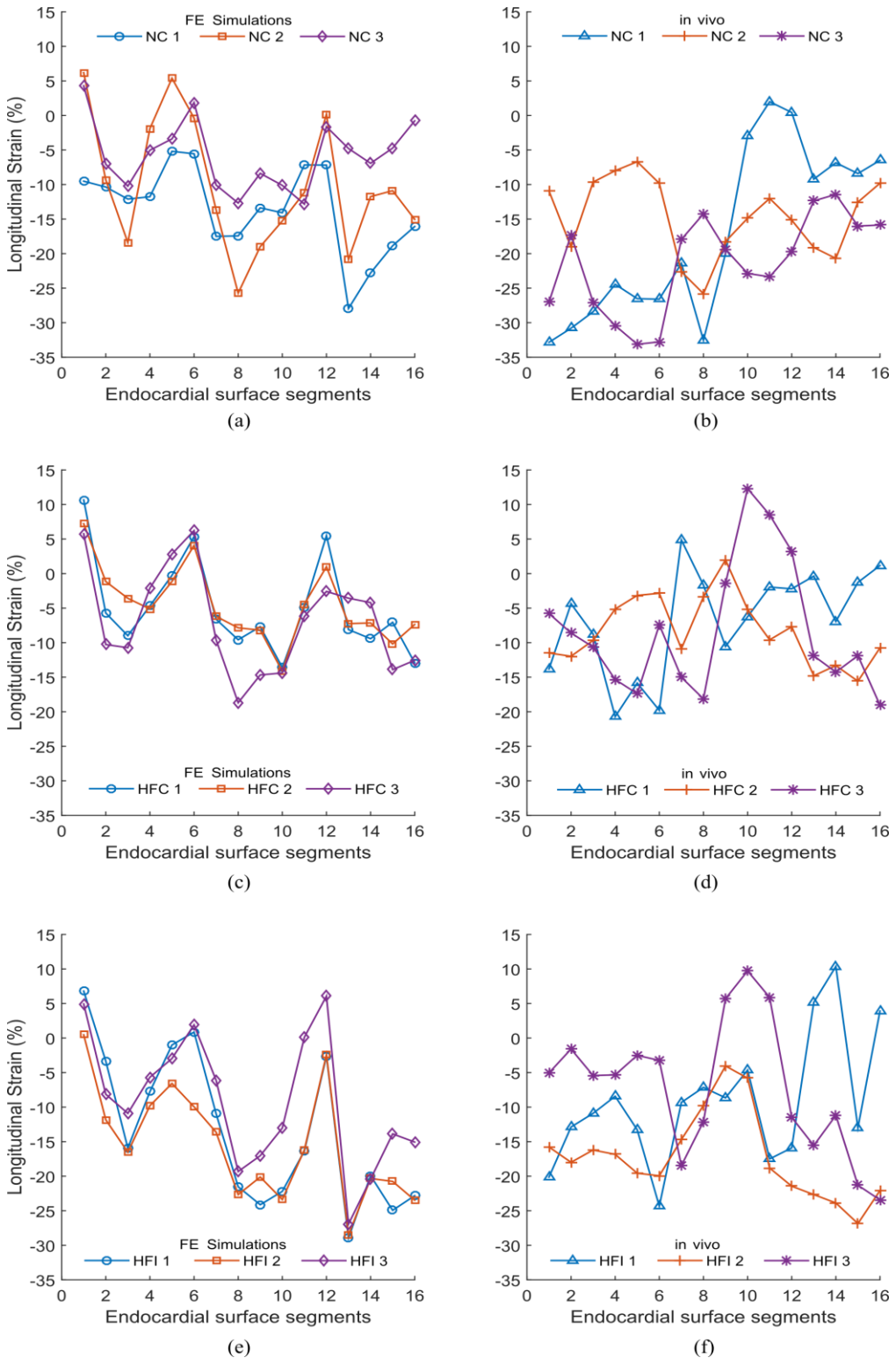

Figure 4.9: (a), (c) and (e): Regional endocardial longitudinal strains derived from FE model simulations for the individual subjects in the NC, HFC and HFI groups respectively. (b), (d) and (f): The comparative in vivo regional values.

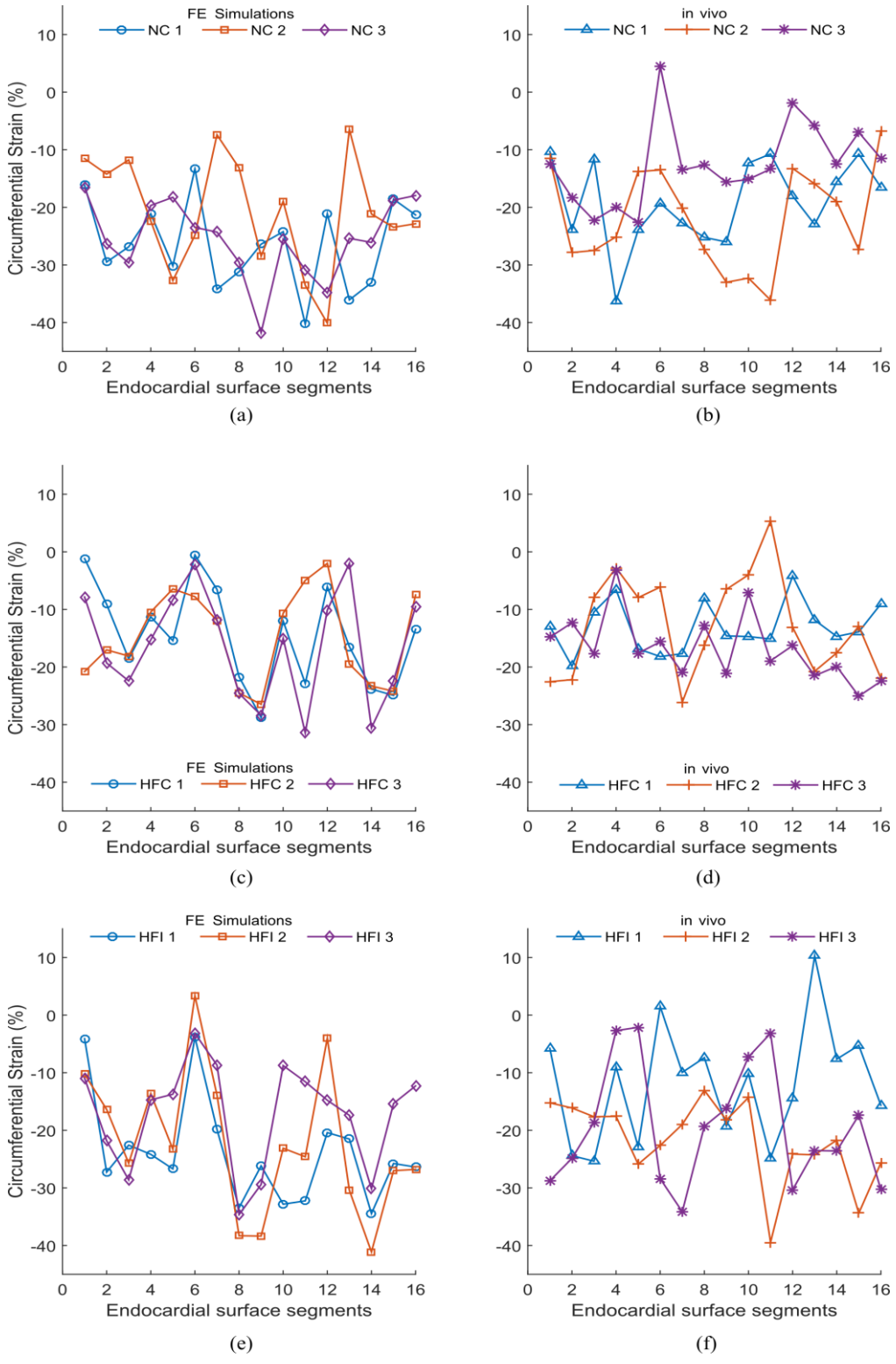

Figure 4.10: (a), (c) and (e): Regional endocardial circumferential strains derived from FE model simulations for the individual subjects in the NC, HFC and HFI groups respectively. (b), (d) and (f): The comparative in vivo regional values.

A comparison between individual subjects reveals a strong agreement between *in vivo* and FE results for *some* subjects. Subject NC 2, HFC 2 and HFC 3 in particular have consistent strains across model predictions and *in vivo* measurements. To illustrate this, the isolated strains of subjects NC 2 and HFI 3 are presented in Figure 4.11 and Figure 4.12 respectively, where it's clear that the qualitative trends are the same.

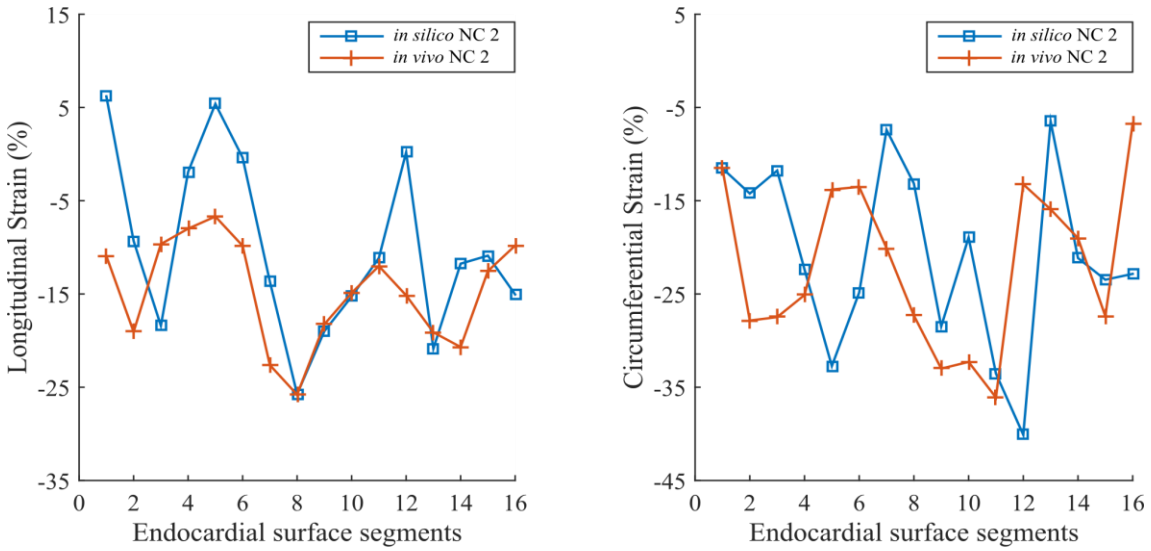

(a) (b)

Figure 4.11: Regional strains from FE model simulations presented with the in vivo values for the individual subject NC 2 for (a) Longitudinal strains and (b) Circumferential strains.

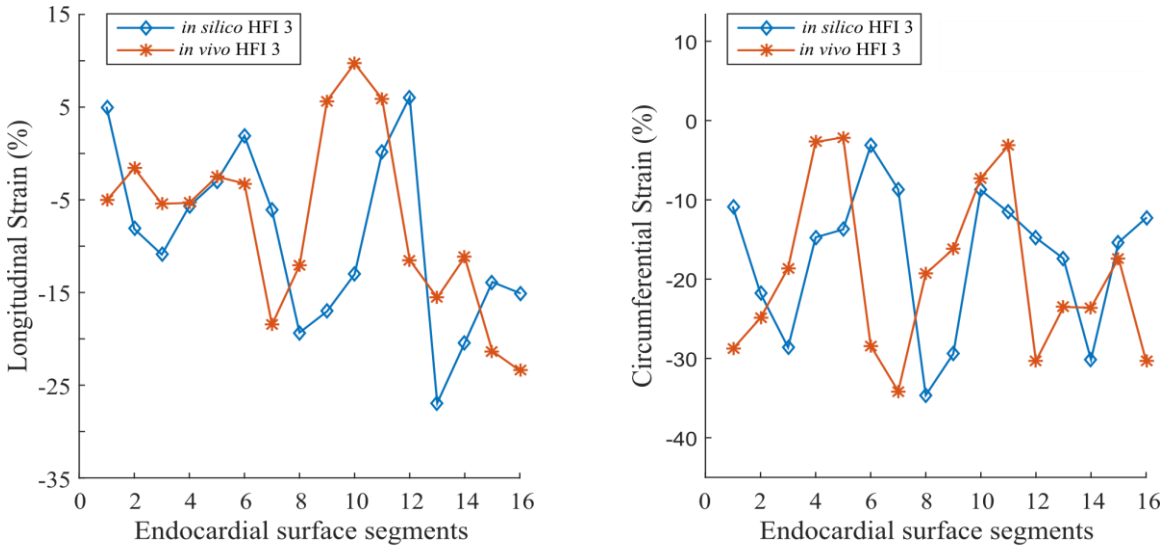

(a) (b)

Figure 4.12: Regional strains from FE model simulations presented with the in vivo values for the individual subject HFI 3 for (a) Longitudinal strains and (b) Circumferential strains.

For subject NC 2, some strains show excellent agreement, such as the longitudinal strains in regions 8, 9, 10 and 11 in Figure 4.11(a). In other regions, there seems to be distinct segmentation differences between *in vivo* and FE strains, such as regions 1-6 in Figure 4.11(b), which show a valley and a peak in both modalities, but clearly out of phase with each other. For subject HFI 3 the qualitative trends are closely in line, however there seems to be a broad miss-segmentation across the domain as the *in vivo* values seem out of phase with FE results by a single region as seen in Figure 4.12.

4.3.5 Stresses

The mean volumetrically averaged myofibre stress in the LV at ED was found to be 2.1 ± 6.1, 2.8 ± 5.5 and 1.9 ± 4.8 kPa ($p<0.05$) for the NC, HFC and HFI group respectively. The corresponding values at ES were found to be 19.2 ± 27.3, 20.5 ± 25.3 and 20.7 ± 25.6 kPa ($p<0.05$). For clarity these values, along with the myofibre stress values in RV, are presented in Table 4.6. At ED, the HFC group experiences elevated myofibre stresses in both ventricles. Comparatively at ED the HFI group experiences decreased myofibre stress values in the LV and RV that are closer to NC values. At ES both the HFC and HFI experience elevated myofibre stresses in both ventricles compared to NC values.

Table 4.6: ED and ES volumetric-averaged mean stress results for the converged cardiac cycle presented separately for the LV and RV. Results are presented with standard deviations.

Time Point	Group	LV myofibre stress (kPa)	RV myofibre stress (kPa)
ED	NC	2.1 ± 6.1	0.6 ± 0.7
	HFC	2.8 ± 5.5	1.5 ± 3.0
	HFI	1.9 ± 4.8	0.8 ± 2.3
ES	NC	19.2 ± 27.3	17.7 ± 18.5
	HFC	20.5 ± 25.3	24.6 ± 21.7
	HFI	20.7 ± 25.6	26.9 ± 39.9

Abbreviations: LV: left ventricle, RV: right ventricle; ED: end-diastole; ES: end-systole.

Myofibre stress contours are presented in Figure 4.13 over long axis cut planes of the ventricular structure at ED. Peak stresses are seen on the endocardial surface of the LV. Complex surface details on the endocardium (some due to papillary structures) are compressed during filling and experience compressive (i.e. dark blue) stress. Some subjects appear to experience lower stresses at the apical regions, although this appears subject-specific and is not consistent across all subjects or within a single group. Additional short axis contour plots at ED are presented in the appendix, in Figure B3.

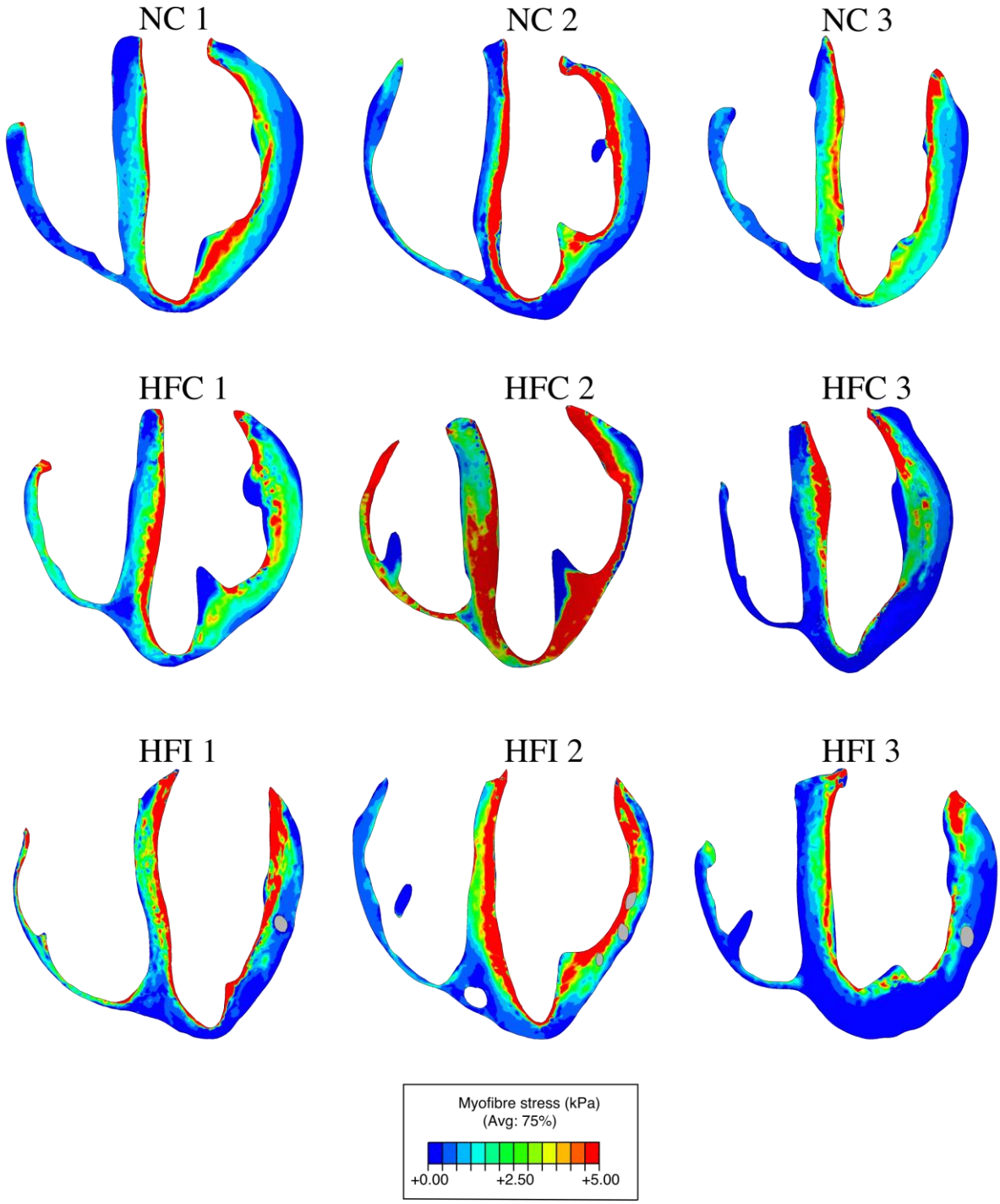

Figure 4.13: Myofibre stress at end-diastole for the NC, HFC and HFI subjects presented along long-axis cut planes of the ventricles. Injectates are coloured grey in the HFI subjects.

Similar Myofibre stress contours are presented for the same cut-planes at ES in Figure 4.14. No apparent patterns are identifiable due to geometric position, pathology, or in proximity to the gel injectates (where applicable).

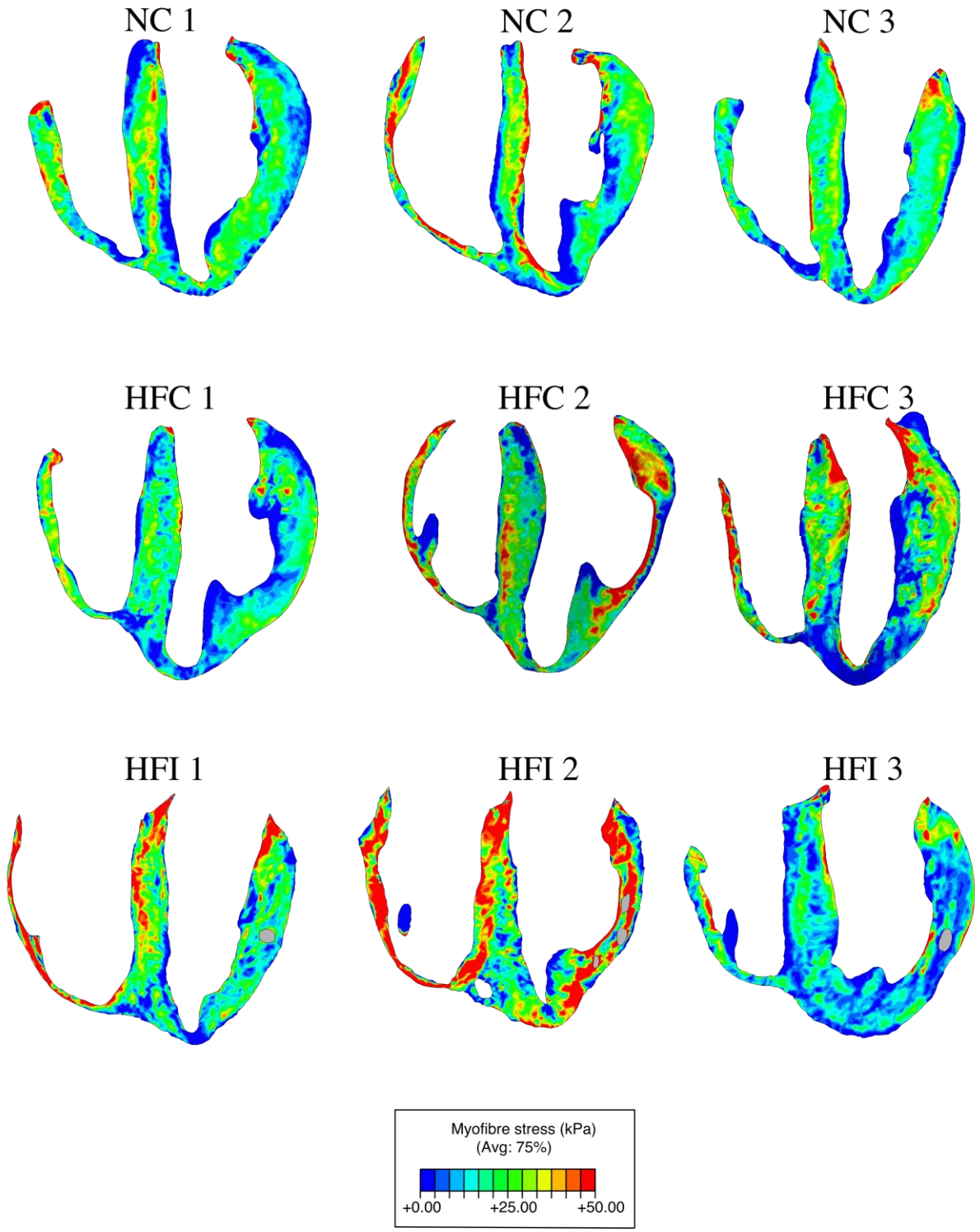

Figure 4.14: Myofibre stress at end-systole for the NC, HFC and HFI subjects presented along long-axis cut planes of the ventricles. Injectates are coloured grey in the HFI subjects.

Inspection of myofibre stresses in proximity to the gel injectates at ED reveals complex, albeit recurring phenomena. Close up contour plots of the myofibre stresses in the vicinity of the gel injectates are presented in Figure 4.15. These myofibre stress fields are complex, heterogeneous and

are likely influenced by the subject-specific loading experienced at ED, the local myofibre orientation and the morphology of the injectates. At the same time, the stress fields around the injectates repeatedly appear with one of three identifiable outcomes. The first is with reduced stress in the ventricular wall radially behind the injectates (i.e. radially outward toward the epicardium) as is seen in Figure 4.15(b) and (d). The second effect is that regions of diminished stress appear to concentrate around the injectates as is seen in Figure 4.15(a) and (d-f). The final outcome is that sometimes the stress field appears mostly unaffected as seen in the upper injectate in Figure 4.15(c). These phenomena are also visible upon close inspection of the myofibre stress contour plots presented in Figure 4.13 and Figure B3 (appendix).

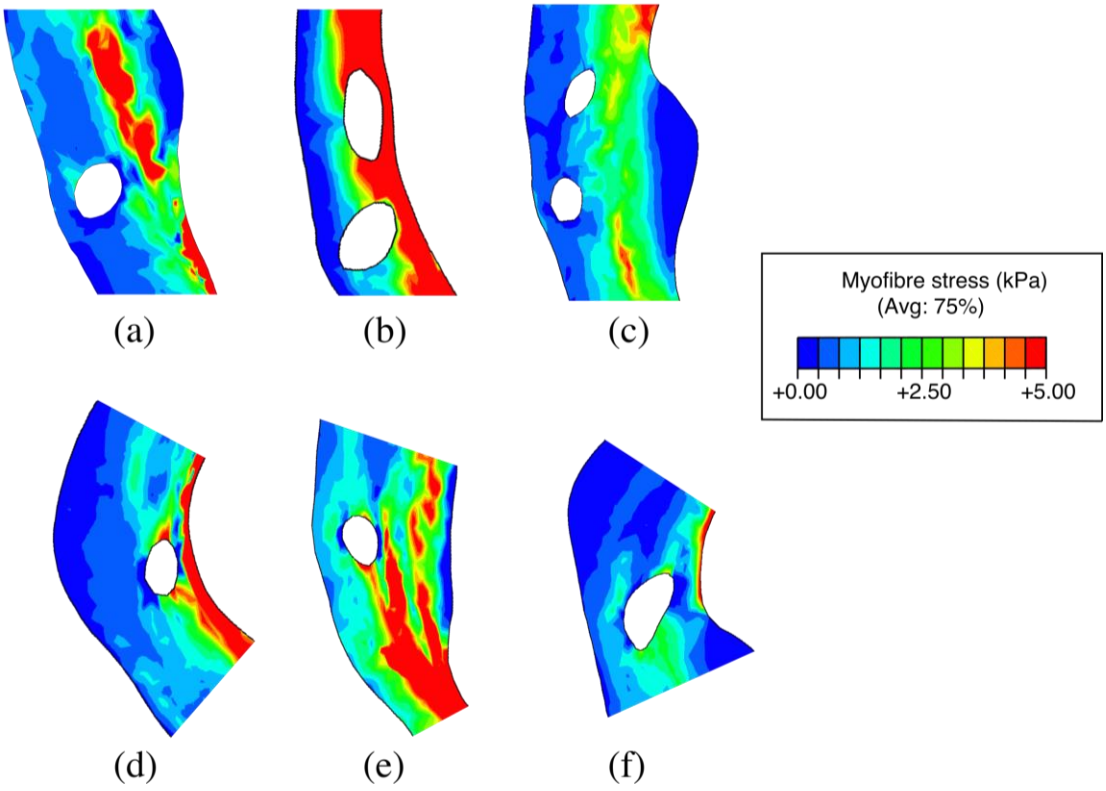

Figure 4.15: Zoomed in myofibre stress at end-diastole in the vicinity of gel injectates embedded within the myocardium walls. Long-axis segments from subjects HFI 1, 2 and 3 are presented in (a), (b) and (c) respectively. Short-axis segments from subjects HFI 1, 2 and 3 are presented in (d), (e) and (f) respectively. Injectates are transparent and appear as white.

Local myofibre stresses can be cross-referenced with geometric features to allow for a more quantitative analysis. Assessing mean myofibre stresses by proximity to pathological tissue (i.e. material points with $H_{INDEX} < 1.0$) reveals that peak myofibre stresses occur roughly 1mm away from the pathological tissue, as shown in Figure 4.16. This is the case for mean results of HFC and HFI

subjects at both ED and ES as shown in Figure 4.16(b) and (d) respectively. While HFC and HFI groups experience the same qualitative behaviour, the HFI group experience typically lower stress values until the distance from the infarcted tissue exceeds approximately 14mm, whereby the stress values converge, as seen in Figure 4.16(a) and (b). An exception to this is at ES, whereby the peak myofibre stress at 1mm in the HFI group exceeds that of the HFC group.

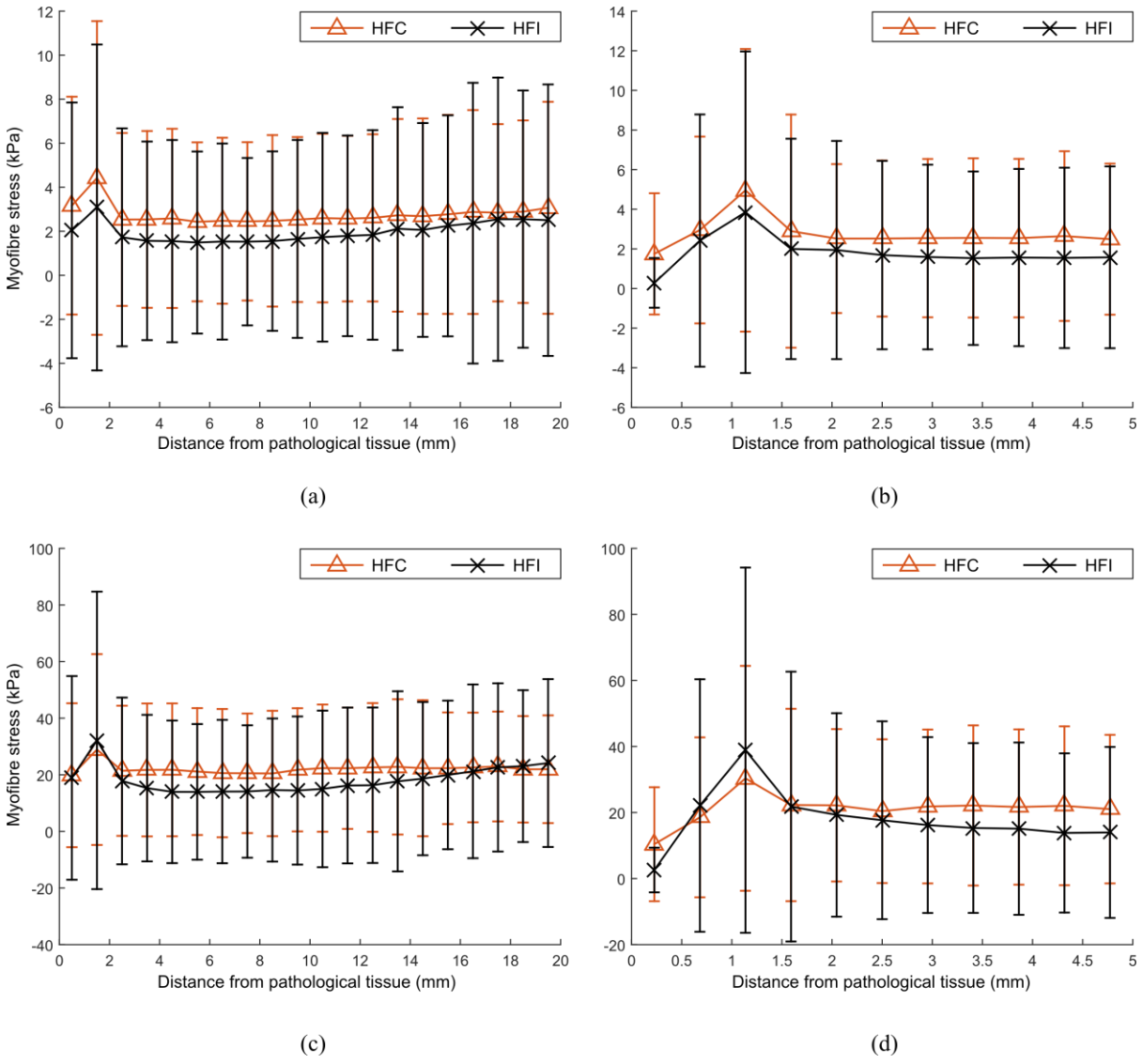

Figure 4.16: LV mean myofibre stress results from HFC and HFI subjects presented by proximity to pathological tissue. (a): Myofibre stress results at ED within 20mm from pathological tissue. (b): Myofibre stress results at ED within 5mm from pathological tissue. (c): Myofibre stress results at ES within 20mm from pathological tissue. (d): Myofibre stress results at ES within 5mm from pathological tissue. Error bars correspond to ± SD.

An assessment of mean myofibre stresses by proximity to the gel injectates reveals that stresses near the injectates are substantially lowered in direct proximity to the gel injectates. This is true for myocardial tissue in the LV at both ED and ES as shown in Figure 4.17(a) and (b) respectively. This analysis reveals that the lowest myofibre stress values are in areas nearest to the gel injectates. As the distance between material points and the gel injectates increases, so do the mean myofibre stress values. At approximately 10 mm from the gel injectates the regional myofibre stress exceed the mean global LV myofibre stress values, thereafter it plateaus as the distance between tissue and gel injectates increases.

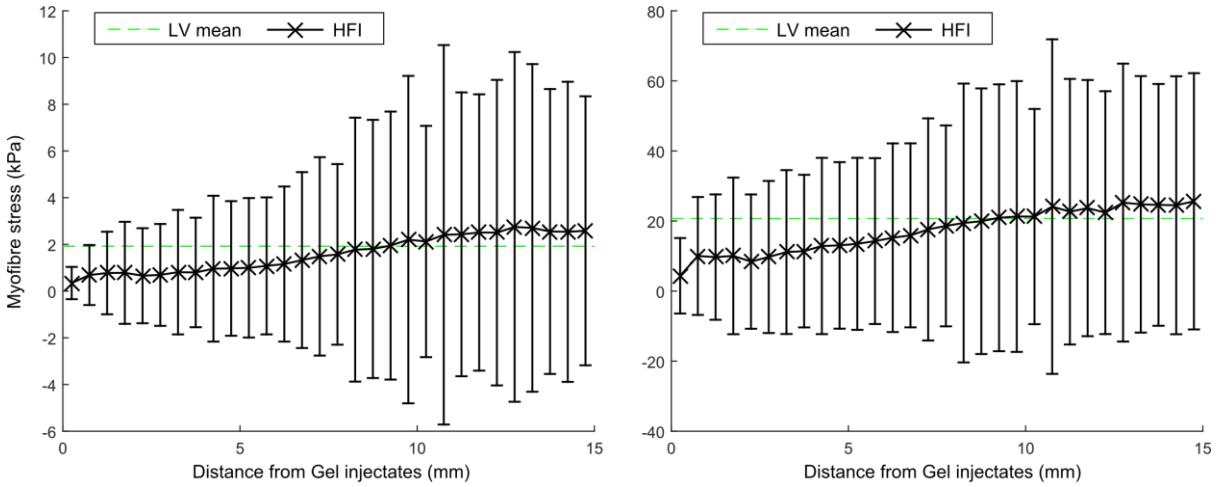

(a) (b)

Figure 4.17: LV mean myofibre stress results from HFI group within 15mm from pathological tissue at (a): ED and (b) ES. Global mean LV values, as presented in Table 4.6*, are plotted as a dashed green line for each result. Error bars correspond to ± SD.*

4.3.6 Injectate pattern and tissue proximity

Investigation into the resulting geometric placing of the injection therapy revealed unique patterns of solidified injectates in the myocardial wall between subjects, even though subjects experienced the same injection procedure (see Chapter 2 for more details). The arrangement of solidified injectates results from liquid Algisyl-LVR™ initially displacing interstitial fluid and subsequently separating myocardium along cleavage planes of least resistance during the injection process. This phenomenon is highly subject-specific, depending on both the global and local tissue mechanics. Even though the injection patter appears differently in solidified form from subject to subject, the distribution of LV tissue proximity to the injections remains consistent. This is shown in Figure 4.18, which reveals that the majority of LV tissue lies within 15mm of the injectate surfaces.

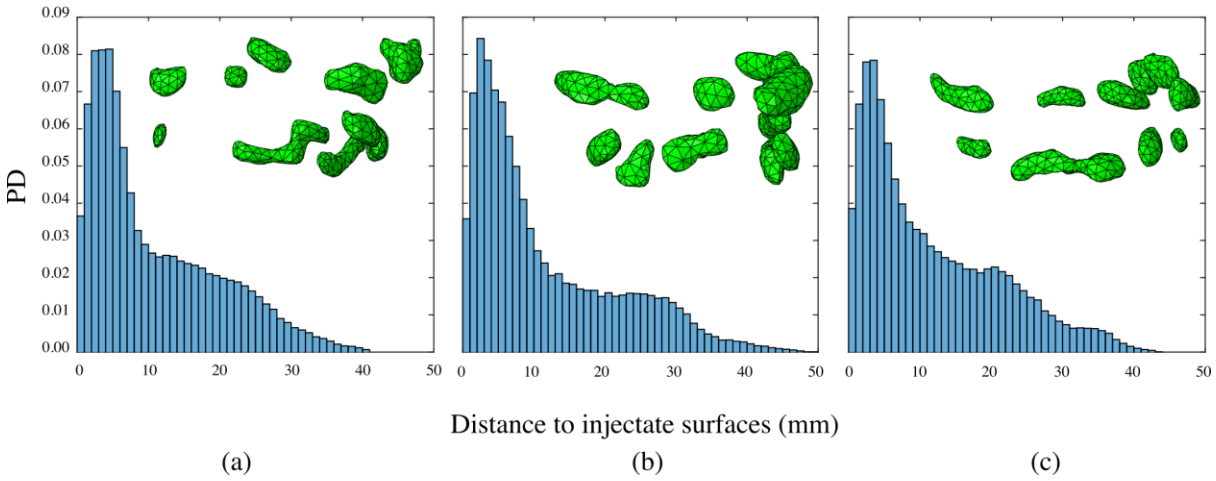

Figure 4.18: Distribution of LV tissue proximity for subjects HFI 1, HFI 2 and HFI 3 given in panels (a) (b) and (c) respectively. An anterior view of the 3D injection pattern for each subject is given in the right-hand upper corner of each panel. Histograms are normalized by probability density (PD), i.e. the area under a distribution sums to 1.

4.4 Discussion

4.4.1 Subject-specific geometric models of heart failure

The geometric models of HF used in this study are a novel extension of how infarcted tissue has typically been presented in mechanical computational studies. Previously, mechanical studies have represented infarcted tissue using discrete concentric zones accounting for infarction and the border-zone as neat self-contained geometric regions [65, 118, 122, 239, 240]. Our study incorporates subject-specific pathological detail, allowing for the description of infarcted material that ranges from concentrated to diffuse descriptions, as can be seen in Figure 4.4.

Moreover, our level of detail included in the geometric representation of the ventricular structure is highly sophisticated (including papillary detail, four valve openings and detailed endocardial surfaces) and likely the first biventricular computational study to investigate the mechanics of heart-failure with subject-specific myofibre detail.

4.4.2 Material parameter identification

Alginate

A Neo-Hookean constitutive relation successfully characterized the alginate biomaterial, as seen in Figure 4.5. Other studies have modelled alginate as a Mooney-Rivlin materiel [121] but we found the Neo-Hookean approach more stable for simulations.

Passive myocardium properties

The determination of passive material parameters for the myocardial tissue ultimately depends on three things: First, the unloaded volumes V_0 of the ventricles; second, the target ED volumes; and finally the assumption regarding infarct stiffness. Our calibration techniques found the HFC group yielded the stiffest material parameters, while the HFI group yielded the most compliant. These results are contextualized when the unloaded volumes are considered, which are 24.9 ± 5.3, 36.1 ± 7.8 and 25.9 ± 5.7 ml for the NC, HFC and HFI groups respectively (see Section 4.3.2).

The HFI group retain similar unloaded volumes to the NC, while the HFC group experience a permanent dilation resulting in an unloaded volume 45% larger than the NC group. Comparatively, the HFI group has an unloaded volume 4% larger than the NC group. At the same time, the target EDV volume for the HFI group is comparable, albeit slightly larger than the HFC group. These physiological demands justify the passive material parameters presented in Table 4.3, and provide key insights into the mechanical characterization of HF tissue with and without treatment of biomaterial injections.

In typical cases of LV HF the combined effect of tissue death, reduced systolic performance and scar formation leads to an overloaded and underperforming LV. This in turn leads to permanent dilation of the LV wall. While both the HFI and HFC group experience increased EDV volumes, indicative of volume overloading, the HFI group retains its elasticity and doesn't permanently deform. The HFC group on the other hand has a dilated LV cavity with myocardial tissue (both infarcted and remote) substantially stiffer than the other groups.

Our investigations found that it was impossible to match the PV filling curves by only altering the infarct stiffness. This is in line with other studies that have found that the remote tissue experiences changes in material properties [82, 244].

The comparative differences in stiffness and unloaded volume between the HFC and HFI groups are highly interesting findings, worthy of further investigation. These findings are also likely linked – the underlying source of stiffness in soft tissues is often explained by undulating fibre constituents acting (such as collagen) on the micro-scale that contribute to stiffness when they are elongated and thus engaged (also referred to as fibre recruitment) [245, 246]. If the HFC group has experienced

permanent deformation that propagates down to the micro-scale (e.g. longer sarcomeres measured in the unloaded state, and/or structural changes to collagen undulation) this would explain both the increase in unloaded volume and the increased stiffness.

Active Myocardium properties

While the HFI group are passively more compliant, the parameters for active tension development T_{MAX} and n_s indicate that the HFI subjects experience greater contractile force. This is indicative of comparative improvements of force generation at the sarcomere level, which must contribute to improved systolic performance.

4.4.3 Functional output

While there are minor differences in LV EDV and LV ESV between the *in vivo* targets and the values the FE model simulations converged on (see Table 4.4), the calibrated models were able to match the overall SV within 1ml and the EF within 1% for each group (Table 4.5).

The cardiac performance of the HFI group is substantially normalized when compared to the HFC group. This is evident in the EDP, which is elevated for the HFC but not the HFI group (16.7 ± 5.9 vs. 12.3 ± 2.7 mmHg), and the EF, which is roughly 10% lower in the HFC group than the HFI (32.6 ± 1.1 vs. 41.9 ± 4.0 %). The HFI group also experiences greater pressures during systole than the HFC group, which can be seen qualitatively in Figure 4.6. The HFI group's PV loop lies almost perfectly in between those of the NC and HFC groups. Collectively these results show increased systolic performance in the HFI group.

It's worth noting that while the HFI group has a higher value of T_{MAX} as a group, this is largely due to a single subject (HFI 2) experiencing exceptionally high values. The other subjects have lower values of T_{MAX} than the average HFC subject yet their subject-specific EF values are still higher. The improvement in systolic function is therefore likely also due to additional factors besides T_{MAX}. The most likely, is due to the morphology of the LV shape and the lessened progression of tissue damage in the border-zone surrounding infarcted tissue.

4.4.4 Strain analysis

Local myofibre strain results reveal that the HFC subjects experience significantly diminished LV myofibre strains during cardiac function than the NC and HFI groups. This is also seen in model predictions of LV circumferential and longitudinal strains, which are consistent with literature

findings [231, 244]. Evidently, diminished strains are an indication of dysfunction: evidence that the LV is unable to properly fill with and expel blood as it should.

In contrast the HFI group experiences *increased* myofibre strains at ED compared to the NC group (9.4 ± 9.3 vs. 8.3 ± 5.9 %). While the HFI group experiences diminished LV myofibre strains compared to the NC group (-8.8 ± 9.9 vs. -10.0 ± 5.0 %), they are still significantly improved compared to the HFC group (-6.4 ± 7.9 %).

Comparing FE model predictions and *in vivo* measured strain values produced conflicting results. While some subjects had excellent agreement (see Figure 4.11 and Figure 4.12) others did not. The shortcomings of deriving regional strains from echocardiogram data are well known [227-229] (and discussed in detail in Section 3.4.6). Considering that our FE model prediction produce qualitative regional strains across all subjects, which are also in line with general literature findings [195, 230-232], we are inclined to conclude that a primary source of disagreement between *in vivo* and *in silico* strain predictions are errors inherent in the *in vivo* data acquisition (likely due to poor image resolution).

Another consideration is that *in vivo* strains do not account for papillary muscles, which pull downward during systole. Endocardial segments that include parts of the papillary muscle in the FE model segmentation will clearly differ from low resolution *in vivo* measured values that exclude these. It should be noted that *in vivo* the papillary muscles would be connected to the valves while *in silico* they are not. This would likely be a source of strain discrepancy between *in vivo* an *in silico* strains. This may explain why septal regions have greater accuracy in subjects that have an overall good agreement between *in vivo* and in silico strain predictions such as NC2 (see Figure 4.11).

Finally, comparing regional strains between different modalities is complicated by the different resolutions (echocardiography is particularly low resolution) and the different segmentation methods. Echocardiography segmentation (i.e. precisely where the different AHA regional borders are determined) likely differs from our own methods, which would explain the “out of phase” results we see in some of our comparisons. Future work for strain comparison could include finding ideal segmentations that minimize differences between modalities.

4.4.5 Stress analysis

Local wall stress is a key factor in assessing heart function, yet under *in vivo* conditions such stresses cannot be measured systematically and quantitatively [87]. Imaging techniques provide high accuracy information regarding the strain distribution in the heart, yet cannot provide local stress information.

Laplace's law, an analytical approach to estimate wall stress, makes large assumptions with respect to the cardiac structure and cannot account for stress in fibre or cross-fibre directions (as fibre orientation is excluded in the formulation). This was demonstrated by Zhang *et al.* [88] who compared Laplace's law and FE methods to evaluate stress in an infarcted LV. Their convincing analysis showed that the average stress from Laplace's law is significantly different to the comprehensive stress analysis produced through anatomically accurate FE techniques.

This is critically important in the context of our results: HFC subjects experience increased stress while simultaneously experiencing reduced strain. Determining stress directly from strain, without accounting for the anatomic features of the infarcted tissue or a proper constitutive characterization of the myocardial tissue (e.g. in Laplace's law), could lead to highly erroneous conclusions about the actual stress state within the failing heart.

Our findings show that HFI subjects experience roughly two thirds of the LV myofibre stress experienced in HFC subjects at ED (1.9 ± 4.8 vs. 2.8 ± 5.5 kPa) and comparable values to the NC group (2.1 ± 6.1 kPa). LV myofibre stress at ES was comparable for all groups being 19.2 ± 27.3, 20.5 ± 25.3 and 20.7 ± 25.6 kPa for the NC, HFC and HFI groups respectively.

RV myofibre stress results show that HFI subjects experience roughly half of the stress experienced in HFC subjects at ED (0.8 ± 2.3 vs. 1.5 ± 3.0 kPa) and comparable values to the NC group (0.6 ± 0.7 kPa). At ES RV myofibre stress was larger in both the HFC and HFI groups (24.6 ± 21.7 and 26.9 ± 39.9 kPa respectively) compared to the NC group (17.7 ± 18.5 kPa).

Evidently, the presence of alginate injectates has a major effect in stress reduction during passive cardiac function. The fact that this effect transcends the LV and also impacts the RV is indicative that the entire cardiovascular system has been affected by the presence of alginate injections. In a close-loop circulatory model this is indicative of changes in pump function. As a consequence of treatment, the HFI subjects experience less abnormal cardiac function leading to comparatively less myofibre stress than non-treated HFC subjects.

A regional analysis of stress based on proximity to infarcted tissue revealed that peak stresses in the failing heart lie roughly 1mm outside the region of pathological tissue. This peak of myofibre stress likely contributes to infarct expansion and remodelling of the functional border-zone near infarcted tissue. Subjects with alginate biomaterial therapy had lower stresses in proximity to pathological tissue less than 14 mm.

Alginate injectates were found to reduce stress regionally. Our quantitative analysis presented in Figure 4.17 reveals that this effect is directly related to proximity of the surrounding tissue to the injectates and is effective up to 10 mm from injectate vicinity. The injection pattern places many of the injectates in the vicinity in and around infarcted tissue, resulting in reduced stress in the infarcted tissue, the adjacent border-zone and even in remote areas of the LV seen in Figure 4.16.

To identify the mechanism of action that produces the regional reduction in myofibre stress, a proximity analysis of other metrics were investigated. It was found that myofibre strain was substantially reduced in proximity of the alginate injections, as shown in Figure 4.19. These results show that the reduction in regional stress is caused by the local interaction between the gel injectates and the surrounding myocardium, with the injectates anchoring the surrounding tissue causing less strain and thereby less stress in the vicinity.

Figure 4.15, which show the myofibre stress field in the surrounding gel injectates in long axis and short axis views, reveal that stress reduction is not a consistent phenomenon that is easily identifiable at every injection site. It likely depends on the regional load, gel morphology and the adjacent myofibre orientations.

The reduction of strain, and consequently stress is the likely mechanism that prevents treated subjects from experiencing permanent dilation of the ventricular wall that is seen in HFC subjects. It appears that the application of the injection therapy at 8 weeks following infarction was sufficient to affect more favourable outcomes in treated subjects by the time the animals were sacrificed (8 weeks later).

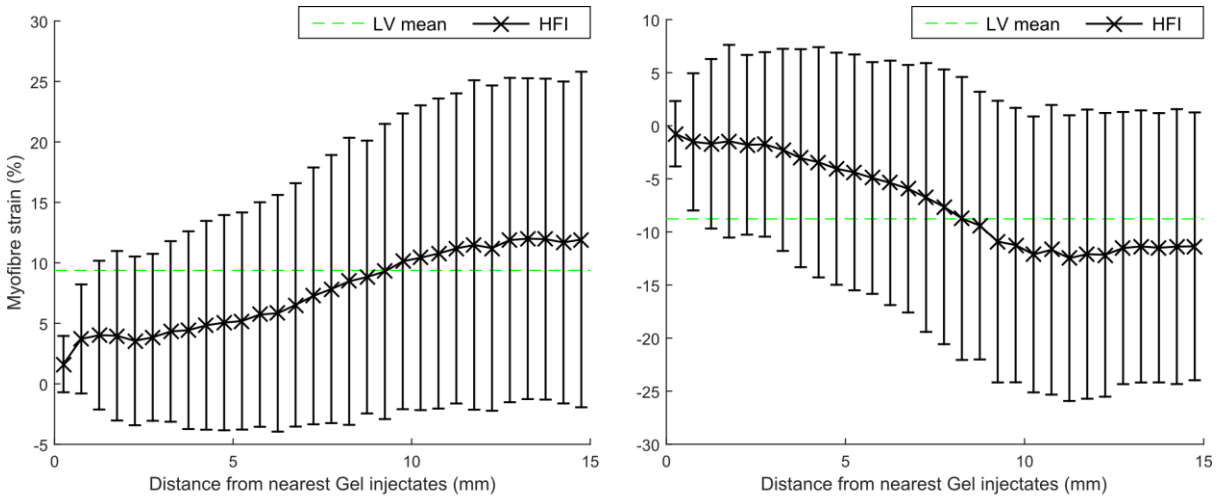

Figure 4.19: LV mean myofibre strain results from HFI group within 15mm from pathological tissue at (a): ED and (b) ES. Global mean LV values are plotted as a dashed green line for each result. Error bars correspond to ± SD.

Our findings are in line with other computational studies of biomaterial injection therapy, which have reported reduction in stresses due to biomaterial inclusion in the myocardial wall [117, 121-123, 247]. These studies compared the same model with and without treatment and using such a controlled comparison they showed reduced strains [122, 123, 247], which is consistent with our regional findings of strain based on proximity to gel injectates.

5.1.1 Injectate pattern and prediction of treatment efficacy

The mechanical impact of the gel injections affects tissue within 10 mm of the solidified gel surfaces, which includes the majority of LV tissue (Figure 4.18) regardless of differences in the solidified injectate pattern. This shows that the injection procedure need not be precise, as long as Algisyl-LVR™ material is placed circumferentially in the LV mid-wall. The equity in treatment outcomes is likely due to the similarity in infarction between subjects (i.e. damaged tissue was primarily located in the LV free wall). Further investigation into dramatic changes of the injection pattern can be investigated using FE simulations where injections can be added *in silico* to different regions of the heart (including the septal wall). This would allow for optimization to identify alternate injection patterns that may be optimal to subject-specific cases of pathology (i.e. inclusion of apical, septal or basal regions in addition to free-wall injections).

4.5 Conclusions

This chapter presents a study of nine fully subject-specific biventricular cardiac computational models in different combinations of pathology and treatment. Realistic subject-specific representations of pathology are included in the failing hearts allowing for a sophisticated model of diseased tissue.

These models were calibrated to *in vivo* subject-specific metrics, and were able to accurately capture functional outputs such as SV and EF. The agreement between *in vivo* and *in* silico strains were closely correlated and illustrated the successful ability to recreate computational models that can serve as *in silico* surrogates for real hearts in healthy, diseased and treated states.

Our findings showed that treatment of HF with alginate injections resulted in hearts that were less dilated when unloaded, more compliant under passive loading and more contractile during systolic performance than non-treated hearts. Improved systolic performance leads to better cardiac output such as EF and SV seen in the HFI subjects.

Myofibre stress results showed that treated subjects experienced lower LV and RV stresses at ED than non-treated subjects. A proximity analysis revealed that the alginate injectates lower stress by reducing the strains in their direct vicinity, a mechanism effective up to 10 mm from the edge of the solidified injectates. This benefits infarcted, border-zone and remote tissue, which was shown to have lower values of myofibre stress than in comparable regions in HF subjects without treatment. Our findings suggest that placing injections in regions within the myocardial wall vulnerable to permanent dilation would maximize the therapeutic benefit to potential patients.

The ability to tune the mechanical properties of the injectates to optimize the desired results is a task that computational modelling is well suited for. Future research will focus on optimizing treatment protocols to maximize outcomes resulting from the injection therapy.

Model limitations presented in Chapter 3 also apply to these models. Having three subjects per group limits the ability to meaningfully compare outcomes between groups. This will improve as more models are added to the study. Additionally, including longitudinal data points in time (i.e. subject performance before and after treatment) would greatly benefit this research. Currently insufficient *in vivo* imaging resolution is available to build comparatively precise models of living subjects, however as technology in this field improves this will become possible.

Chapter 5 Left ventricular assistance in the acutely failing human heart

To investigate alternative mechanical therapies for heart failure (HF), the effect of left ventricular assistance is investigated in this chapter.

Left ventricular assistance devices (LVADs) treat HF by providing the left ventricle with sufficient mechanical circulatory support to allow for offloading. The effect of the device is simulated using the Living Heart Model, which has been modified to enable comparative models of healthy, failing and treated cases of the same subject. This allows for definitive effects of the treatment to be quantified in a subject-specific framework.

A manuscript of this study titled, '*Partial LVAD restores ventricular outputs and normalizes LV but not RV stress distributions in the acutely failing heart in silico*' has been published in the International Journal of Artificial Organs. The sections 5.1-5.4 are taken verbatim from this manuscript with permission of the UCT Doctoral Degree Board. The final section detailing the conclusions has been slightly modified.

5.1 Introduction

Heart failure (HF) is a highly significant medical and economic problem afflicting an estimated 5.7 million Americans [248]. Projections show that the prevalence of HF will increase 46% from 2012 to 2030, resulting in >8 million adults with HF [3]. In 2012, the total cost for HF was estimated to be $30.7 billion. Of this total, 68% was attributable to direct medical costs related to hospitalizations [3]. Projections show that by 2020, the total cost of HF will increase almost 127% to $69.7 billion from 2012 [3]. Left ventricular assist devices (LVADs) are a novel strategy for HF treatment, whereby the heart is provided with sufficient mechanical circulatory support to allow for offloading, which in turn promotes myocardial remodelling and recovery [4-6]. The first-generation pulsatile flow devices have

been replaced by newer generation continuous-flow LVADs that are smaller size and more durable [249]. In particular, LVADs, which can be implanted minimally invasively without sternotomy or cardiopulmonary bypass, remove some of the large risks associated with major surgery [250]. These devices can deliver a range of flow output between 2-10 l/min [251], depending on the level of support needed. These improvements in device technology, coupled with greater clinical expertise surrounding LVADs, led to a decrease in patient risk over the last decade, making LVAD treatment an increasingly viable option for many patients [252]. Furthermore, roughly 5% of LVAD-treated patients experience a full recovery, allowing for reduced support and, in some cases, device explantation [253, 254]. Recent results show that miniaturized, less invasive, partial-support devices operating at low flow rates may have the potential to be used in more patients, particularly those with INTERMACS classification 4 and greater [7, 8].

Although clinical expertise regarding LVADs is increasing, the exact mechanisms responsible for myocardial recovery and reversal of HF are still not fully understood, limiting the ability to predict long-term function, durable recovery or remission of HF [253, 255]. Computational studies have already been identified as a means to accelerate successful LVAD design and treatment protocols due to the inherent ability of cheaply and efficiently perturbing treatment parameters [256]. Additionally, realistic computational models provide a wealth of information for clinical decision making [170], and may elucidate mechanical cues responsible for recovery that are otherwise unobtainable.

In this novel computational study concerned with the normal human heart, acute left HF, and LVAD therapy, we sought to detail significant improvements in the systolic material properties of the Dassault Systémes Living Heart Model (LHM) and use it to compute left and right ventricular (RV) myofibre stress distributions under the following four conditions: (1) normal cardiac function; (2) acute left HF with an LV ejection fraction of 28%; (3) acute left HF using an LVAD flow rate of 2 l/min; and (4) acute left HF treated using an LVAD flow rate of 4.5 l/min. Relatively few computational studies have investigated the effect of LVADs on cardiac function utilizing realistic geometries [138, 257], due to the complexities involved, and to the best of our knowledge, our study is the first to present stress and strain results in both ventricles.

5.2 Methods

5.2.1 Whole heart modelling of the normal human heart

Baillargeon *et al.* [28] created a finite element model of the whole heart on the basis of the existing solid model illustrated in Figure 5.1(a). This made it possible to model all four chambers as electrically excitable, deformable, hyperelastic, electroactive bodies connected via in- and out-flow conditions of viscous resistance type [28]. We refer the interested reader to Baillargeon *et al.* [28] for the full description of the model, including the continuum model of electro-mechanical coupling, the balance equations, and the constitutive equations. Here we only present the changes in the LHM that were pertinent to this study.

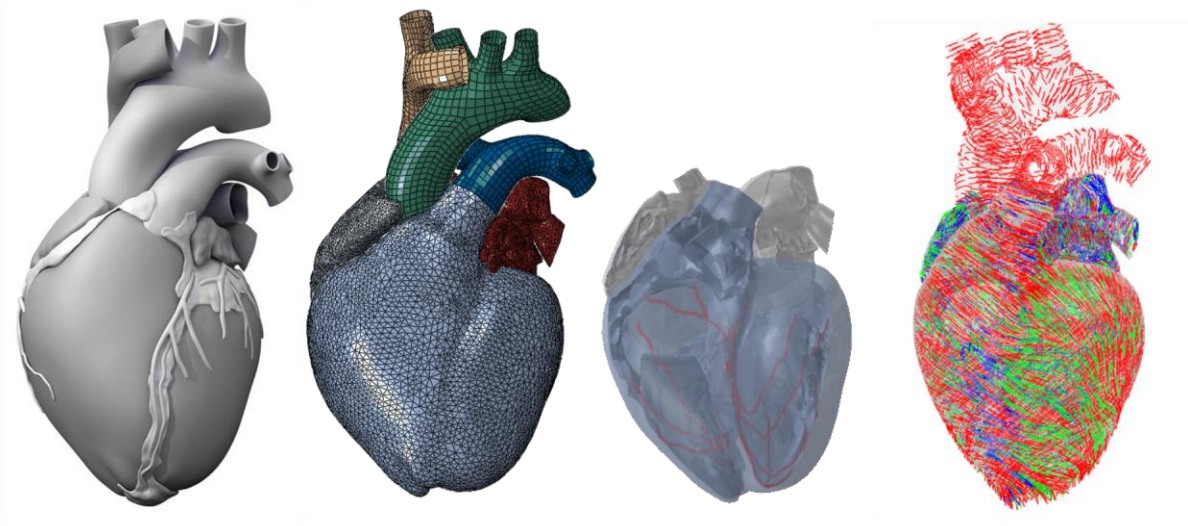

Figure 5.1: (a) Solid model of the human heart used as the basis for our improved model. It was created from computed tomography and magnetic resonance imaging; adapted with permission from (Zygote Media Group and Inc., 2014). (b) Mechanical finite element model of the human heart discretized with 449,560 linear tetrahedral elements, 12,915 linear quadrilateral shells, 7577 linear triangular shells, 636 linear truss elements, 16,824 rigid triangular elements, 130,290 nodes, and 443,564 mechanical degrees of freedom. (c) Electrical finite element model of the human heart discretized with 449,560 linear tetrahedral elements, 655 1D linear conduction elements (red), 103,770 nodes, and 103,770 electrical degrees of freedom. (d) Fibre orientations of the Living Heart Model.

The passive material response of the cardiac tissue uses an anisotropic hyperelastic formulation based on that proposed by Holzapfel and Ogden [56]. In the LHM, this response appears to be more stable

than the Fung response [168]. The deviatoric and volumetric responses are governed by the strain energy potentials in Eqs. (5.1)-(5.2), with parameters defined in Table 3.2:

$$\Psi_{dev} = \frac{a}{2b} e^{b(I_1-3)} + \sum_{i=f,s} \frac{a_i}{2b_i} \left\{ e^{b_i (I_{4i}-1)^2} - 1 \right\} + \frac{a_{fs}}{2b_{fs}} \left\{ e^{b_{fs} (I_{8fs})^2} - 1 \right\}, \tag{5.1}$$

$$\Psi_{vol} = \frac{1}{D} \left(\frac{J^2-1}{2} - \ln(J) \right). \tag{5.2}$$

The passive model parameters used in our study follow from the revised parameters presented in Baillargeon *et al.* [167], which improved the LHM's performance in line with physiological expectations. This material model, Eqs. (5.1)-(5.2), ensures that the material exhibits the well-documented exponential and anisotropic response to strain [74, 75, 258] while enforcing incompressibility.

5.2.2 Improvements to the Living Heart Model

This study incorporates recent improvements to the active-tissue material model, intended to capture the Frank-Starling effect (i.e., the strength of the heart's systolic contraction is directly proportional to its diastolic expansion). The active tissue response now contains length-dependent considerations of regional sarcomere lengths when the active response is determined. This affects the stress components in the fibre and sheet directions in the constitutive model.

The active stress in the cardiac muscle fibre direction is now defined by the following time-varying elastance model [184]:

$$\sigma_{af}(t, E_{ff}) = \frac{T_{max}}{2} \frac{Ca_0^2}{Ca_0^2 + ECa_{50}^2(E_{ff})} \left(1 - \cos\left(\omega(t, E_{ff}) \right) \right), \tag{5.3}$$

where

$$ECa_{50}(l) = \frac{Ca_{0_{max}}}{\sqrt{e^{B(l(E_{ff})-l_0)} - 1}}, \tag{5.4}$$

$$\omega(t, l) = \begin{cases} \pi \dfrac{t}{t_0}, & \text{when } 0 \le t \le t_0 \\ \pi \dfrac{t - t_0 + t_r\left(l(E_{ff})\right)}{t_r}, & \text{when } t_0 \le t \le t_0 + t_r(l) \\ 0, & \text{when } t_0 + t_r(l) \le t \end{cases} \tag{5.5}$$

$$t_r(l) = ml + b, \tag{5.6}$$

$$l(E_{ff}) = l_r\sqrt{2E_{ff}+1}, \tag{5.7}$$

with parameters as defined in Section 3.2.4.2. The mathematical description of active tension, Eqs. (5.3)-(5.7), ensures a smooth yet steep transition from zero to peak active tension, T_{max}, at time t_0 and then a smooth decline back to zero for the specified relaxation time t_r.

As in previous work [28], the total stress in the fibre direction, σ_f, is equal to the active stress, σ_{af}, plus the passive stress, σ_{pf}:

$$\sigma_f = \sigma_{pf} + \sigma_{af} \tag{5.8}$$

Active stress in the sheet direction, σ_s, is the sum of the passive stress, σ_{ps}, and a fraction of the stress in the fibre, $n * \sigma_{af}$ (where n is a scalar value less than 1.0 and represents the interaction between the adjacent muscle fibres):

$$\sigma_s = \sigma_{ps} + n\,\sigma_{af} \tag{5.9}$$

The value of n affects not only the total contractility of the chambers, but also the degree of twist developed in the chamber during the cardiac cycle. The magnitude of contractility for each chamber was tuned to provide the appropriate ejection fraction for that chamber. This involved tuning T_{max}, n (to limit the twist of the LV and RV) and l_0.

Figure 5.1(b) shows the mechanical finite-element model of Zygote's second-generation solid heart geometry, which is discretized with more than 480,000 mixed elements, resulting in 130,290 nodes and 443,564 mechanical degrees of freedom. Figure 5.1(c) illustrates the electrical finite-element model, highlighting the representative Purkinje fibre network, discretized by over 600 1D linear conduction elements embedded in the same mesh for the ventricles and atria as the mechanical model. The muscle fibre model, shown in Figure 5.1(d), is prescribed to all solid elements in the model.

5.2.3 Living Heart Model with simulated acute left heart failure

Systolic heart failure due to left ventricular dysfunction refers to the severely impaired heart function that results from reduced LV contractility. Loss of systolic function causes reduced ventricular emptying, resulting in increased LV end-diastolic volume and pressure. This acute left heart failure (ALHF) is the pathological condition simulated in this study. The loss of contractility was simulated by the single adjustment of parameter T_{max} in the LV until an ejection fraction (EF) symptomatic of

HF was produced in the LHM. This simulation resulted in an EF of 28% with a value of T_{max} at 25% of its normal value. Healthy values for EF are set at values >50%, with 35-50% representing a "grey area" for clinical diagnosis and values <35% clearly indicative of HF [259, 260]. Average EF measurements of patients enrolled in larger trials report even lower values ranging from 27-34% [261, 262], placing our simulated ALHF model as a prominent dysfunction well away from "grey area" values.

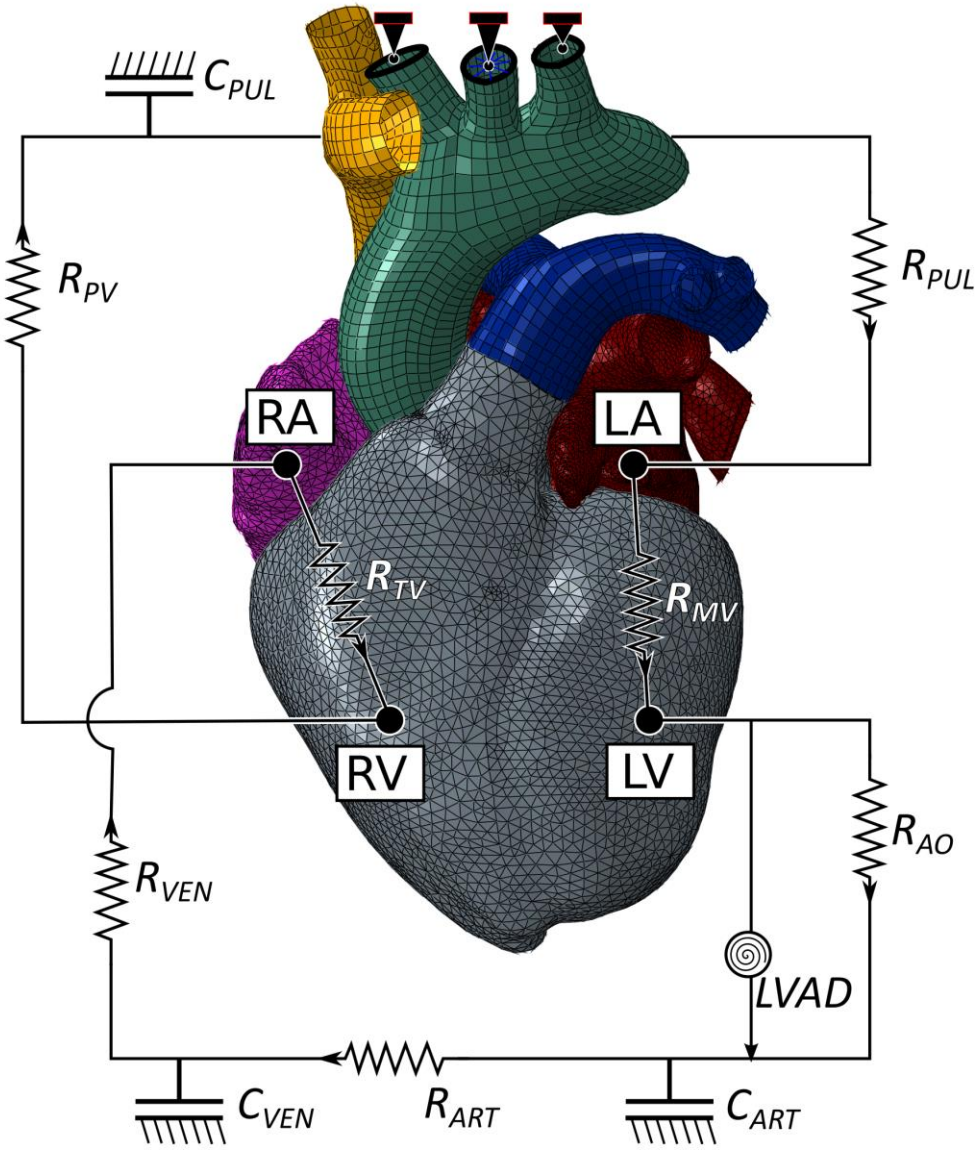

Figure 5.2: Schematic of the electromechanical model coupled with the circulatory system and LVAD. The truncated branched arteries from the aortic arch are fixed to prevent rigid body motion. R_{MV} is mitral valve resistance, R_{AO} is aortic valve resistance, C_{ART} is systemic arterial compliance, R_{ART} is systemic arterial

resistance, C_{VEN} is venous compliance, R_{VEN} is venous resistance, R_{PV} is pulmonary valve resistance, C_{PUL} is pulmonary system compliance, R_{PUL} is pulmonary system resistance, and R_{TV} is tricuspid valve resistance.

5.2.4 *In silico* simulation of a LVAD in the acutely failing human heart

By considering the newer-generation continuous flow devices, whereby the small size of the LVAD allows for minimally invasive attachment, only the effect of the device is simulated, i.e. the flow conditions between the cavities are modified to simulate differing LVAD support. The LVAD inflow cannula tip is inserted into the LV, and the outflow, connecting the device to the arterial network, is usually attached via the aorta. The acutely failing human heart model described above was further modified to simulate the effect of the LVAD through the introduction of an additional fluid exchange between the beating LV fluid cavity and the arterial system. The circulatory system included lumped compliance and resistance parameters representing the viscous fluid exchanges amongst the four-chamber heart, the arterial system, the pulmonary system, and the major linking vasculature. A schematic diagram outlining the fluid connections between the electro-mechanically driven heart and the lumped circulatory system with the LVAD is presented in Figure 5.2. The LVAD has an additive contribution to the arterial system that provides a constant blood flow that complements the LV ejection output while reducing LV physical diastolic loading. In these simulations, output from the LVAD was set at 2.0 l/min and again at 4.5 l/min, indicative of the range of realistic output from the miniaturized newer-generation LVADs [7, 251]. Aside from the LVAD, all other fluid exchanges are pressure-driven by the realistic mechanical model of the four chamber heart.

Because the LVAD resides outside the heart and is surgically connected to the LV via a small inflow cannula, the restraint on LV motion is considered negligible and is ignored in the model set up. To restrict rigid body motion, Dirichlet boundary conditions are applied to the truncated branches stemming off of the aortic arch (see Figure 5.2). The geometric representations of the aorta, pulmonary trunk, and vena cavae are bypassed by the lumped blood-flow model and are connected passively to the model purely as a means to enforce realistic boundary conditions.

5.3 Results

The LHM simulated heart function within the range for healthy human adults; functional parameters are presented in Table 3.6.

The effects of reduced contractility in the LV cause dramatic changes throughout the cardiovascular system. The LV experiencing ALHF undergoes volumetric overloading throughout the cycle, which results in a significant elevation in diastolic pressures. Specifically, there were increases in the end-diastolic volume of 35% and the end-diastolic pressure of 159%. This increased cavity volume of the acutely failing LV throughout the cardiac cycle results in a sustained state of elongation for the cardiac tissue throughout the cycle. In addition, the dependence of RV mechanics on healthy LV function is made clear by the degree of impairment the RV experiences. Both diastolic and systolic RV function is significantly compromised by the enlarged LV.

The introduction of the LVAD changes the hemodynamic state of the entire cardiovascular system. The additional flow conditions simultaneously reduce the diastolic loading of the LV and increase the arterial pressure, establishing a new equilibrium that generates more positive cardiac outcomes throughout the heart. As the flow rate of the device increases, the reduced loading shifts the end-diastolic state of the failing LV towards normal values. As LVAD flow increases, the LV PV-loop becomes more triangular, indicative of the device's effect during the normally isovolumetric periods of the cardiac cycle [263, 264].

Table 5.1: Left ventricular metrics of performance over a cardiac cycle in the normal, acutely failing, and assisted heart.

		Normal	**ALHF**	**LVAD 2 l/min**	**LVAD 4.5 l/min**	**ALHF**	**LVAD 2 l/min**	**LVAD 4.5 l/min**
	Metric	**Values**				**% of normal**		
Left Ventricle	EDV (ml)	152.9	206.3	189.8	155.0	135%	124%	101%
	EDP (mmHg)	10.7	27.7	17.6	6.9	259%	164%	64%
	SV = ED-ESV (ml)	85.5	57.3	37.5	24.0	67%	44%	28%
	Total output (ml)	85.5	57.3	64.4	84.6	67%	75%	99%
	EF (incl. LVAD)	56%	28%	34%	55%	50%	61%	98%
	maxP (mmHg)	135.1	84.3	85.4	97.4	62%	63%	72%
	minP (mmHg)	7.2	19.7	12.5	4.9	274%	174%	68%
Right Ventricle	EDV (ml)	179.9	172.4	175.4	183.0	96%	97%	102%
	EDP (mmHg)	3.3	2.7	2.8	3.1	80%	86%	93%
	SV = ED-ESV (ml)	84.6	54.7	66.1	84.8	65%	78%	100%
	EF	47%	32%	38%	46%	67%	80%	98%
	maxP (mmHg)	28.6	35.1	30.8	26.6	123%	108%	93%
	minP (mmHg)	0.4	1.9	2.0	2.2	416%	452%	499%

Abbreviations: ALHF, acute left heart failure; LVAD, left ventricular assist device; EDV, end-diastolic volume; ESV, end-systolic volume; EDP, end-diastolic pressure; SV, stroke volume; EF, ejection fraction; maxP, maximum ventricular pressure; minP, minimal ventricular pressure.

Stroke volume (SV) and EF quantified from the end-diastolic and end-systolic volumes alone significantly misrepresent the total LV output by neglecting the volume contribution of the device over the other stages of the cardiac cycle. Presented in Table 5.1 alongside SV are the total output results for the LV over a single cardiac cycle and the effective ejection fraction, which include contributions from the LVAD. Whereas the ejection fraction of the LV in the untreated acutely failing heart is 28%, the effective ejection fraction of the LV rises to 34% and then 55% for partial LVAD assistance operating at 2.0 l/min to 4.5 l/min respectively. This was accompanied by reducing the LV end-diastolic volume through LVAD operation to within 1.5% of the normal LV end-diastolic volume. Additionally, the LVAD significantly reduced end-diastolic pressure by 10.1- 20.8 mmHg operating at this range (2.0 – 4.5 l/min). LVAD operation shifts pressures in the LV towards normal ranges over the cardiac cycle, as seen in Table 5.1. The change of function of the RV is significantly dependent on the LV. Because the model circulatory system is a closed loop with pressures, volumes, and resulting flows that depend on the entire system, the RV pump function will naturally adjust to match the pump function of the LV. This is seen in Table 5.1, which shows the SV of the RV matches closely with the total output of the LV in all simulated cases. Although cavity pressure and volume in the RV are not as significantly affected as in the LV, the overall function of the RV is still just as severely compromised due to its dependence on LV function. This dependence works both ways, as seen in the case of LVAD operation at 4.5 l/min, which brings the effective stroke volume and ejection fraction for both ventricles within 2% of normal values.

5.3.1 Strains

Strain profiles of the heart (along the myofibre direction) at the end of diastole are presented in Figure 5.3. The elevated strains experienced in the heart with ALHF, which lead to adverse remodelling, are clearly decreased by the use of the partial LVAD throughout the cardiac cycle. The models with incorporated partial LVADs predict a minor reduction of strains for LVAD operation of 2 l/min and a significant reduction in strains for LVAD operation at 4.5 l/min. Strains are critically reduced at end-diastole (Figure 5.3), the point in the cardiac cycle which would subject the LV to largest strains.

Table 5.2: ED and ES volumetric-averaged mean stress results for the normal, acutely failing, and assisted heart presented separately for the LV and RV. Results are presented with standard deviations.

	Normal	ALHF	LVAD 2 l/min	LVAD 4.5 l/min	ALHF	LVAD 2 l/min	LVAD 4.5 l/min
Metric	**Values (kPa)**				**% of normal**		
LV ED	1.47 ± 20.72	7.47 ± 35.7	4 ± 29.12	1.26 ± 19.59	508%	272%	85%
LV ES	14.45 ± 106.72	16.39 ± 56.81	16.6 ± 56.92	15.81 ± 54.23	113%	115%	109%
RV ED	1.7 ± 18.06	1.59 ± 16.38	1.6 ± 16.73	1.62 ± 17.47	94%	94%	95%
RV ES	1.51 ± 81.78	8.63 ± 74.01	6.89 ± 74.19	5.18 ± 71.52	570%	455%	342%

Abbreviations: ALHF, acute left heart failure; LVAD, left ventricular assist device; ED, end-diastole; ES, end-systole.

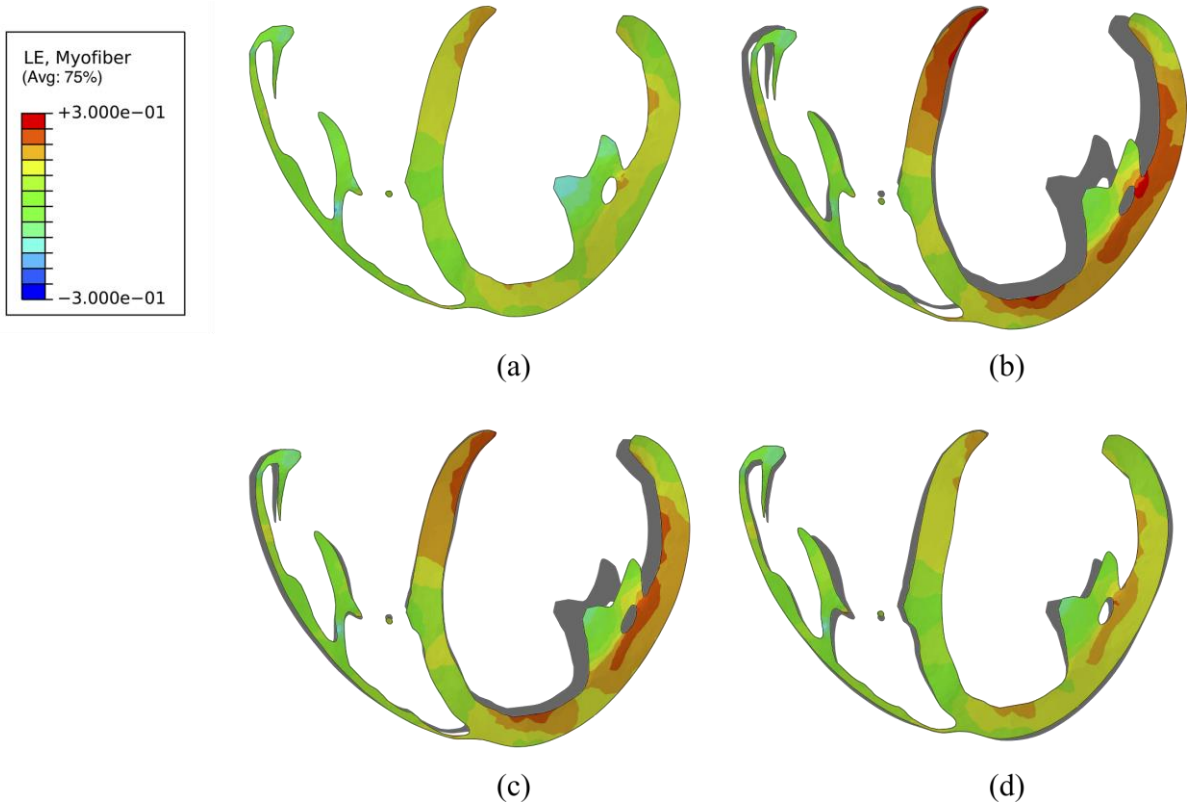

Figure 5.3: Long-axis profiles of the heart at the end of diastole showing contours of logarithmic myofibre strain for a normal healthy heart (a), a heart experiencing ALHF (b), a heart with ALHF and partial LVAD running at 2 l/min (c), and a heart with ALHF and partial LVAD running at 4.5 l/min (d). The deformed profile of normal healthy heart (a) is placed behind profiles of cases (b) to (d) as a grey silhouette for comparison.

5.3.2 Stresses

Stress distributions for myofibre stress (along the local muscle fibre direction) are presented in Figure 5.4 at end-diastole (ED) and Figure 5.5 at end-systole (ES). The volumetric-averaged myofibre stress was calculated at ED and ES and the mean values with standard deviations are presented in Table 5.2 for the RV and LV separately. The resulting mean myofibre stress found in the healthy LV was 1.47 ± 20.72 kPa at ED, and 14.45 ± 106.72 kPa at ES.

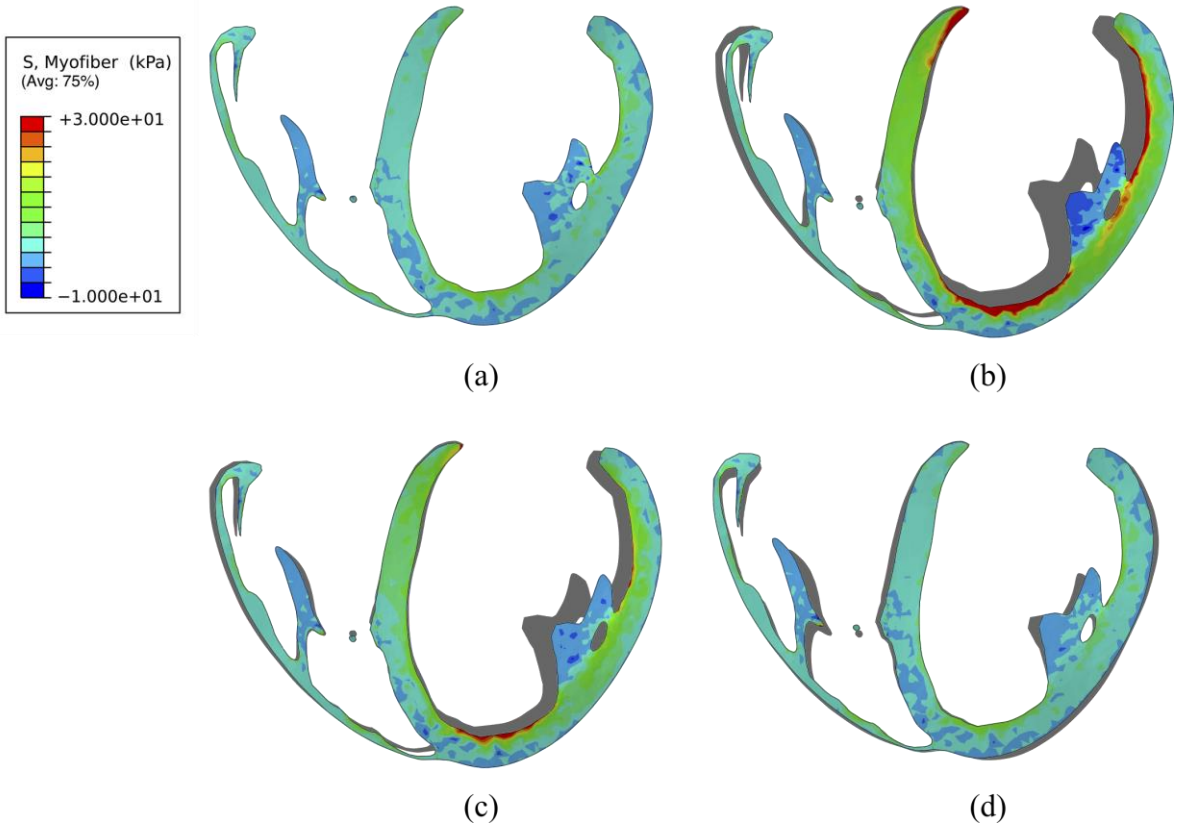

Figure 5.4: Long-axis profiles of the heart at the end of diastole showing contours of myofibre stress for a normal healthy heart (a), a heart experiencing ALHF (b), a heart with ALHF and partial LVAD running at 2 l/min (c), and a heart with ALHF and partial LVAD running at 4.5 l/min (d). The deformed profile of normal healthy heart (a) is placed behind profiles of cases (b) to (d) as a grey silhouette for comparison.

Impaired LV contractility resulted in an increase of LV mean myofibre stress to 7.47 kPa, roughly 5 times the normal values at ED. Increases were similar in RV myofibre stress at ES. For partial LVAD assistance, myofibre stress was significantly reduced in the LV, returning to lower values of 4.00 kPa and 1.26 kPa for LVAD operation at 2.0 and 4.5 l/min respectively. This is seen qualitatively in Figure 5.4, which also shows the assisted LV presenting a more ellipsoidal shape at ED compared to the heart with ALHF. Myofibre stress distributions throughout the cardiac cycle for all four cases are shown in the online-only supplementary video clip (available online as supplementary material at www.artificial-organs.com).

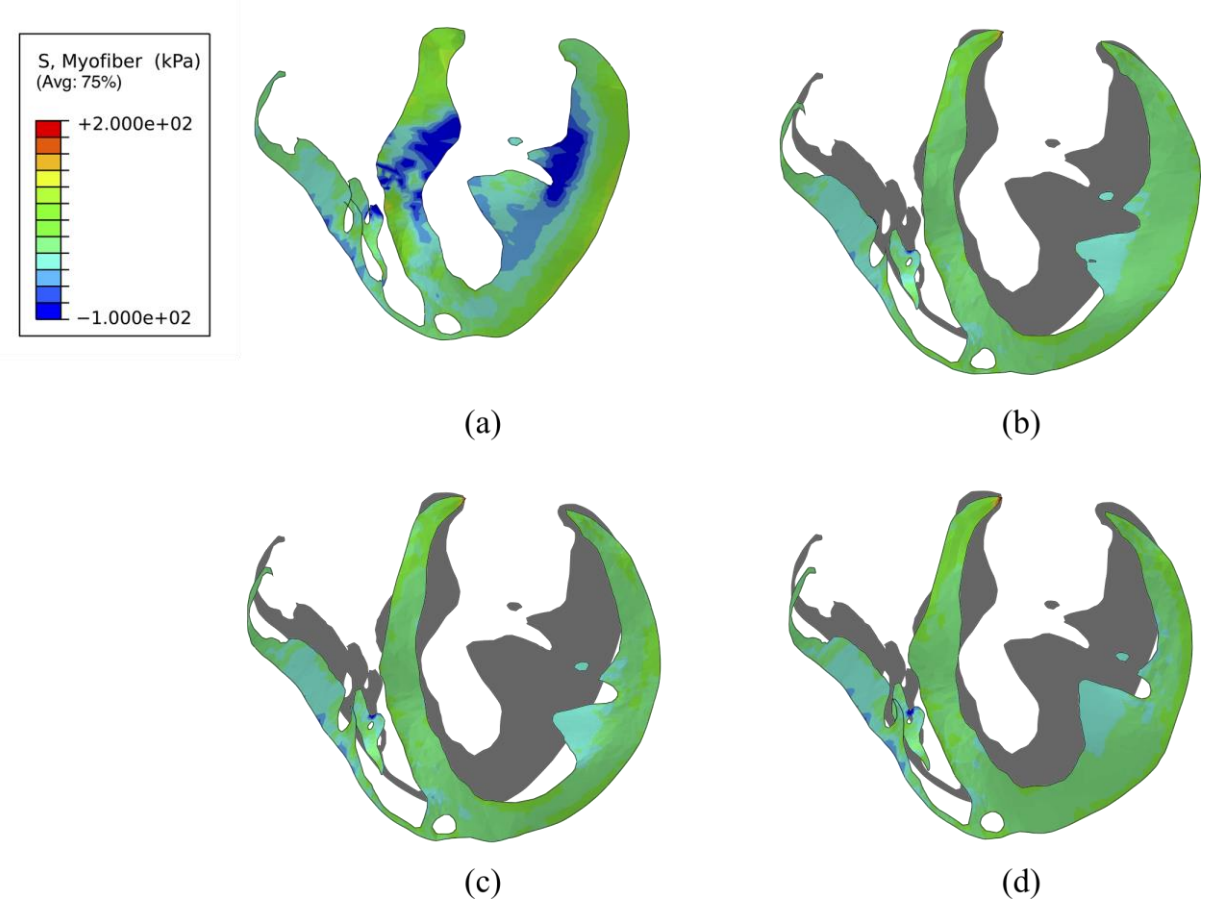

Figure 5.5: Long-axis profiles of the heart at the end of systole showing contours of myofibre stress for a normal healthy heart (a), a heart experiencing ALHF (b), a heart with ALHF and partial LVAD running at 2

l/min (c), and a heart with ALHF and partial LVAD running at 4.5 l/min (d). The deformed profile of normal healthy heart (a) is placed behind profiles of cases (b) to (d) as a grey silhouette for comparison.

5.4 Discussion

The improved LHM allowed us to model the effects of varying flow rate on an LVAD connected to a diseased heart experiencing ALHF. Using the LHM, and simulating a continuous-flow LVAD between 2.0 – 4.5 l/min, provided a brief *in silico* investigation on the effect partial LVAD may have on the acutely failing human heart. Monitoring left and right ventricular mechanics, our study presented clear improvements to cardiac function in the acutely failing human heart. This was seen in the return to normal values for stroke volumes and ejection fractions in both ventricles with LVAD operation at 4.5 l/min. The most dramatic improvement, however, was seen in the reduction of pressure, chamber size and stress in the LV at ED. The reduction in chamber size and LV preload due to LVADs is well established in clinical findings [129, 265] and other numerical investigations [137, 257, 264].

Mean stress results found in our study for the LV at ED and ES match closely to the mean reported values in a recent study outlining stress values for healthy human LV cardiac models [168]. The distribution of stresses is much larger in our model because of its more complex geometric representation and the use of a more sophisticated material model that includes regionally timed activation due to the electro-mechanical coupling [28]. Presented alongside Figure 5.4 and Figure 5.5 (or the online-only supplementary video clip), these values are given greater context: the beating heart is not a homogenous entity and experiences a complex combination of compressive and tensile stresses throughout the cardiac cycle.

The reduction of wall stress found at ED due to LVAD use is critically important. Changes in mechanical loading conditions, particularly ventricular wall stress, are thought to be a fundamental trigger for remodelling in the heart [224-226]. Forces or stresses in the intact heart wall cannot be measured directly [87], and although imaging techniques can provide accurate strain information from in vivo hearts, this does not translate to stress without severe assumptions. For example, Laplace's law, used to estimate average stress across the heart wall, makes considerable assumptions with respect to the cardiac structure and provides considerably different results compared to anatomically accurate finite element models [88].

The modest changes to ES stress in the LV due to ALHF and subsequent LVAD operation are intriguing. A recent finite element study of an isolated LV with reduced contractility and LVAD

support also reported modest changes in ES stress due to LVAD support [137]. It is possible that decreased loading of the acutely failing LV at ED, which would result in a relatively reduced contraction, is offset by the increase in arterial pressure that the LV is working against during ejection, resulting in small changes to ES stress. A similar argument could be made for the changes from the normal to acutely failing heart.

A physiological improvement in contractility for patients with LVADs is likely due to recovery post-unloading, as our model shows that the reduction in ED preload does not directly improve contractility. This can be clearly seen in Figure 5.4, whereby only the healthy heart shows that significant portions of the LV, beyond papillary muscle, experience compressive stress. Although LVAD support reduces the LV chamber volume at ED, chamber volume remains inflated for the remainder of the cardiac cycle. Our model shows that LVAD operation mitigates some of the elevated stresses experienced in the RV at ES, but the overall mean stress in the RV remains high (Table 5.2). The elevated stresses sustained throughout LVAD support in the RV at ES are likely due to the mechanical and structural dependence of the RV on LV contractility, which remain impaired despite LVAD operation. Since the active contraction law in our model includes length-dependent activation, the resulting contractile force within the LV *decreases* with LVAD operation – as strain reduction is a primary outcome of LVAD operation. This is seen in Figure 5.5, where the unassisted heart with ALHF displays increased wall thickness at ES compared to the assisted hearts with ALHF. It is likely that the functional improvements made to the RV through the introduction of the LVAD are partially offset by negative secondary outcomes on the RV. This is in line with clinical findings, which report positive [266], neutral [267] and negative outcomes [268, 269] on RV function through LVAD use. However, reports of RV failure occurring in 10-30% of patients treated with LVADs [268-272], depending on the severity of RV failure, the characteristics of the study population, and the type of LVAD—suggests that the balance between positive and negative outcomes on the RV is often missed. Although our simulated results showed that stresses in the LV were normalized through LVAD use, RV stresses were not as easily recovered. The quantification and monitoring of RV stress may play a critical role in optimizing LVAD treatment to avoid RV dysfunction.

This is the fourth study utilizing the LHM and the first to include length-dependent activation in simulating the contractile behaviour of the heart in systole. To the best of our knowledge, this is also the first computational LVAD study that utilizes a four-chamber anatomical description of the heart. This allowed us to capture the mechanical changes in the ventricles due to reduced LV contractility with and without assistance. The return to normal values for stroke volumes and ejection fractions in both ventricles supports the position that partial LVADs may provide significant benefit for patients

with ALHF [7, 264]. This position was further supported by a strain and stress analysis, showing the reduction of stress in the LV and a qualitative return to shape through the influence of partial LVADs.

The ability to accurately account for and predict changes to the myofibre stress in the heart could significantly aid clinical decision making and therapy optimization for patients undergoing LVAD treatment, whereby stress-driven adverse remodelling could be mitigated or even reversed [273]. Realistic, physics-based computational modelling offers a potential means to tailor treatments in a patient-specific framework. The modelling presented in this study could be advanced by including patient-specific data and utilized in clinical decision-making for patients who may benefit from partial, instead of full, LV support.

Although the LHM exemplifies state-of-the-art modelling techniques in cardiovascular computational modelling, limitations still apply [167]. The functional improvements seen in the LHM model with ALHF treated with a partial LVAD are in part facilitated by the idealized *in silico* description of cardiac tissue, modelled here as purely elastic, and as such, the changes in deformation between healthy and ALHF are inherently more recoverable than such changes would be in a chronically remodelled failing heart. Here, the heart topology was unaltered from the normal heart and ALHF was induced by lowering the contractility in the LV only. In this sense, adverse remodelling due to chronic LHF and reverse remodelling due to the partial LVAD were neglected. The model can be improved by enriching the kinematic and constitutive models to include growth modelling to account for chronic remodelling and reverse remodelling phenomena [209]. Future improvements to coupled fluid structure interactions and patient-specific features would provide a broader and increasingly reliable set of model predictions. Furthermore, our simulated LVAD flow was created using unchanging constant flow specifications, whereas real-life LVADs perform according to motor function and pressure gradients. As such, our simulated LVAD flow is insensitive to mean arterial pressure (afterload), which would induce fluctuations in flow-rate performance. A description of LVAD flow rate sensitive to afterload would also provide another level of sophistication to the model.

5.5 Conclusions

We used this improved LHM to simulate ALHF through the overall reduction in contractility of the LV and simulated the use of a partial-support LVAD on that heart. Our simulations strongly suggest that an LVAD is effective in normalizing LV stresses but not RV stresses that become elevated as a result of ALHF.

Chapter 6 Conclusions

The major aim of this research was to develop subject-specific computational cardiac models that simulate mechanical ventricular function that can be used to investigate mechanically motivated treatments for heart failure. In order to achieve this, biomaterial injection therapy and partial left ventricular assistance were investigated as potential therapies for ischemic and acute heart failure respectively. Objectives were defined to structure the research in a manner best fit to achieve the aforementioned aim. For convenience, these objectives are repeated below:

1. To develop computational models to simulate the mechanical environment in the failing heart.
    a. To establish subject-specific geometries for healthy, failing and treated hearts, suitable for finite element modelling.
    b. To establish physiologically meaningful three-dimensional (3D) descriptions of myofibre orientation to be utilized in healthy, failing and treated hearts. Investigating the spatial distribution and dispersion/reorientation of fibres in regions of the heart injected with biomaterials and utilize this geometric information in computational models.
    c. To establish constitutive models for the healthy and diseased myocardial tissue and the injectable biomaterials. Calibrate subject-specific models utilizing *in vivo* clinical data.
    d. To computationally simulate the ventricular biomechanics of healthy hearts, failing and mechanically treated hearts using biomaterial injection therapy and partial left ventricular assistance devices.
2. To demonstrate the feasibility of the developed methods and models for the computational investigation of subject-specific efficacy of intra-myocardial biomaterial injectate therapies towards clinical prognostic treatment guides.
    a. To determine the extent of fibre reorientation caused by biomaterial injection therapy and to investigate its impact on cardiac function and wall mechanics.

b. To assess therapy efficacy using computational subject-specific model results. Analysing cardiac performance parameters and biomechanical metrics of stress and strain in the myocardial wall, in particular in the infarct region and functional border zone, is expected to provide further insight into therapeutic mechanisms.

3. To assess the therapeutic efficacy of partial left ventricular assistance devices in the treatment of acute left heart failure.
    a. To assess the biomechanical metrics of stress and strain in the left and right ventricle in the healthy, failing and treated heart in order to determine if partial (i.e. low flow rate) left ventricular assistance devices (LVADs) can normalize ventricular stress and function.

This chapter will summarise the major findings of the research, linking them to the fulfilment of these objectives and highlight the novel aspects of the research. The chapter concludes with an acknowledgement of any potential shortcomings and recommendations for ways to extend this research for future work.

6.1 Summary and concluding remarks

6.1.1 The development of computational models to simulate subject-specific healthy, failing and treated hearts.

Subject-specific biventricular models incorporating precise geometric features and myofibre orientations were constructed for healthy and failing porcine hearts. The latter included subject-specific representations of infarcted tissue and solidified biomaterial injectates (where applicable). These developments fulfilled objectives 1a and 1b and introduced the first novel aspects of this research. Specifically, this is the first study of cardiac mechanics to introduce finite element models containing both subject-specific descriptions of infarction and myofibre orientations. Furthermore, the precise segmentation and description of the alginate biomaterial within failing hearts is an additionally novelty. This allowed us to provide detailed descriptions on the solidified biomaterial morphology in addition to our mechanical analysis.

Existing constitutive laws suitable for modelling heart tissue were used and extended to incorporate a description of pathological tissue based on homogenization of material properties dependant on volume fractions of healthy and infarcted tissue. Material parameter characterization incorporated *ex vivo* shear data to identify tissue anisotropy and subjects specific *in vivo* data to personalize the

material parameters for each subject. This enabled the constitutive laws to be calibrated to include orthotropic material properties capable of matching subject-specific heart function during diastolic and systolic stages of the cardiac cycle, achieving objective 1c.

A lumped parameter model of the circulatory system was coupled to the finite element (FE) model of the beating heart, allowing for multiple cardiac cycles enacting in a closed-loop system of fluid exchanges to be simulated. This produces converged simulations, with FE model predictions of cardiac output and function that accurately matches *in vivo* measurements.

Model validation used independent *in vivo* recorded endocardial echocardiogram strain data. Global echocardiogram strains, the only consistent and reliable measure extractable from this imaging modality, compared well with subject-specific FE model predictions. The use of *in vivo* regional strains for comparison was unreliable overall. The difference in endocardial resolution and segmentation between the FE models and echocardiography measured strains further complicates comparison. Even with these difficulties, some FE models of healthy and failing hearts presented with regional strains that matched closely with measured *in vivo* values and physiological expectations..

An investigation of partial left ventricular assistance as a therapy for acute left heart failure (ALHF) was also introduced using the Living Heart Model™. Modifications to the model to account for length-dependant active tension effects, pathology and simulated inclusion of a partial left ventricular assistance device (LVAD) were introduced to study subject-specific outcomes due to heart-failure and LVAD therapy.

These developments summarised in the above paragraphs collectively fulfilled objective 1d. This is the first study to present validated cardiac models that incorporate *fully* subject-specific features capable of matching *in vivo* measured output and function.

6.1.2 Demonstrating the feasibility of the developed methods as a modality to aid clinical decision making for mechanically motivated therapies

Both Algisyl-LVR™ and partial LVAD therapy are promising treatments for subjects with heart failure. The study of their mechanical effect on failing hearts using subject-specific computational models allowed for diverse and otherwise unobtainable data to be collected and analysed. This provided substantial new information that uncovered the underlying mechanisms of action of these treatments.

Our analysis of the *ex vivo* imaging data revealed that myofibre orientation was affected by heart failure, while the alginate injectates had no apparent impact. Furthermore, by quantifying unloaded LV geometries and the myofibre tractography surrounding the injectates, we revealed that Algisyl-LVR™ injections predominantly displace tissue longitudinally in the myocardial wall. We also quantified the injectate morphology, orientation and retention: data which is critical to any computational modelling efforts that wish to simulate an *in silico* inclusion of biomaterial injection therapy in heart models. These detailed and precise findings are the first to be reported for alginate biomaterial injected within myocardium and successfully fulfilled objective 2a.

Studying fully subject-specific FE model predictions of multiple healthy and failing porcine hearts (with and without biomaterial injection therapy) allowed the mechanical outcomes associated with treatment to be quantified and revealed. Our results showed that alginate injectates lowered stress within the heart, both globally (due to better functional outcomes) and locally (due to tissue-gel interactions). This local effect was caused by underlying reductions in strain of the tissue surrounding the alginate injectates, effective up to 10mm from the injectate surfaces. As both the majority of infarcted tissue and the alginate injectates resided in the LV free wall, this resulted in lower stresses in the infarcted tissue and surrounding border-zone of treated subjects compared to their untreated counterparts. These findings are only accessible due to our novel and highly detailed geometric description of the solidified biomaterial injectates and infarcted tissue. Additionally, these findings and the insights they provide into the working mechanisms of alginate injection therapy are critical for the clinical development of this emerging treatment (objective 2b).

Heart failure treated with alginate injection therapy resulted in hearts that were less dilated when unloaded, more compliant under passive loading and more contractile during systolic performance than non-treated hearts. Improvement was also seen in systolic performance, which leads to better cardiac output such as ejection fraction and stroke volume seen in the treated subjects.

Not only is our study unique in terms of the degree of subject-specificity introduced in each model, but also in the scale of the study. To the best of our knowledge this is the largest (n=9) computational study to investigate biventricular heart mechanics through the cardiac cycle.

FE simulations of the same human heart under healthy, ALHF and ALHF with partial assistance were also investigated. Our study showed that the introduction of a partial LVAD was sufficient to mechanically unload the failing heart, restoring ventricular outputs and relieving pathological stresses in the left ventricle caused by the onset of ALHF (objective 3a). However, right ventricular stresses remained elevated. These results offer an explanation for the development of right ventricular failure following LVAD use, a condition that develops in 10-30% of patients treated with LVADs [268-272].

Comparing outcomes between the therapies assists in understanding the underlying mechanism of action in each case. For example, the application of Algisyl-LVR™ in failing pig hearts resulted in improved systolic performance when compared to untreated subjects. This improvement is likely due to the injection therapy slowing down, stopping or even reversing the adverse remodelling process, enabling the treated hearts to pump more effectively than their untreated counterparts. This difference in systolic performance is similar to the differences seen in the ALHF subject with and without mechanical ventricular assistance. This indicates that the global improvements seen in ventricular stress of Algisyl-LVR™ treated subjects is aided by retaining systolic performance.

6.1.3 Relevance to the clinical setting

As shown in this research, reliable subject-specific models are achievable with the proper inclusion of high quality imaging data. It will become feasible to replicate the quality of our models using purely *in vivo* imaging data as the technology and imaging techniques advance. In particular the data capturing of *in vivo* DT-MRI needs to improve, as these could provide both the geometric and fibre-structural detail to create patient-specific models. Additionally, patient-specific pressures within the major components of the cardiovascular system would also be needed. Ideally a non-invasive method to estimate pressures would be needed to enable the acquisition of this data from the most number of patients.This would enable the ability to investigate potential therapies *in silico* prior their application to patients – with medical decisions, treatment plans and interventions being highly patient-specific.

The application of the developed methods presented in this research could be applied to such models, investigating ideal flow rates for partial LVADS or optimizing the placement of alginate injections to maximize their therapeutic benefit.

6.2 Recommendations for future work

While advanced, the models presented in this research have limitations (detailed at the end of each chapter). To address these and improve the reliability of model outcomes the following suggestions are put forward:

1. **Regarding the modelling of cardiac mechanics:**
    a. The atria, connecting vasculature and pericardium of the heart should be included in the mechanical model of the heart; at the very least to investigate the potential impact they may have in modelling predictions.

b. The constitutive description of cardiac tissue can be further enriched to more accurately portray the properties of physiological tissue. This could include a description of fibre dispersion based on regional metrics acquired from diffusion tensor imaging, multi-scale effects, viscoelastic properties and growth modelling.
c. While echocardiogram imaging is prolific and therefore advantageous, alternative *in vivo* strain data acquisition should be explored for a more reliable source of model validation. In particular, MRI is considered the gold-standard for *in vivo* strain quantification and would provide a better opportunity to validate cardiac models. Methods to determine the reliability of strains derived from echocardiography should also be explored. Also a more sophisticated method of segmentation using echocardiography should be explored to reduce errors due to misalignment.
d. Electrophysiology and its coupling with the mechanical model would further advance the material description and more accurately capture the activation sequence experienced within the beating heart.

2. Regarding the computational study investigating biomaterial injection therapy:

a. More subject-specific models should be considered to increase the statistical impact of the findings.
b. An *in silico* process of applying the biomaterial injection therapy should be explored in order to model the same subject at different longitudinal points of pathology and treatment. This would involve introducing methods to modify a healthy model to simulate pathology and treatment similar to the methods explored in the LVAD study.

3. Regarding the computational study investigating partial LVAD therapy:

a. Additional pathologies such as chronic heart failure should be explored whereby dilated failing heats are treated with partial LVAD support.
b. A more realistic description of the LVAD flow accounting for changing pressure-gradients between the LV and the systemic circuit should be investigated.

References

1. Finegold, J.A., P. Asaria and D.P. Francis, *Mortality from ischaemic heart disease by country, region, and age: statistics from World Health Organisation and United Nations.* Int J Cardiol, 2013. **168**(2): p. 934-45.
2. Steyn, K., *Heart Disease in South Africa: Media Data Document*, J.M. Fourie, Editor. 2007, Heart and Stroke Foundation South Africa: Tygerberg. p. 29.
3. Heidenreich, P.A., N.M. Albert, L.A. Allen, D.A. Bluemke, J. Butler, G.C. Fonarow, J.S. Ikonomidis, O. Khavjou, M.A. Konstam, T.M. Maddox, G. Nichol, M. Pham, I.L. Pina, J.G. Trogdon, C. American Heart Association Advocacy Coordinating, T. Council on Arteriosclerosis, B. Vascular, R. Council on Cardiovascular, Intervention, C. Council on Clinical, E. Council on, Prevention and C. Stroke, *Forecasting the impact of heart failure in the United States: a policy statement from the American Heart Association.* Circ Heart Fail, 2013. **6**(3): p. 606-19.
4. Birks, E.J., P.D. Tansley, J. Hardy, R.S. George, C.T. Bowles, M. Burke, N.R. Banner, A. Khaghani and M.H. Yacoub, *Left ventricular assist device and drug therapy for the reversal of heart failure.* N Engl J Med, 2006. **355**(18): p. 1873-84.
5. Burkhoff, D., S. Klotz and D.M. Mancini, *LVAD-induced reverse remodeling: basic and clinical implications for myocardial recovery.* Journal of cardiac failure, 2006. **12**(3): p. 227-239.
6. Wohlschlaeger, J., K.J. Schmitz, C. Schmid, K.W. Schmid, P. Keul, A. Takeda, S. Weis, B. Levkau and H.A. Baba, *Reverse remodeling following insertion of left ventricular assist devices (LVAD): a review of the morphological and molecular changes.* Cardiovascular research, 2005. **68**(3): p. 376-386.
7. Sabashnikov, A., A.F. Popov, C.T. Bowles, P.N. Mohite, A. Weymann, R. Hards, M. Hedger, T. Wittwer, J. Wippermann, T. Wahlers, F.A. Schoendube and A.R. Simon, *Outcomes after implantation of partial-support left ventricular assist devices in inotropic-dependent patients: Do we still need full-support assist devices?* J Thorac Cardiovasc Surg, 2014. **148**(3): p. 1115-21.
8. Mohite, P.N., A. Sabashnikov, A.R. Simon, A. Weymann, N.P. Patil, B. Unsoeld, C. Bireta and A.F. Popov, *Does CircuLite Synergy assist device as partial ventricular support have a place in modern management of advanced heart failure?* Expert review of medical devices, 2014. **12**(1): p. 49-60.
9. Lampropulos, J.F., N. Kim, Y. Wang, M.M. Desai, J.A. Barreto-Filho, J.A. Dodson, D.L. Dries, A.A. Mangi and H.M. Krumholz, *Trends in left ventricular assist device*

use and outcomes among Medicare beneficiaries, 2004-2011. Open Heart, 2014. **1**(1): p. e000109.

10. Topkara, V.K., A.R. Garan, B. Fine, A.F. Godier-Furnémont, A. Breskin, B. Cagliostro, M. Yuzefpolskaya, K. Takeda, H. Takayama and D.M. Mancini, *Myocardial Recovery in Patients Receiving Contemporary Left Ventricular Assist DevicesCLINICAL PERSPECTIVE.* Circulation: Heart Failure, 2016. **9**(7): p. e003157.
11. Kadner, K., S. Dobner, T. Franz, D. Bezuidenhout, M.S. Sirry, P. Zilla and N.H. Davies, *The beneficial effects of deferred delivery on the efficiency of hydrogel therapy post myocardial infarction.* Biomaterials, 2012. **33**(7): p. 2060-2066.
12. Sabbah, H.N., M. Wang, R.C. Gupta, S. Rastogi, I. Ilsar, M.S. Sabbah, S. Kohli, S. Helgerson and R.J. Lee, *Augmentation of left ventricular wall thickness with alginate hydrogel implants improves left ventricular function and prevents progressive remodeling in dogs with chronic heart failure.* JACC: Heart Failure, 2013. **1**(3): p. 252-258.
13. Leor, J., S. Tuvia, V. Guetta, F. Manczur, D. Castel, U. Willenz, Ö. Petneházy, N. Landa, M.S. Feinberg and E. Konen, *Intracoronary injection of in situ forming alginate hydrogel reverses left ventricular remodeling after myocardial infarction in Swine.* Journal of the American College of Cardiology, 2009. **54**(11): p. 1014-1023.
14. Segers, V.F. and R.T. Lee, *Biomaterials to enhance stem cell function in the heart.* Circ Res, 2011. **109**(8): p. 910-22.
15. WHO, *Global status report on noncommunicable diseases 2010: Description of the global burden of NCDs, their risk factors and determinants.* 2011, World Health Organization: Geneva. p. 176.
16. Mathers, C.D. and D. Loncar, *Projections of global mortality and burden of disease from 2002 to 2030.* PLoS Med, 2006. **3**(11): p. e442.
17. Trayanova, N.A., *Whole-Heart Modeling: Applications to Cardiac Electrophysiology and Electromechanics.* Circ Res, 2011. **108**(1): p. 113-128.
18. Meier, G., R. Besson, A. Nanz, S. Safai and A.J. Lomax, *Independent dose calculations for commissioning, quality assurance and dose reconstruction of PBS proton therapy.* Phys Med Biol, 2015. **60**(7): p. 2819-2836.
19. Balasso, A., J.S. Bauer, T. Liebig, F. Dorn, C. Zimmer, D. Liepsch and S. Prothmann, *Evaluation of intra-aneurysmal hemodynamics after flow diverter placement in a patient-specific aneurysm model.* Biorheology, 2015. **51**(6): p. 341-354.
20. Goyal, N. and S.D. Stulberg, *Evaluating the Precision of Preoperative Planning in Patient Specific Instrumentation: Can a Single MRI Yield Different Preoperative Plans?* J Arthroplasty, 2015. **30**(7): p. 1250-1253.
21. Arts, T., R.S. Reneman and P.C. Veenstra, *A model of the mechanics of the left ventricle.* Ann Biomed Eng, 1979. **7**(3-4): p. 299-318.
22. Streeter, D.D., Jr. and W.T. Hanna, *Engineering mechanics for successive states in canine left ventricular myocardium. II. Fiber angle and sarcomere length.* Circ Res, 1973. **33**(6): p. 656-64.

23. Janz, R.F. and A.F. Grimm, *Finite-element model for the mechanical behavior of the left ventricle. Prediction of deformation in the potassium-arrested rat heart.* Circ Res, 1972. **30**(2): p. 244-52.

24. Okajima, M., T. Fujino, T. Kobayashi and K. Yamada, *Computer simulation of the propagation process in excitation of the ventricles.* Circulation research, 1968. **23**(2): p. 203-211.

25. Wei, D., *Whole-heart modeling: progress, principles and applications.* Prog Biophys Mol Biol, 1997. **67**(1): p. 17-66.

26. Nielsen, P.M., I.J. Le Grice, B.H. Smaill and P.J. Hunter, *Mathematical model of geometry and fibrous structure of the heart.* Am J Physiol, 1991. **260**(4 Pt 2): p. H1365-78.

27. Stevens, C., E. Remme, I. LeGrice and P. Hunter, *Ventricular mechanics in diastole: material parameter sensitivity.* Journal of Biomechanics, 2003. **36**(5): p. 737-748.

28. Baillargeon, B., N. Rebelo, D.D. Fox, R.L. Taylor and E. Kuhl, *The Living Heart Project: A robust and integrative simulator for human heart function.* Eur J Mech A Solids, 2014. **48**: p. 38-47.

29. Young, A.A. and A.F. Frangi, *Computational cardiac atlases: from patient to population and back.* Exp Physiol, 2009. **94**(5): p. 578-96.

30. Buckberg, G., A. Mahajan, S. Saleh, J.I. Hoffman and C. Coghlan, *Structure and function relationships of the helical ventricular myocardial band.* J Thorac Cardiovasc Surg, 2008. **136**(3): p. 578-89, 589 e1-11.

31. Gilbert, S.H., A.P. Benson, P. Li and A.V. Holden, *Regional localisation of left ventricular sheet structure: integration with current models of cardiac fibre, sheet and band structure.* Eur J Cardiothorac Surg, 2007. **32**(2): p. 231-49.

32. Pope, A.J., G.B. Sands, B.H. Smaill and I.J. LeGrice, *Three-dimensional transmural organization of perimysial collagen in the heart.* Am J Physiol Heart Circ Physiol, 2008. **295**(3): p. H1243-H1252.

33. LeGrice, I., P. Hunter, A. Young and B. Small, *The architecture of the heart: a data-based model.* Philosophical Transactions of the Royal Society of London Series a-Mathematical Physical and Engineering Sciences, 2001. **359**(1783): p. 1217-1232.

34. Lombaert, H., J.M. Peyrat, P. Croisille, S. Rapacchi, L. Fanton, F. Cheriet, P. Clarysse, I. Magnin, H. Delingette and N. Ayache, *Human atlas of the cardiac fiber architecture: study on a healthy population.* IEEE Trans Med Imaging, 2012. **31**(7): p. 1436-47.

35. Wang, H.M., H. Gao, X.Y. Luo, C. Berry, B.E. Griffith, R.W. Ogden and T.J. Wang, *Structure-based finite strain modelling of the human left ventricle in diastole.* Int J Numer Method Biomed Eng, 2013. **29**(1): p. 83-103.

36. Genet, M., L.C. Lee, R. Nguyen, H. Haraldsson, G. Acevedo-Bolton, Z. Zhang, L. Ge, K. Ordovas, S. Kozerke and J.M. Guccione, *Distribution of normal human left ventricular myofiber stress at end-diastole and end-systole-a target for in silico design of heart failure treatments.* Journal of Applied Physiology, 2014. **117**(2): p. 142-152.

37. Wong, J. and E. Kuhl, *Generating fibre orientation maps in human heart models using Poisson interpolation.* Comput Methods Biomech Biomed Engin, 2014. **17**(11): p. 1217-26.

38. Wang, V.Y., H.I. Lam, D.B. Ennis, B.R. Cowan, A.A. Young and M.P. Nash, *Modelling passive diastolic mechanics with quantitative MRI of cardiac structure and function.* Med Image Anal, 2009. **13**(5): p. 773-84.

39. Krishnamurthy, A., C.T. Villongco, J. Chuang, L.R. Frank, V. Nigam, E. Belezzuoli, P. Stark, D.E. Krummen, S. Narayan, J.H. Omens, A.D. McCulloch and R.C. Kerckhoffs, *Patient-Specific Models of Cardiac Biomechanics.* J Comput Phys, 2013. **244**: p. 4-21.

40. Bayer, J.D., R.C. Blake, G. Plank and N.A. Trayanova, *A Novel Rule-Based Algorithm for Assigning Myocardial Fiber Orientation to Computational Heart Models.* Annals of Biomedical Engineering, 2012. **40**(10): p. 2243-2254.

41. Toussaint, N., C.T. Stoeck, T. Schaeffter, S. Kozerke, M. Sermesant and P.G. Batchelor, *In vivo human cardiac fibre architecture estimation using shape-based diffusion tensor processing.* Med Image Anal, 2013. **17**(8): p. 1243-55.

42. Bovendeerd, P.H., T. Arts, J.M. Huyghe, D.H. van Campen and R.S. Reneman, *Dependence of local left ventricular wall mechanics on myocardial fiber orientation: a model study.* J Biomech, 1992. **25**(10): p. 1129-40.

43. Chen, J., W. Liu, H. Zhang, L. Lacy, X. Yang, S.K. Song, S.A. Wickline and X. Yu, *Regional ventricular wall thickening reflects changes in cardiac fiber and sheet structure during contraction: quantification with diffusion tensor MRI.* Am J Physiol Heart Circ Physiol, 2005. **289**(5): p. H1898-907.

44. Sack, K.L., S. Skatulla and C. Sansour, *Biological tissue mechanics with fibres modelled as one-dimensional Cosserat continua. Applications to cardiac tissue.* International Journal of Solids and Structures, 2015.

45. Eriksson, T.S., A.J. Prassl, G. Plank and G.A. Holzapfel, *Modeling the dispersion in electromechanically coupled myocardium.* Int J Numer Method Biomed Eng, 2013. **29**(11): p. 1267-84.

46. McGill, L.-A., P. Ferreira, A.D. Scott, S. Nielles-Vallespin, R. Silva, P.J. Kilner, D. Firmin and D.J. Pennell, *Comparison of cardiac DTI parameters between systole and diastole.* Journal of Cardiovascular Magnetic Resonance, 2014. **16**(S1): p. P39.

47. von Deuster, C., E. Sammut, L. Asner, D. Nordsletten, P. Lamata, C.T. Stoeck, S. Kozerke and R. Razavi, *Studying dynamic myofiber aggregate reorientation in dilated cardiomyopathy using in vivo magnetic resonance diffusion tensor imaging.* Circulation. Cardiovascular Imaging, 2016. **9**(10): p. e005018.

48. Scott, A.D., P.F. Ferreira, S. Nielles-Vallespin, P. Gatehouse, L.A. McGill, P. Kilner, D.J. Pennell and D.N. Firmin, *Optimal diffusion weighting for in vivo cardiac diffusion tensor imaging.* Magnetic resonance in medicine, 2015. **74**(2): p. 420-430.

49. Holzapfel, G.A., T.C. Gasser and R.W. Ogden, *A new constitutive framework for arterial wall mechanics and a comparative study of material models.* Journal of Elasticity, 2000. **61**(1-3): p. 1-48.

50. Humphrey, J.D., *Review Paper: Continuum biomechanics of soft biological tissues.* Proceedings of the Royal Society A: Mathematical, Physical and Engineering Sciences, 2003. **459**(2029): p. 3-46.

51. Sacks, M.S., *Biaxial mechanical evaluation of planar biological materials.* Journal of Elasticity, 2000. **61**(1-3): p. 199-246.

52. Humphrey, J.D. and F.C. Yin, *A new constitutive formulation for characterizing the mechanical behavior of soft tissues.* Biophys J, 1987. **52**(4): p. 563-70.

53. Costa, K.D., J.W. Holmes and A.D. McCulloch, *Modelling cardiac mechanical properties in three dimensions.* Philosophical Transactions of the Royal Society of London Series a-Mathematical Physical and Engineering Sciences, 2001. **359**(1783): p. 1233-1250.

54. Kerckhoffs, R.C., O.P. Faris, P.H. Bovendeerd, F.W. Prinzen, K. Smits, E.R. McVeigh and T. Arts, *Timing of depolarization and contraction in the paced canine left ventricle: model and experiment.* J Cardiovasc Electrophysiol, 2003. **14**(10 Suppl): p. S188-95.

55. Usyk, T. and A. McCulloch, *Computational Methods for Soft Tissue Biomechanics*, in *Biomechanics of Soft Tissue in Cardiovascular Systems*, G. Holzapfel and R. Ogden, Editors. 2003, Springer Vienna. p. 273-342.

56. Holzapfel, G.A. and R.W. Ogden, *Constitutive modelling of passive myocardium: a structurally based framework for material characterization.* Philos Trans A Math Phys Eng Sci, 2009. **367**(1902): p. 3445-75.

57. Goktepe, S., S.N.S. Acharya, J. Wong and E. Kuhl, *Computational modeling of passive myocardium.* International Journal for Numerical Methods in Biomedical Engineering, 2011. **27**(1): p. 1-12.

58. Nikou, A., S.M. Dorsey, J.R. McGarvey, J.H. Gorman, 3rd, J.A. Burdick, J.J. Pilla, R.C. Gorman and J.F. Wenk, *Computational Modeling of Healthy Myocardium in Diastole.* Ann Biomed Eng, 2015.

59. Hunter, P.J. and B.H. Smaill, *The analysis of cardiac function: a continuum approach.* Progress in biophysics and molecular biology, 1988. **52**(2): p. 101-164.

60. Guccione, J.M., L.K. Waldman and A.D. McCulloch, *Mechanics of active contraction in cardiac muscle: Part II--Cylindrical models of the systolic left ventricle.* J Biomech Eng, 1993. **115**(1): p. 82-90.

61. Usyk, T.P., R. Mazhari and A.D. McCulloch, *Effect of laminar orthotropic myofiber architecture on regional stress and strain in the canine left ventricle.* Journal of Elasticity, 2000. **61**(1-3): p. 143-164.

62. Lee, L.C., L. Ge, Z. Zhang, M. Pease, S.D. Nikolic, R. Mishra, M.B. Ratcliffe and J.M. Guccione, *Patient-specific finite element modeling of the Cardiokinetix Parachute((R)) device: effects on left ventricular wall stress and function.* Med Biol Eng Comput, 2014. **52**(6): p. 557-66.

63. Ambrosi, D. and S. Pezzuto, *Active stress vs. active strain in mechanobiology: constitutive issues.* Journal of Elasticity, 2012. **107**(2): p. 199-212.

64. Rossi, S., R. Ruiz-Baier, L.F. Pavarino and A. Quarteroni, *Orthotropic active strain models for the numerical simulation of cardiac biomechanics.* Int J Numer Method Biomed Eng, 2012. **28**(6-7): p. 761-88.

65. Berberoğlu, E., H.O. Solmaz and S. Göktepe, *Computational modeling of coupled cardiac electromechanics incorporating cardiac dysfunctions.* European Journal of Mechanics-A/Solids, 2014. **48**: p. 60-73.

66. Göktepe, S. and E. Kuhl, *Electromechanics of the heart: a unified approach to the strongly coupled excitation–contraction problem.* Computational Mechanics, 2009. **45**(2-3): p. 227-243.

67. Lafortune, P., R. Aris, M. Vazquez and G. Houzeaux, *Coupled electromechanical model of the heart: Parallel finite element formulation.* International Journal for Numerical Methods in Biomedical Engineering, 2012. **28**(1): p. 72-86.

68. Sainte-Marie, J., D. Chapelle, R. Cimrman and M. Sorine, *Modeling and estimation of the cardiac electromechanical activity.* Computers & Structures, 2006. **84**(28): p. 1743-1759.

69. Kerckhoffs, R.C., P.H. Bovendeerd, J.C. Kotte, F.W. Prinzen, K. Smits and T. Arts, *Homogeneity of cardiac contraction despite physiological asynchrony of depolarization: a model study.* Ann Biomed Eng, 2003. **31**(5): p. 536-47.

70. Nordsletten, D.A., S.A. Niederer, M.P. Nash, P.J. Hunter and N.P. Smith, *Coupling multi-physics models to cardiac mechanics.* Prog Biophys Mol Biol, 2011. **104**(1-3): p. 77-88.

71. Niederer, S.A., G. Plank, P. Chinchapatnam, M. Ginks, P. Lamata, K.S. Rhode, C.A. Rinaldi, R. Razavi and N.P. Smith, *Length-dependent tension in the failing heart and the efficacy of cardiac resynchronization therapy.* Cardiovasc Res, 2011. **89**(2): p. 336-43.

72. Rosolen, A.M., S. Ordas, M. Vazquez and A.F. Frangi, *Numerical schemes for the simulation of three-dimensional cardiac electrical propagation in patient-specific ventricular geometries*, in *European Conference on Computational Fluid Dynamics ECCOMAS CFD 2006*, P. Wesseling, E. Onate, and J. Periaux, Editors. 2006.

73. Sun, K., N. Stander, C.S. Jhun, Z. Zhang, T. Suzuki, G.Y. Wang, M. Saeed, A.W. Wallace, E.E. Tseng, A.J. Baker, D. Saloner, D.R. Einstein, M.B. Ratcliffe and J.M. Guccione, *A computationally efficient formal optimization of regional myocardial contractility in a sheep with left ventricular aneurysm.* J Biomech Eng, 2009. **131**(11): p. 111001.

74. Demer, L.L. and F.C. Yin, *Passive biaxial mechanical properties of isolated canine myocardium.* J Physiol, 1983. **339**: p. 615-30.

75. Dokos, S., B.H. Smaill, A.A. Young and I.J. LeGrice, *Shear properties of passive ventricular myocardium.* Am J Physiol Heart Circ Physiol, 2002. **283**(6): p. H2650-9.

76. Remme, E.W., P.J. Hunter, O. Smiseth, C. Stevens, S.I. Rabben, H. Skulstad and B.B. Angelsen, *Development of an in vivo method for determining material properties of passive myocardium.* J Biomech, 2004. **37**(5): p. 669-78.

77. Zervantonakis, I.K., S.D. Fung-Kee-Fung, W.N. Lee and E.E. Konofagou, *A novel, view-independent method for strain mapping in myocardial elastography: eliminating angle and centroid dependence.* Phys Med Biol, 2007. **52**(14): p. 4063-80.

78. Xi, J., P. Lamata, S. Niederer, S. Land, W. Shi, X. Zhuang, S. Ourselin, S.G. Duckett, A.K. Shetty, C.A. Rinaldi, D. Rueckert, R. Razavi and N.P. Smith, *The estimation of patient-specific cardiac diastolic functions from clinical measurements.* Med Image Anal, 2013. **17**(2): p. 133-46.

79. Sermesant, M., P. Moireau, O. Camara, J. Sainte-Marie, R. Andriantsimiavona, R. Cimrman, D.L.G. Hill, D. Chapelle and R. Razavi, *Cardiac function estimation from MRI using a heart model and data assimilation: advances and difficulties.* Medical Image Analysis, 2006. **10**(4): p. 642-656.

80. Lee, W.N., C.M. Ingrassia, S.D. Fung-Kee-Fung, K.D. Costa, J.W. Holmes and E.E. Konofagou, *Theoretical quality assessment of myocardial elastography with in vivo validation.* IEEE Trans Ultrason Ferroelectr Freq Control, 2007. **54**(11): p. 2233-45.

81. Mojsejenko, D., J.R. McGarvey, S.M. Dorsey, J.H. Gorman, 3rd, J.A. Burdick, J.J. Pilla, R.C. Gorman and J.F. Wenk, *Estimating passive mechanical properties in a myocardial infarction using MRI and finite element simulations.* Biomech Model Mechanobiol, 2015. **14**(3): p. 633-47.

82. McGarvey, J.R., D. Mojsejenko, S.M. Dorsey, A. Nikou, J.A. Burdick, J.H. Gorman, III, B.M. Jackson, J.J. Pilla, R.C. Gorman and J.F. Wenk, *Temporal Changes in Infarct Material Properties: An In Vivo Assessment Using Magnetic Resonance Imaging and Finite Element Simulations.* Annals of Thoracic Surgery, 2015. **100**(2): p. 582-590.

83. Ahern, R.M., R. Lozano, M. Naghavi, K. Foreman, E. Gakidou and C.J. Murray, *Improving the public health utility of global cardiovascular mortality data: the rise of ischemic heart disease.* Population health metrics, 2011. **9**(1): p. 8.

84. Forouzanfar, M.H., A.E. Moran, A.D. Flaxman, G. Roth, G.A. Mensah, M. Ezzati, M. Naghavi and C.J. Murray, *Assessing the global burden of ischemic heart disease: part 2: analytic methods and estimates of the global epidemiology of ischemic heart disease in 2010.* Global Heart, 2012. **7**(4): p. 331-342.

85. Holmes, J.W., T.K. Borg and J.W. Covell, *Structure and mechanics of healing myocardial infarcts.* Annu Rev Biomed Eng, 2005. **7**: p. 223-53.

86. Fomovsky, G.M. and J.W. Holmes, *Evolution of scar structure, mechanics, and ventricular function after myocardial infarction in the rat.* Am J Physiol Heart Circ Physiol, 2010. **298**(1): p. H221-8.

87. Dorri, F., P.F. Niederer and P.P. Lunkenheimer, *A finite element model of the human left ventricular systole.* Comput Methods Biomech Biomed Engin, 2006. **9**(5): p. 319-41.

88. Zhang, Z., A. Tendulkar, K. Sun, D.A. Saloner, A.W. Wallace, L. Ge, J.M. Guccione and M.B. Ratcliffe, *Comparison of the Young-Laplace law and finite element based calculation of ventricular wall stress: implications for postinfarct and surgical ventricular remodeling.* Ann Thorac Surg, 2011. **91**(1): p. 150-6.

89. Shimkunas, R., Z. Zhang, J.F. Wenk, M. Soleimani, M. Khazalpour, G. Acevedo-Bolton, G. Wang, D. Saloner, R. Mishra and A.W. Wallace, *Left ventricular myocardial contractility is depressed in the borderzone after posterolateral myocardial infarction.* Annals of Thoracic Surgery, 2013. **95**(5): p. 1619-1625.

90. Wenk, J.F., P. Eslami, Z. Zhang, C. Xu, E. Kuhl, J.H. Gorman, 3rd, J.D. Robb, M.B. Ratcliffe, R.C. Gorman and J.M. Guccione, *A novel method for quantifying the in-vivo mechanical effect of material injected into a myocardial infarction.* Ann Thorac Surg, 2011. **92**(3): p. 935-41.

91. Bogen, D.K., S.A. Rabinowitz, A. Needleman, T.A. McMahon and W.H. Abelmann, *An analysis of the mechanical disadvantage of myocardial infarction in the canine left ventricle.* Circ Res, 1980. **47**(5): p. 728-41.

92. Mazhari, R., J.H. Omens, J.W. Covell and A.D. McCulloch, *Structural basis of regional dysfunction in acutely ischemic myocardium.* Cardiovasc Res, 2000. **47**(2): p. 284-93.

93. Guccione, J.M., S.M. Moonly, P. Moustakidis, K.D. Costa, M.J. Moulton, M.B. Ratcliffe and M.K. Pasque, *Mechanism underlying mechanical dysfunction in the border zone of left ventricular aneurysm: a finite element model study.* Ann Thorac Surg, 2001. **71**(2): p. 654-62.

94. Kerckhoffs, R.C., M.L. Neal, Q. Gu, J.B. Bassingthwaighte, J.H. Omens and A.D. McCulloch, *Coupling of a 3D finite element model of cardiac ventricular mechanics to lumped systems models of the systemic and pulmonic circulation.* Ann Biomed Eng, 2007. **35**(1): p. 1-18.

95. Aikawa, Y., L. Rohde, J. Plehn, S.C. Greaves, F. Menapace, M.O. Arnold, J.L. Rouleau, M.A. Pfeffer, R.T. Lee and S.D. Solomon, *Regional wall stress predicts ventricular remodeling after anteroseptal myocardial infarction in the Healing and Early Afterload Reducing Trial (HEART): an echocardiography-based structural analysis.* Am Heart J, 2001. **141**(2): p. 234-42.

96. Lee, L.C., S.T. Wall, D. Klepach, L. Ge, Z. Zhang, R.J. Lee, A. Hinson, J.H. Gorman, 3rd, R.C. Gorman and J.M. Guccione, *Algisyl-LVR with coronary artery bypass grafting reduces left ventricular wall stress and improves function in the failing human heart.* Int J Cardiol, 2013. **168**(3): p. 2022-8.

97. Ratcliffe, M.B., J. Hong, A. Salahieh, S. Ruch and A.W. Wallace, *The effect of ventricular volume reduction surgery in the dilated, poorly contractile left ventricle: a simple finite element analysis.* J Thorac Cardiovasc Surg, 1998. **116**(4): p. 566-77.

98. Dang, A.B., J.M. Guccione, P. Zhang, A.W. Wallace, R.C. Gorman, J.H. Gorman, 3rd and M.B. Ratcliffe, *Effect of ventricular size and patch stiffness in surgical anterior ventricular restoration: a finite element model study.* Ann Thorac Surg, 2005. **79**(1): p. 185-93.

99. Lee, L.C., J.F. Wenk, L. Zhong, D. Klepach, Z. Zhang, L. Ge, M.B. Ratcliffe, T.I. Zohdi, E. Hsu, J.L. Navia, G.S. Kassab and J.M. Guccione, *Analysis of patient-specific surgical ventricular restoration: importance of an ellipsoidal left ventricular geometry for diastolic and systolic function.* J Appl Physiol (1985), 2013. **115**(1): p. 136-44.

100. Zhong, L., Y. Su, L. Gobeawan, S. Sola, R.S. Tan, J.L. Navia, D.N. Ghista, T. Chua, J. Guccione and G.S. Kassab, *Impact of surgical ventricular restoration on ventricular shape, wall stress, and function in heart failure patients.* Am J Physiol Heart Circ Physiol, 2011. **300**(5): p. H1653-60.

101. Athanasuleas, C.L., A.W. Stanley, Jr., G.D. Buckberg, V. Dor, M. DiDonato and E.H. Blackstone, *Surgical anterior ventricular endocardial restoration (SAVER) in the dilated remodeled ventricle after anterior myocardial infarction. RESTORE group. Reconstructive Endoventricular Surgery, returning Torsion Original Radius Elliptical Shape to the LV.* J Am Coll Cardiol, 2001. **37**(5): p. 1199-209.

102. Guccione, J.M., A. Salahieh, S.M. Moonly, J. Kortsmit, A.W. Wallace and M.B. Ratcliffe, *Myosplint decreases wall stress without depressing function in the failing heart: a finite element model study.* Ann Thorac Surg, 2003. **76**(4): p. 1171-80; discussion 1180.

103. Wenk, J.F., L. Ge, Z. Zhang, D. Mojsejenko, D.D. Potter, E.E. Tseng, J.M. Guccione and M.B. Ratcliffe, *Biventricular finite element modeling of the Acorn CorCap Cardiac Support Device on a failing heart.* Ann Thorac Surg, 2013. **95**(6): p. 2022-7.

104. Mazzaferri, E.L., Jr., S. Gradinac, D. Sagic, P. Otasevic, A.K. Hasan, T.L. Goff, H. Sievert, N. Wunderlich, S.D. Nikolic and W.T. Abraham, *Percutaneous left ventricular partitioning in patients with chronic heart failure and a prior anterior myocardial infarction: Results of the PercutAneous Ventricular RestorAtion in Chronic Heart failUre PaTiEnts Trial.* Am Heart J, 2012. **163**(5): p. 812-820 e1.

105. Rim, Y., D.D. McPherson and H. Kim, *Mitral valve function following ischemic cardiomyopathy: a biomechanical perspective.* Biomed Mater Eng, 2014. **24**(1): p. 7-13.

106. Wong, V.M., J.F. Wenk, Z. Zhang, G. Cheng, G. Acevedo-Bolton, M. Burger, D.A. Saloner, A.W. Wallace, J.M. Guccione, M.B. Ratcliffe and L. Ge, *The effect of mitral annuloplasty shape in ischemic mitral regurgitation: a finite element simulation.* Ann Thorac Surg, 2012. **93**(3): p. 776-82.

107. Carrick, R., L. Ge, L.C. Lee, Z. Zhang, R. Mishra, L. Axel, J.M. Guccione, E.A. Grossi and M.B. Ratcliffe, *Patient-specific finite element-based analysis of ventricular myofiber stress after Coapsys: importance of residual stress.* Ann Thorac Surg, 2012. **93**(6): p. 1964-71.

108. Wenk, J.F., Z. Zhang, G. Cheng, D. Malhotra, G. Acevedo-Bolton, M. Burger, T. Suzuki, D.A. Saloner, A.W. Wallace, J.M. Guccione and M.B. Ratcliffe, *First finite element model of the left ventricle with mitral valve: insights into ischemic mitral regurgitation.* Ann Thorac Surg, 2010. **89**(5): p. 1546-53.

109. Atkins, B.Z., M.T. Hueman, J. Meuchel, K.A. Hutcheson, D.D. Glower and D.A. Taylor, *Cellular cardiomyoplasty improves diastolic properties of injured heart.* J Surg Res, 1999. **85**(2): p. 234-42.

110. Christman, K.L., H.H. Fok, R.E. Sievers, Q. Fang and R.J. Lee, *Fibrin glue alone and skeletal myoblasts in a fibrin scaffold preserve cardiac function after myocardial infarction.* Tissue Eng, 2004. **10**(3-4): p. 403-9.

111. Landa, N., L. Miller, M.S. Feinberg, R. Holbova, M. Shachar, I. Freeman, S. Cohen and J. Leor, *Effect of injectable alginate implant on cardiac remodeling and function after recent and old infarcts in rat.* Circulation, 2008. **117**(11): p. 1388-96.

112. Plotkin, M., S.R. Vaibavi, A.J. Rufaihah, V. Nithya, J. Wang, Y. Shachaf, T. Kofidis and D. Seliktar, *The effect of matrix stiffness of injectable hydrogels on the preservation of cardiac function after a heart attack.* Biomaterials, 2014. **35**(5): p. 1429-38.

113. Dobner, S., D. Bezuidenhout, P. Govender, P. Zilla and N. Davies, *A Synthetic Non-degradable Polyethylene Glycol Hydrogel Retards Adverse Post-infarct Left Ventricular Remodeling.* Journal of Cardiac Failure, 2009. **15**(7): p. 629-636.

114. Dorsey, S.M., J.R. McGarvey, H. Wang, A. Nikou, L. Arama, K.J. Koomalsingh, N. Kondo, J.H. Gorman, III, J.J. Pilla, R.C. Gorman, J.F. Wenk and J.A. Burdick, *MRI evaluation of injectable hyaluronic acid-based hydrogel therapy to limit ventricular remodeling after myocardial infarction.* Biomaterials, 2015. **69**: p. 65-75.

115. Nelson, D.M., Z. Ma, K.L. Fujimoto, R. Hashizume and W.R. Wagner, *Intra-myocardial biomaterial injection therapy in the treatment of heart failure: Materials, outcomes and challenges.* Acta Biomater, 2011. **7**(1): p. 1-15.

116. Johnson, T.D. and K.L. Christman, *Injectable hydrogel therapies and their delivery strategies for treating myocardial infarction.* Expert Opin Drug Deliv, 2013. **10**(1): p. 59-72.

117. Wall, S.T., J.C. Walker, K.E. Healy, M.B. Ratcliffe and J.M. Guccione, *Theoretical impact of the injection of material into the myocardium - A finite element model simulation.* Circulation, 2006. **114**(24): p. 2627-2635.

118. Legner, D., S. Skatulla, M.B. J, R.R. Rama, B.D. Reddy, C. Sansour, N.H. Davies and T. Franz, *Studying the influence of hydrogel injections into the infarcted left ventricle using the element-free Galerkin method.* Int J Numer Method Biomed Eng, 2014. **30**(3): p. 416-29.

119. Ifkovits, J.L., E. Tous, M. Minakawa, M. Morita, J.D. Robb, K.J. Koomalsingh, J.H. Gorman, R.C. Gorman and J.A. Burdick, *Injectable hydrogel properties influence infarct expansion and extent of postinfarction left ventricular remodeling in an ovine model.* Proceedings of the National Academy of Sciences, 2010. **107**(25): p. 11507-11512.

120. Kichula, E.T., H. Wang, S.M. Dorsey, S.E. Szczesny, D.M. Elliott, J.A. Burdick and J.F. Wenk, *Experimental and computational investigation of altered mechanical properties in myocardium after hydrogel injection.* Ann Biomed Eng, 2014. **42**(7): p. 1546-56.

121. Wenk, J.F., S.T. Wall, R.C. Peterson, S.L. Helgerson, H.N. Sabbah, M. Burger, N. Stander, M.B. Ratcliffe and J.M. Guccione, *A method for automatically optimizing medical devices for treating heart failure: designing polymeric injection patterns.* J Biomech Eng, 2009. **131**(12): p. 121011.

122. Miller, R., N.H. Davies, J. Kortsmit, P. Zilla and T. Franz, *Outcomes of myocardial infarction hydrogel injection therapy in the human left ventricle dependent on*

injectate distribution. International Journal for Numerical Methods in Biomedical Engineering, 2013. **29**(8): p. 870-884.

123. Kortsmit, J., N.H. Davies, R. Miller, P. Zilla and T. Franz, *Computational predictions of improved of wall mechanics and function of the infarcted left ventricle at early and late remodelling stages: comparison of layered and bulk hydrogel injectates.* Advances in Biomechanics and Applications, 2013. **1**(1): p. 41-55.

124. Kortsmit, J., N.H. Davies, R. Miller, J.R. Macadangdang, P. Zilla and T. Franz, *The effect of hydrogel injection on cardiac function and myocardial mechanics in a computational post-infarction model.* Computer Methods in Biomechanics and Biomedical Engineering, 2013. **16**(11): p. 1185-1195.

125. Sirry, M.S., N.H. Davies, K. Kadner, L. Dubuis, M.G. Saleh, E.M. Meintjes, B.S. Spottiswoode, P. Zilla and T. Franz, *Micro-structurally detailed model of a therapeutic hydrogel injectate in a rat biventricular cardiac geometry for computational simulations.* Comput Methods Biomech Biomed Engin, 2015. **18**(3): p. 325-31.

126. Lee, L.C., S.T. Wall, M. Genet, A. Hinson and J.M. Guccione, *Bioinjection treatment: effects of post-injection residual stress on left ventricular wall stress.* J Biomech, 2014. **47**(12): p. 3115-9.

127. Lee, R.J., A. Hinson, S. Helgerson, R. Bauernschmitt and H.N. Sabbah, *Polymer-based restoration of left ventricular mechanics.* Cell Transplant, 2013. **22**(3): p. 529-33.

128. Kirklin, J.K., D.C. Naftel, F.D. Pagani, R.L. Kormos, S. Myers, M.A. Acker, J. Rogers, M.S. Slaughter and L.W. Stevenson, *Pump thrombosis in the Thoratec HeartMate II device: an update analysis of the INTERMACS Registry.* The Journal of Heart and Lung Transplantation, 2015. **34**(12): p. 1515-1526.

129. Levin, H.R., M.C. Oz, J.M. Chen, M. Packer, E.A. Rose and D. Burkhoff, *Reversal of chronic ventricular dilation in patients with end-stage cardiomyopathy by prolonged mechanical unloading.* Circulation, 1995. **91**(11): p. 2717-2720.

130. Vollkron, M., H. Schima, L. Huber and G. Wieselthaler, *Interaction of the cardiovascular system with an implanted rotary assist device: simulation study with a refined computer model.* Artificial organs, 2002. **26**(4): p. 349-359.

131. Morley, D., K. Litwak, P. Ferber, P. Spence, R. Dowling, B. Meyns, B. Griffith and D. Burkhoff, *Hemodynamic effects of partial ventricular support in chronic heart failure: results of simulation validated with in vivo data.* The Journal of Thoracic and Cardiovascular Surgery, 2007. **133**(1): p. 21-28. e4.

132. Lim, E., S. Dokos, S.L. Cloherty, R.F. Salamonsen, D.G. Mason, J.A. Reizes and N.H. Lovell, *Parameter-optimized model of cardiovascular–rotary blood pump interactions.* IEEE Transactions on Biomedical Engineering, 2010. **57**(2): p. 254-266.

133. Donahue, T.H., W. Dehlin, J. Gillespie, W. Weiss and G. Rosenberg, *Finite element analysis of stresses developed in the blood sac of a left ventricular assist device.* Medical engineering & physics, 2009. **31**(4): p. 454-460.

134. Long, C., A. Marsden and Y. Bazilevs, *Fluid–structure interaction simulation of pulsatile ventricular assist devices.* Computational Mechanics, 2013. **52**(5): p. 971-981.

135. Chiu, W.-C., G. Girdhar, M. Xenos, Y. Alemu, J.S. Soares, S. Einav, M. Slepian and D. Bluestein, *Thromboresistance comparison of the HeartMate II ventricular assist device with the device thrombogenicity emulation-optimized HeartAssist 5 VAD.* Journal of biomechanical engineering, 2014. **136**(2): p. 021014.

136. Selishchev, S.V. and D.V. Telyshev, *Optimisation of the Sputnik-VAD design.* Int. J. Artif. Organs, 2016. **39**(8): p. 407-414.

137. Jhun, C.S., K. Sun and J.P. Cysyk, *Continuous flow left ventricular pump support and its effect on regional left ventricular wall stress: finite element analysis study.* Med Biol Eng Comput, 2014. **52**(12): p. 1031-40.

138. McCormick, M., D.A. Nordsletten, D. Kay and N.P. Smith, *Simulating left ventricular fluid-solid mechanics through the cardiac cycle under LVAD support.* Journal of Computational Physics, 2013. **244**: p. 80-96.

139. McCormick, M., D. Nordsletten, P. Lamata and N.P. Smith, *Computational analysis of the importance of flow synchrony for cardiac ventricular assist devices.* Computers in biology and medicine, 2014. **49**: p. 83-94.

140. Lim, K.M., J. Constantino, V. Gurev, R. Zhu, E.B. Shim and N.A. Trayanova, *Comparison of the effects of continuous and pulsatile left ventricular-assist devices on ventricular unloading using a cardiac electromechanics model.* J Physiol Sci, 2012. **62**(1): p. 11-19.

141. Systèmes, D., *Abaqus Theory Guide. Version 6.14*. 2014, Simulia Corp: Providence, RI, USA.

142. Lee, K.Y. and D.J. Mooney, *Hydrogels for tissue engineering.* Chemical reviews, 2001. **101**(7): p. 1869-1880.

143. Cabrales, P., A.G. Tsai and M. Intaglietta, *Alginate plasma expander maintains perfusion and plasma viscosity during extreme hemodilution.* American Journal of Physiology-Heart and Circulatory Physiology, 2005. **288**(4): p. H1708-H1716.

144. Lee, R.J., A. Hinson, R. Bauernschmitt, K. Matschke, Q. Fang, D.L. Mann, R. Dowling, N. Schiller and H.N. Sabbah, *The feasibility and safety of Algisyl-LVR™ as a method of left ventricular augmentation in patients with dilated cardiomyopathy: Initial first in man clinical results.* International journal of cardiology, 2015. **199**: p. 18-24.

145. Mann, D.L., R.J. Lee, A.J. Coats, G. Neagoe, D. Dragomir, E. Pusineri, M. Piredda, L. Bettari, B.A. Kirwan and R. Dowling, *One-year follow-up results from AUGMENT-HF: a multicentre randomized controlled clinical trial of the efficacy of left ventricular augmentation with Algisyl in the treatment of heart failure.* European journal of heart failure, 2015.

146. Nelson, D.M., Z. Ma, K.L. Fujimoto, R. Hashizume and W.R. Wagner, *Intra-myocardial biomaterial injection therapy in the treatment of heart failure: Materials, outcomes and challenges.* Acta biomaterialia, 2011. **7**(1): p. 1-15.

147. Holmes, A.A., D. Scollan and R.L. Winslow, *Direct histological validation of diffusion tensor MRI in formaldehyde-fixed myocardium.* Magnetic resonance in medicine, 2000. **44**(1): p. 157-161.

148. Scollan, D.F., A. Holmes, R. Winslow and J. Forder, *Histological validation of myocardial microstructure obtained from diffusion tensor magnetic resonance imaging.* Am J Physiol, 1998. **275**(6 Pt 2): p. H2308-18.

149. Helm, P.A., H.J. Tseng, L. Younes, E.R. McVeigh and R.L. Winslow, *Ex vivo 3D diffusion tensor imaging and quantification of cardiac laminar structure.* Magnetic resonance in medicine, 2005. **54**(4): p. 850-859.

150. Kung, G.L., T.C. Nguyen, A. Itoh, S. Skare, N.B. Ingels, D.C. Miller and D.B. Ennis, *The presence of two local myocardial sheet populations confirmed by diffusion tensor MRI and histological validation.* Journal of Magnetic Resonance Imaging, 2011. **34**(5): p. 1080-1091.

151. Lee, L.C., Z. Zhihong, A. Hinson and J.M. Guccione, *Reduction in left ventricular wall stress and improvement in function in failing hearts using Algisyl-LVR.* JoVE (Journal of Visualized Experiments), 2013(74): p. e50096-e50096.

152. Porter, D.A. and R.M. Heidemann, *High resolution diffusion-weighted imaging using readout-segmented echo-planar imaging, parallel imaging and a two-dimensional navigator-based reacquisition.* Magnetic resonance in medicine, 2009. **62**(2): p. 468-475.

153. Setarehdan, S.K. and S. Singh, *Advanced algorithmic approaches to medical image segmentation: state-of-the-art applications in cardiology, neurology, mammography and pathology*. 2012: Springer Science & Business Media.

154. Vadakkumpadan, F., H. Arevalo, A.J. Prassl, J.J. Chen, F. Kickinger, P. Kohl, G. Plank and N. Trayanova, *Image-based models of cardiac structure in health and disease.* Wiley Interdisciplinary Reviews-Systems Biology and Medicine, 2010. **2**(4): p. 489-506.

155. Cerqueira, M.D., N.J. Weissman, V. Dilsizian, A.K. Jacobs, S. Kaul, W.K. Laskey, D.J. Pennell, J.A. Rumberger, T. Ryan, M.S. Verani and A.H.A.W. Grp, *Standardized myocardial segmentation and nomenclature for tomographic imaging of the heart - A statement for healthcare professionals from the Cardiac Imaging Committee of the Council on Clinical Cardiology of the American Heart Association.* Circulation, 2002. **105**(4): p. 539-542.

156. Wu, Y., C.W. Chan, J.M. Nicholls, S. Liao, H.F. Tse and E.X. Wu, *MR study of the effect of infarct size and location on left ventricular functional and microstructural alterations in porcine models.* Journal of Magnetic Resonance Imaging, 2009. **29**(2): p. 305-312.

157. Taylor, P.A. and Z.S. Saad, *FATCAT:(an efficient) functional and tractographic connectivity analysis toolbox.* Brain connectivity, 2013. **3**(5): p. 523-535.

158. Cox, R.W., *AFNI: software for analysis and visualization of functional magnetic resonance neuroimages.* Computers and Biomedical research, 1996. **29**(3): p. 162-173.

159. Wu, E.X., Y. Wu, J.M. Nicholls, J. Wang, S. Liao, S. Zhu, C.P. Lau and H.F. Tse, *MR diffusion tensor imaging study of postinfarct myocardium structural remodeling in a porcine model.* Magnetic resonance in medicine, 2007. **58**(4): p. 687-695.

160. Streeter, D.D., H.M. Spotnitz, D.P. Patel, J. Ross and E.H. Sonnenblick, *Fiber orientation in the canine left ventricle during diastole and systole.* Circulation research, 1969. **24**(3): p. 339-347.

161. Streeter, D.D. and D.L. Bassett, *An engineering analysis of myocardial fiber orientation in pig's left ventricle in systole.* The Anatomical Record, 1966. **155**(4): p. 503-511.

162. Ennis, D.B., T.C. Nguyen, J.C. Riboh, L. Wigström, K.B. Harrington, G.T. Daughters, N.B. Ingels and D.C. Miller, *Myofiber angle distributions in the ovine left ventricle do not conform to computationally optimized predictions.* Journal of Biomechanics, 2008. **41**(15): p. 3219-3224.

163. Geerts, L., P. Bovendeerd, K. Nicolay and T. Arts, *Characterization of the normal cardiac myofiber field in goat measured with MR-diffusion tensor imaging.* Am J Physiol Heart Circ Physiol, 2002. **283**(1): p. H139-145.

164. Al Kindi, A., Y. Ge, D. Shum-Tim and R. Chiu, *Cellular cardiomyoplasty: routes of cell delivery and retention.* Front Biosci, 2008. **13**: p. 2421-2434.

165. Malliaras, K., M. Kreke and E. Marban, *The Stuttering Progress of Cell Therapy for Heart Disease.* Clinical Pharmacology & Therapeutics, 2011. **90**(4): p. 532-541.

166. Roche, E.T., C.L. Hastings, S.A. Lewin, D.E. Shvartsman, Y. Brudno, N.V. Vasilyev, F.J. O'Brien, C.J. Walsh, G.P. Duffy and D.J. Mooney, *Comparison of biomaterial delivery vehicles for improving acute retention of stem cells in the infarcted heart.* Biomaterials, 2014. **35**(25): p. 6850-6858.

167. Baillargeon, B., I. Costa, J.R. Leach, L.C. Lee, M. Genet, A. Toutain, J.F. Wenk, M.K. Rausch, N. Rebelo, G. Acevedo-Bolton, E. Kuhl, J.L. Navia and J.M. Guccione, *Human Cardiac Function Simulator for the Optimal Design of a Novel Annuloplasty Ring with a Sub-valvular Element for Correction of Ischemic Mitral Regurgitation.* Cardiovasc Eng Technol, 2015. **6**(2): p. 105-116.

168. Genet, M., L.C. Lee, R. Nguyen, H. Haraldsson, G. Acevedo-Bolton, Z. Zhang, L. Ge, K. Ordovas, S. Kozerke and J.M. Guccione, *Distribution of normal human left ventricular myofiber stress at end diastole and end systole: a target for in silico design of heart failure treatments.* J Appl Physiol (1985), 2014. **117**(2): p. 142-52.

169. Sack, K.L., B. Baillargeon, G. Acevedo-Bolton, M. Genet, N. Rebelo, E. Kuhl, L. Klein, G.M. Weiselthaler, D. Burkhoff, T. Franz and J.M. Guccione, *Partial LVAD restores ventricular outputs and normalizes LV but not RV stress distributions in the acutely failing heart in silico.* Int J Artif Organs, 2016. **39**(8): p. 421-430.

170. Sack, K.L., N.H. Davies, J.M. Guccione and T. Franz, *Personalised computational cardiology: Patient-specific modelling in cardiac mechanics and biomaterial injection therapies for myocardial infarction.* Heart Fail Rev, 2016. **21**(6): p. 815-826.

171. Fukuta, H. and W.C. Little, *The cardiac cycle and the physiologic basis of left ventricular contraction, ejection, relaxation, and filling.* Heart failure clinics, 2008. **4**(1): p. 1-11.

172. Mann, D.L., D.P. Zipes, P. Libby, R.O. Bonow and E. Braunwald, *Braunwald's heart disease.* 2015.

173. Guyton, A.C. and J.E. Hall, *Textbook of Medical Physiology*. 11th ed. 2006, Philadelphia: Elsevier Saunders. 1116.

174. Beyar, R. and S. Sideman, *A computer study of the left ventricular performance based on fiber structure, sarcomere dynamics, and transmural electrical propagation velocity.* Circulation Research, 1984. **55**(3): p. 358.

175. Bishop, M.J., P. Hales, G. Plank, D.J. Gavaghan, J. Scheider and V. Grau, *Comparison of rule-based and DTMRI-derived fibre architecture in a whole rat ventricular computational model*, in *Functional Imaging and Modeling of the Heart*. 2009, Springer. p. 87-96.

176. Gahm, J.K., N. Wisniewski, G. Kindlmann, G.L. Kung, W.S. Klug, A. Garfinkel and D.B. Ennis, *Linear invariant tensor interpolation applied to cardiac diffusion tensor MRI*, in *Medical Image Computing and Computer-Assisted Intervention–MICCAI 2012*. 2012, Springer. p. 494-501.

177. Yang, F., Y.M. Zhu, J.H. Luo, M. Robini, J. Liu and P. Croisille, *A comparative study of different level interpolations for improving spatial resolution in diffusion tensor imaging.* IEEE J Biomed Health Inform, 2014. **18**(4): p. 1317-27.

178. Yang, F., Y.M. Zhu, I.E. Magnin, J.H. Luo, P. Croisille and P.B. Kingsley, *Feature-based interpolation of diffusion tensor fields and application to human cardiac DT-MRI.* Med Image Anal, 2012. **16**(2): p. 459-81.

179. Rohmer, D., A. Sitek and G.T. Gullberg, *Reconstruction and Visualization of Fiber and Laminar Structure in the Normal Human Heart from Ex Vivo Diffusion Tensor Magnetic Resonance Imaging (DTMRI) Data.* Investigative Radiology, 2007. **42**(11): p. 777-789 10.1097/RLI.0b013e3181238330.

180. Cox, R.W., *AFNI: software for analysis and visualization of functional magnetic resonance neuroimages.* Comput Biomed Res, 1996. **29**(3): p. 162-73.

181. Sommer, G., A.J. Schriefl, M. Andrä, M. Sacherer, C. Viertler, H. Wolinski and G.A. Holzapfel, *Biomechanical properties and microstructure of human ventricular myocardium.* Acta biomaterialia, 2015. **24**: p. 172-192.

182. Klotz, S., I. Hay, M.L. Dickstein, G.H. Yi, J. Wang, M.S. Maurer, D.A. Kass and D. Burkhoff, *Single-beat estimation of end-diastolic pressure-volume relationship: a novel method with potential for noninvasive application.* Am J Physiol Heart Circ Physiol, 2006. **291**(1): p. H403-12.

183. Guccione, J.M. and A.D. McCulloch, *Mechanics of active contraction in cardiac muscle: Part I--Constitutive relations for fiber stress that describe deactivation.* J Biomech Eng, 1993. **115**(1): p. 72-81.

184. Walker, J.C., M.B. Ratcliffe, P. Zhang, A.W. Wallace, B. Fata, E.W. Hsu, D. Saloner and J.M. Guccione, *MRI-based finite-element analysis of left ventricular aneurysm.* Am J Physiol Heart Circ Physiol, 2005. **289**(2): p. H692-700.

185. Hanley, P.J., A.A. Young, I.J. LeGrice, S.G. Edgar and D.S. Loiselle, *3-Dimensional configuration of perimysial collagen fibres in rat cardiac muscle at resting and extended sarcomere lengths.* The Journal of physiology, 1999. **517**(3): p. 831-837.

186. Rodriguez, E.K., J.H. Omens, L. Waldman and A. McCulloch, *Effect of residual stress on transmural sarcomere length distributions in rat left ventricle.* American Journal of Physiology-Heart and Circulatory Physiology, 1993. **264**(4): p. H1048-H1056.

187. Lin, D. and F. Yin, *A multiaxial constitutive law for mammalian left ventricular myocardium in steady-state barium contracture or tetanus.* Journal of biomechanical engineering, 1998. **120**(4): p. 504-517.

188. Carreras, F., J. Garcia-Barnes, D. Gil, S. Pujadas, C.H. Li, R. Suarez-Arias, R. Leta, X. Alomar, M. Ballester and G. Pons-Llado, *Left ventricular torsion and longitudinal shortening: two fundamental components of myocardial mechanics assessed by tagged cine-MRI in normal subjects.* The international journal of cardiovascular imaging, 2012. **28**(2): p. 273-284.

189. Dumesnil, J., R. Shoucri, J. Laurenceau and J. Turcot, *A mathematical model of the dynamic geometry of the intact left ventricle and its application to clinical data.* Circulation, 1979. **59**(5): p. 1024-1034.

190. Hoppensteadt, F.C. and C.S. Peskin, *Mathematics in medicine and the life sciences.* 1992.

191. Pilla, J.J., J.H. Gorman III and R.C. Gorman, *Theoretic Impact of Infarct Compliance on Left Ventricular Function.* Annals of Thoracic Surgery, 2009. **87**(3): p. 803-810.

192. Santamore, W.P. and D. Burkhoff, *Hemodynamic consequences of ventricular interaction as assessed by model analysis.* American Journal of Physiology-Heart and Circulatory Physiology, 1991. **260**(1): p. H146-H157.

193. Watanabe, H., S. Sugiura, H. Kafuku and T. Hisada, *Multiphysics simulation of left ventricular filling dynamics using fluid-structure interaction finite element method.* Biophysical journal, 2004. **87**(3): p. 2074-2085.

194. Quinn, T.A., G. Berberian, S.E. Cabreriza, L.J. Maskin, A.D. Weinberg, J.W. Holmes and H.M. Spotnitz, *Effects of sequential biventricular pacing during acute right ventricular pressure overload.* American Journal of Physiology-Heart and Circulatory Physiology, 2006. **60**(5): p. H2380.

195. Sengupta, P.P., B.K. Khandheria, J. Korinek, J. Wang, A. Jahangir, J.B. Seward and M. Belohlavek, *Apex-to-base dispersion in regional timing of left ventricular shortening and lengthening.* Journal of the American College of Cardiology, 2006. **47**(1): p. 163-172.

196. Beyar, R. and S. Sideman, *Model for left ventricular contraction combining the force length velocity relationship with the time varying elastance theory.* Biophysical journal, 1984. **45**(6): p. 1167-1177.

197. Hanrath, P., D.G. Mathey, P. Kremer, F. Sonntag and W. Bleifeld, *Effect of verapamil on left ventricular isovolumic relaxation time and regional left ventricular filling in hypertrophic cardiomyopathy.* The American journal of cardiology, 1980. **45**(6): p. 1258-1264.

198. Hughes, T.J., *The Finite Element Method: Linear Static and Dynamic Finite Element Analysis*. 2000: Courier Corporation.

199. Pedrizzetti, G., S. Sengupta, G. Caracciolo, C.S. Park, M. Amaki, G. Goliasch, J. Narula and P.P. Sengupta, *Three-dimensional principal strain analysis for characterizing subclinical changes in left ventricular function.* Journal of the American Society of Echocardiography, 2014. **27**(10): p. 1041-1050. e1.

200. Crick, S.J., M.N. Sheppard, S.Y. HO, L. Gebstein and R.H. Anderson, *Anatomy of the pig heart: comparisons with normal human cardiac structure.* Journal of anatomy, 1998. **193**(01): p. 105-119.

201. Wang, H., H. Gao, X. Luo, C. Berry, B.E. Griffith, R. Ogden and T. Wang, *Structure-based finite strain modelling of the human left ventricle in diastole.* International journal for numerical methods in biomedical engineering, 2013. **29**(1): p. 83-103.

202. Wenk, J.F., L. Ge, Z. Zhang, M. Soleimani, D.D. Potter, A.W. Wallace, E. Tseng, M.B. Ratcliffe and J.M. Guccione, *A coupled biventricular finite element and lumped-parameter circulatory system model of heart failure.* Computer Methods in Biomechanics and Biomedical Engineering, 2012: p. 1-12.

203. Wong, J., S. Göktepe and E. Kuhl, *Computational modeling of chemo-electro-mechanical coupling: A novel implicit monolithic finite element approach.* International Journal for Numerical Methods in Biomedical Engineering, 2013. **29**(10): p. 1104-1133.

204. Berberoğlu, E., H.O. Solmaz and S. Göktepe, *Computational modeling of coupled cardiac electromechanics incorporating cardiac dysfunctions.* European Journal of Mechanics-A/Solids, 2014.

205. Quarteroni, A., T. Lassila, S. Rossi and R. Ruiz-Baier, *Integrated Heart—Coupling multiscale and multiphysics models for the simulation of the cardiac function.* Computer Methods in Applied Mechanics and Engineering, 2017. **314**: p. 345-407.

206. Palit, A., P. Franciosa, S.K. Bhudia, T.N. Arvanitis, G.A. Turley and M.A. Williams, *Passive diastolic modelling of human ventricles: effects of base movement and geometrical heterogeneity.* Journal of Biomechanics, 2016.

207. Krishnamurthy, A., M.J. Gonzales, G. Sturgeon, W.P. Segars and A.D. McCulloch, *Biomechanics simulations using cubic Hermite meshes with extraordinary nodes for isogeometric cardiac modeling.* Computer aided geometric design, 2016. **43**: p. 27-38.

208. Fritz, T., C. Wieners, G. Seemann, H. Steen and O. Dössel, *Simulation of the contraction of the ventricles in a human heart model including atria and pericardium.* Biomechanics and modeling in mechanobiology, 2014. **13**(3): p. 627-641.

209. Genet, M., L.C. Lee, B. Baillargeon, J.M. Guccione and E. Kuhl, *Modeling Pathologies of Diastolic and Systolic Heart Failure.* Ann Biomed Eng, 2016. **44**(1): p. 112-27.

210. Bishop, M.J., G. Plank, R.A.B. Burton, J.E. Schneider, D.J. Gavaghan, V. Grau and P. Kohl, *Development of an anatomically detailed MRI-derived rabbit ventricular model and assessment of its impact on simulations of electrophysiological function.* American Journal of Physiology-Heart and Circulatory Physiology, 2010. **298**(2): p. H699-H718.

211. Bishop, M.J. and G. Plank, *The role of fine-scale anatomical structure in the dynamics of reentry in computational models of the rabbit ventricles.* J Physiol, 2012. **590**(Pt 18): p. 4515-35.

212. Hooks, D.A., K.A. Tomlinson, S.G. Marsden, I.J. LeGrice, B.H. Smaill, A.J. Pullan and P.J. Hunter, *Cardiac microstructure: implications for electrical propagation and defibrillation in the heart.* Circ Res, 2002. **91**(4): p. 331-8.

213. LeGrice, I.J., B. Smaill, L. Chai, S. Edgar, J. Gavin and P.J. Hunter, *Laminar structure of the heart: ventricular myocyte arrangement and connective tissue architecture in the dog.* American Journal of Physiology-Heart and Circulatory Physiology, 1995. **269**(2): p. H571-H582.

214. Young, A., I. Legrice, M. Young and B. Smaill, *Extended confocal microscopy of myocardial laminae and collagen network.* Journal of Microscopy, 1998. **192**(2): p. 139-150.

215. Costa, K.D., K. May-Newman, D. Farr, W.G. O'Dell, A.D. McCulloch and J.H. Omens, *Three-dimensional residual strain in midanterior canine left ventricle.* Am J Physiol, 1997. **273**(4 Pt 2): p. H1968-76.

216. Chen, J., W. Liu, H. Zhang, L. Lacy, X. Yang, S.-K. Song, S.A. Wickline and X. Yu, *Regional ventricular wall thickening reflects changes in cardiac fiber and sheet structure during contraction: quantification with diffusion tensor MRI.* American Journal of Physiology-Heart and Circulatory Physiology, 2005. **289**(5): p. H1898-H1907.

217. Hooks, D.A., M.L. Trew, B.J. Caldwell, G.B. Sands, I.J. LeGrice and B.H. Smaill, *Laminar arrangement of ventricular myocytes influences electrical behavior of the heart.* Circ Res, 2007. **101**(10): p. e103-12.

218. Sack, K.L., S. Skatulla and C. Sansour, *Biological tissue mechanics with fibres modelled as one-dimensional Cosserat continua. Applications to cardiac tissue.* International Journal of Solids and Structures, 2016. **81**: p. 84-94.

219. Gao, H., W. Li, L. Cai, C. Berry and X. Luo, *Parameter estimation in a Holzapfel–Ogden law for healthy myocardium.* Journal of engineering mathematics, 2015. **95**(1): p. 231-248.

220. Burkhoff, D., I. Mirsky and H. Suga, *Assessment of systolic and diastolic ventricular properties via pressure-volume analysis: a guide for clinical, translational, and basic researchers.* American Journal of Physiology-Heart and Circulatory Physiology, 2005. **289**(2): p. H501-H512.

221. Allen, D. and J. Kentish, *The cellular basis of the length-tension relation in cardiac muscle.* Journal of molecular and cellular cardiology, 1985. **17**(9): p. 821-840.

222. Hanft, L.M., F.S. Korte and K.S. McDonald, *Cardiac function and modulation of sarcomeric function by length.* Cardiovascular research, 2008. **77**(4): p. 627-636.

223. Botcherby, E.J., A. Corbett, R.A. Burton, C.W. Smith, C. Bollensdorff, M.J. Booth, P. Kohl, T. Wilson and G. Bub, *Fast Measurement of Sarcomere Length and Cell Orientation in Langendorff-Perfused Hearts Using Remote Focusing MicroscopyNovelty and Significance.* Circulation research, 2013. **113**(7): p. 863-870.

224. Matiwala, S. and K.B. Margulies, *Mechanical approaches to alter remodeling.* Current heart failure reports, 2004. **1**(1): p. 14-18.

225. Sutton, M.G.S.J. and N. Sharpe, *Left ventricular remodeling after myocardial infarction pathophysiology and therapy.* Circulation, 2000. **101**(25): p. 2981-2988.

226. Pfeffer, M.A. and E. Braunwald, *Ventricular remodeling after myocardial infarction. Experimental observations and clinical implications.* Circulation, 1990. **81**(4): p. 1161-1172.

227. Gayat, E., H. Ahmad, L. Weinert, R.M. Lang and V. Mor-Avi, *Reproducibility and inter-vendor variability of left ventricular deformation measurements by three-dimensional speckle-tracking echocardiography.* Journal of the American Society of Echocardiography, 2011. **24**(8): p. 878-885.

228. Badano, L.P., U. Cucchini, D. Muraru, O. Al Nono, C. Sarais and S. Iliceto, *Use of three-dimensional speckle tracking to assess left ventricular myocardial mechanics: inter-vendor consistency and reproducibility of strain measurements.* European Heart Journal-Cardiovascular Imaging, 2012: p. jes184.

229. Lang, R.M., L.P. Badano, V. Mor-Avi, J. Afilalo, A. Armstrong, L. Ernande, F.A. Flachskampf, E. Foster, S.A. Goldstein and T. Kuznetsova, *Recommendations for cardiac chamber quantification by echocardiography in adults: an update from the American Society of Echocardiography and the European Association of Cardiovascular Imaging.* Journal of the American Society of Echocardiography, 2015. **28**(1): p. 1-39. e14.

230. Bachner-Hinenzon, N., O. Ertracht, M. Leitman, Z. Vered, S. Shimoni, R. Beeri, O. Binah and D. Adam, *Layer-specific strain analysis by speckle tracking echocardiography reveals differences in left ventricular function between rats and humans.* American Journal of Physiology-Heart and Circulatory Physiology, 2010.

231. Leitman, M., M. Lysiansky, P. Lysyansky, Z. Friedman, V. Tyomkin, T. Fuchs, D. Adam, R. Krakover and Z. Vered, *Circumferential and longitudinal strain in 3 myocardial layers in normal subjects and in patients with regional left ventricular dysfunction.* Journal of the American Society of Echocardiography, 2010. **23**(1): p. 64-70.

232. Takigiku, K., M. Takeuchi, C. Izumi, S. Yuda, K. Sakata, N. Ohte, K. Tanabe, S. Nakatani and J. investigators, *Normal range of left ventricular 2-dimensional strain.* Circulation Journal, 2012. **76**(11): p. 2623-2632.

233. Finegold, J.A., P. Asaria and D.P. Francis, *Mortality from ischaemic heart disease by country, region, and age: statistics from World Health Organisation and United Nations.* International journal of cardiology, 2013. **168**(2): p. 934-945.

234. Mozaffarian, D., E.J. Benjamin, A.S. Go, D.K. Arnett, M.J. Blaha, M. Cushman, S.R. Das, S. de Ferranti, J.-P. Després and H.J. Fullerton, *Heart Disease and Stroke Statistics—2016 Update A Report From the American Heart Association.* Circulation, 2015: p. CIR. 0000000000000350.

235. Chen, J., A. Hsieh, K. Dharmarajan, F.A. Masoudi and H.M. Krumholz, *National Trends in Heart Failure Hospitalization after Acute Myocardial Infarction for Medicare Beneficiaries: 1998-2010.* Circulation, 2013. **128**(24): p. 2577.

236. Hellermann, J.P., T.Y. Goraya, S.J. Jacobsen, S.A. Weston, G.S. Reeder, B.J. Gersh, M.M. Redfield, R.J. Rodeheffer, B.P. Yawn and V.L. Roger, *Incidence of heart failure after myocardial infarction: is it changing over time?* American journal of epidemiology, 2003. **157**(12): p. 1101-1107.

237. Desta, L., T. Jernberg, I. Löfman, C. Hofman-Bang, I. Hagerman, J. Spaak and H. Persson, *Incidence, temporal trends, and prognostic impact of heart failure complicating acute myocardial infarction. The SWEDEHEART Registry (Swedish Web-System for Enhancement and Development of Evidence-Based Care in Heart Disease Evaluated According to Recommended Therapies): a study of 199,851 patients admitted with index acute myocardial infarctions, 1996 to 2008.* JACC. Heart failure, 2015. **3**(3): p. 234.

238. Fomovsky, G.M., J.R. Macadangdang, G. Ailawadi and J.W. Holmes, *Model-based design of mechanical therapies for myocardial infarction.* J Cardiovasc Transl Res, 2011. **4**(1): p. 82-91.

239. Wenk, J.F., K. Sun, Z. Zhang, M. Soleimani, L. Ge, D. Saloner, A.W. Wallace, M.B. Ratcliffe and J.M. Guccione, *Regional Left Ventricular Myocardial Contractility and Stress in a Finite Element Model of Posterobasal Myocardial Infarction.* Journal of Biomechanical Engineering, 2011. **133**(4): p. 044501.

240. Wenk, J.F., D. Klepach, L.C. Lee, Z.H. Zhang, L. Ge, E.E. Tseng, A. Martin, S. Kozerke, J.H. Gorman, R.C. Gorman and J.M. Guccione, *First Evidence of Depressed Contractility in the Border Zone of a Human Myocardial Infarction.* Annals of Thoracic Surgery, 2012. **93**(4): p. 1188-1194.

241. Boyce, M.C. and E.M. Arruda, *Constitutive models of rubber elasticity: a review.* Rubber chemistry and technology, 2000. **73**(3): p. 504-523.

242. Gupta, K.B., M.B. Ratcliffe, M.A. Fallert, L.H. Edmunds, Jr. and D.K. Bogen, *Changes in passive mechanical stiffness of myocardial tissue with aneurysm formation.* Circulation, 1994. **89**(5): p. 2315-26.

243. Connelly, C.M., W.M. Vogel, A.W. Wiegner, E.L. Osmers, O.H. Bing, R.A. Kloner, D.M. Dunn-Lanchantin, C. Franzblau and C.S. Apstein, *Effects of reperfusion after coronary artery occlusion on post-infarction scar tissue.* Circulation research, 1985. **57**(4): p. 562-577.

244. Bogaert, J., H. Bosmans, A. Maes, P. Suetens, G. Marchal and F.E. Rademakers, *Remote myocardial dysfunction after acute anterior myocardial infarction: impact of left ventricular shape on regional function: a magnetic resonance myocardial tagging study.* Journal of the American College of Cardiology, 2000. **35**(6): p. 1525-1534.

245. Holzapfel, G.A., *Biomechanics of soft tissue.* The handbook of materials behavior models, 2001. **3**: p. 1049-1063.

246. Kassab, G.S. and M.S. Sacks, *Structure-based mechanics of tissues and organs*. 2016: Springer.

247. Wise, P., N.H. Davies, M.S. Sirry, J. Kortsmit, L. Dubuis, C.K. Chai, F. Baaijens and T. Franz, *Excessive volume of hydrogel injectates may compromise the efficacy for the treatment of acute myocardial infarction.* International journal for numerical methods in biomedical engineering, 2016. **32**(12).

248. Go, A.S., D. Mozaffarian, V.L. Roger, E.J. Benjamin, J.D. Berry, M.J. Blaha, S. Dai, E.S. Ford, C.S. Fox and S. Franco, *Heart disease and stroke statistics - 2014 update: a report from the American Heart Association.* Circulation, 2014. **129**(3): p. e28-e292.

249. McIlvennan, C.K., K.H. Magid, A.V. Ambardekar, J.S. Thompson, D.D. Matlock and L.A. Allen, *Clinical outcomes after continuous-flow left ventricular assist device: a systematic review.* Circ Heart Fail, 2014. **7**(6): p. 1003-13.

250. Meyns, B.P., A. Simon, S. Klotz, T. Wittwer, C. Schlensak, F. Rega and D. Burkhoff, *Clinical benefits of partial circulatory support in New York Heart Association Class IIIB and Early Class IV patients.* Eur J Cardiothorac Surg, 2011. **39**(5): p. 693-8.

251. Timms, D., *A review of clinical ventricular assist devices.* Med Eng Phys, 2011. **33**(9): p. 1041-7.

252. Lampropulos, J.F., N. Kim, Y. Wang, M.M. Desai, J.A.S. Barreto-Filho, J.A. Dodson, D.L. Dries, A.A. Mangi and H.M. Krumholz, *Trends in left ventricular assist device use and outcomes among Medicare beneficiaries, 2004–2011.* Open heart, 2014. **1**(1): p. e000109.

253. Pan, S., B. Aksut, O.E. Wever-Pinzon, S.D. Rao, A.P. Levin, A.R. Garan, J.A. Fried, K. Takeda, T. Hiroo, M. Yuzefpolskaya, N. Uriel, U.P. Jorde, D.M. Mancini, Y. Naka, P.C. Colombo and V.K. Topkara, *Incidence and predictors of myocardial recovery on long-term left ventricular assist device support: Results from the United Network for Organ Sharing database.* J Heart Lung Transplant, 2015. **34**(12): p. 1624-9.

254. Mancini, D.M., A. Beniaminovitz, H. Levin, K. Catanese, M. Flannery, M. DiTullio, S. Savin, M.E. Cordisco, E. Rose and M. Oz, *Low incidence of myocardial recovery after left ventricular assist device implantation in patients with chronic heart failure.* Circulation, 1998. **98**(22): p. 2383-9.

255. Helman, D.N., S.W. Maybaum, D.L. Morales, M.R. Williams, A. Beniaminovitz, N.M. Edwards, D.M. Mancini and M.C. Oz, *Recurrent remodeling after ventricular assistance: is long-term myocardial recovery attainable?* Ann Thoracic Surg, 2000. **70**(4): p. 1255-1258.

256. Marsden, A.L., Y. Bazilevs, C.C. Long and M. Behr, *Recent advances in computational methodology for simulation of mechanical circulatory assist devices.* Wiley Interdiscip Rev Syst Bio Med, 2014. **6**(2): p. 169-188.

257. Lim, K.M., J. Constantino, V. Gurev, R. Zhu, E.B. Shim and N.A. Trayanova, *Comparison of the effects of continuous and pulsatile left ventricular-assist devices on ventricular unloading using a cardiac electromechanics model.* J Physiol Sci, 2012. **62**(1): p. 11-9.

258. Hunter, P.J., A.D. McCulloch and H.E. ter Keurs, *Modelling the mechanical properties of cardiac muscle.* Prog Biophys Mol Biol, 1998. **69**(2-3): p. 289-331.

259. McMurray, J.J., S. Adamopoulos, S.D. Anker, A. Auricchio, M. Böhm, K. Dickstein, V. Falk, G. Filippatos, C. Fonseca and M.A. Gomez-Sanchez, *ESC Guidelines for the diagnosis and treatment of acute and chronic heart failure 2012.* European journal of heart failure, 2012. **14**(8): p. 803-869.

260. Mann, D.L., D.P. Zipes, P. Libby and R.O. Bonow, *Braunwald's heart disease: a textbook of cardiovascular medicine*. 2014: Elsevier Health Sciences.

261. Adams, K.F., G.C. Fonarow, C.L. Emerman, T.H. LeJemtel, M.R. Costanzo, W.T. Abraham, R.L. Berkowitz, M. Galvao, D.P. Horton, A.S.A. Committee and Investigators, *Characteristics and outcomes of patients hospitalized for heart failure in the United States: rationale, design, and preliminary observations from the first 100,000 cases in the Acute Decompensated Heart Failure National Registry (ADHERE).* American heart journal, 2005. **149**(2): p. 209-216.

262. Publication Committee for the, V.I., *Intravenous nesiritide vs nitroglycerin for treatment of decompensated congestive heart failure: A randomized controlled trial.* JAMA, 2002. **287**(12): p. 1531-1540.

263. Wang, Y., N. Loghmanpour, S. Vandenberghe, A. Ferreira, B. Keller, J. Gorcsan and J. Antaki, *Simulation of dilated heart failure with continuous flow circulatory support.* PLoS One, 2014. **9**(1): p. e85234.

264. Morley, D., K. Litwak, P. Ferber, P. Spence, R. Dowling, B. Meyns, B. Griffith and D. Burkhoff, *Hemodynamic effects of partial ventricular support in chronic heart failure: results of simulation validated with in vivo data.* J Thorac Cardiovasc Surg, 2007. **133**(1): p. 21-8.

265. Barbone, A., J.W. Holmes, P.M. Heerdt, Y. Naka, N. Joshi, M. Daines, A.R. Marks, M.C. Oz and D. Burkhoff, *Comparison of Right and Left Ventricular Responses to Left Ventricular Assist Device Support in Patients With Severe Heart Failure A Primary Role of Mechanical Unloading Underlying Reverse Remodeling.* Circulation, 2001. **104**(6): p. 670-675.

266. Küçüker, S.A., S.J. Stetson, K.A. Becker, A. Akgül, M. Loebe, J.A. Lafuente, G.P. Noon, M.M. Koerner, M.L. Entman and G. Torre-Amione, *Evidence of improved right ventricular structure after LVAD support in patients with end-stage cardiomyopathy.* J Heart Lung Transplant, 2004. **23**(1): p. 28-35.

267. Maeder, M.T., A. Leet, A. Ross, D. Esmore and D.M. Kaye, *Changes in right ventricular function during continuous-low left ventricular assist device support.* J Heart Lung Transplant, 2009. **28**(4): p. 360-366.

268. Kavarana, M.N., M.S. Pessin-Minsley, J. Urtecho, K.A. Catanese, M. Flannery, M.C. Oz and Y. Naka, *Right ventricular dysfunction and organ failure in left ventricular assist device recipients: a continuing problem.* Ann Thorac Surg, 2002. **73**(3): p. 745-750.

269. Dang, N.C., V.K. Topkara, M. Mercando, J. Kay, K.H. Kruger, M.S. Aboodi, M.C. Oz and Y. Naka, *Right heart failure after left ventricular assist device implantation in patients with chronic congestive heart failure.* J Heart Lung Transplant, 2006. **25**(1): p. 1-6.

270. Argiriou, M., S.-M. Kolokotron, T. Sakellaridis, O. Argiriou, C. Charitos, P. Zarogoulidis, N. Katsikogiannis, I. Kougioumtzi, N. Machairiotis and T. Tsiouda, *Right heart failure post left ventricular assist device implantation.* J Thoracic Dis, 2014. **6 Suppl 1**: p. S52-59.

271. Baumwol, J., P.S. Macdonald, A.M. Keogh, E. Kotlyar, P. Spratt, P. Jansz and C.S. Hayward, *Right heart failure and "failure to thrive" after left ventricular assist device: clinical predictors and outcomes.* J Heart Lung Transplant, 2011. **30**(8): p. 888-895.

272. Kormos, R.L., J.J. Teuteberg, F.D. Pagani, S.D. Russell, R. John, L.W. Miller, T. Massey, C.A. Milano, N. Moazami and K.S. Sundareswaran, *Right ventricular failure in patients with the HeartMate II continuous-flow left ventricular assist device: incidence, risk factors, and effect on outcomes.* J Thorac Ccardiovasc Surg, 2010. **139**(5): p. 1316-1324.

273. Drakos, S.G., A.G. Kfoury, C.H. Selzman, D.R. Verma, J.N. Nanas, D.Y. Li and J. Stehlik, *Left ventricular assist device unloading effects on myocardial structure and function: Current status of the field and call for action.* Current opinion in cardiology, 2011. **26**(3): p. 245.

Appendix A Supplementary data for Chapter 3

A.1 Mesh convergence analysis

Mesh convergence was performed using sample meshes ranging from 29,000 to 330,000 elements to simulate a single cardiac cycle. P1 linear tetrahedral element meshes were found to be significantly stiffer than their quadratic counterparts (P2). This is best illustrated in Figure A1 whereby the finest P1 mesh (330,000 elements) is still considerably stiffer than a relatively coarse P2 mesh response, motivating the choice of quadratic tetrahedral elements for simulations.

Fig. A.1: Mesh Convergence of P1 (linear) tetrahedral elements (solid lines) ranging from 47,000 – 330,000 elements. The PV loop of the left ventricle was plotted under the same conditions in all simulations. The PV loop of the coarsest mesh was repeated using P2 (quadratic) elements (dashed line).

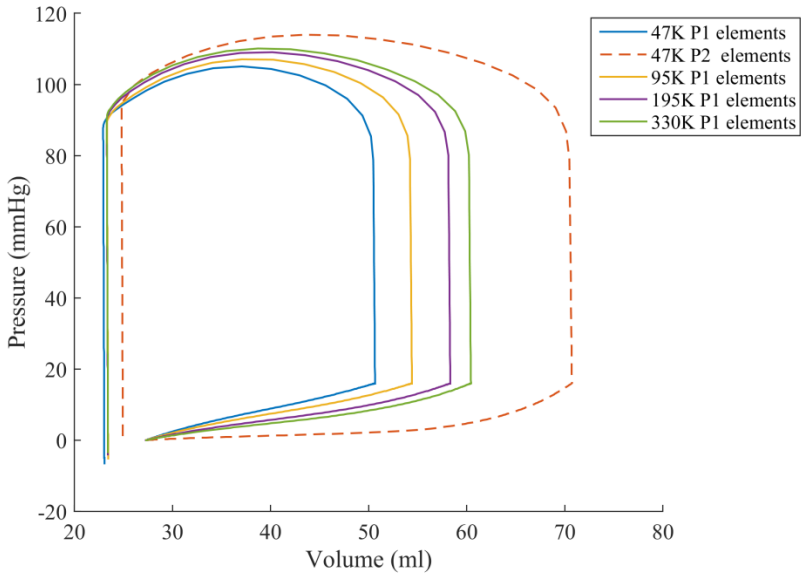

An illustration of mesh density used for this study is presented in Figure A2.

29,000 elements was the minimum possible number of elements that the BV domain could be meshed with and still retain key geometric features. The mesh size was increased until convergence was found, and these results are presented in Table A1. Here we see that P2 meshes perform consistently for almost all mesh refinements

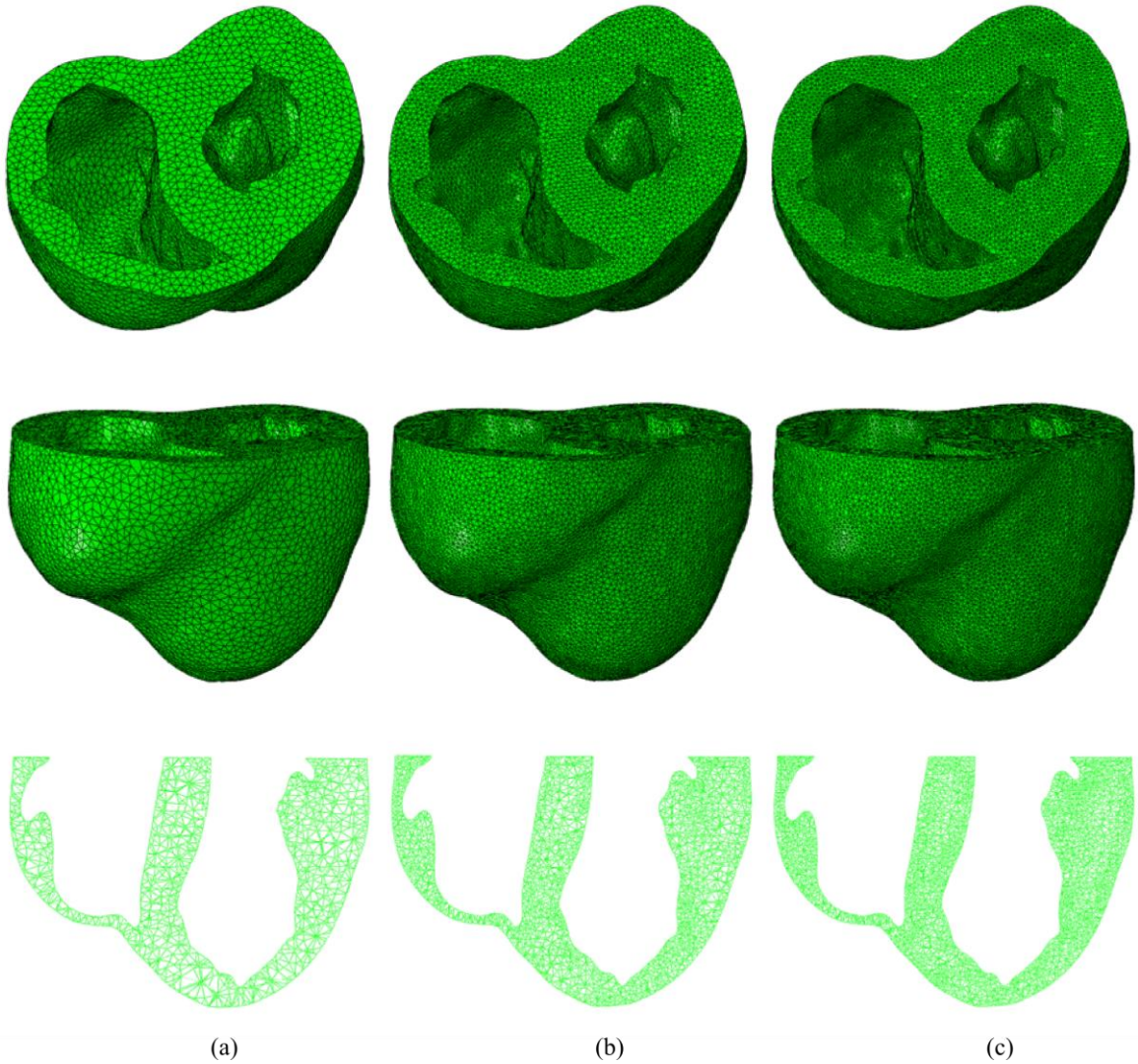

Fig. A.2:Illustrations of the meshes used in the convergence analysis. Examples presented here are of meshes with 47,000 elements (a), through to 195,000 elements (b) and 330,000 elements (c). Top, middle rows reveal different viewpoints of the mesh, and the bottom row revealing LA cut profile roughly bisecting the ventricular cavities.

Considering pressure volume behaviour and using a tolerance of 1%, the passive filling simulations result in converge for all P2 mesh resolution. For systolic performance, convergence occurs for mesh refinement exceeding 95,000 elements. Even so, the smallest error is <3% for quadratic meshes, making even the coarsest mesh reliable for rough simulations. When looking at myofibre stress at ED and ES as a measure of convergence we again find convergence for mesh refinement exceeding 95,000 elements. For brevity, only the myofibre stress results at ED (this metric showed the most error) are reported in Table A1.

While tolerable, 47,000 elements should be the lower limit of acceptable mesh resolution in order to model global function. However, in order to ensure the ventricular wall has enough element refinement to represent multiple fibre orientations and to ensure a more precise determination of stress, mesh resolution exceeding 80,000 elements is recommended.

Table A.1: End systolic volumes (ESV), end diastolic volumes (EDV) and ED stress of all the mesh convergence results. Percentages of the converged solution (195,000 P2 elements) are shown next to the volume amounts.

Mesh Size	Element Type	EDV (ml)	% of converged	ESV (ml)	% of converged	ED Myofibre Stress (kPa)	% of converged
47K	P1	50.64	71.5%	22.93	90.3%	2.2 ± 52.2	73%
95K	P1	54.40	76.8%	23.31	91.8%	2.0 ± 52.3	67%
195K	P1	58.32	82.3%	23.30	91.8%	2.2 ± 49.6	73%
330K	P1	60.42	85.3%	23.30	91.8%	2.2 ± 45.7	73%
29K	P2	70.59	99.7%	25.01	98.5%	2.9 ± 6.1	97%
47K	P2	70.71	99.8%	24.81	97.7%	3.2 ± 6.4	107%
95K	P2	70.77	99.9%	25.16	99.1%	3.0 ± 5.8	100%
143K	P2	70.82	100.0%	25.39	100.0%	3.0 ± 5.6	100%
195K	P2	70.83	100.0%	25.39	100.0%	3.0 ± 5.7	100%

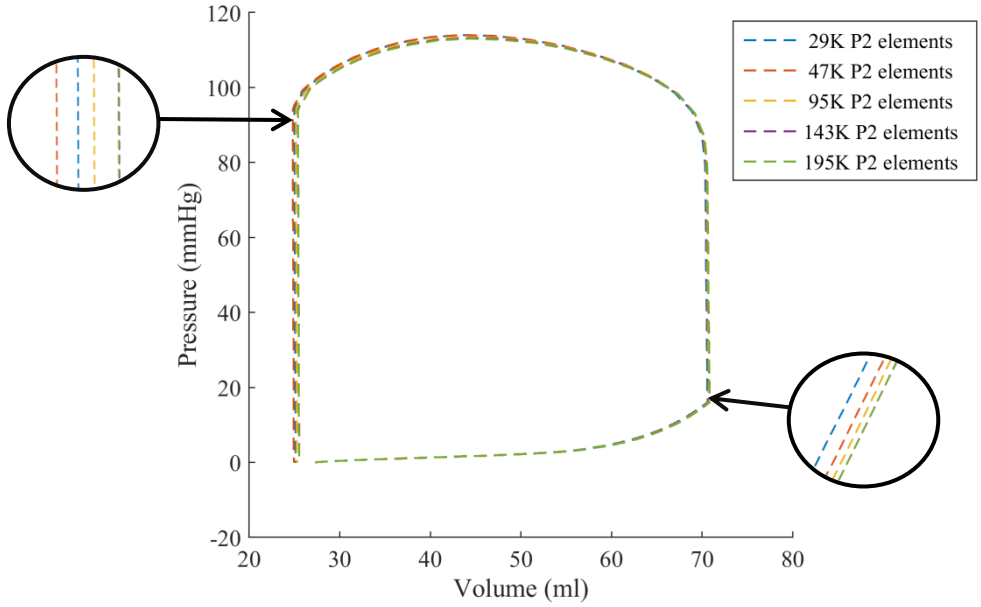

Fig. A.3: Mesh Convergence of P2 (quadratic) tetrahedral ranging from 29,000 – 195,000 elements. The PV loop of the left ventricle was plotted under the same conditions in all simulations. Even the coarsest mesh matches closely to the converged state. The ED state and ES state are zoomed in to minor differences in mesh response. For a mesh density exceeding 143,000 elements (purple lines) model results are fully converged.

A.2 Boundary condition analysis

To identify if boundary conditions dramatically influence model predicted strains, the model simulations were rerun using multiple configurations of enforced boundary conditions. The following configurations were considered:

I. The slave node of the truncated pulmonary trunk was fixed in all directions (PT).
II. The slave node of the truncated aortic root was fixed in all directions (AO).
III. The apex of the ventricles was fixed in all directions (AP).
IV. The slave node of the mitral valve was fixed in all directions (MV).
V. The slave node of the tricuspid valve was fixed in all directions (TV).
VI. All slave nodes of the ventricular valves were fixed in all directions (ALL).

None of these configurations had a significant effect on the Global circumferential strain as seen in Figure A4.

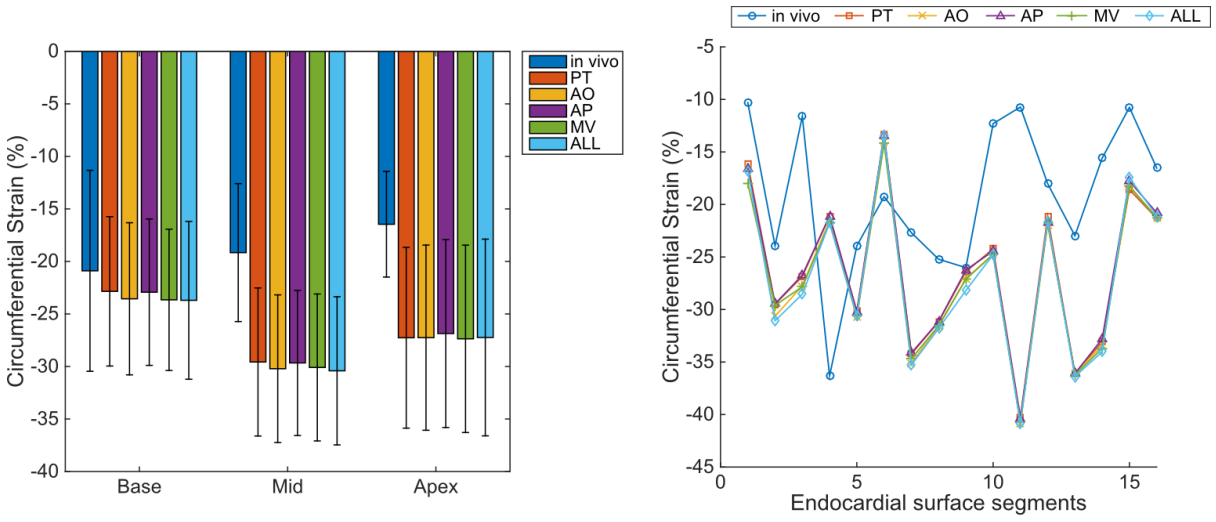

(a) (b)

Fig. A.4: Circumferential endocardial strain comparison between the in vivo measurements and the FE model strain under differing boundary conditions. (a) Mean strain results for each longitudinal region. (b): Strain results for each of the 16 endocardial surface regions. Abbreviations correspond to the boundary conditions outlined in the opening paragraph of this section.

Boundary conditions had a larger impact on longitudinal strains, although none if the configurations qualitatively changed the model predictions of strains, as seen in Figure A5.

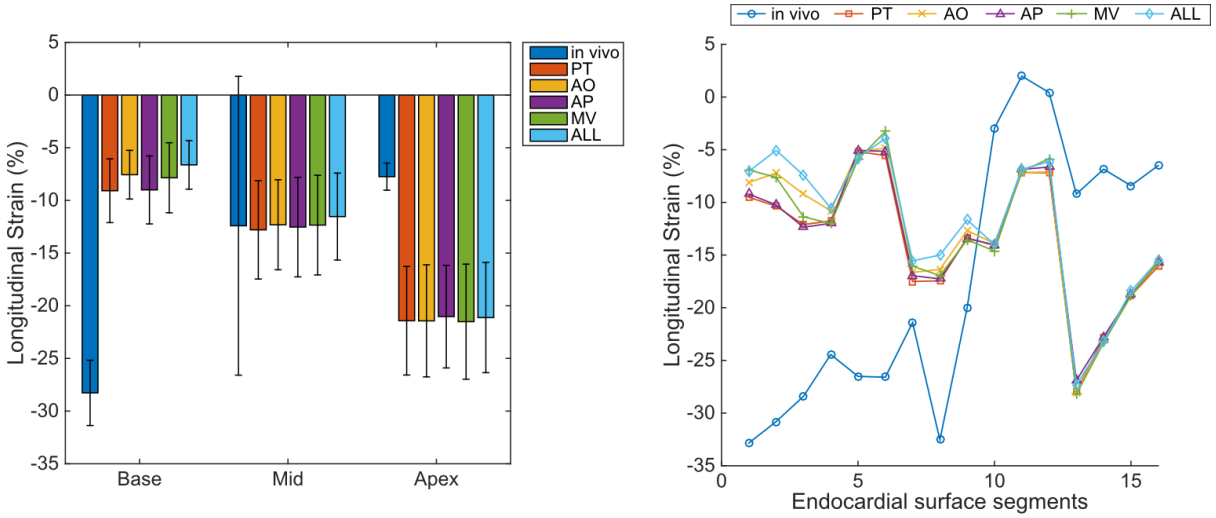

Fig. A.5: Longitudinal endocardial strain comparison between the in vivo measurements and the FE model strain under differing boundary conditions. (a) Mean strain results for each longitudinal region. (b): Strain results for each of the 16 endocardial surface regions. Abbreviations correspond to the boundary conditions outlined in the opening paragraph of this section.

Fixing the heart at the apex had no further benefit to longitudinal strains than fixing the node of the pulmonary trunk. This shows that the implementation of boundary conditions does not fundamentally alter the strain behavior of the ventricles.

It is likely, that the lack of the atria and the pericardium sac that encloses the four-chamber would have a much larger influence. Fritz *et al.* [208] studied the computational impact of including the pericardium in their simulations and discovered it contributed to the longitudinal motion of the atrial-ventricular plane.

Appendix B Supplementary data for Chapter 4

B.1 Geometric representations of NC subjects

A comparative figure revealing the geometric detail for the NC subjects is provided in Figure B1.

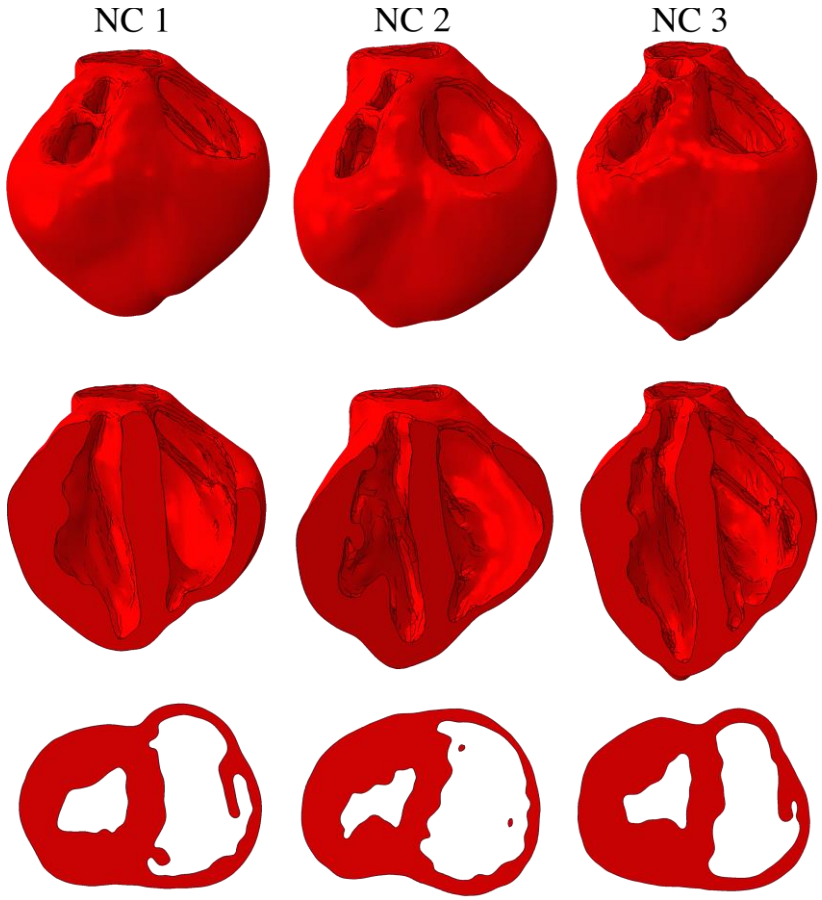

Fig. B.1: Unloaded FE model geometry of each of the NC subjects (columns) displaying the H_{INDEX} field. As these models are composed entirely with healthy tissue, this field is homogeneous (and equal to 1.0). Top row displays the full geometry, the middle row displays a long-axis bisected view and the bottom row displays a short-axis slice.

B.2 Detailed passive stiffness analysis

Calibrated passive filling curves for the NC, HFC and HFI subjects are presented in Figure B2, where the PV response for each LV inflated to 13.5 mmHg is given, normalized by the initial unloaded volume V_0. This is done so that each curve starts at 0% (i.e. initial unloaded volume) and at 100% the cavity is twice V_0. Worth noting, the two most compliant curves belong to the HFI group, while the stiffest curves belong to the HFC group.

The NC subjects experience the most clustered response seen qualitatively in Figure B2 and quantitatively in Table 4.3 that shows that the B value (the exponential scaling term, which has the dominant influence on the passive response) of the NC group has a very low SD.

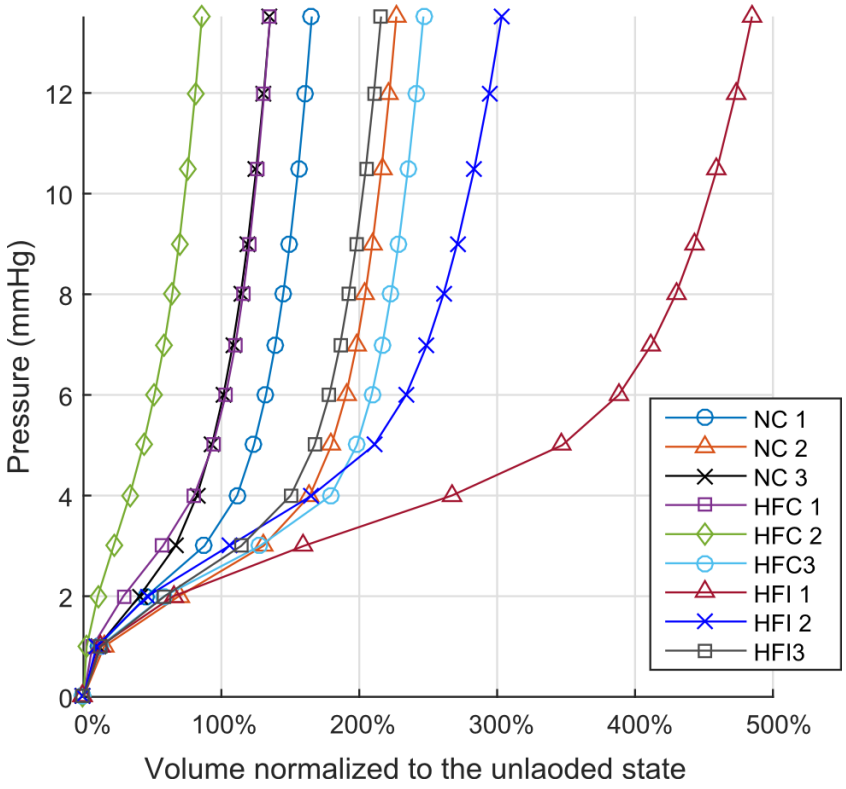

Fig. B.2: Passive filling curves for each subject loaded until 13.5mmHg. Volume was normalized to the unloaded configurations.

B.3 Subjects specific values of volumetrically averaged myofiber strain

Volumetrically averaged myofiber strain results for each ventricle of each subject at ED and ES are presented in Table B2. These strains reference the unloaded configuration as the strain free configuration.

Table B.2: ED and ES volumetric-averaged mean strain results for the converged cardiac cycle presented separately for the LV and RV. Results are presented with standard deviations.

	LV Myofiber strain (%)		**RV Myofiber strain (%)**	
Subject	ED	ES	ED	ES
NC 1	8.5 ± 5.3	-11.1 ± 4.7	6.6 ± 3.9	-10.6 ± 4.8
NC 2	8.5 ± 6.7	-8.8 ± 5.0	11.5 ± 5.7	-12.3 ± 6.5
NC 3	9.0 ± 4.2	-10.0 ± 3.8	3.9 ± 3.9	-6.6 ± 4.4
HFC 1	6.2 ± 5.1	-6.2 ± 6.7	6.5 ± 4.5	-7.6 ± 5.1
HFC 2	7.0 ± 4.3	-5.4 ± 6.5	5.4 ± 5.0	-8.2 ± 3.7
HFC 3	8.7 ± 8.3	-7.2 ± 10.2	4.4 ± 6.0	-9.7 ± 7.4
HFI 1	9.9 ± 11.5	-8.2 ± 11.6	13.7 ± 11.3	-14.4 ± 13.1
HFI 2	8.8 ± 8.2	-7.2 ± 9.2	14.1 ± 6.6	-18.4 ± 7.7
HFI 3	6.9 ± 6.4	-8.0 ± 7.5	6.7 ± 5.2	-12.4 ± 4.2

B.4 Short axis views of myofibre stress contours

Myofibre stress contours are presented in Figure B3 over short axis cut planes of the ventricular structures at ED.

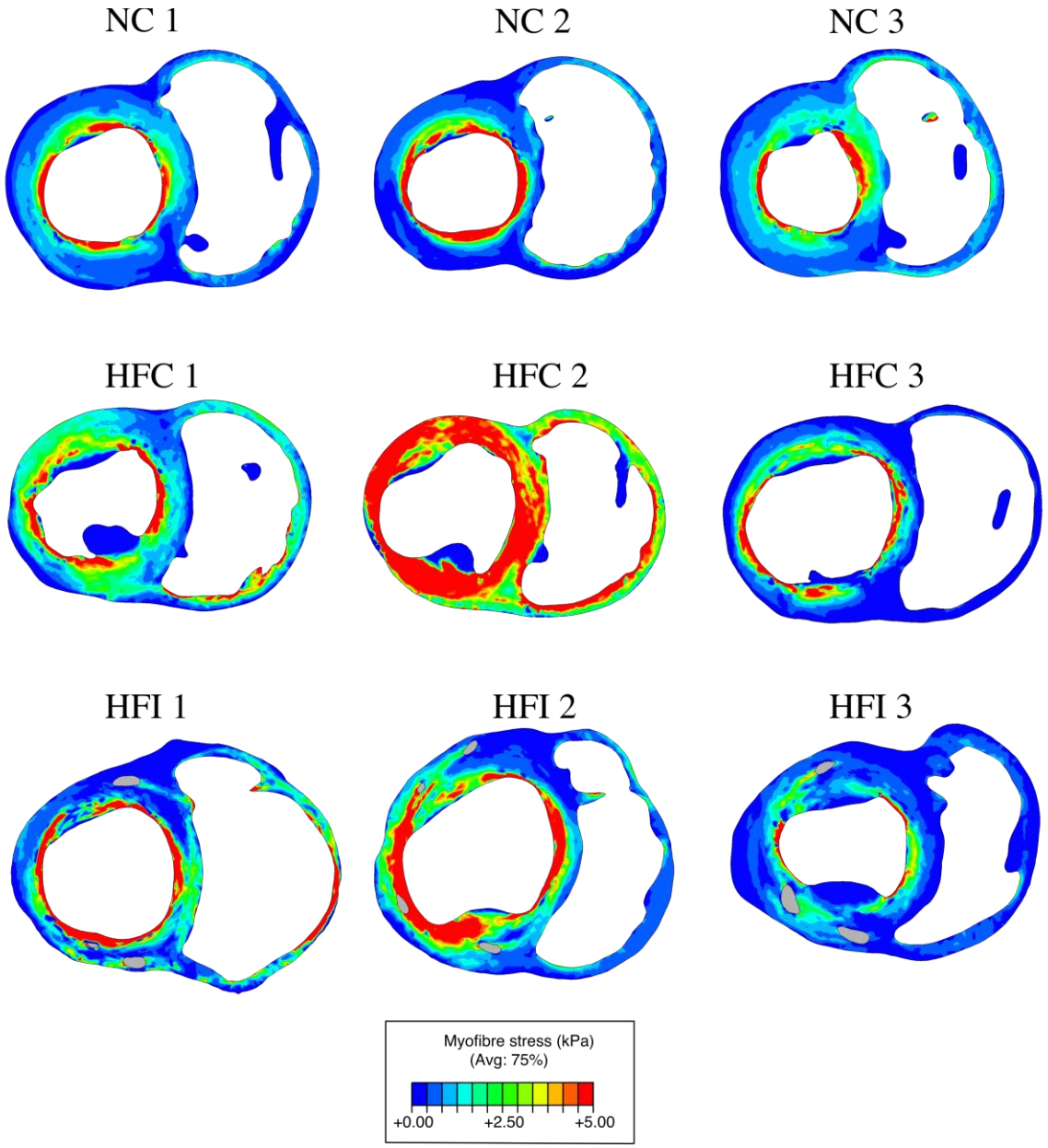

Fig. B.3: Myofibre stress at end-diastole for the NC, HFC and HFI subjects presented along short-axis cut planes of the ventricles. Injectates are coloured grey in the HFI subjects.